Multiphase Particle Engineering for Next-Generation Battery Electrode Manufacturing

A thesis submitted in partial fulfilment of the requirement for the degree of

DOCTOR OF PHILOSOPHY

By

Jediah Capindale

Under the supervision of Professor Rachel Smith and Dr Denis Cumming

University of Sheffield

Faculty of Engineering

Department of Chemical & Biological Engineering

August 2024

2024
Jediah Capindale

DECLARATION

I, the author, confirm that the Thesis is my own work. I am aware of the University's Guidance on the Use of Unfair Means. This work has not been previously presented for an award at this, or any other, university.

LIST OF OUTPUTS

Publications

- *Spherical Agglomeration for Local Control of Electrode Microstructure: Generation of Structured Agglomerates (2024)*. Pardikar. K, **Capindale. J**, Pitt. K, Abdi-Rahman. I, Cumming. D, Smith. R.M., *Powder Technology Journal*. (**Published, 2025**)

Conferences

- Faraday Institution ECR Conference, *Warwick (UK)*, 2022. **Poster Presentation**
- 10th International Granulation Conference, *Sheffield (UK)*, 2023. **Poster Presentation**
- Faraday Institution Conference, *Birmingham (UK)*, 2023. **Poster Presentation**
- PARTEC, *Nuremberg (Germany)*, 2023. **Poster Presentation**
- ChemEngDay, *London (UK), 2024.* **Poster Presentation**
- Nextrode Consortium Meeting, *Sheffield (UK)*, 2024. **Oral Presentation**
- AIChE, *San Diego (USA)*, 2024. **Oral Presentation**

ABSTRACT

Spherical agglomeration is a particle engineering technique used to generate novel secondary structures from primary particles through high shear agitation of a solid suspension in a continuous phase. A bridging liquid is added to the suspension which has a higher affinity to the suspended solids. The solids in suspension transfer from the continuous phase to the bridging liquid droplets due to an interfacial energy gradient. Spherical agglomeration is predominantly being researched for potential benefits in the pharmaceutical industry. The research presented in this thesis is the first to implement this particle engineering technique to improve battery manufacturing processes. The main aim is to improve primary particle handling and generate novel structures that could be used for dry electrode manufacturing, including both active material and conductive additive in one product. This will result in reduced operating time and cost involved with intensive battery manufacturing processes.

This thesis presents the design and implementation of spherical agglomeration for battery active materials and conductive additives to generate coagglomerates of the two materials. As expected, the true bridging liquid to solids ratio and impeller speed required for suitable suspension are key parameters to successful coagglomeration. It was also found that the interfacial energy gradient, determined through surface energy analysis of the solids and solvents, is vital for a thermodynamically spontaneous transfer of particles from the continuous phase to the bridging liquid droplets, and therefore, coagglomerates to be formed. Additionally, reducing the bridging liquid drop size reduced the coagglomerate size significantly, such that coagglomerates < 100 μm were produced. Increasing the bridging liquid droplet viscosity was seen to successfully reduce the rate of immersion and produce novel hollow coagglomerates. X-ray computer tomography was used to resolve the internal structure of the core shell and quantify the wall thickness and void volume of hollow coagglomerates. An energy balance was used to propose a modified capillary number and growth number, which describe the coagglomeration process as dimensionless numbers. A regime map was plotted with regions of coagglomerate structures seen throughout this research to help improve the efficiency of finding successful solvent systems required for coagglomeration. Finally an outlook on commercial application of spherical agglomeration was carried out, which found that the drying process was 2.7x less energy intensive than a traditional slurry cast process.

Dedicated to my Mum, Joby, Charlie,

and my dear grandparents,

Jacqueline & Denis Capindale

ACKNOWLEDGEMENTS

To my Mum, Joby and Charlie, thank you! Your support and encouragement throughout my life has lead me to where I am today. Without you, none of this would have been possible and I extend my greatest appreciation and love to you all! To Lesley and Alice, thank you for looking after me when I come down south to run away from Sheffield and PhD responsibilities, I am looking forward to spending time with the newest members of the Capindale family. To my Aunts, Uncles and Cousins, thank you for constantly taking an interest and asking how I am getting on, I think I am finished being a student now. This time for sure. Unless.

I would like to extend my gratitude to Professor Rachel Smith and Dr Denis Cumming, for their supervision over the past 4 years, and for constantly inspiring, motivating and challenging me. Your advice has been invaluable, and you have taught me more than just how to be a good researcher.

To Dr Kate Pitt, thank you for always being present and available, even in your free time outside of work. I cannot express how grateful I am to have had such a kind and enthusiastic mentor and friend for the past 6 years. Thank you for reading my work, teaching me academia survival skills and, most importantly, being there for a good old chat when things get stressful.

To oldest and dearest friends JP, Chris, Tom and Tommy, thank you for maintaining contact with me, even when I disappeared into my thesis for days on end. I promise to be better at replying now. To my Sheffield friends, Emily, Ben, Vicky, Sofia, Kyle, Pat, Guo, Kavi and James, thank you for dragging me outside for a coffee or a drink to maintain my sanity over the years. I cannot express the impact you all have had and my love for this city stems from you all.

To my colleagues and friends in the Nextrode group and Particle Technology Group, thank you for making me laugh day after day, and being such great collaborators and team members, both past and present. I will never forget the names and faces of everyone that has passed through and I look forward to working with you all in the future.

Finally, to the workshop and admin staff in the Department, without you none of the research we carry out would be possible. Mario Dorna, thank you for always having time to sit down and discuss a project, without you the XRCT work would not have been possible. Carla Teale, thank you for helping me organise all my admin work and constantly being available to answer my questions, however small they may be.

TABLE OF CONTENTS

LIST OF TABLES

LIST OF FIGURES

NOMENCLATURE

Bulk Density (kg/m^3)	ρ_{bulk}
Tapped Density (kg/m^3)	ρ_{tapped}
True Density (kg/m^3)	ρ_{true}
Envelope Density (kg/m^3)	$\rho_{envelope}$
Mass of Agglomerates (kg)	m_{agg}
Mass of Active Material (kg)	m_{AM}
Mass of Conductive Additive (kg)	m_{CA}
True Bridging liquid to Solids Ratio	$TBSR$
Beaker Internal Diameter (m)	D, T
Impeller Diameter (m)	D_i
Impeller Clearance (m)	C
Continuous Phase Liquid Height (m)	H
Baffle Width (m)	W
Normalised Volume-based Frequency (for a given bin range) (μm^{-1})	f_{vi}
Number-based Frequency (for a given bin range)	f_i
Midpoint of a Bin Range (μm)	$\bar{x}_i$
Bin Range (μm)	Δx_i
Just Suspended Impeller Speed	N_{JS}
Zwietering Correlation	S
Kinematic Viscosity (m^2/s)	v
Gravitational Acceleration (m/s^2)	g
Solids Loading (wt/wt)	X
Particle Diameter (m)	d_p
Volume of Agglomerate	V_{agg}
Bridging Liquid – Particle Interfacial Energy (mJ/m^2)	$\gamma_{\mathrm{BL,P}}$
Continuous Phase – Particle Interfacial Energy (mJ/m^2)	$\gamma_{CP,P}$
Bridging Liquid Surface Tension (mJ/m^2)	γ_{BL}
Continuous Phase Surface Tension (mJ/m^2)	γ_{CP}
Bridging Liquid Contact Angle (°)	θ_{BL}
Continuous Phase Contact Angle (°)	θ_{CP}
Dispersive Surface Energy (mJ/m^2)	γ_s^d

Polar Surface Energy (mJ/m^2)	γ_s^p
Work of Particle Transfer (mJ/m^2)	ΔW
Weber Number	We
Sphericity Factor of The Particle	Ψ
Sauter Mean Particle Diameter (m)	D_p
Interfacial Tension (mJ/m^2)	γ
Contact Angle	θ
Wall Thickness (for time = t) (m)	$H_2(t) - H_1(t)$
Critical Packing Liquid Volume Fraction	ϕ_{cp}
Capillary Length (m)	l_c
Worthington Number	Wo
Needle Diameter (mm)	D_n
Droplet Volume (mm^3)	V_d
Radius of a Sphere (mm)	r
Hollow Sphere Wall Thickness (mm)	τ
Radius of Envelope Volume (mm)	r_e
Radius of Void Volume (mm)	r_v
Capillary Number	Ca
Modified Capillary Number	Ca*
Agglomerate Volume Mean Diameter (m)	$d_{agg_{4,3}}$
Droplet Volume Mean Diameter (m)	$d_{drop_{4,3}}$

Chapter 1 - Introduction

With an ever-increasing demand for 'clean' energy, rise in popularity of portable electronic devices and government environmental targets being more important than ever, energy storage solutions are becoming increasingly vital for societal demands [1]. Electric vehicles (EV's) are of particular interest to governing bodies and consumers, reducing the mobile pollution that fuel-based vehicles emit. However, the problem with EV's is meeting the demands of the user, particularly with increasing range on a single charge, lifespan of the batteries and reduced cost of entry. These factors are driving the consumer opinion on whether to invest. Therefore, it is important for battery technology to advance to meet the consumer criteria. The upfront cost of EV's is heavily reliant on the battery cost [2]. Reduction of battery cost depends on a multitude of factors in the battery production life cycle, however implementing both new materials, and novel manufacturing processes are the key strategies.

The work surrounding new material chemistries is particularly saturated in the literature with less focus on the improvement of manufacturing processes. For example, when manufacturing electrodes, harmful solvents are used to enable spreading of electrode material on the current collector, and therefore an expensive drying stage is required to achieve the final electrode product. Additionally, during this drying stage as the solvent evaporates, the carbon additive can migrate creating a heterogeneous electrode cross section [3,4]. Another issue associated with electrode manufacturing is the handling of fine cohesive powders used as active material and carbon additives. This thesis aims to offer a solution to these issues through introduction of a novel particle engineering technique called spherical agglomeration.

Spherical agglomeration is used as a process intensification technique, in the pharmaceutical industry, to carry out the crystallisation and agglomeration process in one system. However, for systems that do not require crystallisation, the process can be operated using particles in suspension. This is often referred to as agglomeration in suspension and requires a continuous phase fluid that makes up the bulk suspension, and a bridging liquid that has preferential wettability with the solid and is immiscible in the good solvent. The process then is well agitated to capture the primary particles in the bridging liquid droplets through immersion. This process could be used for electrode active materials and conductive additives, as a way of tailoring secondary structures of particles, and is an interesting area of research that has yet to be investigated.

Implementation of spherical agglomeration for battery materials has the potential to remedy the processing issues mentioned previously. The high shear agitation imparted by the stirred tank enhances distribution of the active material and conductive additive between one another. This creates agglomerates with an interlocked matrix of the two materials which, when distributed on the current

collector, may improve the homogeneous distribution of components across the electrode. The particle enlargement from primary particles to agglomerates also improves the flowability/handling of the feedstock for electrodes. The well distributed components and improved handling means the agglomerates would serve well in a dry electrode production process. An example is the roller pressed electrode process where dry electrode material is pressed onto a current collector by passing through a thin gap between two rollers. By having pre-distributed active material – conductive additive agglomerates, which handle well without dust, the need for dangerous solvents and expensive drying stage is negated. Additionally, in the spherical agglomeration process the agglomerates formed can be separated out as product and the solvents can be recycled easily.

1.1 Research Aims

The aim of this research is to develop a successful agglomeration process for battery electrode materials to alleviate some of the challenges associated with wet slurry cast electrodes. The process aims to reduce the need for highly toxic solvents and create directly compressible secondary structures which can be implemented into a dry electrode manufacturing process. Due to the novelty of this process, this will involve identifying a suitable solvent system with appropriate preferential wettability criteria. Additionally, since there is a wide variety of active materials, a thermodynamic analysis of the immersion process will be investigated. This is to aid in quicker identification of feasible solvent systems required for future studies into spherical agglomeration of different material. To help direct the research the following objectives have been identified:

- Design a batch agglomeration process for an active material and conductive additive suspension
- Quantify the effect of solvent wettability on the thermodynamic feasibility of solids to immerse in bridging liquid droplets
- Investigate how process parameters of an agglomeration process in a stirred tank effect the agglomerate properties
- Further develop the mechanistic understanding behind the immersion of particles
- Investigate how to reduce the rate of immersion into droplets to generate hollow structures beneficial to dry compressive electrode manufacturing processes
- Investigate how surfactant and addition method effect the agglomerate size with the aim of generating agglomerates at length scales suitable for electrode design
- Develop techniques for analysis of agglomerate size and structure via image analysis, x-ray computer tomography etc.

1.2 Thesis Structure

Chapter 2 will outline a study of the literature surrounding both spherical agglomeration and battery manufacturing processes. Understanding of the issues involved in battery manufacturing and methods to solve them will be critically discussed and gaps in the knowledge will be highlighted. There will be a particular focus on the particle engineering solutions to issues relating to battery manufacturing, with less of a focus on the material chemistry.

Chapter 3 discusses the materials used in this work and their characterisation, detailing the general properties they exhibit. Additionally, routine methods used throughout this thesis and experimental studies, are discussed in this chapter. Any materials or methods specific to a chapter, or experiment, are detailed in that respective chapter.

Chapter 4 presents the findings from developing a successful spherical agglomeration system for battery active materials and characterises the products generated. This chapter also conducts a parametric study of the process and the effect on agglomerate product properties. A thermodynamic analysis is introduced to quantify the feasibility of spherical agglomeration systems based on the interfacial energies of solvents used.

Chapter 5 develops the spherical agglomeration process further to generate <100 μm agglomerates by controlling the bridging liquid droplet size.

Chapter 6 investigates the effect of reducing immersion rate in agglomerate formation by increasing the bridging liquid viscosity. X-ray Computer Tomography is used to investigate the internal structure. The thermodynamic analysis developed in Chapter 4 is assessed for viscous bridging liquids.

Chapter 7 develops the theory of particle immersion into the bridging liquids droplets. Novel dimensionless numbers and a regime map are proposed to predict the agglomerate structures generated, based on mechanistic understanding developed throughout this research.

Chapter 8 discusses the potential for spherical agglomeration to be implemented at an industrial scale and the benefits to sustainability. This includes an energy analysis of the intensive drying process when compared to a traditional wet slurry cast process.

Chapter 9 concludes the thesis outlining the understanding developed in each chapter and proposes future work that would help propel this research further.

Chapter 2 - Literature Review

This chapter will present a review of the literature surrounding both lithium-ion batteries and spherical crystallisation. Battery research is vast in its documentation and for the purpose of this thesis, the focus will be narrowed towards to the research surrounding lithium-ion battery electrodes. Spherical crystallisation is a particle processing technique found commonly in the pharmaceutical industry and has more limited literature surrounding it. However, it also has a subset of different techniques that can be employed under the umbrella term of spherical crystallisation; including spherical agglomeration, quasi-emulsion solvent diffusion and ammonia diffusion [5]. This literature review will focus on the spherical agglomeration technique, also branching into the area of co-agglomeration, which is an extension of the spherical agglomeration technique, however working with two solids of interest rather than one [6].

Lithium-ion battery research is particularly important for achieving the environmental targets set out by governing bodies for reducing CO_2 emissions, whilst being able to help reduce the burden on increasing global demand for energy [7]. Electric vehicles will play a significant role in reducing 'mobile' emissions and help reach environmental targets. Therefore, a particular focus of the research presented in this literature review will be the potential to increase energy density of a lithium-ion battery. This is primarily for increasing the distance electric vehicles can travel as a result of increased energy density and capacity. This is commonly done through the implementation of new chemical compositions of anode and cathodes with valuable benefits [8–10]. However, a less populated area of research is the manipulation of electrode structures for given electrode chemistries. Tailoring electrode structure can help mitigate issues that arise through charge/discharge cycles such as electrode cracking, volume changes cell degradation and gas evolution, and therefore improve the energy density and lifetime of the cells [10,11].

Spherical crystallisation offers a novel technique for particle design that is currently being researched in the pharmaceutical industry as a way of improving particle mechanical properties, whilst also being a process intensification technique combining crystallisation and agglomeration [12]. The secondary structures generated help improve the process line of the manufacturing process through improved flowability of the solids, and when incorporated in electrode manufacturing hold potential for improved dry manufacturing processes. Spherical crystallisation typically uses a three-phase system, where a good solvent and anti-solvent drives a solvent change mechanism to precipitate out a solid from solution [5,13]. The presence of a third solvent, called the bridging liquid, with preferential wettability for the solid is used to capture these solids through immersion or distribution mechanisms. There is less research on spherical crystallisation when compared to lithium-ion battery research, due to the novelty of the process. However, for the research that is available it must be viewed critically as the mechanistic

understanding can vary depending on the components used in the process; for example, what works for a salicylic acid system might not work the same as for paracetamol system [14,15].

Spherical agglomeration is the main technique analysed in this thesis, and this literature review will report how process conditions affect the properties of the agglomerates. Bridging liquid to solid ratio is one of the most important factors to assess when identifying a new system of agglomeration. Most commonly spherical agglomeration uses the three-phase system, however spherical agglomeration in suspension can be used for systems that do not require precipitation of solids [16–18]. For this thesis, the main solid to be agglomerated is graphite for use in the anode. The graphite particles are already synthesised and agglomeration in suspension will be employed as a post processing technique. This will require only two solvents: the good solvent (continuous phase) and bridging liquid (dispersed phase).

2.1 Lithium-Ion Batteries

2.1.1 Overview

Battery research fulfils a fundamental need for improved energy storage throughout multiple sectors. Portable electronic devices such as mobile phones are becoming increasingly common with demand for greater charge capacity and more powerful technology. The UK and Global demand for a more varied and sustainable energy grid will require the use of energy storage systems; in particular, for ‘greener’ technologies such as wind and solar which cannot be tuned to operate on-demand, whether this be to store excess energy or provide a buffer for lower production days. Furthermore, with increased drive towards decarbonisation and more sustainable energy practises, the sale of electric vehicles (EV) is increasing steadily with consumer demand for improved batteries that can last longer and charge faster. By 2032, 30 % of all passenger vehicles globally are forecast to be EV’s [19]. For these reasons it is clear why battery technology is a well populated and important area of research.

Lithium-ion batteries (LIBs) are considered the most common systems due to their advantageous properties, particularly high energy density, long lifetime, low cost and environmental friendliness [20]. There are many components that make up LIBs and research spans across all of them, with attempts to optimise performance and capacity. Figure 2.1 shows the components that generally make up a LIB; of which the main components are the anode, cathode, respective current collectors and electrolyte.

LIB’s utilise potential energy between the anode and cathode through which lithium ions are transferred by means of diffusion through the electrolyte and subsequent transfer of electrons through the current collector and attached circuit [21]. This can be seen in Figure 2.1, where upon discharging, the lithium ions diffuse from the anode and into the cathode. Likewise, the electrons transfer through the circuit providing energy as they travel to the cathode. The opposite occurs when the cell is being charged

utilising the work done by an external charging source to transfer the lithium ions and electrons to the anode.

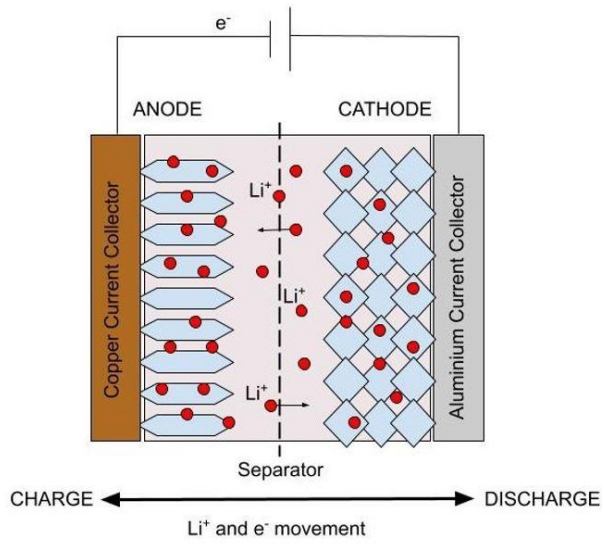

Figure 2.1: The general components required to manufacture a lithium-ion battery and the flow of lithium ions and electrons during charge and discharge

At a smaller scale, the anode and cathode have similar components comprising the active material (AM), carbon additive (CA) and some form of binder (B), this can be seen more clearly in Figure 2.2 [22]. This figure shows a form of idealised structure where the AM is coated by CA and is homogeneous in distribution of each component. This would enable ideal diffusion of lithium ions with less tortuous ion diffusion pathways and enhance the transfer and interaction with the electrons. Figure 2.2 shows relevant resistances to the mechanism within the electrode and electrolyte, and these are discussed further in Table 2.1.

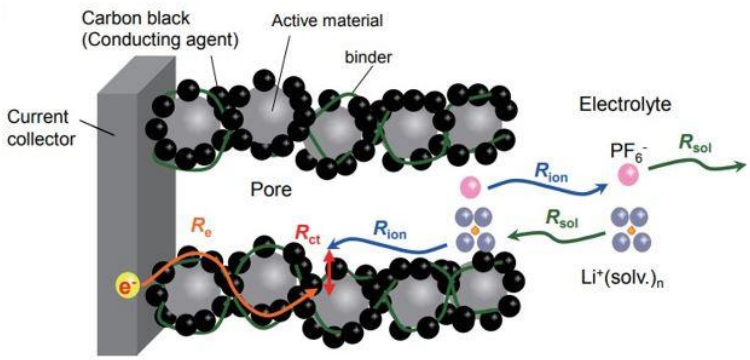

Figure 2.2: Standard electrode components including the active material, conductive additive and binder distribution. Relative resistances during the lithiation/delithiation process are also shown [22]

Table 2.1: Relevant resistances within an electrode and electrolyte during charge or discharge, shown in Figure 2.2 [22]

Resistance	Description
Electronic Resistance (R_e)	The resistance to electron flow between conductive additives within the electrode
Charge Transfer Resistance (R_{ct})	The resistance to lithium-ion transfer from the electrolyte into the active material
Ionic Resistance (R_{ion})	The resistance to lithium ions breaking ionic bonds with the electrolyte solution molecules before transfer to the active material
Solution Resistance (R_{sol})	The resistance to bulk movement of the electrolyte molecules through the solution, from one electrode to the other

2.1.2 Active Material Research

Many cathodes are formed from a lithium oxide as the electrode active material, commonly $LiCoO_2$ or $LiNiO_2$. Transition metals may also be substituted to improve some property of the electrode, be it capacity, stability or flammability. There can be a variety of transition metals used at the same time in the cathode compound with different ratios and this generates a vast amount of research and literature that investigates the benefits and limitations of different chemistries. There are alternative cathode materials which exhibit different crystal structures such as layered ($LiCoO_2$), spinel ($LiMn_2O_4$), olivine ($LiFePO_4$) and tavorite ($LiFeSO_4F$) [8], as can be seen in Figure 2.3. These material structures utilise the same intercalation mechanisms, however with different layouts in which the guest lithium ions are hosted.

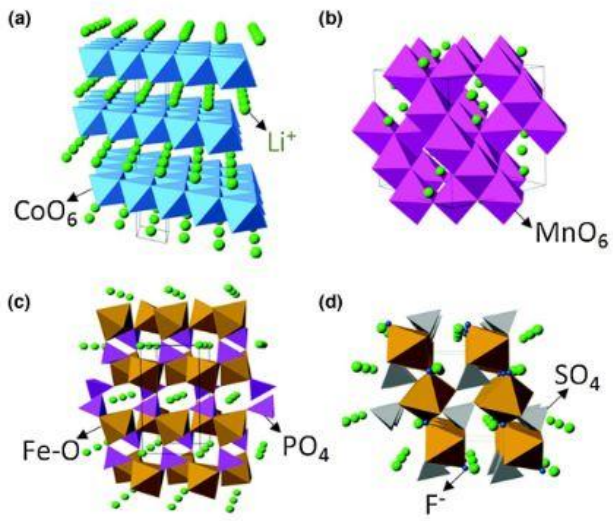

Figure 2.3: Example cathode active material crystal structures, a) layered, b) spinel, c) olivine, d) tavorite [8]

The focus of most battery manufacturers is the layered cathode, such as $LiCoO_2$ or $LiNiO_2$. However, there is a particular rise in popularity of $LiFePO_4$ cathode materials due to the greater relative abundance, cheaper cost and reduced flammability. Lu et al. (2020) [9] reported recent advances and limitations in commercial cathodes, and outlined how $LiCoO_2$ cathodes are the main choice for portable electronics since they display high theoretical capacity and good cycling performance [8]. However, due to lower discharge capacity and toxic cobalt increasing environmental concerns and raising the cost of LIB's, research focus has shifted away from $LiCoO_2$. Lu et al. (2020) also stated that Ni-rich cathodes ($LiNiO_2$) prove to be the future for EV batteries due to their high energy density and lower cost when compared to cobalt rich cathodes [19,23,24]. As with most cathode choices, Ni-rich cathodes come with drawbacks particularly in thermal stability and cost of production, and particularly in lithium loss due to reduced nickel ions (from Ni^{3+} to Ni^{2+}) replacing lithium-ion sites in the structure during delithiation [8,25].

To combat the Ni-rich cathode limitations transition metals are used to replace some of the nickel content within the active material structure and improve stability and kinetics of the electrode. The most common transition metals used are cobalt, manganese and aluminium to produce cathode material of the form $LiNi_{(x)}Co_{(y)}Mn_{(z)}O_2$ called NMC, and $LiNi_{(x)}Co_{(y)}Al_{(z)}O_2$ called NCA (where $x + y + z = 1$). There are many different formulations of NMC, however common compounds that are found in literature, particularly for next generation electrodes, are; NMC-811, NMC-622 and NMC-955. The number included after the NMC acronyms refers to a particular ratio for the x, y and z mentioned previously. Hence for NMC-811, this refers to 80 % nickel, 10 % cobalt and 10 % manganese. The ratio of these depends on the qualities that are required from the electrode, which is usually a balance between the properties nickel, cobalt and manganese offer; being capacity, rate and safety respectively [25]. In most compositions the nickel content is comparatively high to maximise the energy density and improve

capacity. However, increasing manganese improves the safety by reducing flammability, and increasing the cobalt ratio improves the rate capabilities of the active material. These are highly beneficial, but by increasing the ratio of cobalt and/or manganese the trade-off is a reduction in the active material capacity as nickel concentration reduces. If the safety and rate properties that cobalt and manganese offer can be incorporated through other methods, such as particle or electrode engineering, then the concentration of transition metals can be reduced, therefore increasing the nickel concentration.

Due to the versatility of graphite in accepting lithium ions and ability to cope with the accompanying volume change, it is often used as the anode material [26]. Graphite has a hexagonal plate-like structure with covalently bonded carbon atoms, and weak van der Waals forces holding the horizontal basal planes together. It is this layered structure that provides graphite with versatile intercalation properties. In between the loosely packed plates exists a gap of approximately 3.35 Å, in which the guest lithium ions can be hosted during intercalation [26,27]. Graphite anodes appear to be less of a limiting factor compared to issues that affect NMC cathodes, due to better thermal and mechanical stability. However, Chang-Jian et al. (2018) [28] suggest that graphite is unable to cope with the demand of electric vehicles for use as an anode material. This is attributed to graphite being susceptible to low-rate capability, poor cycling stability and the potential for lithium dendrite formation. Lithium dendrites are formed when lithium is deposited at the electrolyte interface and can grow long enough to penetrate the separator and short circuit the cell when contacting with the cathode [29]. This has serious implications in that short circuiting can lead to explosions and/or fires. Dendrites that break can also form a layer of 'dead' lithium that reacts with the electrolyte and forms a solid electrolyte interface (SEI) layer. This is an example of irreversible capacity loss and an increase in the internal resistance.

Therefore, there is still research taking place in improving anode chemistry. One area of research focuses on silicon active materials instead of graphite, as silicon anodes have a very high theoretical capacity. The issue that these anodes face is that they suffer large volume changes during charge/discharge leading to loss of stability, side reactions and poor cycle life [30]. As part of the Chang-Jian et al. (2018) [28] work, another anode active material was proposed called lithium titanite ($Li_4Ti_5O_{12}$, LTO), which has a spinel type structure, similar to that seen in Figure 2.3b. LTO exhibits good lithiation/delithiation characteristics with a low anisotropic volume change (low strain on active material), and this enhances the materials cycling stability and lifetime. However, low conductivity and lithium-ion diffusion coefficients affect LTO's feasibility as an anode material (particularly in EV applications). These properties limit the anode materials rate capability, which is not ideal, particularly for EV's, which require fast charging for consumers to consider adopting the technology.

2.1.3 Electrode Manufacturing

Industrial manufacturing of lithium-ion battery electrodes operates continuously using conveyer systems and requires a manufacturing site with a large footprint. Production of the anode and cathode

begins with slurry mixing of the active material, conductive additive and binder with a solvent. A high shear mixer is used to distribute the primary particles homogeneously within the slurry, due to the highly branched nature of conductive additives and binder components [31]. The extent of distribution within the slurry directly impacts the electrode structure, therefore the initial slurry mixing step is crucial for manufacturing an effective electrode. The anode or cathode slurry is then coated onto the current collector, made of copper or aluminium foil respectively, using a slot – die coater to keep the thickness of the spread as even as possible. The slurry cast electrodes are then passed through a drying stage, using hot air to evaporate the solvents, which were used to distribute the primary particles. The drying step helps to solidify bonds between the electrode material and the current collector. The electrode is then calendered using a roller press to achieve a desired thickness/porosity and also to promote connections between the active material, conductive additive and current collector [32]. Once the anode and cathode have been manufactured, they can be processed into different batteries depending on the intended use. Figure 2.4 shows the general production life cycle from primary particles to the formed battery. There are many steps however work presented in this thesis will identify and develop manufacturing techniques for improving the first two unit operations of electrode mixing and electrode coating and drying.

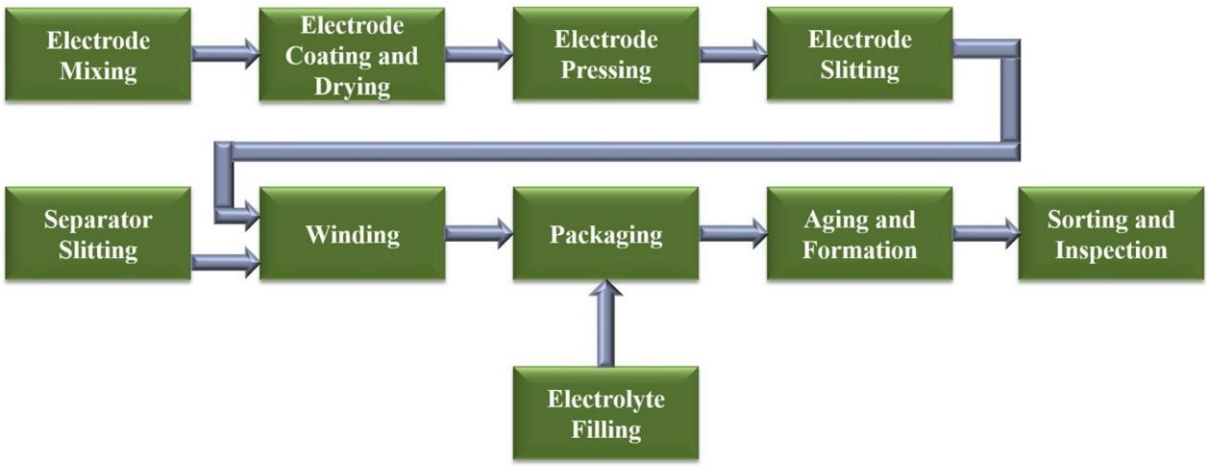

Figure 2.4: Unit operations of electrode manufacturing in an industrial setting [33]

In research, two types of cells are commonly used to analyse the electrochemical properties of produced electrodes. Coin cells and pouch cells are not designed to be long lasting or particularly high-capacity cells, however they provide insight to the research.

Coin Cells

An example of a CR2032 coin cell can be seen in Figure 2.5, where the number CR2032 refers to the type of coin cell based on its dimensions being 20 mm in diameter and 3.2 mm thick. This shows how small these coin cells are and make testing fast and easily repeatable due to the small amount of material required. Just like the industrial process, the active material, conductive additive and binder are mixed

to make a slurry using an appropriate solvent. This slurry is then coated onto the relevant current collector for the anode or cathode, using a piece of equipment called a doctor blade to keep the thickness of the spread as even as possible. The slurry cast electrode is dried and then calendered to a desired thickness, as discussed earlier.

For a coin cell, circular discs of the electrode material are 'punched' out from the electrode sheets. These are then used as the respective anode and cathode material, as seen in Figure 2.5. It is important to know the dimensions of the disc so that active material loading can be calculated such that measurements can be compared between different cells created for testing. This is important for coin cells where multiple tests must be carried out due to random variations in electrode composition across the casted slurry [34]. Figure 2.5 also shows the separator which is usually a glass microfiber soaked in electrolyte and placed between the two electrodes. The spring shown in Figure 2.5 is used to maintain a pressure such that contact is maintained between components in the coin cell [35]. When the coin cell is complete the casing is sealed together using a crimper, this prevents both leakage of cell components and ingress of moisture. Although coin cells can be beneficial for being able to test several repeats in a single batch of electrode material, there are also some limitations. An excess of electrolyte is used and "the cell body has a relatively large thermal mass" [34] which can mask problems that will only become evident at a larger cell scale. Equally, the creation of a coin cell can be difficult with small parts when making a large amount of them to test and sometimes they will not offer a full understanding of the cell electrochemical potential and issues when compared to a larger stacked cell. Additionally, due to heterogeneity across the total cast electrode, coin cells could show inaccurate data and good sampling is required.

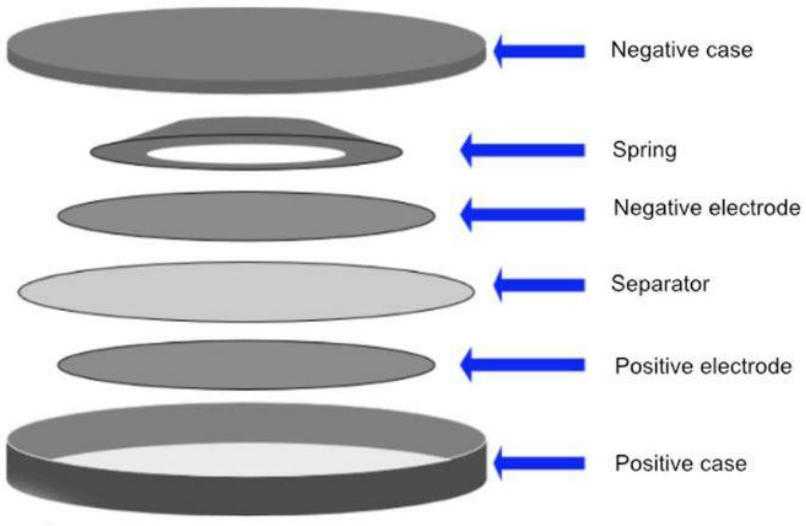

Figure 2.5: Order of the components that comprise a typical coin cell [36]

Pouch Cells

An example of a pouch cell can be seen in Figure 2.6. The slurry cast electrode is made in the same way as the coin cell, however instead of a circular disc, rectangle sheets are generally used. These sheets can either be stacked to create a multiple layer pouch cell, or instead one cathode and one anode can be used to create a single layer pouch cell. The electrodes are layered together and the cathode and anode current collectors have a small tab extruding from the main part of the layers to which the terminals are attached post production [37]. In between each layer is a separator which will become saturated with the electrolyte. The stack is then packaged using a heat seal on the packaging material and dried, after which electrolyte is added and the pouch is fully sealed and degassed [38]. The pouch cell will tend to have higher electrochemical potential than a coin cell simply due to increased loading of active material in the larger cell. This is why it is important to know the active material loading, so that the results can be compared between cells on a 'per mass' basis. The pouch cell has light, flexible packaging which allows for volume change during charge/discharge. This can be important from a safety perspective too, if the cell has an unexpected temperature rise during testing and a volume change occurs. Conversely, having a soft, flexible packaging material also introduces the possibility for cell damage, both to the packaging and to the internal electrode.

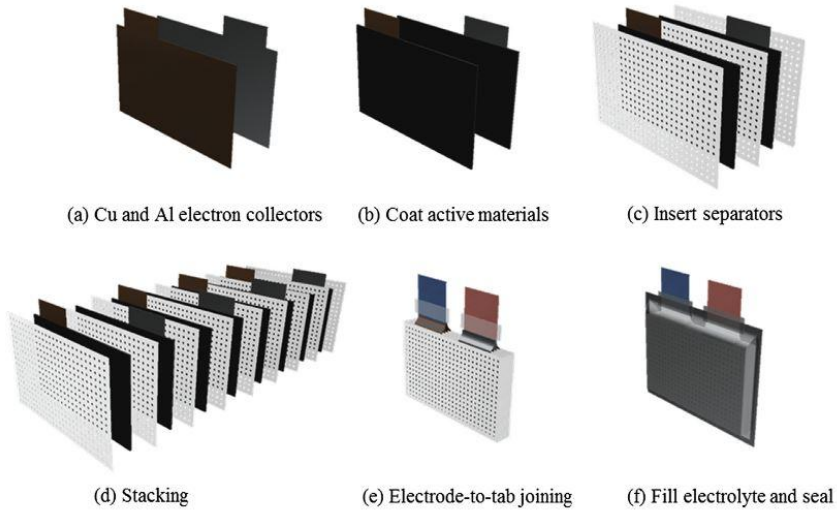

Figure 2.6: Production and configuration process for a typical multilayered pouch cell [37]

2.1.4 Electrochemical Characterisation

To understand the effect that engineering research has on an electrode, electrochemical testing is carried out, generally the two cell configurations mentioned previously are used: coin cell and pouch cell. Although electrochemical characterisation was not carried out during the experimental work discussed in this thesis, understanding of basic electrochemical characterisation is important for understanding the context of electrode performance. Dugas et al. (2019) [35] review the best methods and protocols for reliable electrochemical testing of cells, in this case specifically coin cells were used in the research

for testing. The paper describes how through multiple charge and discharge cycles three key electrochemical measurements can provide insight to the performance of a test cell. These are capacity, coulombic efficiency and capacity retention. Although there are a multitude of electrochemical tests that could be carried out these three are quoted in literature the most frequently.

Capacity is the characteristic that defines how much charge a cell can hold when charged, and equally it is the amount of charge a cell can release on discharge. In the literature, capacity is generally reported on a a gravimetric or volumetric basis, with units of mAh/g and mAh/L respectively, called the specific capacity. This is done so that cells can be compared rather than using the nominal capacity, which is a function on the amount of active material in the electrode. The process through which capacity is measured is a complex process of charge and discharge cycles. First, the cell is subjected to a constant current charge up until the upper cut off voltage is achieved (normally 4.2 V for high voltage cells) and then instantly the charging switches to constant voltage charge until a minimum current is achieved [39,40]. This whole process is called constant current constant voltage (CCCV) charge. The next step can either involve discharging at a constant current to reach a given lower voltage, known as a CC discharge. Alternatively, the cell can be discharged at a constant voltage to reach a given lower current. The capacity (mAh) can be calculated by multiplying the discharge current (mA) by the time taken (h) to discharge to a cut off voltage.

The capacity defines a key term used in electrochemical testing called the C-rate. The C-rate is defined as a rate at which a cell discharges in relation to the capacity. Cycling cells for characterisation is carried out at a specific C-rate, where 1C is a specific discharge current at which discharge takes 1 hour. Therefore, a C-rate of C/2 would be a current for which discharge takes 2 hours to complete. This is due to a reduced current loading on the cell. Table 2.2 shows the discharge times for the most common C-rates used in electrochemical testing.

Table 2.2: Discharge times for common C-rates used for battery cycling during electrochemical characterisation

C-Rate	Discharge Time
0.1 C	10 hours
0.2 C	5 hours
0.5 C	2 hours
1 C	**1 hour**
2 C	30 minutes
5 C	12 minutes

Electric vehicles operate at high C-rates due to the rate at which power is required for acceleration. Generally, specific capacities are lower at higher C-rates and degradation can occur faster due to more

stressful charge and discharge. Therefore, research into high C-rate batteries is an important area to consider. A common form of comparable electrochemical characterisation used in the literature is the specific capacity (mAh/g) measured against the cycle number at different C-rates. Cycles are initially run at low C-rates such at C/5 for several cycles and then increase through C/2, 1C, 2C, 3C, 5C, for several cycles each, measuring how the specific capacity changes. Then after several cycles at a high C-rate the test will then reduce the C-rate back to a low value such as C/5. By reducing the C-rate back to a low value after cycling at high C-rate, the effect of the stressful high-power cycles can be assessed more clearly, and capacity loss can be compared to the initial cycles measured at C/5.

The capacity retention is another key metric, which is a measure of the charge/discharge capacity after a high number of cycles. The specific capacity generally reduces over multiple charge/discharge cycles, due to degradation of the electrode. A higher capacity retention is indicative of a longer battery life and is given as a percentage of the initial charge/discharge capacity. The cycle life is the number of cycles that it takes for the battery to reach a specified capacity retention. For example, some portable electronics are “end of life” when they reach 80 % capacity retention, and a new battery is required. Finally, the coulombic efficiency is a measure of the efficiency of discharge capacity with respect to charge capacity, also given as a percentage. A high coulombic efficiency indicates that there are less unwanted side reactions, and the battery operates more efficiently for each cycle.

2.1.5 Particle Engineering

The majority of research focuses on new chemistries for cathode and anode materials, however, there is merit in understanding and researching the effect of structure on electrode performance. As mentioned in Section 2.1.2 , nickel-rich cathodes are a key area of research for improving capacity of batteries with a focus on EV’s. The main issues suggested as ‘areas of improvement’ by Lu et al. (2020) [9] for Ni-rich cathodes are: thermal runaway, transient-metal ion dissolution, gas evolution, rock salt phase formation, residual lithium species and finally microcracks. These problems propagate as nickel concentration is increased.

Microcracking is considered one of the biggest issues facing cathode structures in batteries, particularly when they are Ni-rich [10,11,41]. The anisotropic volume changes from nickel in cathode structures can create microcracks. The issue propagates as more surfaces of the active material are then present for degradation and reaction with the electrolyte. Yin et al. (2021) [41] further discusses how this affects multiple aspects of the battery quality, ‘decreasing thermal stability, structural stability and cyclic stability of the cathode simultaneously’.

Lu et al. (2020) [9] outlines how reshaping the structure of the primary particles that make up the active material could mitigate some of the issues with Ni-rich cathodes. Park et al. (2018) [10] shows how boron doping of NMC, even at a low concentration of 1 mol%, can lead to surface energy changes

which affect the growth of the primary crystal structure, this can be seen in Figure 2.7. In this case, the usually rounded crystals show more columnar elongation/growth to create needle like particles. After coalescence both the doped and non-doped secondary structures appear spherical. However, looking at a cross-sectional SEM image of the secondary structure it is evident that the packing and primary particle ordering is different. The rhomboidal non-doped NMC appears to have random packing, whereas the boron doped acicular primary particles organise themselves radially. This radially organised structure of acicular primary particles reduced the tortuosity and microcracking from anisotropic volume changes during (de)lithiation. Which in turn prevents degradation of the active material and maintains its capacity over multiple charge/discharge cycles.

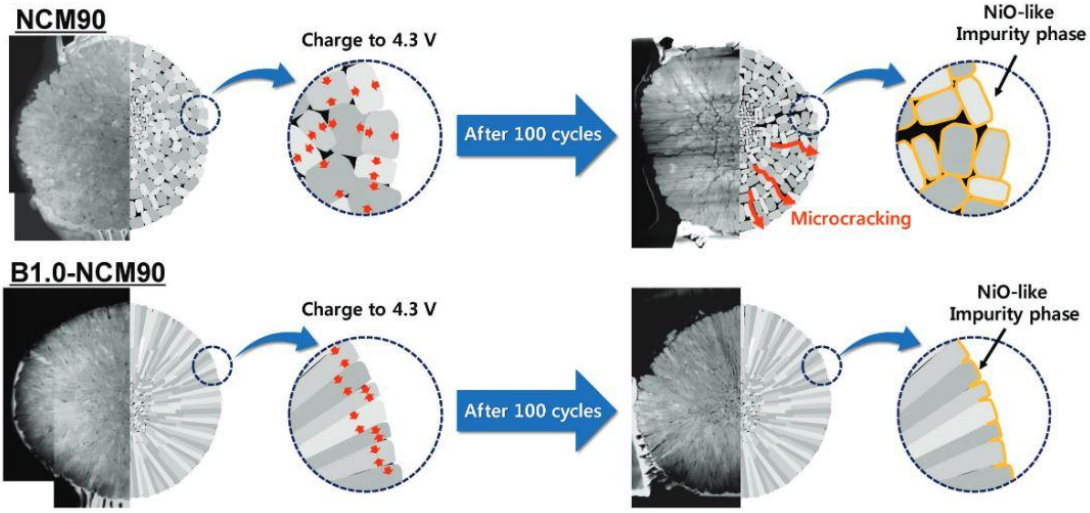

Figure 2.7: Structure of NMC secondary particles, comparing how boron doping has affected the primary particles and the packing orientation [10]

Jung et al. (2020) [11] showed similar results, where needle like primary particles with radial secondary structure were compared to standard randomly oriented NMC secondary structures. The radially oriented NMC has a full concentration gradient with a rod-like structure. Jung et al. (2020) and Park et al. (2018) both show the possibility to mitigate the structural issues Ni-rich cathodes face during anisotropic volume change and subsequent microcracking of radially oriented secondary structures of acicular primary particles. Thus, improving the capacity retention, thermal and structural stability, this in turn will extend the life of the battery. Whilst the novel structure of the secondary particles provides beneficial properties during electrochemical processes, the application of doping on a commercial scale can be challenging and costly. Achieving a uniform coating is vital as dopant concentrations above a critical point can lead to reduced electrochemical properties due to limiting ionic conductivity [42].

Another area of research for cathode engineering is surface coating of the AM. This can be particularly useful for preventing side reactions that could lead to degradation or unwanted oxygen formation and prevent gas evolution (reducing fire/explosions hazard). Additionally, by maintaining the integrity of AM through use of surface coatings, the capacity retention increases and shows improved energy

density [43]. Metal oxides were initially used for coating, but due to reducing charge transfer, the next investigations involved coating using conductive materials which reduced the resistance to charge transfer. These, however, also create an ultra-thin cation-mixed layer. Kalluri et al. (2017) [43] goes on to present work such as coating of $LiCoO_2$ and $Li(Mn,Ni)O_2$ with an ultra-thin coating of ceramic oxide. This provides superficial doping of manganese and nickel for beneficial electrochemical properties whilst maintaining that surface coating barrier, to prevent microcracks and unwanted side reactions. This method involved the use of atomic layer deposition and is considered the one of the most useful methods for deposition due to its uniformity and adjustable layer thickness. Niu et al. (2021) [44] also used atomic layer deposition was also used to generate an ultrathin layer of Li_3PO_4 as a surface coating on lithium metal anodes. The coating was found to reduce the effect of lithium dendrite formation and form a stable interfacial layer between the electrode and electrolyte. Although ALD shows good uniformity and adjustability, the process is time consuming and high cost, limiting its ability to be adopted on a commercial scale. Additionally, the requirement to operate under vacuum adds another cost barrier for industrial scale up [45]. Another surface coating process utilised was mechanofusion, however, in this case for anode materials [46]. The technique is a more physical process, utilising high shear mixing of two powders in a mixer. The process involves a rotating mill that creates a region of high pressure between the chamber wall and press-head, then a trailing scraper removes the compressed material off the chamber wall. Through this process eventually, over many rotations, a material is coated onto another to create a surface coating. Mechanofusion is less investigated in the literature however the ability to achieve uniform coatings can be challenging, and intense processing conditions can lead to aggregation and particle breakage. Finally, for all surface coating processes there is a careful balance between improving the electrochemical performance and limiting ionic conductivity. If the surface does not allow the free movement of ions from the electrolyte to the active material this will inhibit the rate kinetics and reduce the performance of the electrode.

Doping of cations, anions or multiple ions has potential to prevent some of the issues raised by Lu et al. (2020) [9]. One particularly interesting dopant is magnesium cations that occupy lithium-ion sites and prevent the nickel migration to lithium-ion sites. This reduces volume change and microcracking and, in turn, leads to higher capacity and longer capacity retention during cycling. Lu et al. (2020) [9], presents a range of dopants and their effect on Ni-rich layered oxide cathodes [47–50]. The effects of doping, that are shown through various pieces of literature include suppressing Li/Ni mixing, restraining phase transition, inhibiting O_2 release and promoting Li^+ diffusion. These are all mentioned as issues that currently affect most Ni-rich cathodes in research and, as such, doping can clearly provide beneficial properties.

Another form of particle engineering for active materials for improving Ni-rich cathodes is the formation of concentration gradients in secondary particle structures. Lu et al. (2020) [9] states that the

main concentration gradient structures designed for active materials are shell concentration gradient, full concentration gradient and two-sloped full concentration gradient. Figure 2.8 shows an example of a concentration gradient designed AM of NMC. It is worth noting how nickel content is high in the centre of the AM to maintain capacity, but then it is reduced nearer the surface to improve stability and safety of the material. Although this reduces the nickel content and thus capacity, it also prevents any side reaction and issues with microcracks and stability. This is the trade-off that concentration gradient designed AM's offer [51]. Unfortunately, the process for concentration gradient synthesis is much more complex than the synthesis required for a standard active material and as such increases the cost of manufacturing. In addition, the precise control required and difficulty in scalability, can inhibit the application of this technology at a commercial scale.

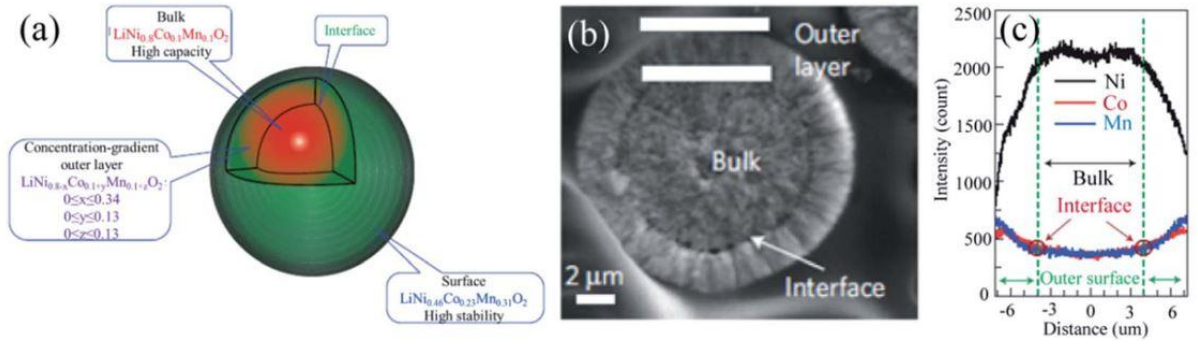

Figure 2.8: Concentration gradient design of an NMC active material a) shows how composition changes from centre to surface, with transition metal ion compositions shown, b) shows an SEM image of a typical concentration gradient designed active material, c) shows transition metal concentration changes across the active material cross section [51]

As mentioned earlier Chang-Jian et al. (2018) [28] discuss the issues surrounding the alternative anode active material chemistry, LTO. They also discuss how the use of dopants can improve electrode rate kinetics. Magnesium and chromium ions were used as dopants to improve the electronic conductivity. Additionally, phosphidation was used to create a 'glassy lithium' surface coating which reduced impedance and enhanced lithium transfer. Chang-Jian et al. (2018) [28] used spray-drying to create microspheres out of the LTO material and they attribute the porous structures to improved conductivity and lithium diffusion rates. This spray-drying process, however, operates at 120 °C and 3 Mbar, which are intensive operating conditions and will lead to increased cost of production when manufacturing at a larger scale. Takami et al. (2015) [52] employed a similar method for creating spherical anode materials using boron-doped TiO_2. The spray-drying method also showed promising results but would require intensive energy input and increase cost of production drastically at larger scales. Similarly, Pol et al. (2014) [53] utilised spherical hard-carbon as an anode in sodium ion batteries, this process operated at high conditions of 700 °C and 3 MPa, but did not use the same spray drying approach. These papers on spherical structures all offer insight regarding improved electrochemical potential with the novel porous structures. However, the process conditions are not suitable for scale up and this presents

a gap in the literature with regards to secondary spherical particles being produced at ambient conditions for tailored electrode design.

Table 2.3: Summary of particle engineering processes carried out for improving electrode performance

Technique	Benefits	Ref
Boron doping of NMC	Columnar NMC crystals radially oriented into a secondary structure, decreased the susceptibility to microcracking during volume change and improved tortuosity of lithium	[10]
Surface coating through atomic layer deposition	Ultra-thin layers of cations or ceramic oxides prevent unwanted side reactions and even dendrite formation in some anodes, O_2 release is inhibited, and lithium diffusion is enhanced. This ensures a longer capacity and capacity retention during cycling.	[47–50]
Surface coating through mechanofusion	Generation of silicon-graphite composites reduce the susceptibility to microcracking during volume change. This improved the cycling and rate capability.	[46]
Concentration gradient design	Active materials with varying composition across a cross section, which for a concentration gradient can enable surface particles to possess greater stability and safety properties whilst maintaining the high-capacity materials at the core of the active material. This prevents unwanted side reactions and ensure longer cycling potential of the electrode.	[11,51]
Spray drying to generate porous microspheres	Porous microspheres are attributed to greater conductivity and lithium diffusion rates. Spherical structures have a higher packing density compared to irregular ones and thus improved electrochemical performance.	[28,52]

2.1.6 Manufacturing Concerns

Electrode manufacturing has a vast array of operations that require process improvements, as can be seen in Figure 2.4. Electrode mixing, coating and drying make up the first three unit processes of a general electrode manufacturing line and will be the focus of this literature review. Figure 2.9 shows some common issues that surround the mixing, coating and drying processes from a manufacturing perspective and present areas for particle engineering to resolve.

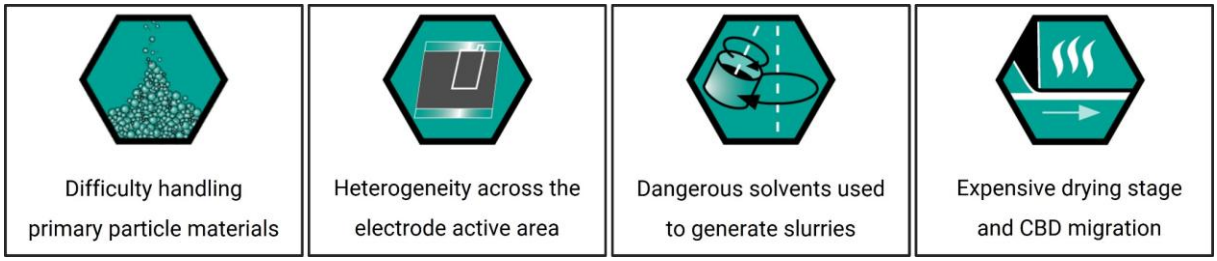

Figure 2.9: Some common issues surrounding electrode manufacturing in the mixing and coating stages

During the mixing process, the distribution of active material, conductive additive and binder is dispersed in a solvent, such as N-methyl-2-pyrrolidone (NMP) which is used for generating slurries with PVDF binder. Homogeneous distribution of conductive additive is vital for electrode performance as this enhances the conductivity, which reduces the internal resistance [54,55]. One study found that a uniform distribution of carbon black had 50 % higher discharge capacity than the electrode with non – uniform carbon black distribution [56]. The conductive additives tend to have branched structures which agglomerate, and as they are distributed in the solvent the viscosity increases drastically that required mixing power increases. Therefore, high shear mixing is required to break the agglomerates and distribute the conductive additive between the active material particles, however control and design over the conductive additive arrangement within the electrode proves difficult [57]. Additionally, during the mixing process the functionality and ease of use of the powder materials is limited. This is due to the cohesive and electrostatic nature of the primary particles, which leads to poor flowability and high dust risk.

The slurry cast electrodes formed require intensive drying before they are functional. Most of the solvents used, including NMP, are highly toxic and present safety concerns as well as large cost involved with the drying and a necessary solvent recovery step. During this drying step, the conductive additive and binder, known as the carbon binder domain (CBD), tend to migrate towards the surface of the electrode due to the movement of the solvent during evaporation. This migration can lead to a decrease in the adhesion of the electrode to the current collector and increases the risk of delamination [58–60]. Additionally, as the CBD migrates the distribution of conductive additive also decreases and becomes more heterogeneous, which leads to poor electrode performance as discussed previously. The risk and cost factors are strongly driving the movement away from wet slurry-based electrodes to dry manufactured electrodes, with benefits in the lack of solvents required. Dry manufacturing processes often retain a mixing step without the need for solvents, this is to enable good distribution of the electrode components throughout the dry mixture. If the mixture is not well distributed this can negatively impact the electrochemical performance [61,62]. Once the dry mix is generated the deposition onto the current collector differs from the wet method, where spray deposition, polymer fibrillation or extrusion processes are commonly used [63]. Generally, the process required direct compression of particles onto the current collector through some calendering process. Ultimately, the

dry process differs mainly in that it does not require solvents to generate electrode films. Dry electrode manufacturing has been estimated to reduce the cost of manufacturing by 10 – 15 %, and this comes from the removal of the slurry casting, drying and solvent recovery steps required in a wet electrode manufacturing process [63–65]. It was found that the drying and solvent recovery step of NMP based slurries accounted for 47 % of the total energy consumption in a wet slurry cast manufacturing process [64]. This clearly shows why the current commercial strategy is to transition to dry electrode manufacturing.

However, there are consequent issues with particle distribution and adhesion between particles and current collector. Additionally, during dry manufacturing similar processing issues arise surrounding particle handling of the cohesive materials used for electrodes, as discussed earlier. Dry roller processing which uses two rollers with a small gap to compress the primary particles and binder onto a current collector at 20 MPa is often used [66]. However, distribution of the materials homogeneously across the electrode could still present an issue. While dry processing techniques are not completely robust, they are still relatively new areas of research in the electrode manufacturing process and further work will aim to improve the process.

Particle processing of the active material and conductive additive into a locally well dispersed interlocked matrix, such that small well distributed secondary structures are used to generate dry manufactured electrodes, would therefore ensure homogeneity across the entire electrode structure. These structures would also ensure that short- and long-range conductive networks are sufficient to reduce internal resistance. Dry electrode manufacturing mitigates the issues surrounding the utilisation of solvents for electrode slurries and the energy intensive drying steps. The next section will introduce a method that enables these beneficial secondary structures to be generated at low temperature and pressure, whilst allowing solvents used to be recovered and recycled back into the process.

2.2 Spherical Crystallisation

2.2.1 Overview

Spherical crystallisation is a particle design and process intensification technique in which particles are agglomerated to produce a spherical structure using a bridging liquid [12]. The mechanism and rate through which agglomerates are formed is dependent on particle and solvent characteristics, as well as operating parameters. A review of the literature shows there has been a vast amount of research on these processes within the pharmaceutical industry. The technique is used as a process intensification technique which combines the crystallisation and agglomeration steps of a pharmaceutical active ingredient. This generates improved secondary structures for particle handling and reduces the cost of manufacturing. Spherical crystallisation in pharmaceutical industry can also improve functional properties of the active substance such as enhanced dissolution. There are multiple techniques and

choice of method depends on the components used and desired outcome of the agglomeration process. There are three main techniques: Spherical Agglomeration (SA) and Quasi-Emulsion Solvent Diffusion (QESD) are the main two, and Ammonia Diffusion (AD) [5]. A further technique, called Crystallo - Co Agglomeration (CCA), involves agglomeration of two active substances in the same system to create agglomerates of mixed composition. There are subtle differences between the systems used and benefits and limitations to each. Spherical crystallisation may vary between these techniques, but the main equipment used does not vary that much. Generally, a stirred tank reactor is used to carry out the process and will be fitted with equipment such as impellers, baffles, heating/cooling jacket, condenser, sensors, input and output pipes etc. The design of a stirred tank reactor will be discussed in more detail in a later section of this report, as it is a pivotal part of the design process for optimising spherical crystallisation output.

Kovačič et al. (2012) [5] quotes that the prerequisite for QESD is that the 'good' solvent and drug interactions are stronger than those between the 'good' and anti-solvent. This is a method that does not use a bridging liquid for preferential wettability but instead, when the drug solution is introduced to the anti-solvent, an emulsion forms to which the good solvent slowly diffuses out and the anti-solvent diffuses in leading to crystallisation [13]. To enhance stability of agglomerates formed a polymeric binder can be used. As with most crystallisation/diffusion processes a slight increase in temperature can increase the rate of mass transfer between the good and anti-solvent increasing the rate of solvent change. However, Kovacic et al. (2012) [5] notes how the mass ratio of good solvent to anti-solvent affects the rate of solvent transfer, but also affect agglomerate density. It is also noted that an increase in temperature increased sphericity and agglomerate size. Chen et al. (2020) [67] analysed the difference in agglomerates formed through the QESD process when compared to alternative processes, for example, spherical agglomeration through anti-solvent change and pH shift for ferulic acid agglomeration process. The QESD process displayed increased sphericity in its secondary structures formed, smaller median particle size with a narrower PSD. The QESD agglomerates showed more densely packed structures than the other processes. Chen et al. (2020) [67] suggests that from their experience QESD agglomerates have generally exhibited better flowability than when other spherical crystallisation techniques are used, however they suggest this must not be taken as being true for all systems as sometimes QESD is not capable of producing well agglomerated structures with good flowability.

Ammonia diffusion (AD) is an extension of spherical crystallisation for substances that are soluble only in acidic or alkaline solutions, and as such normal processes cannot be used [13]. The changes to the system involve using ammonia as the good solvent. The poor solvent must be soluble in ammonia and is involved in a solvent change by entering the ammonia droplets and creating a precipitation reaction, whilst the ammonia leaves the droplets. This diffusion is induced by a water immiscible solvent such

as a hydrocarbon being present, to which the ammonia diffuses to. The AD process tends to produce agglomerates comparable to the spherical agglomeration process as is an extension of the SA process and therefore will exhibit similar properties. The AD process works well when a solid is amphoteric in nature, that is to be soluble only in acidic or alkaline solutions, such as metal oxides or hydroxides [68]. Thus, AD presents an option for solids of this nature, and is inherently a well-functioning process. However, the use of ammonia presents safety issues, particularly with pharmaceutical products, and ensuring there is no residual ammonia in the product. The issues arising from using harmful solvents can lead to increased downstream processing when scaled up to a commercial processing scale, which in turn leads to increased cost and energy demand depending on the purification steps required.

Table 2.4: Benefits and limitations of QESD and Ammonia diffusion spherical crystallisation methods

Spherical Crystallisation Technique	Benefits	Limitations	References
QESD	Smaller median particle size and narrower PSD. Solvent diffusion process that only requires two solvents. Produces higher density agglomerates.	Polymeric binder is required to improve the strength of the agglomerates. QESD is not always capable of generating well-formed agglomerates with good flowability.	[5,13,67]
Ammonia Diffusion	For amphoteric materials that are soluble in acidic/alkaline solutions.	The use of ammonia presents safety concerns. More downstream processing to remove residual ammonia.	[13,68]

2.2.2 Spherical Agglomeration (SA)

The focus of this work, however, is the particle processing technique labelled spherical agglomeration. This is a novel technique currently being used in the pharmaceutical industry to improve properties of particulate material both for processing and benefits for medicinal purposes. Kovačič et al. (2012) [5] discuss how this process can have different names depending on the primary function of the process. The main process found in literature is the three phase system utilising a precipitation reaction and agglomeration process in tandem, this takes the principal name of spherical agglomeration. The other process commonly seen in literature is called agglomeration in suspension which does not involve the precipitation reaction, but instead agglomerates solids from a suspension using a continuous phase and dispersed phase droplets, often called a bridging liquid.

For standard spherical agglomeration three solvents are commonly used [5,13]; the ‘good’ solvent, the anti-solvent, and the bridging liquid. The ‘good solvent’ tends to be the solution of material to be

agglomerated and the anti-solvent is introduced to initiate a precipitation reaction. Certain properties between these two solvents must be adhered to for efficient processing [5,12,13]. The good solvent must be miscible with the anti-solvent and the affinity must be greater when compared to the affinity between good solvent and the particle of interest. The reason for adding the anti-solvent is to create an environment of supersaturation in which the solubility of the solute is decreased, leading to precipitation of the crystals. The bridging liquid is the third liquid phase to be added and differentiates the process from the other spherical crystallisation techniques. This is required to be immiscible with the anti-solvent and have a high affinity to the precipitated crystals [12] so the particles transfer from the suspension to the bridging liquid droplets. A review paper by Kovačič et al. (2012) [5] on spherical crystallisation outlines ideal bridging liquids for various solvent systems and their properties, whilst discussing how Amaro-Gonźalez and Biscans (2002) [69] focused on the wettability characteristic between the solid particles and bridging liquid to identify a suitable bridging liquid. It was suggested that a low contact angle is beneficial to good bridging liquid choice. Amaro-Gonźalez and Biscans (2002) [69] used a typical Washburn test that measures the capillary action of a liquid up through a powder bed. Thati and Rasmuson (2012) [70] agree with this statement and add to it that interfacial tension between bridging liquid and the anti-solvent should be high for the solvent system. Whereas Chow and Leung (1996) [71] laid out some general 'rules of thumb' for various compound properties, these can be seen in Table 2.5. Generally, research now operates primarily on the contact angle measurement as a method for identifying suitable solvents for continuous phase and bridging liquid solvents [69,70]. The method uses either a Washburn test or sessile drop method, which allow the three-phase contact angle to be measured.

The selection of the solvent system and bridging liquid is important for sufficient crystallisation and agglomeration to occur. Furthermore, the amount added for each of these solvents is also an important factor [12]. Tertiary phase diagrams have been used to find optimised solvent system selection based on solubility and miscibility between each component. This has been shown in several pieces of research [72,73] to be an effective method for selecting the correct composition of solvents and bridging liquids in the spherical agglomeration system. An example of a ternary phase diagram is given in Figure 2.10 showing how there is a miscible and an immiscible zone for which spherical agglomeration occurs within the shaded region, as specified by Zhang et al. (2010) [73]. The curved line shows the points at which phase separation occurs, and below the line in the shaded region is where the bridging liquid is immiscible and spherical crystallisation occurs.

Table 2.5: General solvent choices for the anti-solvent and bridging liquid used for spherical agglomeration based on the work carried out by Chow and Leung (1996) [71]

Particle Properties	Anti-Solvent Choice	Bridging Liquid Choice
Water soluble compounds	Water miscible organic solvent	Salt solution of high concentration without common ions
Organic solvent soluble compounds	Water	Water immiscible organic solvent
Water miscible organic solvent soluble compounds	Saturated aqueous solution of the compound	Organic solvent
Not soluble in water or organic solvents	Water immiscible organic solvent	Salt solution of high concentration with no common ions. Also, a binding agent is required for agglomeration due to low solubility preventing liquid bridges

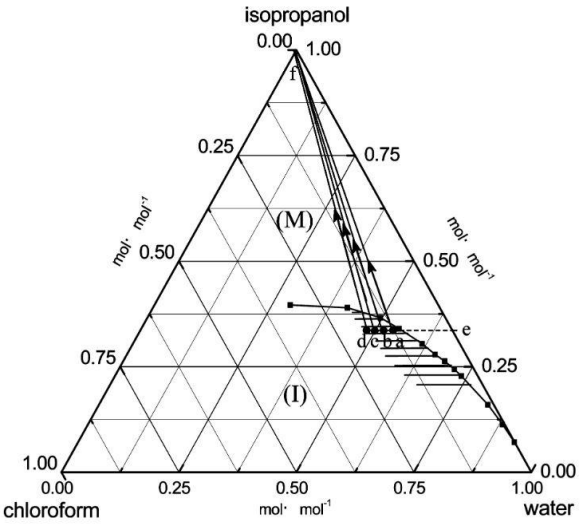

Figure 2.10: Diagram showing the different regions of solubility between three solvents in a spherical agglomeration system, where (M) indicates the miscible region and (I) indicates the immiscible region, and successful agglomeration occurring in the shaded region [73]

Spherical agglomeration in suspension is similar to spherical agglomeration but operates without the precipitation step involved with the good and anti-solvents. Spherical agglomeration in suspension requires a continuous phase in which the particles are dispersed, and an immiscible bridging liquid. The bridging liquid must have preferential wettability with the solids to be agglomerated, as was discussed earlier [5,69,70].

One of the most important parameters for successful agglomeration and high yield is called the bridging liquid to solids ratio (BSR). This is the ratio of bridging liquid to solids on a volume basis. It has been comprehensively reviewed in literature [12,14,16,72], and is unique to every system depending on interaction between components, and therefore is a very important design characteristic to be considered. There is a range for which the BSR is considered optimum [69], below this range no significant agglomeration occurs due to lack of bridging liquid. Above this optimum range, a 'paste' is formed due to an excess of bridging liquid present. Thati and Rasmuson (2011) [74] observed an increase in particle sphericity with increased BSR (within the optimum range), and agglomerate size increased, which was also seen by Blandin et al. (2003) [16]. This was expanded in a paper by Tew et al. (2023) [75] which proposed a new term that accounts for the bridging liquid solvent miscibility, called the true bridging liquid to solids ratio (TBSR). In spherical agglomeration in suspension, where the bridging liquid exhibits solubility in the continuous phase excess is added to account for this. Therefore, the TBSR is "calculated based on the actual amount of dispersed phase bridging liquid" [75].

2.2.2.1 Spherical Agglomeration Mechanisms

Work investigating the mechanistic understanding of spherical agglomeration found that agglomerates form through either a distribution mechanism or an immersion mechanism. Figure 2.11 shows the general mechanisms of spherical agglomeration [12]. With the crystals suspended and bridging liquid available in droplet forms, the initial nuclei are formed through two routes. Firstly, the distribution mechanism occurs when the droplets of bridging liquid are smaller in diameter to the particle size. Here, bridging liquid droplets adhere to the surface of the solid and connect them together as the solids combine through contact. The second route is the immersion mechanism; this occurs when the bridging liquid has larger droplet size than the particle size and therefore the solids become immersed within the bridging liquid droplet connecting the solids together in spherical form. The immersion mechanism is the preferred option as the size of agglomerates can be limited through droplet sizing and design.

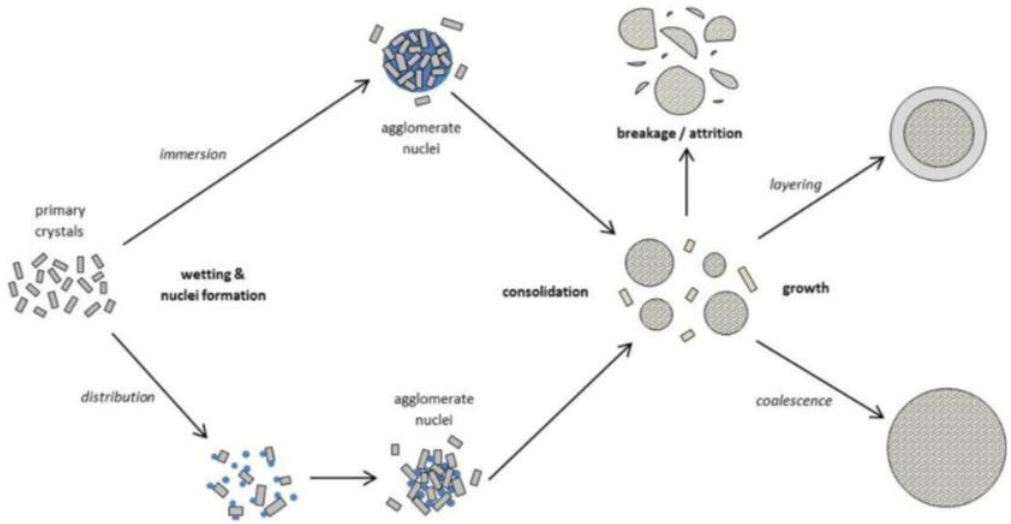

Figure 2.11: Mechanisms through which spherical agglomeration occurs when bridging liquid is added to a suspension of primary particles, to form secondary structures. Modified from Pitt et al (2018) [12]

After the initial nuclei are formed, the consolidation and growth phase occur. During this phase, breakage and attrition can also occur through collisions and impacts during the agitation process. As the particles immerse within the droplets and consolidate, bridging liquid is forced to the surface through capillary action and can then interact with solid material of primary particles or agglomerate breakage. This creates a layering effect and leads to growth of the dense agglomerates under agitation. Coalescence occurs when nuclei interact with each other and combine to add mass and grow. It is through these mechanisms that primary particles, suspended in solution, interact with the bridging liquid to form spherical secondary structures.

Research by Arjmandi-Tash et al. (2019) [76] has made strides in understanding the mechanisms using a mathematical model and introduces a new kinetic understanding of the rate processes involved with spherical agglomeration. The model is based on the understanding of the immersion process for which nuclei are formed as discussed in the paper by Pitt et al. (2018) [12]. Figure 2.12 shows the general mechanism through which particulate material becomes immersed in the bridging liquid during the spherical agglomeration process. Arjmandi-Tash et al. (2019) [76] discusses how particles first must collide with the bridging liquid droplet and then have a chance of interacting with the surface. As the solids interact and cover the surface, they immerse into the droplet over time until the droplet is sufficiently saturated with solids. It is important to note that in Figure 2.12 the binder droplet and mother solution refers to the bridging liquid droplet and continuous phase respectively, this is nomenclature commonly used in spherical crystallisation processes in the pharmaceutical industry.

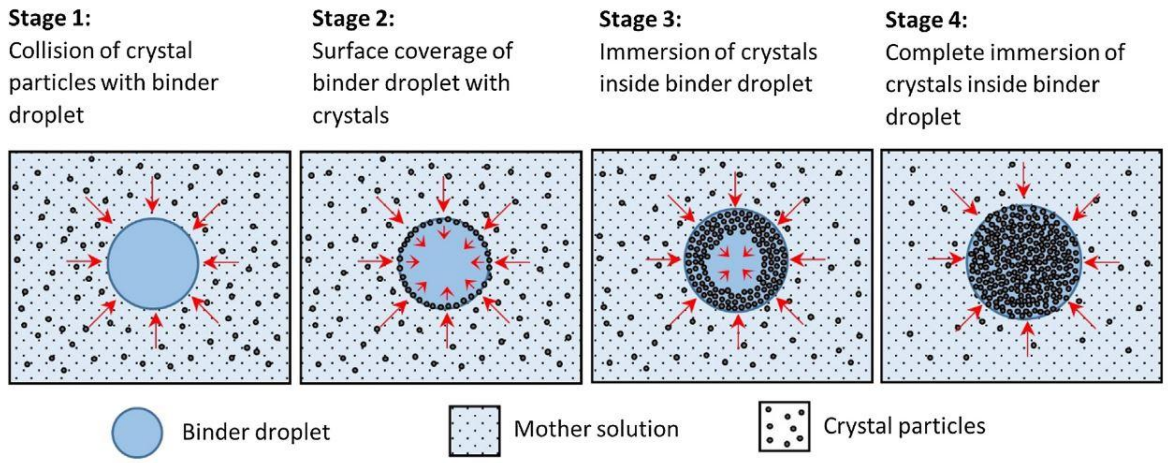

Figure 2.12: Mechanism through which particles immersion into bridging liquid droplets during the nucleation process [76]

The paper also introduces two mathematical models that aim to describe the rate limiting mechanisms for nucleation formation in the spherical agglomeration process – the immersion rate limited model and the collision rate limited model. In a real system both models will affect the rate limiting mechanisms. Additionally, the models assume a static system and do not account for dynamic interactions. Figure 2.13 shows the difference between the two different rate limiting models, where a 2D slice of a droplet – continuous phase interface is shown.

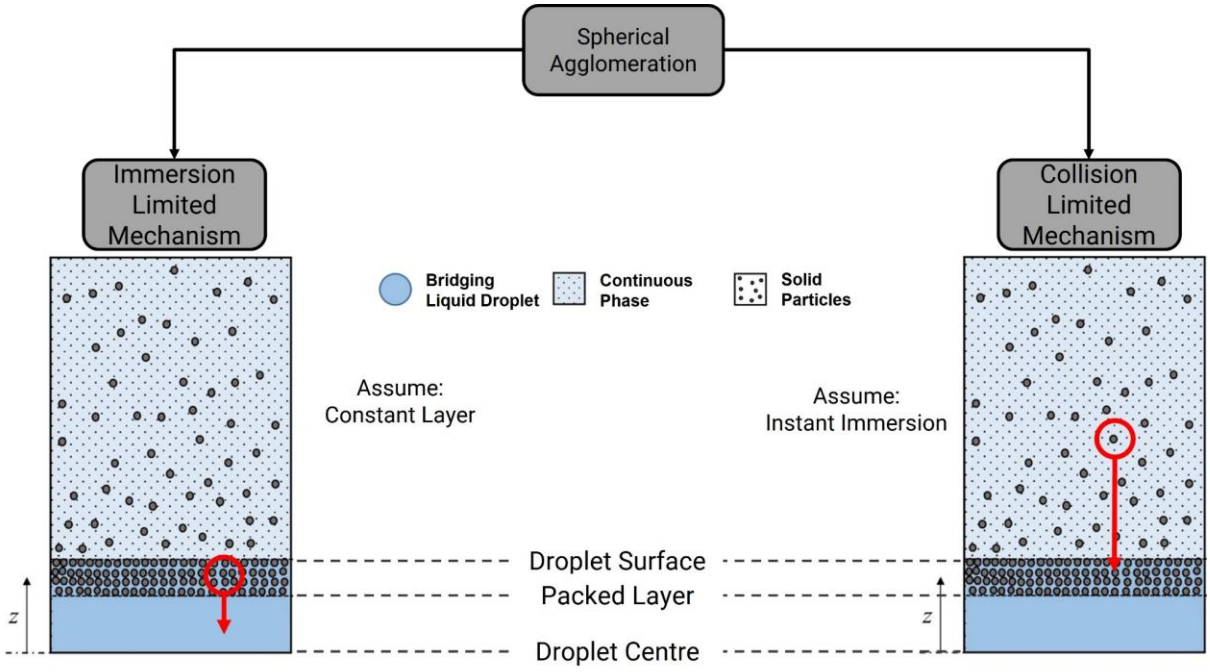

Figure 2.13: Modified figure of the rate limiting mechanisms for the nucleation process taken from Arjmandi-Tash et al. (2019) [76], showing the immersion rate limiting mechanism (left) and the collision limited mechanism (right) for a 2D slice of a bridging liquid - continuous phase interface

The immersion limited model assumes that the rate of collisions between the bridging liquid and solids are always high and that the bridging liquid can be assumed as having a constant layer of solids on the

surface of the droplet. Therefore, the immersion model assumes that the rate is limited due to the rate at which particles from transfer from the surface of the droplet to the centre. The rate of immersion is given by Equation 2.1, as proposed by Arjmandi-Tash et al. (2019) [76].

$$Q_{imm} = \frac{\Psi D_p \gamma Cos\theta}{30\mu_d} \frac{1}{H_2(t) - H_1(t)} \frac{\phi_{cp}^2}{(1 - \phi_{cp})} \tag{2.1}$$

Where:

Ψ	Sphericity factor of the particle
D_p	Sauter mean particle diameter (m)
γ	Interfacial tension (mJ/m^2)
θ	Contact angle
μ_d	Bridging liquid viscosity (Pa.s)
$H_2(t) - H_1(t)$	Wall thickness (for time = t) (m)
ϕ_{cp}	Critical packing liquid volume fraction

The collision limited model assumes that the immersion of particles into the bridging liquid would be very fast. Therefore, the model assumes the rate is limited by the arrival of particles to the surface of the bridging liquid during agitation. For which the proposed rate of collision equation proposed by Arjmandi-Tash et al. (2019) is given by Equation 2.2.

$$Q_{coll} = \left[\frac{16}{225} \frac{(\rho_p - \rho_L)^2 g}{\rho_L \mu_L}\right] \frac{D_p}{D_d} \left[u(D_p)^2 + u(D_d)^2\right] \phi_{pb} \tag{2.2}$$

Where:

ρ_p	Particle true density (kg/m^3)
ρ_L	Continuous phase liquid density (kg/m^3)
μ_L	Continuous phase liquid viscosity (Pa.s)
D_p	Particle diameter (m)
g	Gravitational acceleration constant (m/s^2)
D_d	Droplet diameter (m)
$u(D_p)$	Particle – continuous phase relative velocity (m/s)
$u(D_d)$	Droplet – continuous phase relative velocity (m/s)
ϕ_{pb}	Particle solid fraction in the continuous phase

Interestingly, no study has been carried out for manipulation of these rate mechanisms to generate tailored structures. This makes up a section of this thesis where the immersion rate limiting mechanism is limited purposely to generate hollow structures, which have beneficial properties for electrode dry manufacturing through compression onto current collectors.

Whilst Arjmandi-Tash et al. (2019) [76] has investigated the first stage of spherical agglomeration looking at the nucleation kinetics, further work is required to understand the second stage which incorporates the growth and consolidation of nuclei into dense agglomerates. A study of the kinetics for spherical agglomeration of paracetamol carried out by Pitt et al. (2024) [15] which introduces a "model for agglomerate consolidation and growth". It is known that there is an optimum TBSR range for successful agglomeration as discussed earlier [12,14,16,72]. If the agglomeration process is carried out at a TBSR higher than the optimum range, a paste forms. Additionally, the time to form a paste decreased exponentially as TBSR was increased. By assuming a first order decay profile the exponential decay of porosity over time was successfully fit to experimental data using Equation 2.3.

$$\frac{\left(\phi(t)-\phi_{cp}\right)}{\left(\phi_0-\phi_{cp}\right)} = exp\left(-K_C(t-t_0)\right) \tag{2.3}$$

Where:

$\phi(t)$	Porosity at time (t)
ϕ_{cp}	Minimum porosity/critical packing fraction
ϕ_0	Porosity at time = 0
K_C	Consolidation rate constant (min^{-1})
t	time (min)

It is important to note that the parameters at time equal to zero, refers to the start of the growth and consolidation stage. Equation 2.3 can be rearranged to be a function of TBSR, $TBSR_{min}$ and $TBSR_{crit}$ by substituting in Equation 2.4 and rearranging, to give Equation 2.5.

$$\phi_{agg} = \frac{TBSR}{1+TBSR} \tag{2.4}$$

$$t_{agg} - t_0 = -\frac{1}{K_C} ln\left[\frac{TBSR_{min} - TBSR_{crit}}{1+TBSR_{min}}\right] \tag{2.5}$$

From these relationships a non-dimensional relationship between TBSR and time to paste, porosity and agglomerate strength was predicted. This is particularly important as this allows a more tailored approach to identifying TBSR based on agglomerate porosity and time to paste. Whilst also identifying how agglomerate properties can be manipulated based on the growth and consolidation stage kinetics.

However, while the trends will follow similar kinetics for all agglomeration systems, the magnitude of the values will differ. This study was carried out for a paracetamol/heptane/water spherical agglomeration system and operated at 500 RPM and 5 % solids loading. If these process parameters are changed then the kinetics will also change. This was discussed briefly in the work as the model successfully predicted the smaller, denser agglomerates formed due to increasing impeller speed. The model also successfully predicted the reduction in agglomeration time and critical TBSR at higher impeller speeds [15]. The growth and consolidation kinetic model is a powerful tool for predicting agglomerate properties particularly when coupled with the nucleation model proposed by Arjmandi-Tash et al. (2019) [76].

Whilst the kinetic models for agglomeration are beginning to become more widely understood for spherical agglomeration, thermodynamic analyses are less prevalent. The benefit of which is to identify solvent systems that are predicted to successfully agglomerate. A study by Cheng et al. (2020) [77] introduced the idea of using thermodynamic adhesion criteria for identifying optimal bridging liquids. The work discusses adhesion free energy calculations for two solid particles when in the bridging liquid phase. The work utilises contact angle and known surface energy characteristics of solvents to identify the free energy of adhesion, ΔG_{SLS}. For two solids that adhere to each other inside the bridging liquid solvent this value should be negative, which suggests an attractive energy between the two particles. While the assessment of the particle adhesion within the bridging liquid droplets is clearly aided in this assessment. The study falls short of identifying successful bridging liquids when particle transfer from the continuous phase to the bridging liquid takes place. Further work is required to develop a thermodynamic criterion for bridging liquid identification based on spherical agglomeration in suspension techniques where particle transfer takes place. This is to account for the wetting effect that the continuous phase has on the particles when compared to the bridging liquid.

2.2.2.2 Effect of Operating Parameters

There are many other parameters that affect spherical agglomeration and have been covered in various parts of literature [16,72,73] and these have been reviewed by Pitt et al. (2018) [12]. These are important factors to understand as they can be used to tailor most systems for required agglomerate properties.

Temperature

An increase in temperature leads to changes in solubility of solvents and bridging liquid, and it also changes crystal growth and supersaturation during the precipitation stage. However, the general consensus is that increasing temperature leads to reduced yield and size of agglomerates [70]. This is due to solute solubility being affected by temperature. One observed effect is that crystals tend to be larger at higher temperatures and thus bulk agglomerates have decreased density and sphericity [72]. However, each system will be different depending on the chemicals used, so there could be some discrepancy on the effects that temperature has on crystal growth and solute solubility. These studies

focus primarily on spherical crystallisation and relate the effects of temperature to the effect on the precipitation step. For spherical agglomeration in suspension systems the effect of temperature is less well known, however the increase in solubility of bridging liquid droplets could lead to a reduced working volume which therefore would reduce the operating TBSR value.

Mixing Speed

Agitation is important to stirred tank design such that the suspension is sufficiently dispersed using a stirred tank impeller. Laminar flow will not create enough agitation to disperse the materials used for electrode manufacturing. Therefore, creating a turbulent flow within the vessel is necessary and is a function of mixing power and tank design, for example using baffles. Turbulence ensures sufficient agitation and interaction between the components in the multiphase system, but it is also important to operate at an impeller speed that does not lead to excessive breakage preventing successful agglomerate formation. As discussed previously, immersion mechanism agglomeration could be limited by collision rate [76] and therefore increased impeller speed will increase the rate of collisions and nuclei/agglomerate formation. This is up until a point where attrition and breakage become the dominant mechanisms if the shear imparted by the impeller becomes too large [12]. Increasing the impeller speed also increases the compressive force acting upon the agglomerates, which has been seen to increase the density and reduce the porosity of the formed agglomerates [16]. Pitt et al. (2024) [15] argue that the increase in impeller speed has more effect on the initial droplet dispersion leading to smaller nuclei formed, which in turn generates smaller final agglomerates. Subero-Couroyer et al. (2006) [14] agree with this assessment and state that initial dispersion of the bridging liquid is important to final agglomerate size, and as expected, higher impeller speeds decrease the size of bridging liquid droplets. As can be seen in Figure 2.14, it was found that operating the impeller at a higher stirring speeds during initial bridging liquid injection, then reducing the impeller speed during the agglomerate formation stage generated smaller final agglomerates [14].

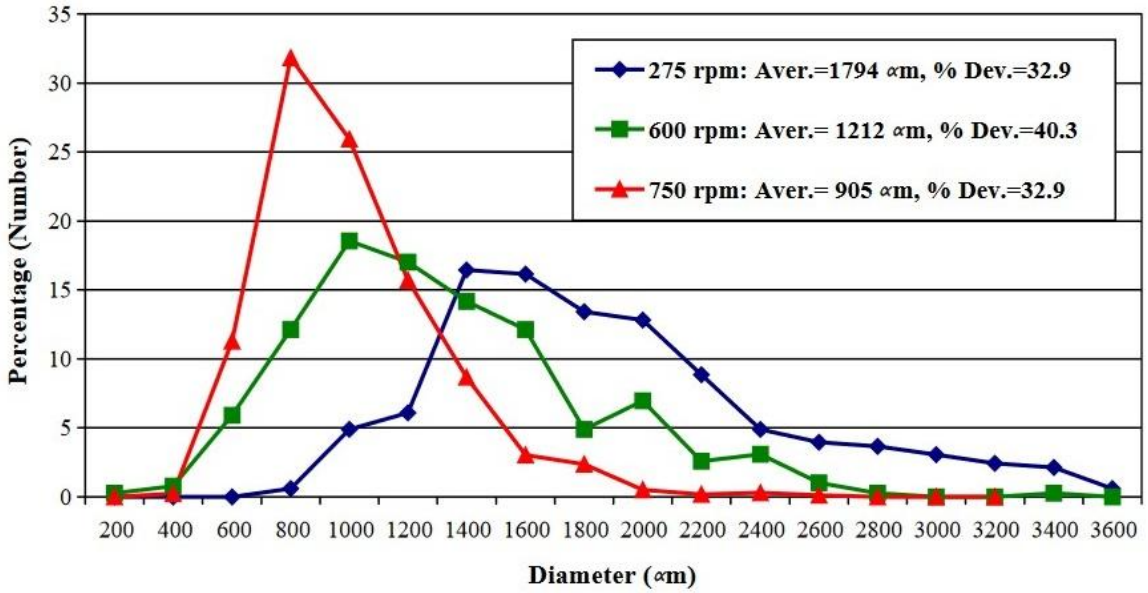

Figure 2.14: Number density particle size distribution showing the reduction of agglomerate size by increasing the impeller speed during the initial bridging liquid injection stage [14]

Madec et al. (2002) [78] discusses a similar observation by pre-dispersing bridging liquid droplet emulsions in the continuous phase. It was found that agglomerate size was reduced by forming emulsions of the bridging liquid before adding the solids. Additionally, by increasing the number of smaller bridging liquid droplets, the surface area available for particle transfer increased, thus reducing the time for particle wetting during the nucleation stage [78].

Different impellers generate different flow patterns and shear stress in a stirred vessel. For low - medium viscosity systems operating in a turbulent regime there are three general mixing regimes: axial, radial and mixed flow. Axial flow forces fluid down towards the base of the beaker to generate a mixing pattern. A pitched blade turbine, as seen in Figure 2.15, is an impeller that generates an axial flow and is considered low stress. Radial flow primarily involves forcing fluid towards the beakers wall in a radial fashion. A Rushton turbine is an example of an impeller exhibiting radial flow and is considered high shear and good for dispersion mechanisms, as can be seen in Figure 2.15. Then the third regime involves mixed flow which generates both axial and radial mixing, an example of this is an axial radial impeller, seen in Figure 2.15 [79].

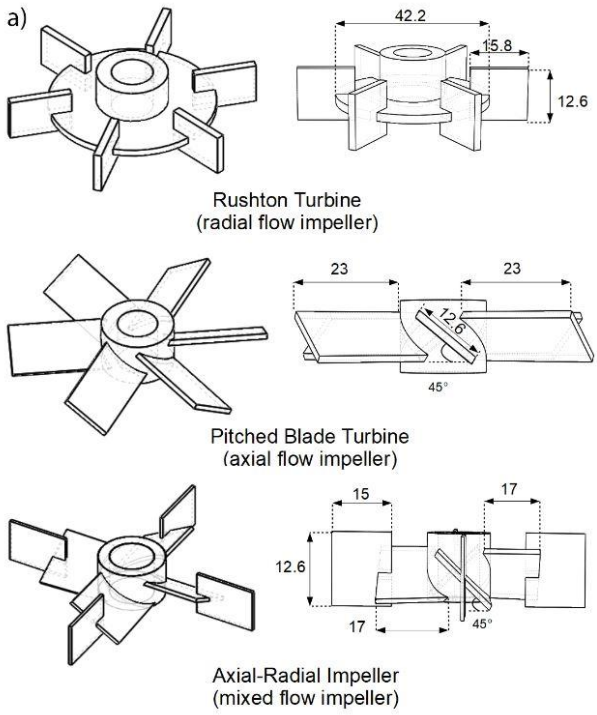

Figure 2.15: Example of impellers which generate different flow patterns in a stirred vessel [79]

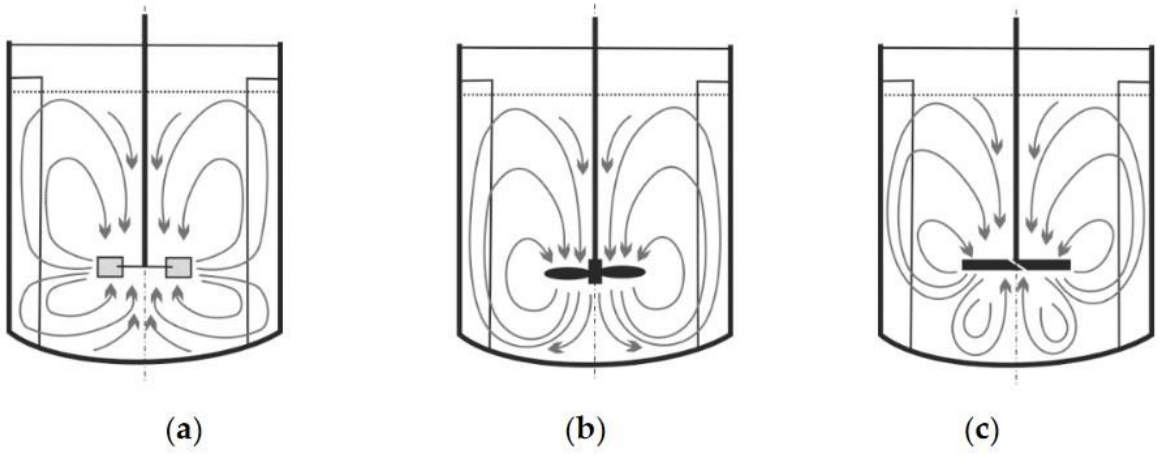

Figure 2.16: Flow patterns in a stirred tank where a) radial flow impeller, b) axial flow impeller, c) mixed flow impeller are used to agitate the flow [80]

A systematic review has yet to be carried out regarding the effect of spherical agglomerate formation based on flow type. However, a study that uses a similar setup for secondary particle formation of NMC precursor suggests that the flow regime effects the structure of the secondary particles based on the shear imparted by each flow field. Axial flow was found to produce milder conditions of producing larger, denser secondary particles with more consolidation occurring. Whereas radial flow operates at a higher shear leading to a more heterogeneous distribution of secondary particles [80,81]. Similar effects are assumed to be present in the formation of spherical agglomerates, however further work would be required to confirm these assumptions.

Agglomeration Time

Increasing agglomeration time increases the number of collisions and time under compressive force, leading to increased densification. However, Morishima et al. (1993) [82] found that longer agglomeration time did not lead to a change in the agglomerate size, when operating at the optimum TBSR value for the system. However, when the TBSR is increased the agglomerate size increased over time due to excess bridging liquid available for growth, through coalescence or layering.

Particle Size and Concentration

Blandin et al. (2003) [16] found that increased solids concentration also increased the agglomerate size, but reduce the porosity and increased the density due to increased frequency of collisions and extent of compaction with a higher concentration of solids. Subero-Couroyer et al. (2006) [14] found that increased initial primary particle size reduced the solids surface area for which the bridging liquid could interact with. This, in turn, reduced the agglomerate strength due to reduced adhesion between primary particles in the secondary structure. This allowed the agglomerate to be more deformable under stress.

Blandin et al. (2003) [16] carried out a systematic review of three key operating parameters: impeller speed (N), solids concentration (C_S) and BSR. The authors agglomerated salicylic acid in suspension to experimentally investigate the effects on agglomerate size properties. This was then used to create an empirical relationship between the operating parameters, which could be used to tailor agglomerate size distribution. It was found that arithmetic mean particle diameter (L) and variation of the final agglomerate size distribution (C_V) could be described by Equation 2.6 and 2.7, respectively.

$$L = 7.6 \times 10^{-3} \cdot C_S^{0.3} \cdot BSR^{2.1} \cdot N^{-0.6} \tag{2.6}$$

$$C_V = 9.99 \cdot C_S^{0.4} \cdot BSR^{-0.6} \cdot N^{0.4} \tag{2.7}$$

For this salicylic acid system, it was found that BSR had the most effect on the final agglomerate size which is to be expected [16]. The limitation of this work is that the empirical relations provided hold true for the systems discussed in the paper, but other materials would require a new study on the effect of process parameters to draw a similar conclusion with empirical relationships.

2.2.3 Crystallo Coagglomeration

The principal aim of this technique in spherical crystallisation is to be able to crystallise and agglomerate two or more species, or crystallisation of a singular species and it's simultaneous agglomeration with another species or excipient [83]. This adds a layer of difficulty to the spherical crystallisation process as the two solids being used must both adhere to the rules of preferential wettability in the three solvent system to agglomerate equally [5]. There is an array of literature in the pharmaceutical industry where excipients such as binders, surfactants or another drug, are incorporated

to enhance the mechanical strength of the formed agglomerates or improve the compressibility. Additionally, the CCA technique is beneficial for generating directly compressible agglomerates, thus reducing the number of unit operations required in a process line. Table 2.6 outlines some of the work carried out in the pharmaceutical industry, with drug particles and various coagglomeration excipients.

Table 2.6: Example of crystallo co-agglomeration practices seen in relevant pharmaceutical literature for different drug - excipient combinations, chosen based on a desired function

Coagglomeration Components	Benefits	References
Drug / Diluent	Drug coagglomerated with diluent dispersed in the good solvent (often including polymer). Generated directly compressible agglomerates in the correct proportions of active pharmaceutical ingredient and filler. Coagglomerates showed improved compressibility, flowability and dissolution properties suitable for tabletting.	[84–88]
Drug / Polymer	Drug coagglomerated with polymers that improve the dissolution and compressibility. Additionally, the polymer enhances mechanical strength of the material and stability as a tablet.	[89,90]
Drug / Drug	Drug coagglomerated with another drug (such as paracetamol/ibuprofen) in the correct proportion for generating directly compressible agglomerates. This improves the distribution of components in the tablet and reduces the required unit operations.	[83]
Drug / Disintegrant	Drug coagglomerated with a disintegrant increased the dissolution rate of tabletted coagglomerates vastly. Control of the ratio of drug/disintegrant enabled drug dissolution rate to be tailored to the application.	[91]

The research into coagglomeration of multiple components for direct compressibility of pharmaceutical materials is still relatively new, therefore there is a limited number of mechanistic studies surrounding the process. The process appears to use similar mechanisms to spherical crystallisation, except with an additional component in the dispersed phase. In spherical agglomeration in suspension, the successful coagglomeration of two solids simultaneously requires similar wettability properties so that both components are captured by the bridging liquid. The crystallisation step is not required and both components of coagglomeration are dispersed in the continuous phase. Coagglomeration was developed as a method to be able to agglomerate two species in one process to create directly compressible drugs [6,83,84,86,88,89]. Therefore, it would be beneficial to generate directly compressible coagglomerates

of electrode material, of which, there is both the active material and conductive additive. Agglomeration of the active material and conductive additive together to create an interlocked matrix which is directly compressible onto a current collector foil, would show great potential in a dry manufacturing process line, preventing the issues discussed in Section 2.1.6

2.3 Spherical Agglomeration of Graphite

The main focus of this thesis will be working with graphite which, as discussed in Section 2.1.2 is a particularly versatile and commonly used active material in lithium-ion battery anodes. Additionally, graphite is a particularly non-hazardous material to work with and therefore is an ideal starting point for investigating the spherical agglomeration procedure with electrode materials. As with most electrodes, the bulk of the anode is made up of the active material, but conductive additives will also be investigated when generating interlocked coagglomerates of the two materials. There is a lack of direct research into spherical agglomeration of electrode materials and is a novel area of research in this sector. Spherical agglomeration is still a relatively novel technique with potential to be used in pharmaceutical research, and as such the application of this technique in electrode research is also particularly novel. There is some limited research on the application of spherical agglomeration for graphite, but not for the purpose of electrode formation.

The earliest literature regarding spherical agglomeration of graphite discusses how adsorbed solvents on the surface of graphite particles leads to selective wetting and therefore separation from a bulk mixture [17]. This work by Farnand et al. (1961) [17] reported that use of solvents such as toluene, kerosene, nitrobenzene and chlorinated hydrocarbons act as successful binding agents when graphite is dispersed in a water suspension, also containing calcium carbonate and zinc sulphide. The process was not carried out using a stirred tank, instead, a tumbling drum was used. The suspension and bridging liquid were agitated to assess the selective separation of components. The ability for material separation was shown to be feasible, but the effect of process parameters on the spherical agglomerate properties was not assessed in this work.

Sutherland et al. (1962) [18] expands on the spherical agglomeration process for graphite using a rotating drum, and began to assess the process parameters that effect agglomerate properties. The process uses a method originally designed for collecting coal fines, using a liquid that preferentially wets the solid, called the Convertol process. Sutherland (1962) [18] utilised two different rotating drums, one with corrugated walls, and the other using smooth wall and baffles. The bridging liquid was added in droplet form. Graphite was suspended in an aqueous suspension - the continuous phase. The bridging liquid was a 1:2 vol/vol mixture of kerosene and lubricating oil. Sutherland (1962) [18] also built upon the work carried out by Farnand et al. (1961) [17] by testing the same agglomeration system in a rotary drum, using a different bridging liquid called Stanolax, which is a mineral oil product that is

no longer produced. Sutherland (1962) [18] had some interesting observations that correlate with modern literature.

Firstly, increasing solids loading tended to show greater agglomerate diameter due to enhanced growth phase. However, drum speed had to be increased to maintain turbulent flow regime, for efficient collision frequencies. Another observation found was that bridging liquid concentration was one of the most important factors, which agrees with the work surrounding BSR [14,16,74]. It was found that there is a small region for which optimum agglomeration occurs, and above this region a paste is formed, and below this region agglomerates are barely formed, or lack mechanical stability. Increasing bridging liquid viscosity appeared to slow the agglomeration process which was assumed to be due to reduced distribution potential of the bridging liquid. Finally, Sutherland (1962) [18] found that operation variables for mixing play an important role in agglomerate formation. The baffled drum was found to agglomerate particles more quickly due to increased turbulence compared to the corrugated wall drum. Increasing the solids loading was found to reduce the mean particle size when compared at equal rotation speeds, this was due to the reduced turbulence. However, if the rotating speed is increased with solids loading then it can lead to an increase in mean agglomerate size.

Sutherland (1962) [18] outlines two distinct mechanisms for agglomerate growth, taken from the particle size distribution (PSD) changes. Initially a mono-modal PSD is observed but then as agglomerate growth continues a bi-modal PSD emerges eventually tending towards a mono-modal PSD at a higher agglomerate size. This indicates that there are two growth mechanisms, where initially the bridging liquid is distributed and flocs form. The second growth mechanism involves combining of flocs to form more spherical and dense agglomerates. This aligns with the mechanisms proposed regarding a nuclei formation stage and then a growth/densification stage, seen in Figure 2.11 presented by Pitt et al. (2018) [12]. The paper by Sutherland et al. (1962) has some limitations particularly with a lack of images to validate the results presented in the text. Equally, to adopt this process for electrode materials there is an issue with non-volatile oils and hydrocarbons as bridging liquids.

A further study of graphite spherical agglomeration was conducted by Drzymala et al. (1988) [92] where the focus was related to separation of coal fines. It was reported that graphite was used because of its similar surface properties to coal, whilst being more stable for experimentation. The authors discuss how receding contact angle was used to identify a suitable bridging liquid, which resulted in heptane being used. It was observed that as heptane volume increased the size of graphite agglomerates increased. Relating to modern literature surrounding spherical agglomeration what the authors observe here is that the BSR had increased, and agglomerates were becoming overwetted, leading to layering or coalescence.

Since this work by Sutherland et al. (1962) [18] and Drzymala et al. (1988) [92] there has been limited research directly on the agglomeration of graphite. Recently though, Schreier et al. (2023) [93] has

begun working on agglomeration of graphite in a quartz suspension. The work does not have a focus on electrode formation but instead for selective separation of graphite. Much like previous studies [17,18] an oil based bridging liquid is used, paraffin. The quartz is not wetted by the paraffin and therefore graphite transfers from the suspension to the bridging liquid droplets whilst the quartz remains in the aqueous phase. The work does not discuss the effect of process parameters on the agglomerate properties.

Table 2.7 shows the solvent – solid suspensions used for spherical agglomeration of graphite from the studies discussed. The work to date on spherical agglomeration of graphite focuses primarily on selective separation of graphite from suspensions of multiple components, and it was seen that an oil-based bridging liquid in an aqueous suspension successfully generates agglomerates.

Table 2.7: Summary of components used for agglomeration of graphite as seen in literature

Research Paper	Solid Suspension	Continuous Phase	Bridging liquid	Ref
Farnand et al. (1961)	Graphite, calcium carbonate and zinc sulphide	Water	Toluene, kerosene, nitrobenzene and chlorinated hydrocarbons	[17]
Sutherland et al. (1962)	Graphite and calcium carbonate	Water	Mineral oil and kerosene	[18]
Drzymala et al. (1988)	Graphite	Water	Heptane	[92]
Schreier et al. (2023)	Graphite and quartz	Water	Paraffin	[93]

For using the agglomerates in electrode manufacturing there must be as little bridging liquid as possible. This is because it will affect the electrochemical potential of the cell but also has potential for side reactions and consequent issues regarding safety. Therefore, choosing a bridging liquid for spherical agglomeration of battery electrode materials must account for efficient evaporation and drying of the agglomerates, perhaps through volatile solvents. There has yet to be a study on generating structured coagglomerates of graphite and conductive additive, for use in electrode manufacturing processes.

2.4 Critical Summary

The review of literature has outlined areas of study currently being focused on with regards to lithium-ion batteries and spherical agglomeration techniques. It has been determined that lithium-ion battery research for different chemical compositions of electrodes is a vast area of research. The main focus of lithium-ion battery research for EV's is attempting to identify areas where energy density can be increased. This is to improve the distance that these EV's can travel due to enhanced capacity. It was

found that NMC is one of the most promising of these cathode material choices due to its high capacity and relative stability due to the incorporation of manganese and cobalt ions in the crystal structure. For EV's high nickel content cathodes are regarded as the one of the main aims of electrode research due to high nickel content increasing the energy density of the cells and thus capacity. However, due to thermal, mechanical and chemical stability issues arising from high nickel content, manganese and cobalt are adopted into the structure replacing some of the nickel sites. For the anode there is vast research into different chemical compositions to be used as alternatives to the most common choice, graphite. Graphite is considered stable and versatile as an anode with a high relative abundance; however, the theoretical capacity of the anode could be enhanced if a different material was used. Silicon anodes were seen to have very high theoretical capacity; however, they are setback by large volume changes during charge/discharge cycles.

It was found that investigating the secondary structure of standard electrode materials has taken a side line in the research, with less work being published with regards to structure when compared to chemical composition. Research that does investigate tailoring secondary structure of active materials, showed promising results, particularly in improving conductivity and lithium diffusivity. The tailoring of secondary structures can also be utilised to reduce microcracking and gas evolution, which were identified as major issues facing nickel rich cathodes by Lu et al. (2020). For the work that has been published investigating particle processing of active material particularly in spherical structures or agglomerates, the use of intensive process conditions makes the scale up potential limited. This is because the process would require large operating costs and energy usage to implement on a commercial scale. Therefore, there is a gap in research with regards to electrode manufacturing, or particle processing of electrode materials, at ambient temperature and pressures. There are various processes, but spherical agglomeration will be the focus of this research, particularly in developing a successful process for generating graphite and conductive additive coagglomerates. Spherical agglomeration of graphite was found to have limited literature due to the novelty of the process. Several studies managed to generate agglomerates of graphite and observed similar trends regarding process parameters to modern spherical agglomeration literature [17,18,93]. However, the bridging liquid solvents used would not be suitable for electrode manufacturing.

The implementation of spherical agglomeration into the electrode manufacturing process could alleviate some of the limitations and concerns discussed in Section 2.1.6 . Generating secondary spherical structures enables good packing of the active material and conductive additive into a well distributed electrode. The local homogeneity of the small, interlocked structures generated through spherical agglomeration ensure successful homogeneity across the larger electrode area, with improved long and short-range conductive networks owing to the distribution of conductive additive through high shear processing. The agglomerates formed have potential to be used in direct compression processes such as

dry roller to roller compaction onto current collectors. This enables dangerous solvents such as NMP to be eradicated from the process line, which also reduces the cost and time associated with drying of wet slurry cast electrodes. For the solvents used in the spherical agglomeration process, recovery and recycling is possible with a potential to operate continuously. Additionally, generation of agglomerate structures will improve the particle handling and flowability when implementing into the dry processes which also reduces any dust risks associated with cohesive powders such as those used in electrode manufacturing. Finally, compared to other processes which generate spherical structures of active material, such as spray drying, spherical agglomeration generally operates at ambient temperature and pressure, reducing the cost of production. Finally, the porous spherical structures formed might expand the life span of developed batteries, due to the advantageous capacity for volume change during charge and discharge, this will enable consumer goods to be charged/discharged for many cycles before reaching end of life due to microcracking. The porosity will also promote improved ionic conductivity as ions from the electrolyte can access a higher amount of active material surfaces, this allows for faster charge/discharge which is beneficial for consumer goods. The spherical structures will improve the packing density and therefore the energy or power density of the formed electrode, vital for high capacity or fast charge/discharge respectively. Therefore, the proposed solution of spherical agglomeration could benefit the lifespan and operational efficiency of manufactured batteries.

Due to the gaps identified in this literature review, an investigation into spherical agglomeration of graphite and conductive additive to generate well dispersed interlocked secondary structures was carried out. The effect of process parameters will be assessed to investigate how they compare to relevant previous literature. The use of excipients such as surfactants and polymers will be explored with the aim of generating novel secondary structures. Additionally, further work developing the thermodynamic energy balance of particle transfer will be carried out to be able to identify successful spherical agglomeration solvent systems for a given solid. Moreover, a regime map will aim to be proposed based on the thermodynamic properties of spherical agglomeration identified throughout the spherical agglomeration experiments.

Chapter 3 - Materials and Methods

This section will discuss common materials and methods used throughout this thesis. More specific methods will be discussed in detail in their relevant results chapters throughout.

3.1 Materials

Spherical agglomeration was carried out to generate secondary particle structures of the active material and carbon additive particles used within electrode manufacturing. In this process primary particles are suspended in a continuous phase (e.g. DI water) and agitated in a stirred vessel. A bridging liquid with preferential wettability to the solids is injected to the suspension. Particles then transfer from the continuous phase to the bridging liquid droplets and over time consolidate to form stable agglomerates. Polymeric binder soluble in the bridging liquid was used to improve agglomerate strength and surfactant was used in the continuous phase to enhance dispersion of particles and droplets. These materials were characterised and will be described in the following sections.

3.1.1 Primary Particles

A wide range of primary particles were used for this thesis. As discussed in Section 2.1.1 of the literature review, an electrode is composed of active material, carbon additive and binder particles; of which 90 % is active material. Therefore, most primary particles assessed in this thesis will relate to the active materials.

3.1.1.1 Active Materials

Of these active materials three types of graphite were used for spherical agglomeration experiments, which is a common active material for lithium-ion battery anodes. Timrex KS4 and KS6 synthetic graphite (Imerys, France) can be seen in Figure 3.1 and Figure 3.2, and S360-E3 synthetic graphite (BTR, China) can be seen in Figure 3.3. These SEM images show the differences in the material structures and size. For easier readability the S360-E3 graphite will be referred to as S3 graphite from herein.

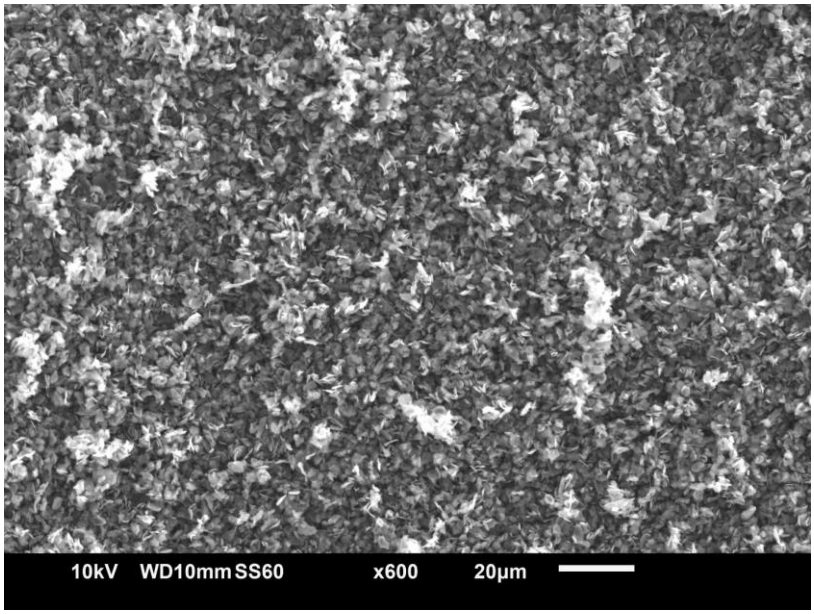

Figure 3.1: SEM images of Timrex KS4 graphite (Supplier: Imerys)

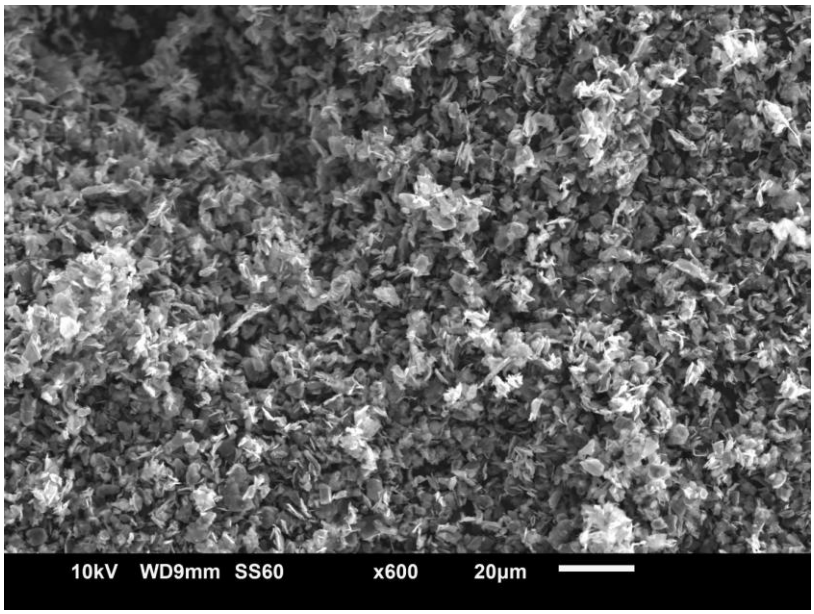

Figure 3.2: SEM image of Timrex KS6 graphite (Supplier: Imerys)

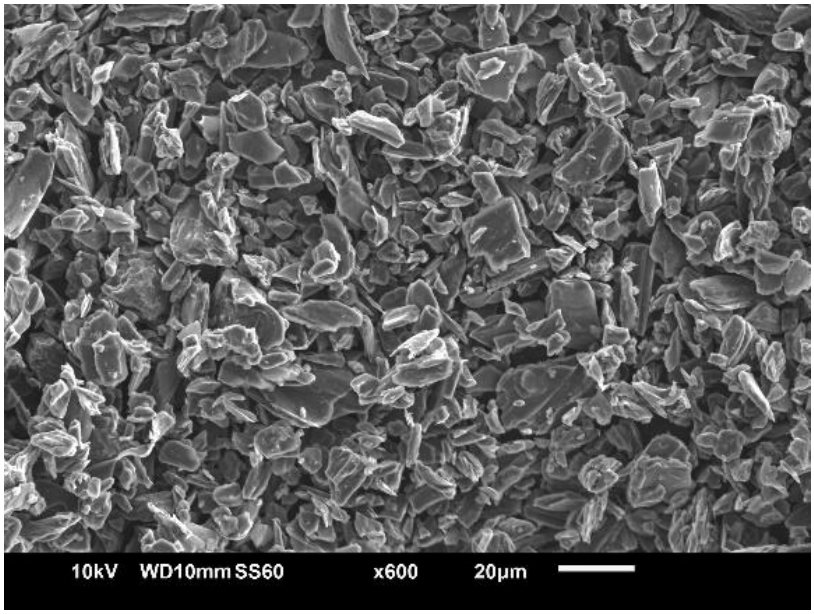

Figure 3.3: SEM image of S360-E3 graphite (Supplier: BTR)

KS4 and KS6 graphite shows a plate-like structure with approximate d_{50} diameters of 3.34 and 4.49 µm respectively. The S3 graphite has a larger average d_{50} of 16.3 µm. The method for analysing particle size distribution can be found in Section 3.2.1 .

For the cathode there is often more variability about which active material is chosen. Although there is debate regarding which cathode material will be the most popular in the future, lithium iron phosphate (LFP) shows promise owing to its low flammability and low material cost since iron is a highly abundant material. Carbon coated LFP (PI-KEM, UK) was used as an alternative active material to compare with graphite. An SEM image of the primary material can be seen in Figure 3.4.

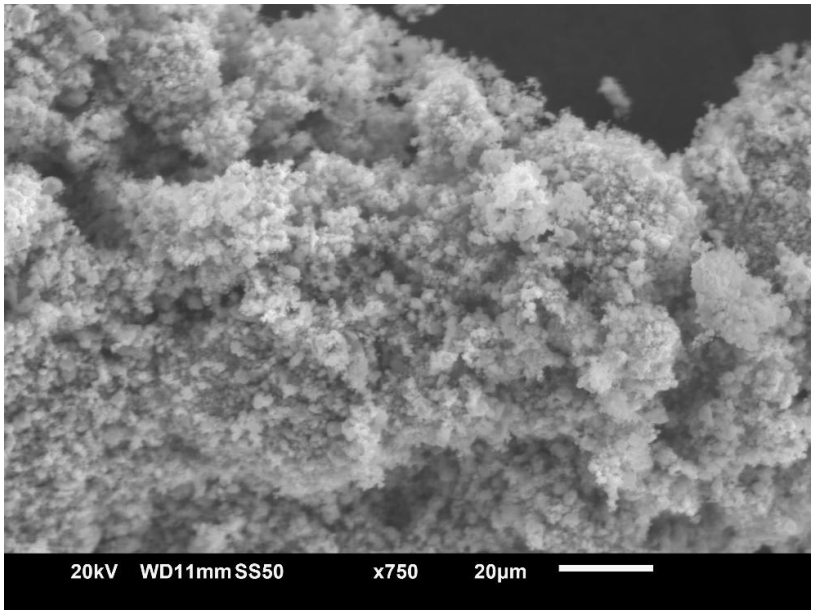

Figure 3.4: SEM image of LFP primary particles (Supplier: PIKEM)

The primary particles of carbon coated LFP appear more spherical than the graphite particles which appear needle-like for KS4 and KS6 graphite, and rhombohedral/planar for S3 graphite. The primary particles can be seen to be part of an aggregate/agglomerate suggesting a cohesive nature, which reduces flowability. Flowability of the primary material was assessed in Section 3.2.2.2 through tapped density and Hausner ratio.

3.1.1.2 Carbon Additive

To generate functioning electrode particulate structures both an active material and carbon additive are required. Therefore, the agglomeration processes discussed herein primarily relate specifically to a coagglomeration process, where both active material and carbon additive are agglomerated together to form an active material – carbon additive matrix. For this reason, C-Nergy Super C65 carbon black (Imerys, France) was included in the agglomeration procedure. C65 carbon black is a nanomaterial with a chain-like structure and high specific surface area. Due to this nature, acquiring informative SEM images of the C65 proved difficult, due to limitations of the SEM, as can be seen in Figure 3.5.

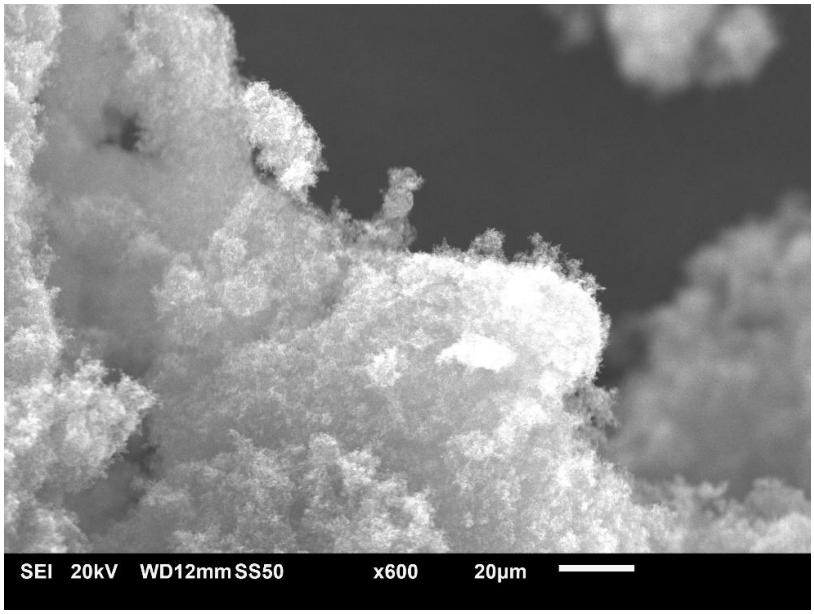

Figure 3.5: SEM image of C-Nergy Super C65 Carbon Black (Supplier: Imerys)

C65 carbon black has high electrostatic potential and handling of the primary powder can be difficult. However, carbon black is one of the most common conductive additives used in electrode manufacturing for both the anode and the cathode.

3.1.2 Solvents

Deionised water was used as the continuous phase in all the coagglomeration experiments, this was taken from a Purite deionisation water dispenser with a purity level of 18.2 MΩ.

Bridging liquids used were chosen dependent on wettability criteria discussed in Section 4.2.1.1. A breakdown of the solvents discussed and tested throughout this thesis are detailed in Table 3.1, below:

Table 3.1: Solvents investigated for bridging liquid options in spherical agglomeration experiments with solubility in water taken from supplier data sheets (Sigma-Aldrich).

Supplier	Chemical	Solubility (g/ml) @ 25°C
Sigma Aldrich/Merck	Chloroform	8.7
Sigma Aldrich/Merck	Toluene	0.58
Sigma Aldrich/Merck	Heptane	Insoluble

For spherical agglomeration it is important that a bridging liquid solvent has preferential wettability with the solids of interest. However, solubility is also important for generating dispersed droplets for particles to immerse into. Ideally the solvents should be immiscible in the continuous phase and thus low solubility. The solubility values found from literature are given in Table 3.1.

3.1.2.1 Binding Agent

In standard spherical agglomeration, agglomerates formed are bound through liquid bridges which solidify to form solid bridges between crystalline particles that were initially precipitated out of solution. The process which this thesis refers to as spherical agglomeration does not involve a crystallisation step. Instead, the particles that are suspended are bound by droplets of a bridging liquid which has a preferential wettability to the solid than the continuous phase. Once the, then, agglomerated suspension is filtered and dried these solvents evaporate and the agglomerate binding forces are primarily controlled Van der Waal's forces and some electrostatic attraction. For this reason, the agglomerates would not be particularly strong and break apart to their primary material. Therefore, polymeric binder is used in the process to improve structural integrity of the agglomerates.

For these purposes, ethyl cellulose (Sigma – Aldrich) was used as it is highly soluble in the solvents used for bridging liquids whilst being non-aqueous, as distilled water is primarily used as the continuous phase. Ethyl cellulose is a polymeric binder with chain-like structure, and for most coagglomeration experiments is used at 0.5 wt% with respect to the bridging liquid. A low amount of binder was used to maintain structure with minimal effect on the bridging liquid properties, such as droplet formation or surface tension.

Sodium dodecyl sulphate surfactant (Sigma – Aldrich) was also used in certain cases to aid in dispersion of particles and droplets and will be detailed in the relevant results chapters.

3.2 Primary Particle Characterisation

3.2.1 Particle Size Distribution

Particle size distribution of the primary materials and sometimes generated agglomerates was carried out using the Mastersizer 3000 (Supplier: Malvern Panalytical), which can distinguish particle sizes between 0.01 μm – 3500 μm. Since the primary particles were known to be in the micron scale, this method was chosen over sieving to calculate the size distribution. Sieving of fine particles becomes increasingly difficult, as the particles can begin to aggregate and block the sieve holes. Using the Mastersizer allowed the particles to be dispersed under higher disruptive forces due to the agitation and sonication settings reducing the potential for aggregation or agglomeration during sizing.

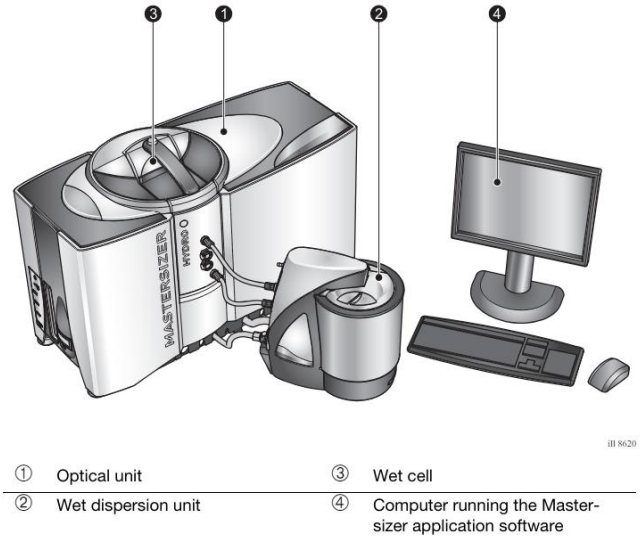

Figure 3.6: Diagram of Malvern Mastersizer 3000 with wet dispersion cell attached (Sourced from the Malvern Panalytical Mastersizer 3000 user manual [94])

The Mastersizer 3000 uses scattering patterns by red and blue light through a suspension of particles to determine particle sizes [94]. As the light interacts with the particles the beam scatters off at different angles, detected by multiple sensors within the instrument. The software implements Mie theory of light scattering [95] to develop a size distribution based on volume equivalent spheres. The unit can be operated in wet or dry format depending on material characteristics. The wet cell was used for dispersion of primary particles in a distilled water continuous phase. The particles were added to the stirred tank, operating at a given impeller speed and sonication level. Process parameter details for the different materials will be given in the following sections. The particles were added until the obscuration level of the light sensors reached 10 – 20 %. As the dispersed sample was pumped through the wet cell loop, the particles passed by the laser's beam and, when at the correct obscuration level, were measured for size characteristics. The refractive and absorption index were required as inputs for the Mastersizer 3000 software to analyse the scattering patterns to develop a particle size distribution based on Mie theory and these values were taken from literature and supplier datasheets.

3.2.1.1 Graphite Primary Particles

The three graphite particles used, herein termed KS4, KS6 and S3 graphite, were measured using the same analysis conditions. The details for Mastersizer 3000 runs can be seen in Table 3.2, with optical properties of the graphite and water taken from the Malvern Instruments Ltd. material database at the blue light wavelength of 400 nm.

Table 3.2: Run conditions for KS4, KS6 and S3 graphite particle size distribution measurements using the Mastersizer 3000

Particle Name	Graphite
Particle Refractive Index	2.680
Particle Absorption Index	1.000
Water Dispersant Scattering Index	1.330
Scattering Model	Mie theory
RPM	2000
Sonication (%)	0

Ten repeats of the dispersed sample were measured to generate individual PSD's and an average PSD. The data presented for the primary material will be based on the average measurement. Important values include the d_{10}, d_{50} and d_{90} which represent the diameter at which the cumulative volume fraction accounts for 10, 50 and 90 % respectively of the total volume of material. These values are given in Table 3.3 as a summary of the three different graphite primary particle size data.

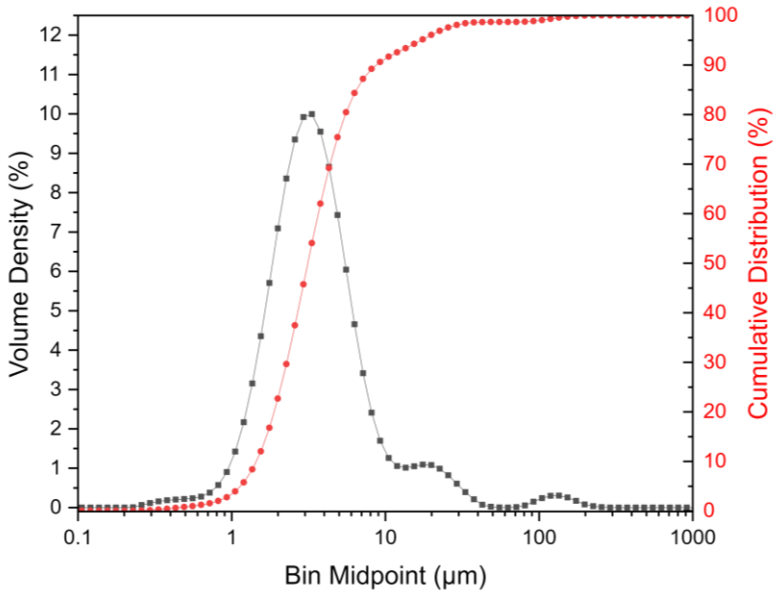

Figure 3.7: Equivalent volume-based particle size distribution and cumulative size distribution for KS4 primary particles using the Mastersizer 3000 (average of ten repeats)

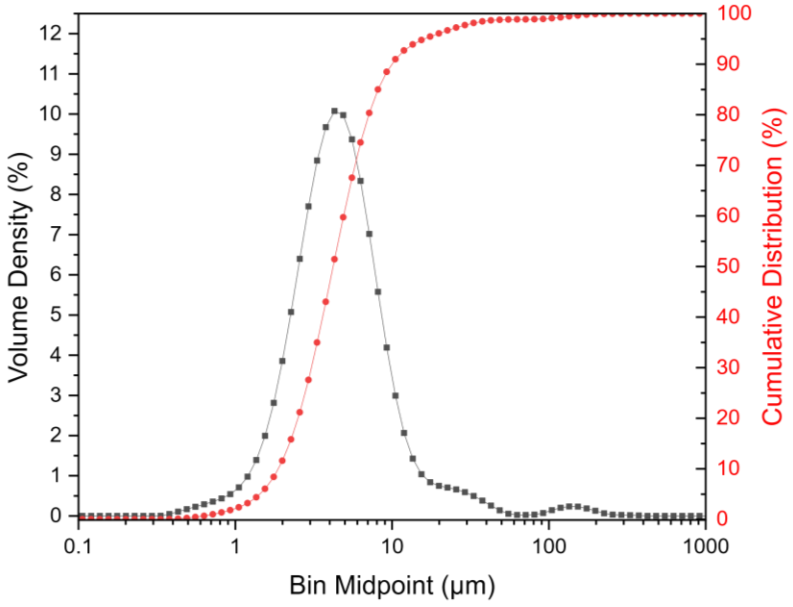

Figure 3.8: Equivalent volume-based particle size distribution and cumulative size distribution for KS6 primary particles using the Mastersizer 3000 (average of ten repeats)

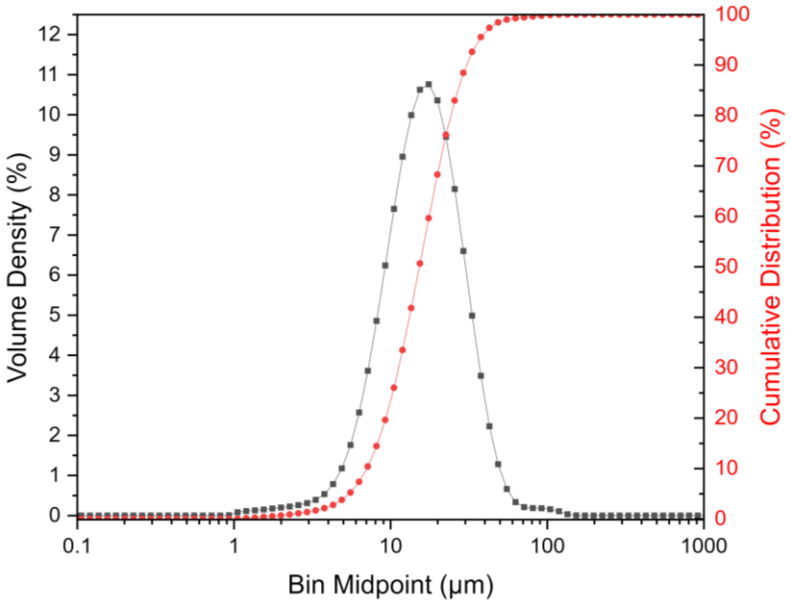

Figure 3.9: Equivalent volume-based particle size distribution and cumulative size distribution for S3 primary particles using the Mastersizer 3000 (average of ten repeats)

Further to the SEM images seen in Figure 3.1 to Figure 3.3, the particle size distribution provides characteristic data for the primary particles. As seen in Figure 3.7 to Figure 3.9, the KS4 graphite has the smallest average particle size with S3 graphite d_{50} being over three times the size of both KS4 and KS6 graphite. However, as seen in Table 3.3, the specific surface area (SSA) was seen to be much larger for the smaller particle size graphite - KS4 and KS6. Specific surface area is an important characteristic for spherical agglomeration, in particular particle packing, and is discussed briefly in Section 4.3.1.3. The specific surface area was calculated during the size analysis by using the calculated particle $d_{3,2}$ (Sauter mean diameter), a user provided density value and an assumption that the particle is spherical.

These were used to calculate the surface area and mass for a given particle mean diameter, and therefore specific surface area.

At the higher end of the particle size distribution, there were some unexpected larger particles measured, which was due to aggregates and/or agglomerates of the primary material not being fully dispersed in the water dispersant. This is particularly prominent for the KS4 graphite. However, the peaks at larger diameters represent less than 10 % of the cumulative volume which can be seen by the d_{90} being less than the peaks seen at the larger diameters. This provides assurance that the results calculated from the PSD data given by the Mastersizer (e.g. span, specific surface area etc.) are not largely skewed and can be considered reliable. Comparing the size data measured by the Mastersizer with the scale bars on the SEM micrographs also provides assurance that the data is reliable and accurate. For KS6 and KS4 graphite the primary particles are much smaller than the 20 µm scale bar provided. However, for the S3 graphite the particles are approximately the same diameter as the 20 µm scale bar. This compares well with the size data seen in Table 3.3.

Table 3.3: Summary of KS4, KS6 and S3 graphite primary particle size data measured through the Mastersizer 3000

Graphite	d_{10} (µm)	d_{50} **(µm)**	d_{90} (µm)	$d_{3,2}$ (µm)	$d_{4,3}$ (µm)	**SSA (m^2/kg)**
KS4	1.54	**3.34**	9.30	2.74	6.48	**2188**
KS6	2.01	**4.49**	10.6	3.59	7.56	**1669**
S3	7.54	**16.3**	32.5	12.8	18.8	**469.6**

3.2.1.2 Cathode Active Material Primary Particles

Particle size distribution of LFP was also analysed using the Mastersizer 3000. Ten repeats were conducted, and average data was used for further analysis. The same method was employed, however with different input parameters, taken from supplier datasheet, dependant on the material properties just as in Section 3.2.1.1. The input parameters can be seen in Table 3.4:

Table 3.4: Run conditions LFP particle size distribution measurements using the Mastersizer 3000

Particle Name	**LFP**
Particle Refractive Index	1.630
Particle Absorption Index	0.1
Water Dispersant Scattering Index	1.330
Scattering Model	Mie theory
RPM	2000
Sonication (%)	0

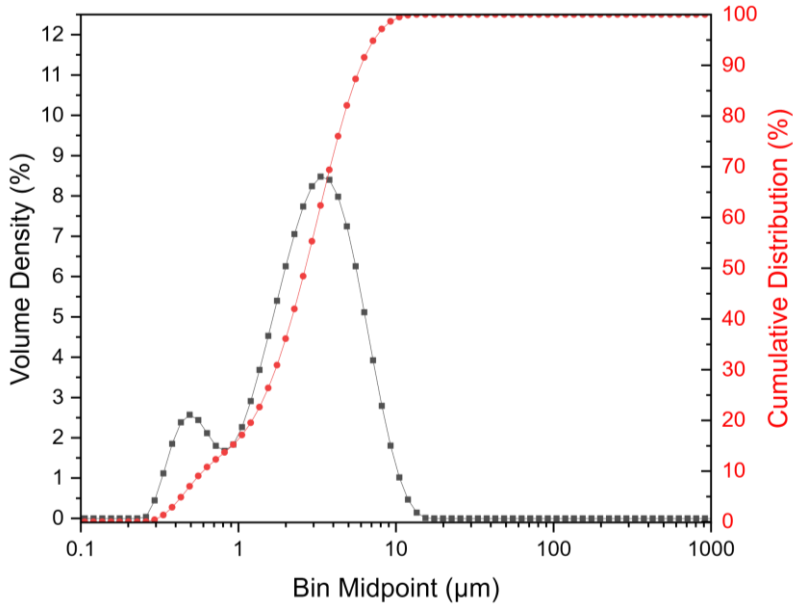

Figure 3.10: Equivalent volume-based particle size distribution and cumulative size distribution for LFP primary particles using the Mastersizer 3000 (average of ten repeats)

The particle size distribution seen in Figure 3.10 shows that the primary particle size is on average smaller than the graphite primary particles. The PSD shows bimodal distribution with two peaks. The larger peak at approximately 3 µm indicates most of the volume fraction measured. Whilst the smaller peak at approximately 0.5 µm indicates detached carbon that makes up the carbon coating on the LFP particles. This can be broken away from the LFP particles by the shear forces applied during agitation in the Mastersizer wet cell.

Table 3.5: Summary of LFP primary particle size data measured through the Mastersizer 3000

Chemical	d_{10} (µm)	$\boldsymbol{d_{50}}$ **(µm)**	d_{90} (µm)	$d_{3,2}$ (µm)	$d_{4,3}$ (µm)	**SSA (m^2/kg)**
LFP	0.636	**2.82**	6.43	1.68	3.27	**1021**

3.2.1.3 Carbon Additive

The particle size distribution, measured using the Mastersizer 3000, produced unexpected results for C65 due to the particles self-agglomerating when using the wet dispersion method. Sonication at 10 % was attempted to break up the C65 agglomerates, however, the size data does not match what is expected of the carbon black nanomaterial. The size data gathered using the Mastersizer 3000 can be seen in Figure 3.11.

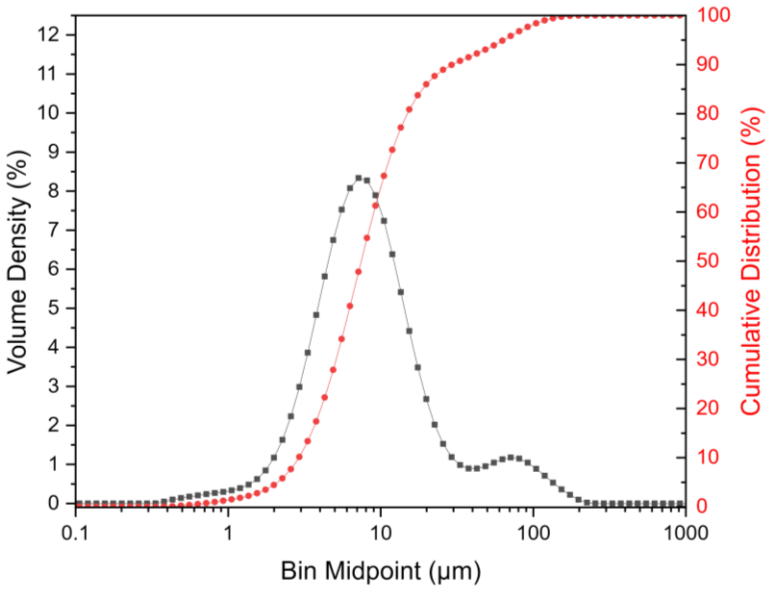

Figure 3.11: Equivalent volume-based particle size distribution and cumulative size distribution for C65 primary particles using the Mastersizer 3000 (average of ten repeats)

As can be seen in the particle size distribution shown in Figure 3.11, the average particle size suggested is approximately at 10 µm which is larger than that suggested by literature which used transmission electron microscopy [96]. The secondary peak, observed at 100 µm, shows how agglomerates of the primary material form in the wet dispersion and are much larger than those seen in literature. Primary particles of C65 carbon black are between 30 and 50 nm with aggregates forming at approximately 500 nm [96]. The size data measured using the Malvern Mastersizer 3000 was therefore not used for carbon black C65 particle sizing.

3.2.2 Particle Density

Density is a key value required for spherical agglomeration and for primary powders this value can hold many different meanings. The types of densities discussed herein include true density, tapped density and bulk density.

3.2.2.1 True Density

For calculating the TBSR, a true density value is required. True density is defined as the mass per unit volume of a material, where voidage and space between particles is discounted. This is sometimes referred to as skeletal density. This was measured using helium pycnometry using a Micromeritics Accupyc II 1340 which can be seen in Figure 3.12. Helium is able to penetrate nanopores in particle beds and provide a highly accurate analysis of the total porosity for a given sample. Thus allowing the particle true density to be calculated from a powder sample.

Figure 3.12: Image of Accupyc II 1340 (Supplier: Micromeritics) used for analysis of primary particle true density

A known mass of sample was loaded into a sample cup, with a fill volume of 1 cm^3, such that between half and two thirds of the sample cell was full. This was transferred to the chamber and closed off with a lid that locks into place so that the chamber was airtight.

The chamber then ran through 5 repeat cycles of evacuating the chamber and using high pressure helium to refill the chamber and the voids that were present within the powder bed. This allowed a true volume of powder to be calculated which was taken as an average of the 5 runs. This was then converted to a true density based on the known mass input. Upon completion, the chamber returned to atmospheric pressure and the sample was unloaded and disposed. This was carried out for the primary particles of active material and carbon additive as discussed in Section 3.1.1.1 and Section 3.1.1.2 respectively. A summary of the measured values can be seen in Table 3.6.

Table 3.6: Summary of primary particle true density values measured using Accupyc II 1340 Helium Pycnometry

Primary Particle	Mass (g)	Volume (cm^3)	**Avg. Density (g/cm^3)**	Std. Dev (g/cm^3)
KS4 Graphite	0.1480	0.0635	**2.3313**	0.0027
KS6 Graphite	0.1904	0.0816	**2.3326**	0.0042
S3 Graphite	0.4011	0.1765	**2.2719**	0.0027
LFP	0.5040	0.1406	**3.5841**	0.0057
C65 Carbon [97]	-	-	**1.9**	-

The true density for the three graphite primary particles is almost identical within acceptable error. This is expected as removing voidage through helium insertion the true density should be solely based on the material used which in this case is graphitic carbon.

The true density value for LFP was seen to be higher than the graphite samples due to the higher density elements that the primary particles are composed of. A noteworthy result was the consistency between different graphite samples.

True density measurement of carbon black C65 was not able to be measured due to high voidage in the branched primary particle powder bed. For this reason, a reference value from literature [97] was used for the true density of C65, seen in Table 3.6.

3.2.2.2 Bulk and Tapped Density

Two further important density values were bulk and tapped density which is a measure of the powder bed properties rather than singular primary particle properties. The bulk density was a simple measurement and was carried out before measuring tapped density.

The bulk powder was added to a 5 ml volumetric cylinder with an error of ±0.1 ml. As per the ISO 3953 standards, a given mass of powder was added to the volumetric cylinder and, with a gloved hand placed on top, the cylinder was rotated approximately 360° to enable dispersion of the powder and for settling of the material not to be skewed by addition method of powder into the cylinder. The volume of the powder was measured by reading off the top point of the graduated cylinder. This value was used to calculate the bulk density (ρ_b) by dividing by the mass, the values of which can be seen in Table 3.7.

Tapped density (ρ_t) was measured after the bulk density by taking the cylinder containing the bulk material and measuring the volume after a set number of taps. The cylinder was placed in the sample holder and locked in place using the plastic clips on the AntonPaar Autotap. The machine was set using the LCD display to 100 taps. The machine was run and after the 100 taps the volume was, once again, read off the graduated volumetric cylinder. This volume was then divided by the mass of sample. A summary of both the bulk and tapped density results can be found in Table 3.7.

The benefit of using this machine is that the force of ‘tap’ is consistent and therefore measurements for tapped density can be compared more reliably. If the measurement had been done by hand the force applied would have varied between taps and the rearrangement of particles in the cylinder may have had more, or less, force assisting in the movement. By having consistent force applied by the instrument the tapped density compared between samples is instead a function of the particle cohesivity only. Bulk and tapped density are key parameters in measuring the particle cohesion under both standard conditions and during application of force. The values of which are then used to calculate flowability of the primary powders using Hausner ratio which defines ranges for flowability characterisation. The formula for calculating Hausner ratio can be seen in Equation 3.1 [98]. The values of primary particle flowability and Hausner ratio definitions can be seen in Table 3.7.

$$Hausner\ Ratio = \frac{\rho_{tapped}}{\rho_{bulk}} \quad (3.1)$$

Table 3.7: Summary of bulk, tapped density and Hausner ratio for characterising primary material flowability and cohesiveness. Error based on three repeats for density calculations with mean and standard deviation shown.

Primary Particle	ρ_b (g/cm^3)	ρ_t (g/cm^3)	Hausner Ratio	Flow Characteristic
KS4 Graphite	0.116 ± 0.005	0.152 ± 0.003	1.31	Passable
KS6 Graphite	0.134 ± 0.001	0.177 ± 0.004	1.32	Passable
S3 Graphite	0.643 ± 0.062	0.850 ± 0.013	1.32	Passable
LFP	0.629 ± 0.005	0.854 ± 0.020	1.36	Poor

As can be seen in Table 3.7, the Hausner ratio for each material are within the same range, with LFP just falling outside the "passable" flow characteristic to exhibit "poor" flow. The Hausner ratio is an empirical measurement of flow behaviour observed for powders based on the ratio of tapped to bulk density. It is an indication of the particle – particle interactions, however, some particle – wall interactions will also inevitably affect the results. A higher Hausner ratio is indicative of more cohesive material, and thus, less flowable. In electrode manufacturing homogeneous distribution of cohesive powders can prove difficult, and higher shear is required to overcome the attractive forces [99,100]. Therefore, it is hypothesised that the application of spherical coagglomeration, to generate secondary structures of well dispersed active material – conductive additives, will improve the issues surrounding homogeneous distribution by improving flowability.

3.3 Agglomerate Generation

A general method for spherical agglomeration of primary particles was developed and will be described in this section. However, there were some alterations in the method for certain studies, which will be detailed in the relevant results chapters. A stirred tank was designed and consisted of a borosilicate glass beaker (250 ml), to which baffles attached to an acrylic lid were fabricated in-house at the University of Sheffield. Four baffles were spaced around the beaker walls every 90° to improve homogeneity of mixing and prevent vortex formation around the impeller. The beaker was designed following ideal size specifications for dispersion. Figure 3.13 shows the beaker dimensions which were all related based on the internal beaker diameter, which are detailed in Table 3.8, where the beaker was chosen, and all other parts were designed around that.

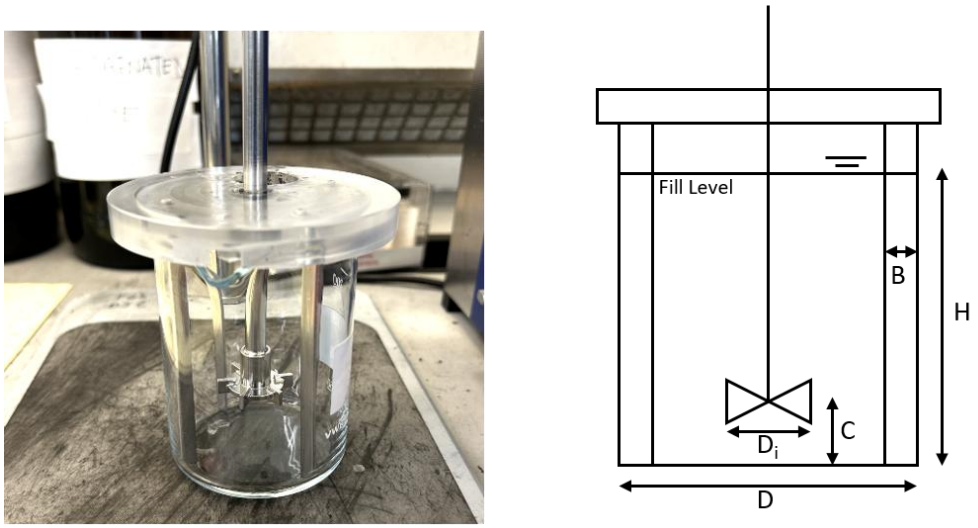

Figure 3.13: Stirred tank setup (left) and diagram of dimensions for ideal mixing in a stirred tank (right) detailed in Table 3.8

Table 3.8: Dimensions of stirred tank related to the internal beaker diameter

Dimension	Relation to Diameter (D)	Dimensions (mm)
Beaker Internal Diameter (D)	D = D	66
Impeller Diameter (D_i)	D_i = 1/3D - 1/2D	30
Impeller Clearance (C)	C = 1/3 D	20
Cont. Phase Liq Height (H)	H = D	66
Baffle Width (B)	B = 1/10 D	6

A 30 mm 6-blade Rushton turbine was used as the impeller which generated a radial flow field [101], as seen in Figure 3.14. The radial flow was beneficial in lifting primary particles up from the base of the beaker, which was required due the high density of the particles and bridging liquid droplets.

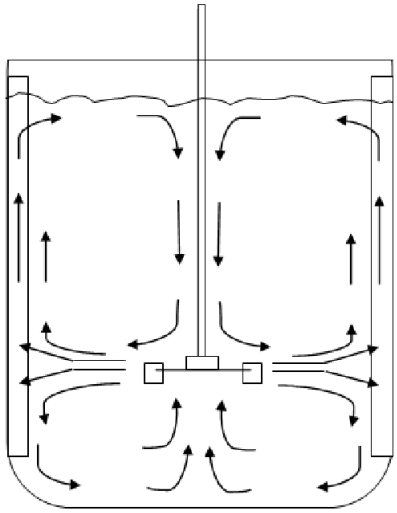

Figure 3.14: Radial flow pattern during agitation using a 6-blade Rushton turbine impeller in a baffled stirred tank, adapted from [101]

It is important to note that all experimental work that used the active material, conductive additive or any toxic solvents were carried out in a fume hood to prevent exposure to these hazardous materials. This includes all spherical agglomeration experiments and any handling of dry powder. Therefore, it was important to have a closed balance which prevents any effects on the measured mass from the fume hood extraction. The standard agglomerate generation method started with weighing out 198 g of DI water in the beaker where 20 ml of which was transferred to a 30 ml vial. The remaining 178 g of DI water was placed under an overhead stirrer (IKA Eurostar 20) where the impeller and lid were attached. The impeller speed was varied using the digital screen on the overhead stirrer which alters the power to increase/decrease the impeller RPM. Where surfactant was involved 0.022 g of sodium dodecyl sulphate was added to the DI water in the beaker. Sodium dodecyl sulphate surfactant was chosen as, since most of the agglomeration systems operated as an oil-in-water dispersion, the hydrophilic-lipophilic balance (HLB) had to be high so that the interfacial tension was higher on the oil side of the interface promoting droplet formation. Once the setup was complete the overhead stirrer was turned on and set to the chosen impeller speed required for the experiment and left to distribute the surfactant in the water and equilibrate for 5 minutes.

Whilst the water and surfactant were being mixed, 0.2 g of carbon black and 1.8 g of active material were weighed out and added to the vial of water, such that the solids loading was 1 wt% with respect to the bulk continuous phase. The vial was placed in an ultrasonic bath to break up aggregates/agglomerates and disperse the primary particles in the water for 2 minutes. The suspension was added to the stirred tank and allowed to disperse further for 5 minutes, after which the bridging liquid was added through a port in the lid using a micropipette. Solutions of bridging liquid containing ethyl cellulose were created prior to the experiment and kept in glass bottles in the dark, as they can be oxidised in the presence of light [102]. Ethyl cellulose was used as a binder as it is insoluble in water

and is an environmentally friendly cellulose derivative binder, compared to other petrochemical-based polymers such as PTFE. The stopwatch was started, and experiment ran for the desired agglomeration time. The standard proportions of material used in the spherical coagglomeration experiments can be seen in Table 3.9, some of which are based with respect to the volume/mass of bridging liquid used which was dependant on the TBSR value for the system. If deviations from this standard setup were used, this will be discussed in the relevant sections.

Table 3.9: Standard mass of components in a typical coagglomeration experiment

Component	Mass (g)	Comments
Water	198	Continuous phase
Active Material	1.8	In a 90:10 wt/wt ratio generally used for electrode manufacturing in research. Add to be 1% wt/wt solids loading w.r.t cont. phase.
Carbon Additive	0.2	
Bridging Liquid	To be determined	(Dependant on TBSR)
Ethyl Cellulose Binder	0.5% wt/wt w.r.t BL	(Dependant on bridging liquid)
Sodium Dodecyl Sulfate Surfactant	0.5% wt/wt w.r.t BL	(Dependant on bridging liquid)

After the agglomeration was complete any agglomerates stuck to the baffles or stirrer were washed off into the beaker using a water filled wash bottle. The beaker with agglomerates was then filtered through a mesh and Buchner filter combination, as seen in Figure 3.15.

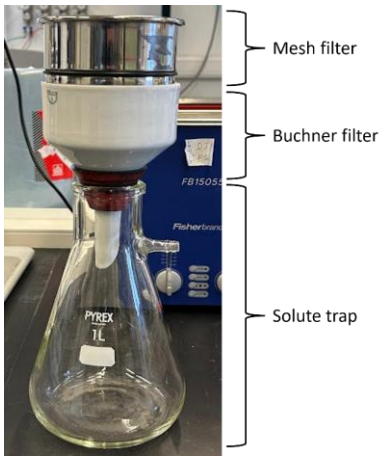

Figure 3.15: Image of filter setup, where the agglomerates in suspension pass through a mesh sieve where material >32 µm is captured, material <32 µm passed through to the Buchner filter and was filtered through 2.7 µm filter paper to capture waste solids

The Retsch mesh had a pore size of 32 µm; this was defined as the minimum agglomerate size and therefore the yield was based on the collection of material from the mesh sieve. The Buchner filter

placed beneath the mesh sieve was used for collection of any remaining primary material from the suspension using 2.7 μm pore size filter paper. Material caught on the filter paper was disposed.

The agglomerates were dried in a drying cabinet at 50 °C for 24 hours. This ensured evaporation of the water and bridging liquid from the agglomerates. Once dry, the agglomerates were transferred from the sieve for further analysis.

3.4 Agglomerate Characterisation

Agglomerates were characterised using a variety of methods. Certain methods were similar to those described in previous sections for the primary particle characterisation and where necessary will be referred to in these sections.

3.4.1 Agglomerate Size Distribution

Agglomerates were characterised using optical microscopy and image processing. This process was developed as dispersion in the Mastersizer 3000 wet cell would likely have led to breakage of the agglomerates and unreliable data for the size distribution. In some cases, however, this was necessary due to the small nature of some agglomerates, and this is detailed in the relevant section.

Images were taken using an optical microscope at 6.96x magnification. For a chosen working distance, the microscope was calibrated at each magnification. This was done by measuring the pixels for a given length using a small-scale ruler provided by the manufacturer. The scale at this magnification was 0.126 pixels/μm, therefore, if the minimum reliable agglomerate feret diameter using this sizing method was represented by 10 pixels this was equivalent to 79.4 μm. Between 40 – 60 images were taken dependent on yield of agglomerates using a grid to line up the camera. Light was transmitted from underneath the staging as the outline of the agglomerates was required not the surface detail. The setup for this can be seen in Figure 3.16.

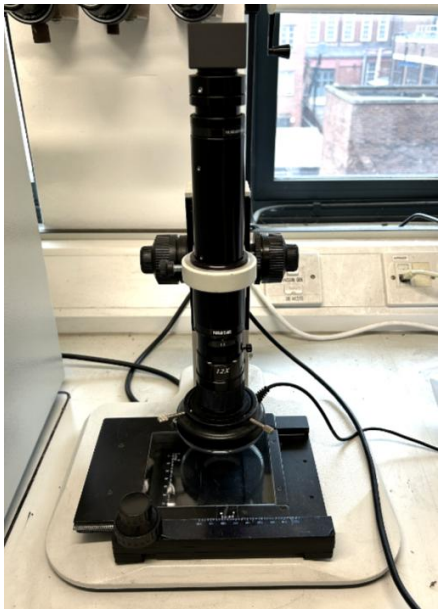

Figure 3.16: Optical microscope camera setup with bottom and top lighting, linked to a PC for live analysis

When the image collection process was completed, the data was analysed in ImageJ, the process involved included macros to run commands on the bulk set of images in an automated way[1]. In this section, the details for image processing described in this section will be related to one image as an example. The first step included taking the RGB colour image and converting it to an 8-bit grayscale image.

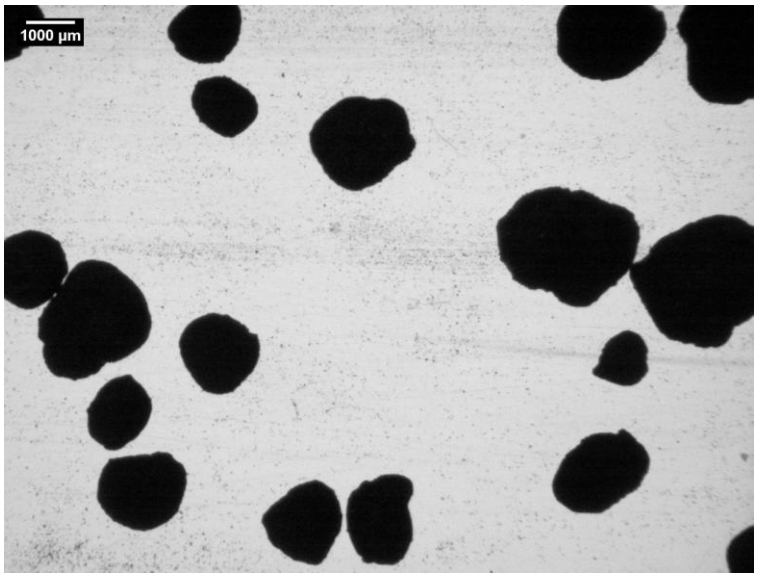

Figure 3.17: Outline of agglomerates imaged and converted to an 8-bit greyscale image

[1] Method developed by Dr Kunal Pardikar (University of Sheffield).

The 8-bit image was cropped to remove any unwanted artefacts from the image. This was then contrasted to improve the clarity of the darker agglomerates.

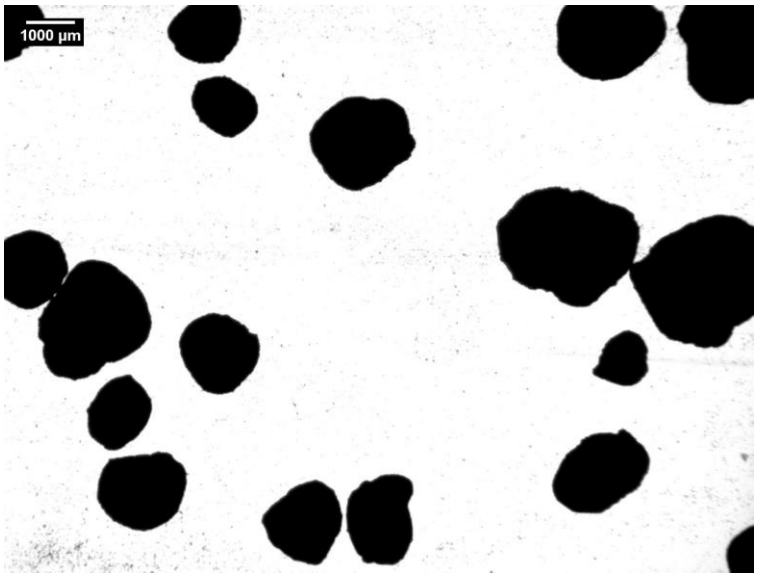

Figure 3.18: Cropped and contrasted image of agglomerates to improve the clarity for edge detection when running the Particlesizer plugin

From these contrasted and cropped images, the Particlesizer plugin [103] was used to generate size data, which was exported to an excel sheet for the total set of 40 – 60 images. Figure 3.19 highlights the input parameters which the Particlesizer plugin was run with. The circle equivalent diameter generated through the Particlesizer plugin was used for defining an agglomerate size distribution and is the diameter for a circle with an area equivalent to that of the agglomerate area found using the Particlesizer plugin based on pixel area. As can be seen in Figure 3.19, the only constraint applied was that the minimum feret diameter for size analysis was 10 px, equivalent to 79.4 µm.

The Particlesizer plugin was validated for accuracy by Dr Kunal Pardikar as part of the aforementioned publication [104] supplementary information, by using the plugin on uniform sized precision spheres. Four types and sizes of spheres were tested with sizes ranging from 150 µm to 1500µm. It was found that the plugin was capable of accurately sizing the spherical particles consistently across this range of sizes. The author states that using this method for particles <100 µm is not validated well enough, but the agglomerates produced as part of this thesis are measured using this technique are generally >200 µm.

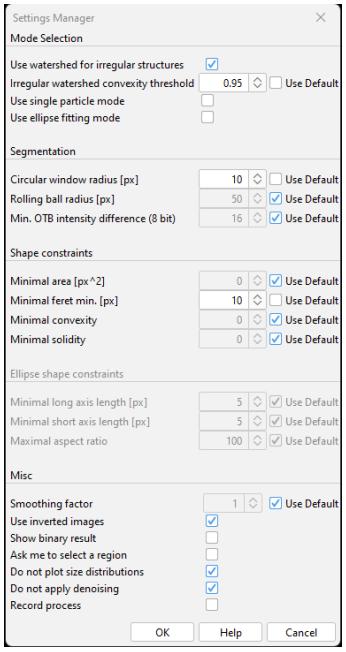

Figure 3.19: Run conditions for the Particlesizer plugin used to size the agglomerates based on a circle equivalent diameter

The circle equivalent diameters were separated and used for developing the agglomerate size distribution. The first step was to define bin sizes used for 'counting' the number of agglomerates in that given size range (bin). This is called a number distribution and is one way of showing the size distribution data. However, for the purposes of agglomerates it was important to see how the volume-based size distribution developed. Therefore, the number distribution was converted to a volume distribution through Equation 3.2, below:

$$f_{vi} = \frac{f_i \bar{x}_i^3}{\sum f_i \bar{x}_i^3 \Delta x_i} \tag{3.2}$$

Where:

f_{vi} Volume based frequency for a given bin range

f_i Number based frequency for a given bin range

$\bar{x}_i$ Midpoint of a given bin range (µm)

Δx_i Bin range (µm)

The conversion from the number distribution provided a volume-based distribution which was plotted against the midpoint diameter of the bin sizes, alongside the cumulative volume-based distribution.

Chapter 4 - Viability of Spherical Agglomeration for Battery Materials: A Study of Agglomeration Procedures and Active Materials

Part of the experimental work in this chapter was carried out in collaboration with Dr Kunal Pardikar (University of Sheffield) as part of the Nextrode project (Faraday Institution) and has since been published [104].

Initial experimental design and characterisation methods were developed by both Dr Kunal Pardikar and the author of this thesis. Dr Pardikar conducted the initial experiments for the modified dispersed phase method for lithium iron phosphate coagglomeration and novel characterisation and analysis methods (such as coagglomerate imaging). Further experiments, repeats and characterisation for LFP coagglomeration were carried out in collaboration. However, all graphite-based experiments were carried out by the author of this thesis.

4.1 Introduction

One of the key parameters for generating spherical agglomerates is the determination of the True Bridging to Liquid Solid Ratio (TBSR) [75] which is a ratio of bridging liquid to solids on a volume-by-volume basis, discussed in Section 2.2.2 . This parameter is an adapted version of the original BSR [12], where the 'True' part refers to the BSR when solubility of the bridging liquid in the continuous phase is considered. For this thesis, TBSR will be used throughout and will include the excess bridging liquid required to account for solubility in the continuous phase.

This parameter will be investigated with the aim of developing a functioning spherical agglomeration procedure that can capture the primary particles of active material and carbon additive to generate coagglomerates. As mentioned in Section 2.2.2 of the literature review, the agglomeration process must operate in the ideal region. This is where there is enough bridging liquid present for full agglomeration with no primary particles remaining in the product, but without forming a paste-like substance where the TBSR is too high.

To aid in this system development the solid/liquid and liquid/liquid interactions had to be mapped particularly with regards to wettability and immiscibility, respectively. This was required to identify an appropriate bridging liquid – continuous phase solvent setup required for a given solid of interest. For coagglomeration experiments where active materials and carbon additives were agglomerated together this was particularly important as both solids needed to have preferential wettability with the bridging liquid. Furthermore, the effect of process parameters (impeller speed, solids loading, agglomeration

time, particle size and TBSR) were investigated to explore how they might affect agglomerate formation and properties.

4.1.1 Objectives

The main research question of this chapter is ‘can spherical agglomeration be used to generate coagglomerates out of battery active materials and carbon additive, and how can it be optimised?’. The main objectives are:

- Investigate the wettability characteristics of solids to be agglomerated with respect to the continuous phase and bridging liquids.
- Explore the effect of TBSR on agglomerate properties and yield.
- Understand how process parameters (such as impeller speed, particle size, time and solids loading) effect agglomerate properties and yield.

4.2 Methods

For the majority of coagglomeration experiments a standard procedure was followed, detailed in Section 3.3 However, for some materials to be agglomerated, new methods were adapted to enable successful generation. This chapter discusses several types of active material coagglomeration experiments and primary particle characterisation is key to the methods carried out. For the active materials and carbon additive discussed in this chapter, the methods of characterisation followed the method outlined in Section 3.1.2.1 for SEM, particle size distribution, true density and flowability characteristics. A summary of these measured values and results is given in Section 3.1.2.1 and will be referred to in this chapter.

4.2.1 Graphite Coagglomeration

The three types of graphite discussed in Section 3.1.1.1 were used to generate agglomerates and compare the effect of primary particle size and surface area with the generated coagglomerate properties.

4.2.1.1 Contact Angle & Solvent Characteristics

Wettability is a key term when discussing the feasibility of spherical agglomeration systems. As discussed in Section 2.2.2 of the literature review, the bridging liquid must show preferential wettability to the solids of interest when compared to the continuous phase. The wettability at a solid-liquid interface is dependent on the surface energy characteristics of the two components. This interaction can be measured using the contact angle of a sessile drop method. Figure 4.1 shows the goniometer and syringe setup used for measuring contact angle. The method is quite simple and involved dropping the solvent onto a bed of particles. A high frame rate camera was used to capture an image of the first

metastable phase of the droplet on the surface of the powder bed. Due to the toxicity of some solvents used the contact angle and surface tension experiments were also carried out in a fume hood.

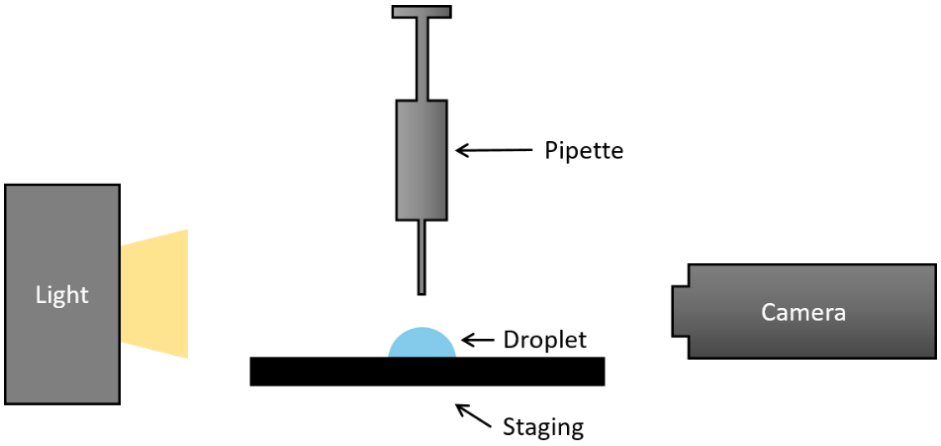

Figure 4.1: Diagram of a typical contact angle goniometer, where a droplet is placed on to a substrate and imaged using a camera whilst being backlit by a light box

For the contact angle work discussed in this thesis a new method was proposed for creating powder bed samples with ease and consistency. Previous attempts included using double sided 'sticky' tape to create a monolayer of particles. The tape was stuck to a glass slide and pressed into a bed of powder to create a powder layer on the tape. However, some issues arose with this method. Surface coverage was unreliable and there were concerns regarding any adhesive still being present at the interface that could have led to inaccurate results. Additionally, the images from the camera were obscured by loose particles and a clear interface line could not be drawn using the software.

A second method involved tablet pressing of the primary material to create a solid structure to place a droplet on. Again, with this method there were some issues that prevented accuracy and reliability in the data. The tablets formed were not very stable and often crumbled once removed from the punch die. Where tablets were managed to be made, the surface was often very smooth with a shiny surface suggesting that the pressure of the press had created some surface modification that could skew the result. For example, the compression may generate a sample with preferred orientation of the particles. It is known that the basal plane of a highly oriented pyrolytic graphite (HOPG) sample has a higher hydrophobicity compared to the edge plane [105], therefore a method which ensures random orientation of the particles is preferred.

Finally, a method for sample preparation taking inspiration from XRD sample preparation was designed. This involved the use of a backfill sample preparation kit (Malvern Panalytical), for which the process can be seen in Figure 4.2 - Figure 4.4.

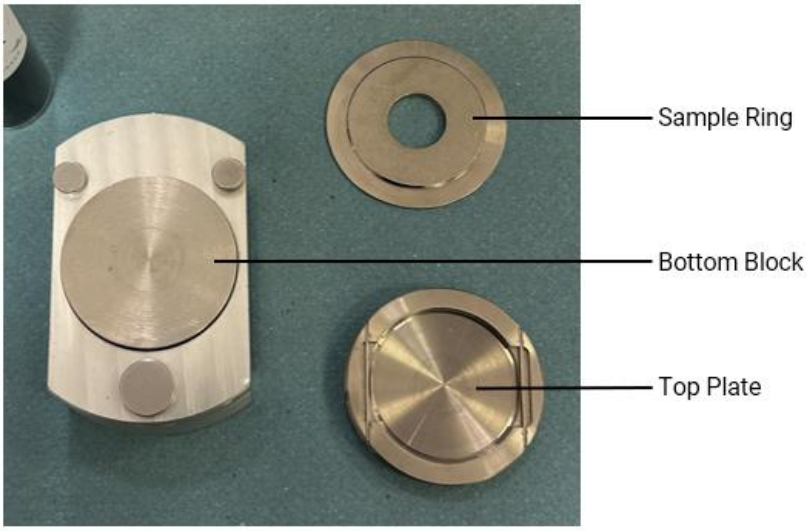

Figure 4.2: XRD sample preparation kit used for generating particle beds for contact angle (components labelled)

First the sample ring was locked into the bottom block using the spring button on the side. Once locked in place the primary powder was deposited into the hole of the sample ring to create a mound.

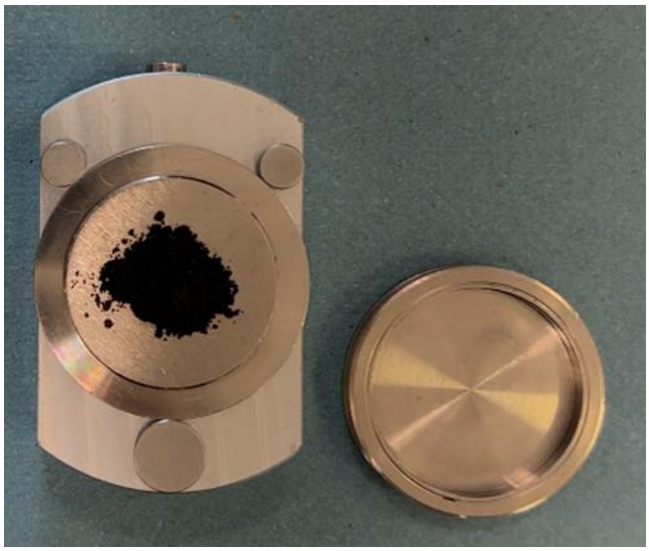

Figure 4.3: Particles placed into sample slot before being levelled with a sharp blade and edges cleaned

Either a sharp blade or microscope slide was used to gently press and swipe across the sample mound. This pressed the powder bed down slightly whilst helping to level the surface. A brush was then used to clean the sample ring and remove any excess powder. Once cleaned the top plate was placed on the top clicking in place.

The whole sample preparation kit was then inverted so that the top plate was now at the bottom of the stack. Then, with the top plate on the benchtop, the bottom block was removed using the spring button to release the sample ring and top plate. What remained was a consistent powder bed surface that was

used for sessile drop contact angle measurements with a randomly oriented powder bed preventing preferential orientation of the particles.

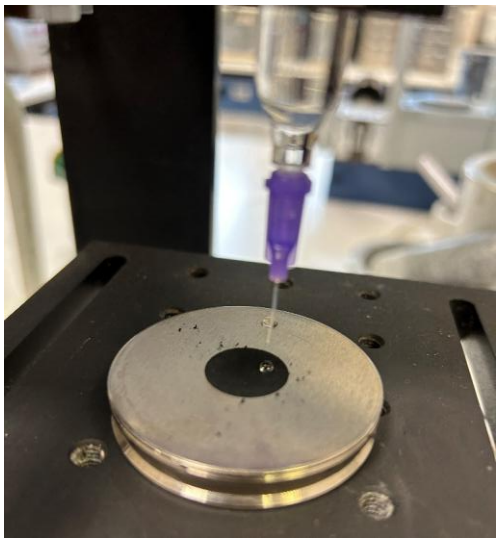

Figure 4.4: Particle bed formed after inverting the XRD preparation kit forming a consistent bed of particles without preferential orientation

The prepared sample was then placed on the goniometer staging and lined up with the camera and needle from the syringe as can be seen in Figure 4.1. First Ten Angstroms (FTA) 3.2 software for contact angle image analysis was used to capture the data for further processing. Once loaded, the software was run in video mode that captures 60 frames per second, and the syringe needle was placed approximately 2 mm from the sample surface and a droplet was deposited on the surface. The droplet was dispensed close to the surface to reduce the inertial effects that dropping from height would have on the droplet profile. The ease of placing a droplet was significantly harder for non-wetting surfaces, as the droplet had a stronger adhesion to the needle surface than the sample. Once the droplet was on the surface, time was allowed to pass to capture any time dependent effects of the solid-liquid interface. Wetting fluids tended to reduce in contact angle over time whereas non-wetting fluids tended to remain in steady state and maintain their droplet profile and thus contact angle value. The initial image frame when the droplet rested on the surface was used for the contact angle measurement, and as such is limited by the frames per second of the camera. This wasn't considered to be an issue and comparative contact angle measurements were able to be captured.

Once the droplet had reached equilibrium the video was stopped, and the sample was able to be processed in the software. Using the frame-by-frame selection, the images were cycled until the initial droplet was chosen. Then, using the software, a baseline was drawn between the two furthest points on the interfacial line. From this, an arc was drawn over the droplet to provide the software with an estimation of the droplet profile. Then, the contact angle processing was run. The FTA 3.2 software was generally good at outlining the droplet profile and where there were errors in the accuracy, the lines

were redrawn and contact angle processing was run again. The initial contact angle was the key result to take from the process as this indicates how the solid-liquid interface interacts before any droplet immersion or spreading effects take place in the powder bed. It was important to take repeat measurements as contact may vary across the powder bed due to local minimum in surface energies. Surface roughness and particle orientation may affect the local contact angle, therefore, it was important to try and capture the global minimum using an average of the three contact angle repeats [106]. Contact angle hysteresis is where droplet volume is increased to describe the advancing and receding contact angle. This would allow a global minimum to be identified rather than a metastable state. Unfortunately, for highly wetting solvents in contact with porous particle beds, immersion effects can dominate compared to spreading and make contact angle hysteresis difficult to examine.

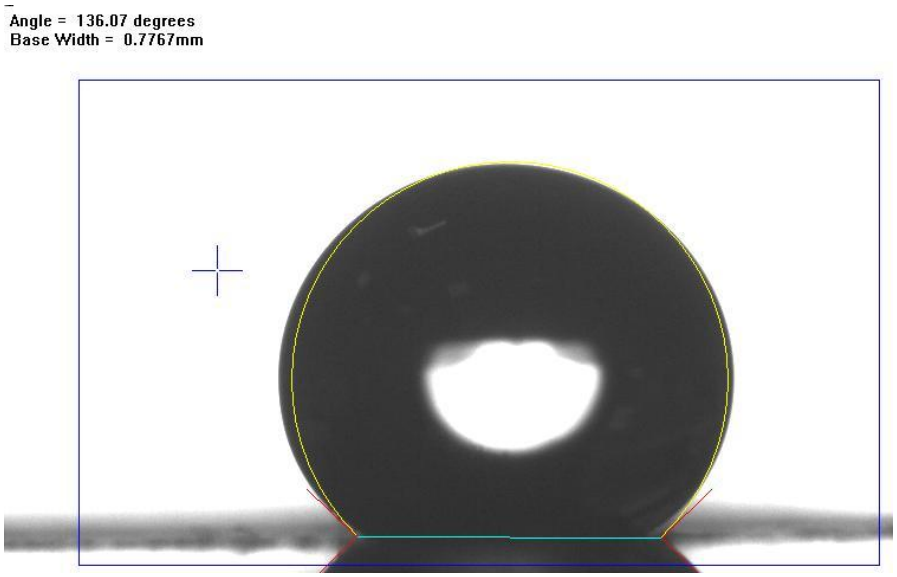

Figure 4.5: Error from large droplets subject to gravitational effects whilst measuring contact angle using FTA 3.2 software which fits for a circle

For solvents with high hydrophobicity detachment from the syringe needle onto the powder surface was difficult. Therefore, larger droplet volumes were required to enable droplet detachment. However, for larger volume droplets of hydrophobic solvents gravity affected the shape of the droplet. Instead of being circular, large volume droplets showed an ellipse shape, seen in Figure 4.5. ImageJ Fiji was used therefore to measure a reliable value using the Contact Angle plugin[2]. Two points were manually chosen for the baseline where the droplet contacted the powder surface, and an additional 3 points were manually placed around the droplet surface. This plugin was able to account for this error and fit an arc to the ellipse rather than a circle. This can be seen in Figure 4.6 and this method was used to measure the initial contact angle rather than the FTA 3.2 software.

[2] Contact Angle plugin (imageJ), developed by Marco Brugnara (University of Trento, Italy), https://imagej.net/ij/plugins/contact-angle.html (2006)

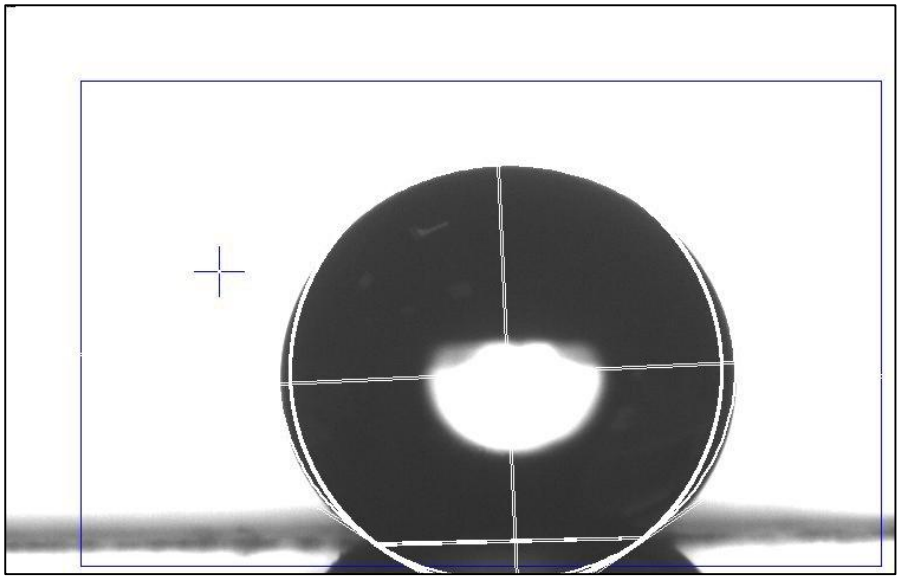

Figure 4.6: Contact angle fitting using an ellipse (outer lines) and circle (inner lines) to measure contact angle

4.2.1.2 Coagglomerate Generation & Characterisation

Spherical agglomerates were processed following the methodology discussed in Section 3.3 which, to summarise, involved adding solids to be agglomerated to a stirred tank with the continuous phase (and surfactant if required) to be dispersed and then injecting bridging liquid and left to agglomerate over time. In these experiments, the agglomeration time was 15 minutes with no surfactants present. The TBSR was optimised through generation of agglomerates across a range of bridging liquid volumes, and optimising based on maximising yield and generating agglomerates which fall in the 'excellent flow' properties according to Hausner ratio. This involved working from a chosen TBSR and interpolating to find the optimum, based on these design characteristics.

As discussed in Section 3.4 coagglomerates were characterised based on size distribution, Hausner ratio (flowability) and, in certain cases, porosity. Additionally, yield was used to compare effectiveness of agglomeration based on maximising product formed.

Yield was calculated by measuring the mass of obtained coagglomerates (m_{agg}) on a 35 µm sieve after being dried and comparing that to the total mass of active material (m_{AM}) and carbon additive (m_{CA}) input as feedstock. This was a simple calculation given by Equation 4.1:

$$yield = \frac{m_{agg}}{m_{AM} + m_{CA}} \times 100\% \tag{4.1}$$

4.2.2 LFP Coagglomeration & Parametric Study

LFP is becoming a more popular material in cathode research and therefore coagglomeration of LFP was carried out to assess feasibility of the process due to the upcoming demand for this material.

4.2.2.1 Contact angle & Solvent Characteristics

LFP has different surface energy characteristics, compared to graphite, and a contact angle wettability assessment was carried out to identify an appropriate continuous phase and bridging liquid setup. The method for this was the same as for graphite contact angle assessment and is detailed in Section 4.2.1.1. Once the contact angle assessment was carried out the optimum solvent setup was used for the coagglomerate generation process.

4.2.2.2 Coagglomerate generation

The stirred tank dimensions and setup used for coagglomeration of LFP with carbon black (C65), were identical to that used for graphite coagglomeration as discussed in Section 3.3 However, an alternative method of coagglomerate generation was employed, due to wettability characteristics of the LFP primary particles and the inability to form spherical agglomerates using the conventional method, used for graphite. Therefore, the modified dispersed phase method[3] was used to achieve spherical agglomerates. This method involved dispersing the 1.8 g of the LFP in the bridging liquid thus creating this "Modified Dispersed Phase" (MDP), with ethyl cellulose also dissolved at 0.6 wt% in chloroform for improved strength of the agglomerates once dried. C65 carbon additive (0.2 g) was dispersed in 20 g DI water in a vial and hand shaken for 3 minutes before being sonicated in a sonication bath. The vial of DI water and carbon additive was then added to a tall beaker with 100 g of DI water and then sonicated using a sonication probe for 2 minutes with interval pulses every other 5 seconds at 80 % amplitude (Fisherbrand™ 505 Sonicator with Probe). Once the C65 and DI water had been sonicated to help break up any aggregates/agglomerates, it was added to the stirred tank beaker and allowed to stir at 1000 RPM with an impeller clearance of 20 mm. The MDP was injected to the stirred tank and allowed to coagglomerate for 10 minutes. Over the agglomeration time growth and coalescence occurred just as in the standard spherical agglomeration systems. However, in this case, the growth occurred due to the carbon additive layering and/or immersion into the droplets. The active material dispersed in the MDP was already locked in the matrix wetted by the immiscible bridging liquid, and therefore was assumed not to play a key role in the growth stages.

Once agglomeration was complete, the collection stage was the same as described in Section 3.3 A mesh sieve (32 μm), on top of a Buchner filter, was used to retain the spherical agglomerates with the waste material passing through the sieve and being retained on the filter paper.

[3] Method developed by Dr Kunal Pardikar (University of Sheffield).

4.2.2.3 Parametric Study

Various process parameters were investigated for their effect on the coagglomerate properties such as size and porosity. Impeller speed, agglomeration time, solids loading and TBSR were investigated as part of this study.

The coagglomerates were then characterised for size, porosity and tapped density. The coagglomerate size distribution used the same image analysis method as that discussed in Section 3.4.1 However, a Canon EOS 2000D (24MP) camera was used to image the samples where the coagglomerates were spread across a similar grid system. Backlighting was used to ensure good contrast of the coagglomerates when imaging.

Porosity (φ) of the coagglomerates was determined using Mercury Intrusion Porosimetry (MIP) to find the envelope density[4]. An Accupyc was used to measure the true density (discussed in Section 3.2.2.1). These values can then be used in Equation 4.2 to calculate the porosity.

$$\varphi = 1 - \frac{\rho_{envelope}}{\rho_{true}} \times 100\% \tag{4.2}$$

4.3 Results and Discussion

4.3.1 Graphite Coagglomeration

The aim of this section of the chapter is to identify a system setup that reliably produces graphite – carbon black coagglomerates and then explore how different morphologies of graphite affect the coagglomerate properties – size distribution, porosity and flow characteristics.

4.3.1.1 Contact Angle and Solvent Characteristics

Powder beds were created using the XRD sample preparation method discussed in Section 4.2.1.1 and potential bridging liquids and continuous phases of water, chloroform, toluene and heptane were measured for wettability characteristics against the three types of graphite; KS4, KS6 and S3. The initial frame of the droplet when adhered to the surface was used as the reference image for measuring contact angle, as over time immersion due to capillary effect and droplet spreading will occur, and the contact angle will reduce for highly wetting solvents.

Three measurements were taken and averaged for contact angle, shown in Table 4.1, with standard deviation. Solubility and boiling point data is given in Table 4.2 as this was also important in solvent selection.

[4] Mercury intrusion porosimetry measurements carried out by Dr Kunal Pardikar (University of Sheffield).

Table 4.1: Summary of solvent wettability, based on contact angle with the respective graphite samples. Values based on three repeats with a standard deviation error given

	Contact Angle (°)		
	KS4 Graphite	KS6 Graphite	S3 Graphite
Water	131.6 ± 2.8	116.7 ± 10.0	145.5 ± 0.7
Chloroform	88.0 ± 2.9	65.2 ± 4.5	71.6 ± 7.9
Toluene	57.5 ± 25.3	56.4 ± 7.0	27.1 ± 4.5
Heptane	104.6 ± 6.1	72.7 ± 3.0	74.4 ± 6.7

Table 4.2: Solvent solubility in water and boiling point at 20 - 25 °C and 1.01 bar atmospheric pressure (properties taken from the supplier specification from Sigma – Aldrich)

	Solubility in water (g/L)	Boiling point (°C)	Vapour Pressure (hPa)
Water	-	100	20
Chloroform	8.7	60.5 - 61.5	210
Toluene	0.58	110 - 111	30.88
Heptane	Insoluble	98	48

The three graphite varieties show preferential wettability properties with the chloroform, toluene and heptane solvents when compared to water. The solubility of the solvents in water is low and therefore suit the desired characteristics of a bridging liquid. The boiling points of the solvents vary with chloroform showing the lowest value of approximately 61 °C whereas toluene and heptane have higher boiling points. The vapour pressure is a useful metric for quantifying ability of a solvent to evaporate important for the post coagglomeration drying stage, where it is beneficial for the bridging liquids to evaporate and leave the dry coagglomerates. Chloroform shows a much higher vapour pressure suggesting a much higher tendency to evaporate during drying than toluene and heptane.

Due to water having such a high contact angle with the graphite samples, it was chosen as the continuous phase. The chloroform was chosen as a bridging liquid for the three graphite types. Chloroform shows 'good' wettability characteristics. Additionally, the low solubility in water, low boiling point and high vapour pressure, will benefit the agglomeration and drying stage. Chloroform also has good solvation of the polymeric binder – ethyl cellulose, which was used to enhance strength of the coagglomerate once dried. The chloroform bridging liquid will not dissolve the solids used and therefore the crystalline bridges commonly seen in spherical agglomeration literature will not occur. Therefore, it is important to use a polymer binder to strengthen the coagglomerates formed.

4.3.1.2 Coagglomerate Generation

Coagglomeration experiments were carried out using the standard parameters given in Table 3.9, where the only variable was the TBSR value. Since chloroform is slightly soluble in the continuous phase water, excess was added to account for this. For a 198 ml continuous phase at 8.7 g/L chloroform solubility, the system required an additional 1.09 ml of bridging liquid so that the TBSR was accurate.

Coagglomeration experiments were firstly carried out with KS6 graphite. Initial probing experiments run at 900 RPM exhibited poor agglomeration with a paste formed at the base of the beaker and deposition on the beaker walls.

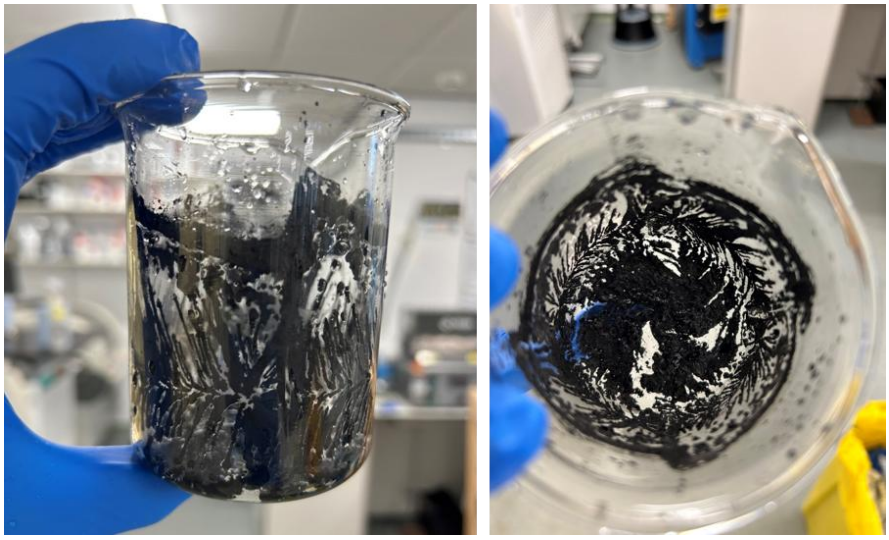

Figure 4.7: Coagglomeration solids and bridging liquid deposited on the beaker walls due to insufficient suspension speed (N_{JS})

This is different to the type of paste seen when the TBSR is too high and was, considered to be, a dispersion issue with the process parameters used. The just suspended speed (N_{JS}) was calculated for the coagglomeration system as an estimate for required impeller speed to disperse the components in the stirred tank [107]. Equation 4.3 describes this empirical relationship:

$$N_{JS} = S\, v^{0.1} \left[\frac{g(\rho_s - \rho_l)}{\rho_l}\right]^{0.45} X^{0.13} d_p^{0.2} D^{-0.85} \qquad (4.3)$$

Where:

- S Zwietering Correlation
- v Kinematic Viscosity (m^2/s)
- g Gravitational Acceleration (m/s^2)
- ρ_s Solid Density (kg/m^3)
- ρ_l Liquid Density (continuous phase) (kg/m^3)
- X Solid Loading

d_p Particle Diameter (m) (d_{50} based average particle diameter)

D Impeller Diameter (m)

The Zwietering correlation is based on the stirred tank and impeller dimensions based on stirred tank experiments for a 6 blade Rushton Turbine impeller [107]. The value for this was estimated using Equation 4.4:

$$S = 8.54\left(\frac{C}{T}\right)^{0.218}\left(\frac{H}{T}\right)^{-0.248} \quad (4.4)$$

Where:

S Zwietering Correlation

C Impeller Clearance (m)

T Vessel Diameter (m)

H Liquid Height (m)

Therefore, for a stirred tank as described in Section 3.3 (as used in all the experimental setups), the just suspended speeds for the impeller were calculated for the active material and chloroform droplets. The d_{50} values for primary particles and Accupyc true density data shown in Section 3.1.2.1 were used in the primary particle calculations. For the chloroform droplets, assuming they act as a solid particle, the droplet size distribution method as discussed later in Section 6.2.2.2 was used for the d_{50} of the chloroform.

Table 4.3: Calculated just suspended impeller speeds required for suspension of primary particles and bridging liquid droplets

Material	Just Suspended Impeller Speed (RPM)
KS6 Graphite	1227
KS4 Graphite	1157
S3 Graphite	1556
Chloroform Droplets (avg. d_{50} = 50 µm)	1388

This represents an estimate for well suspended systems based on particle and fluid properties. The experiments were therefore carried out using 1250 RPM to prevent any settling and deposition of the material and generate 'just' dispersed mixing, whilst making RPM constant between experiments.

Upon using these values, agglomeration was more reliable and coagglomerates were formed consistently.

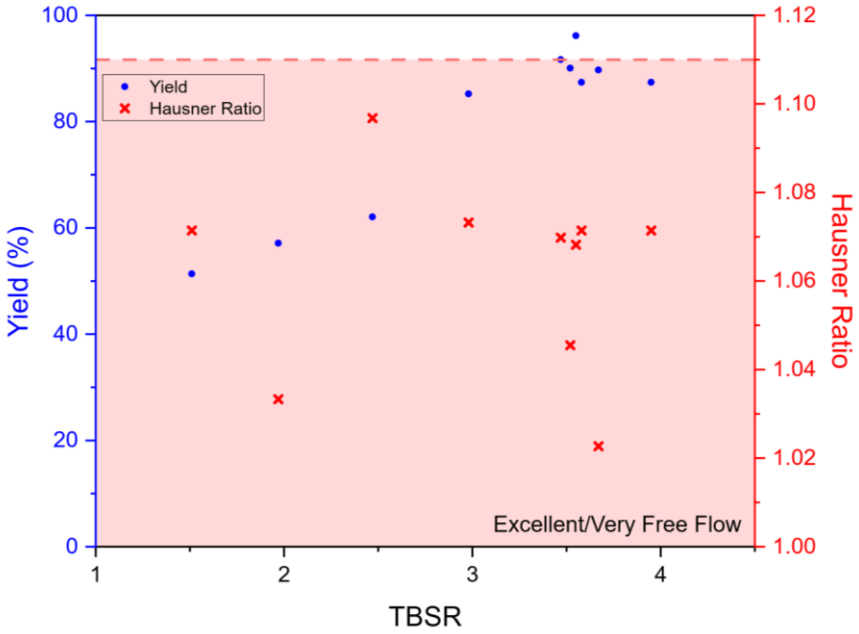

Figure 4.8: KS6 graphite coagglomerate properties used to identify optimum TBSR (red highlighted region indicates 'Excellent flow' according to the Hausner ratio)

Figure 4.8 shows the measured design characteristics of coagglomerates formed at varying TBSR values. This was used to identify the optimal TBSR value ($TBSR_{opt}$) based on maximising yield and optimising Hausner ratio for 'excellent' flowability. A highlighted red zone for the Hausner ratio's 'excellent' flow region (<1.11) is marked on the graph.

All the experiments carried out show 'excellent' flowability according to the measured Hausner ratio. However, at TBSR of 3.55 the yield can be seen as maximised compared to the other experiments at 96.15 % recovery (based on mass), therefore the $TBSR_{opt}$ is approximately 3.55. The agglomerate size and porosity data were calculated for coagglomerates formed at $TBSR_{opt}$; this is discussed further in Section 3.4.1

When TBSR < $TBSR_{opt}$ it can be seen in Figure 4.8 that the yield is low compared to the $TBSR_{opt}$ this is due to the volume of bridging liquid available for coagglomeration is too low and some primary material is not captured during the process, as can be seen in Figure 4.9 (A). This primary material passed through the sieve and therefore was not considered as part of the yield. Additionally, when TBSR > $TBSR_{opt}$, there was too much bridging liquid present in the system. This resulted in coalescence and/or paste formation during the coagglomeration. This paste would then deposit on the baffles or impeller, thus reducing the yield. Figure 4.9 (E – F), shows this effect with larger particles and non-spherical shaped artefacts present in the images. The effects of TBSR outside the $TBSR_{opt}$ range is well documented in literature [12,75,108] for different materials such as those used in pharmaceuticals, and

the findings of this study agree with the proposed theories but for a novel process using battery particulate materials.

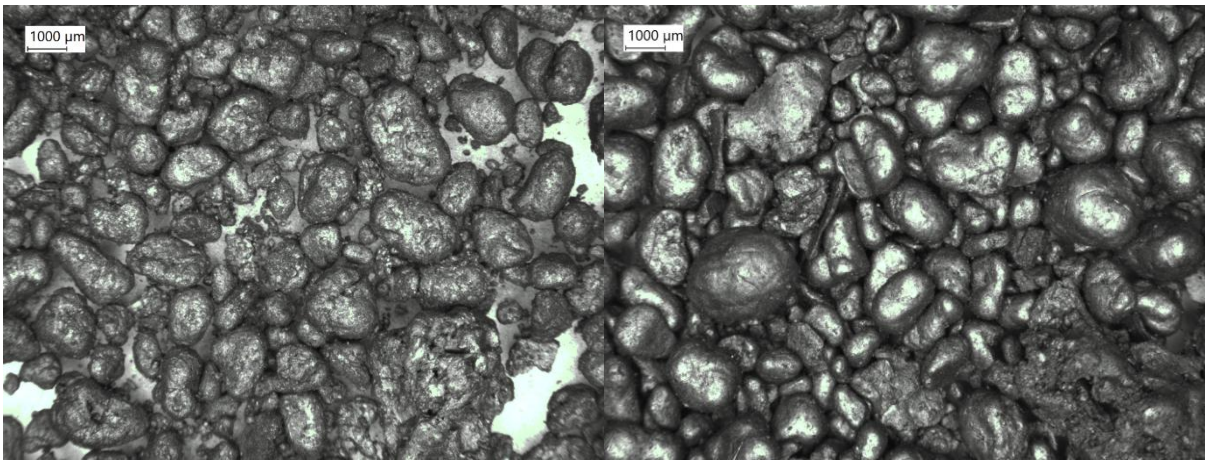

A) TBSR = 1.51 B) TBSR = 2.98

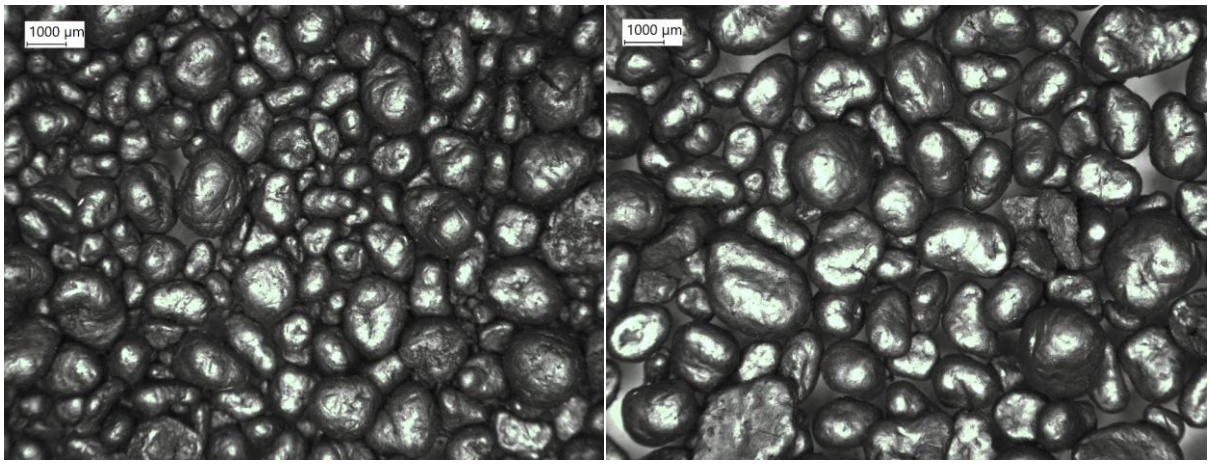

C) TBSR = 3.52 D) **$TBSR_{opt}$ = 3.55**

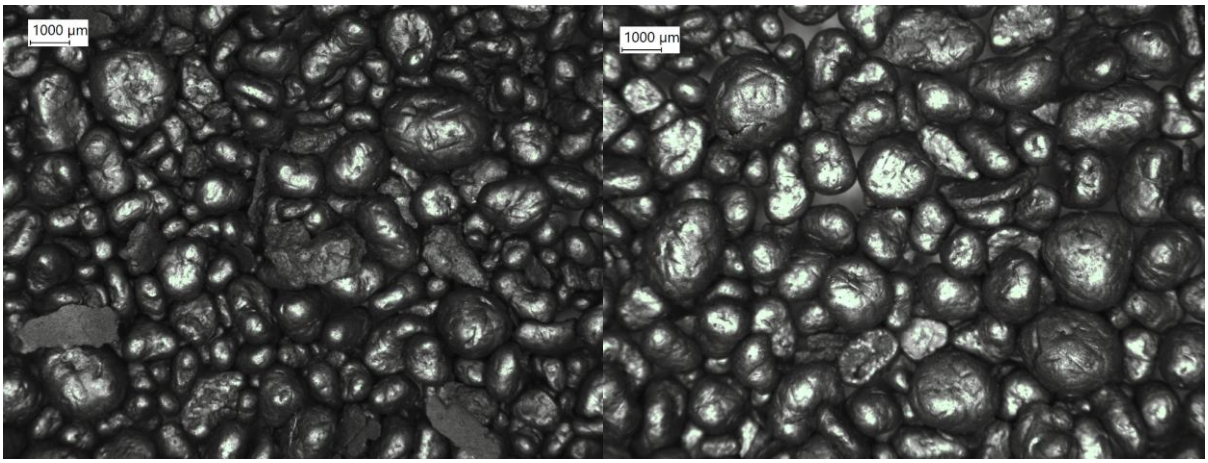

E) TBSR = 3.67 F) TBSR = 3.95

Figure 4.9: Images of generated KS6 coagglomerates at varying TBSR values shown below each image as TBSR is optimised

The same process was carried out for KS4 and S3 graphite using an interpolation approach to optimising TBSR based on yield and Hausner ratio. The results of the KS6 coagglomerate experiments were used

as a starting point for this process. It was found that using this starting point less experiments were required to find $TBSR_{opt}$.

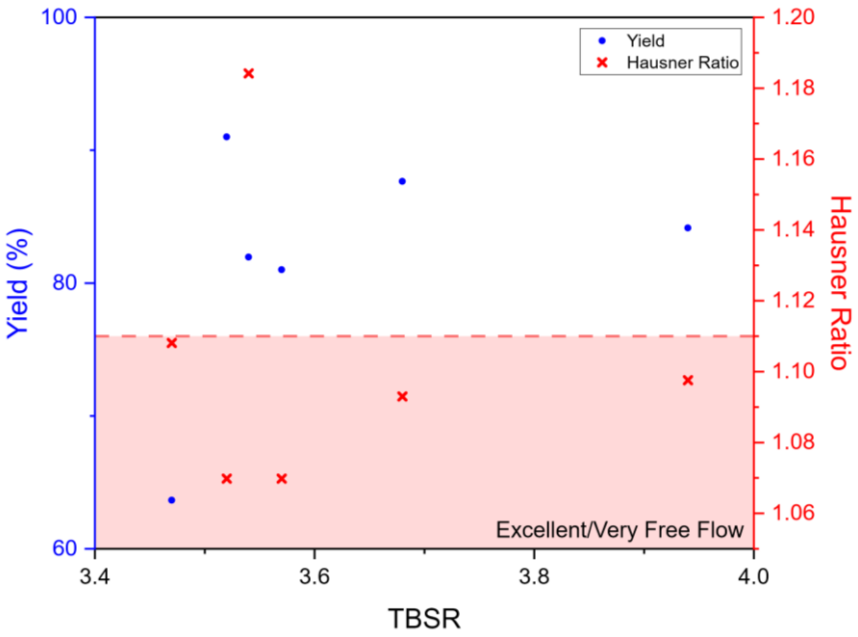

Figure 4.10: KS4 graphite coagglomerate properties used to identify optimum TBSR (red highlighted region indicates 'Excellent flow' according to the Hausner ratio)

Figure 4.10 shows that the yield was highest at 91.00 % for the experiment carried out at a TBSR of 3.52 and these coagglomerates also exhibited 'Excellent' flowability with respect to the Hausner ratio. This was defined as the $TBSR_{opt}$ for KS4.

Images taken using the optical microscope, seen in Figure 4.11, show that when the TBSR > $TBSR_{opt}$ more irregular coagglomerates are formed and non-spherical artefacts seen in Figure 4.11 (D – F). This is due to excess bridging liquid being present allowing coalescence to occur. Additionally, any paste-like deposits from the beaker wall/baffles and impeller detach and are captured in the product. These irregular structures lead to more cohesion between agglomerates and a slight increase in the Hausner ratio.

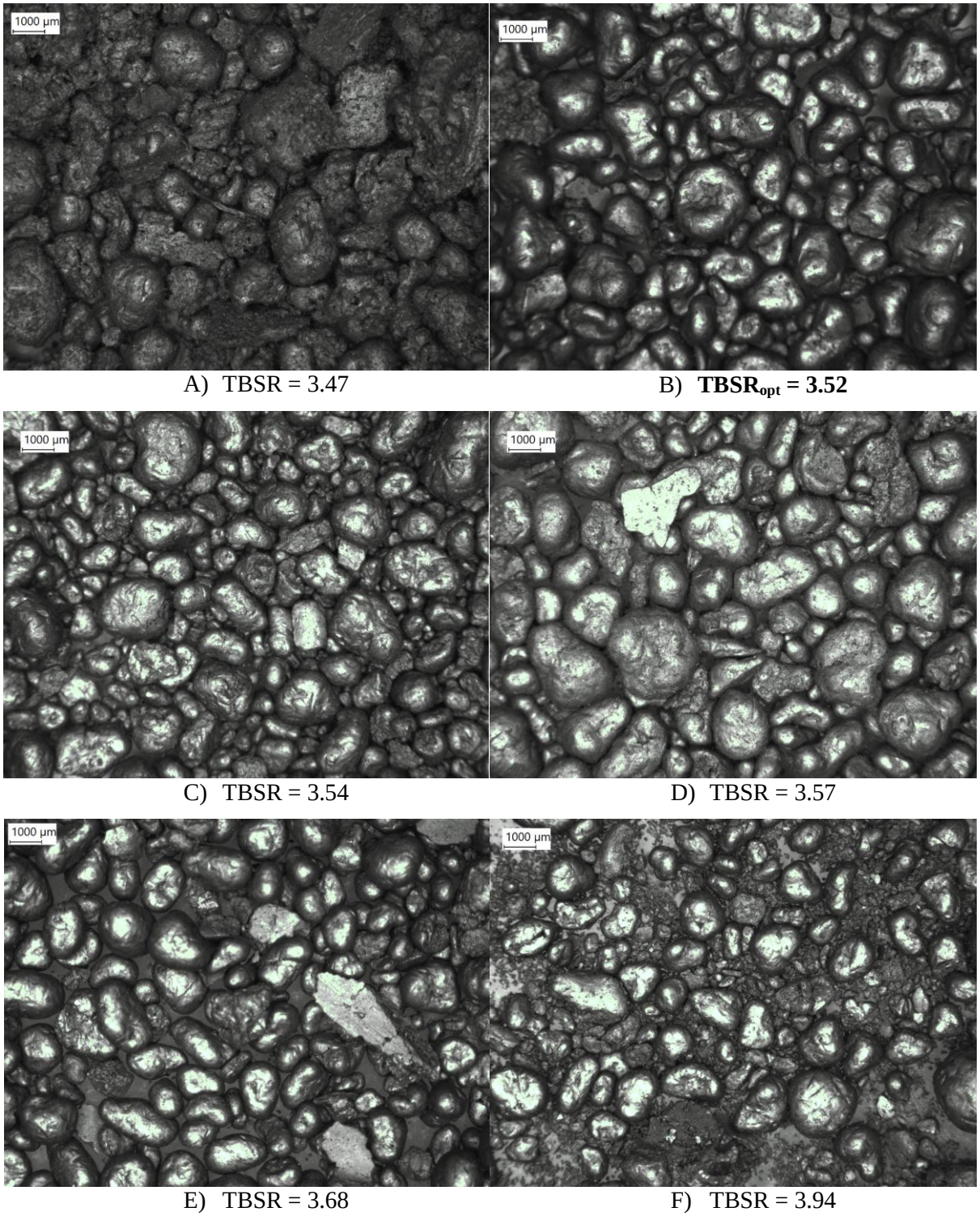

A) TBSR = 3.47 B) **$TBSR_{opt}$ = 3.52**

C) TBSR = 3.54 D) TBSR = 3.57

E) TBSR = 3.68 F) TBSR = 3.94

Figure 4.11: Images of generated KS4 coagglomerates at varying TBSR values shown below each image as TBSR is optimised

When TBSR < $TBSR_{opt}$, seen in Figure 4.11 (A), there is a higher amount of primary material. The coagglomerates appear less reflective due to loose primary particles being adhered to the surface. For these low TBSR systems of 3.47, the yield is significantly lower as primary material is filtered out using the mesh sieve. Additionally, the Hausner ratio is higher due to the increased particle-particle cohesivity of the coagglomerates formed with loose primary material adhered to the coagglomerate surface.

The experiments carried out for evaluating $TBSR_{opt}$ for S3 graphite proved more difficult. There was a high level of deposition on the beaker walls, baffles and impeller leading to poor coagglomeration. Therefore, some of the experiments were discounted as they formed pastes and/or deposition in the stirred vessel.

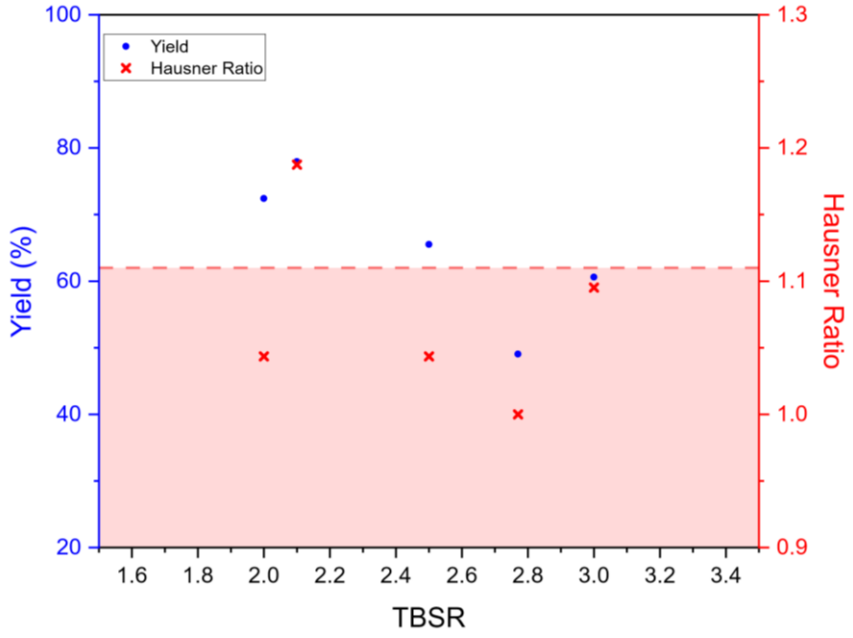

Figure 4.12: S3 graphite coagglomerate properties used to identify optimum TBSR (red region indicates 'Excellent flow' according to the Hausner ratio)

Coagglomeration of S3 was carried out at the same conditions as KS6 and KS4 so that analysis of the coagglomerates formed and $TBSR_{opt}$ was dependent on the primary particles with no effect from other stirred tank variables. As can be seen from Table 4.3 though, it was found that the just suspended impeller speed was 1556 RPM, which explains the issues associated with poor distribution and deposition in the stirred vessel.

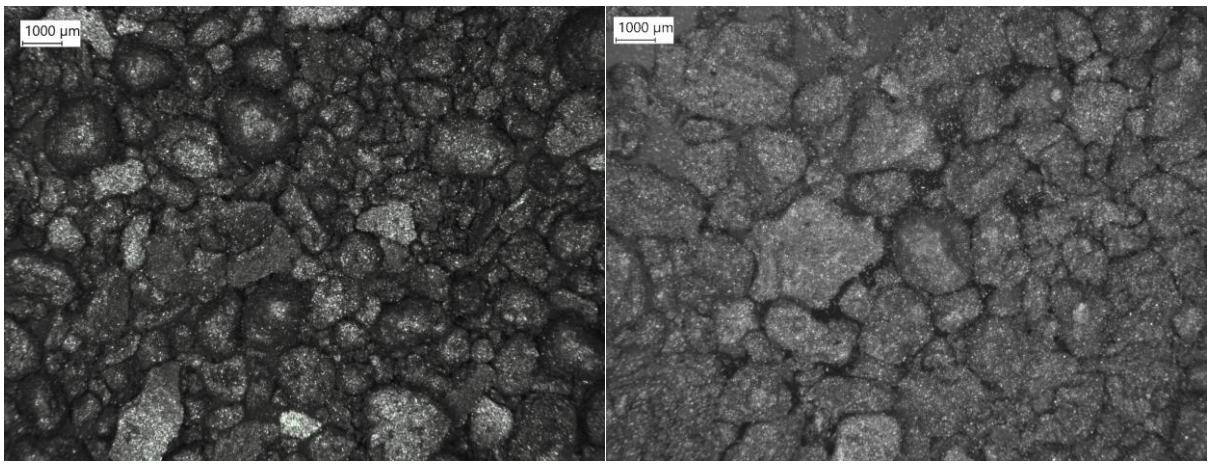

A) TBSR = 2.00 B) TBSR = 2.10

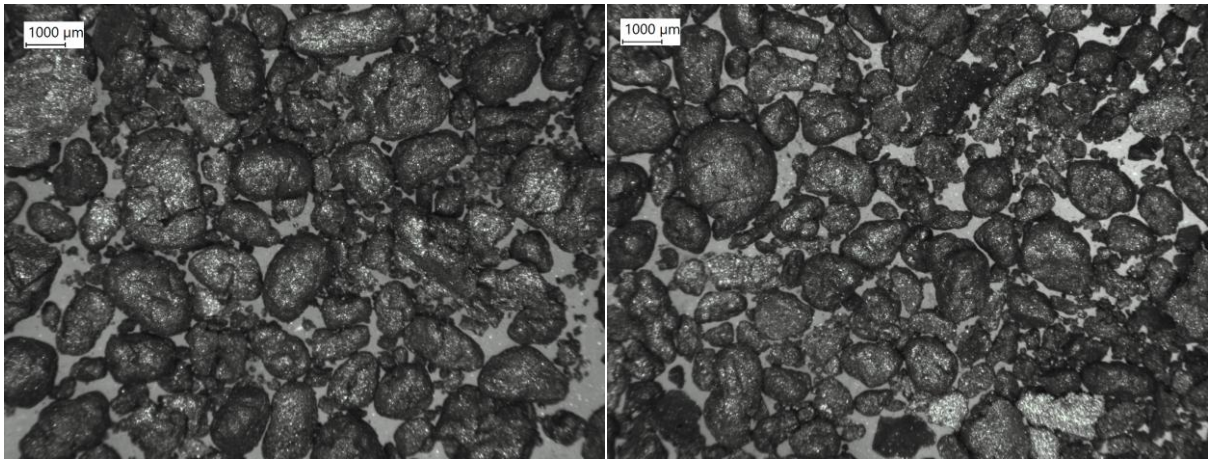

C) TBSR = 2.50 D) TBSR = 2.77

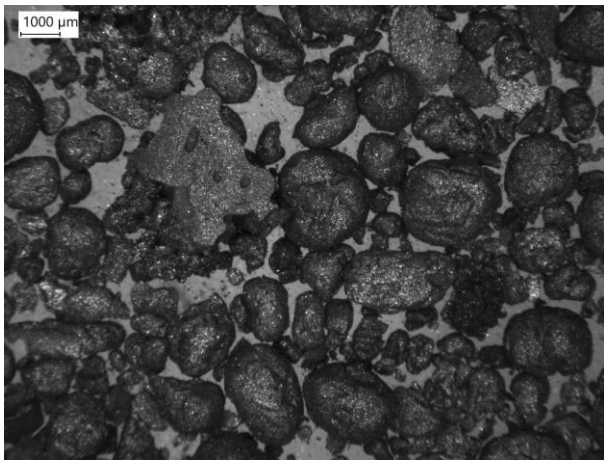

E) TBSR = 3.00

Figure 4.13: Images of generated S3 coagglomerates at varying TBSR values shown below each image as TBSR is optimised

Using the design characteristics of yield and Hausner ratio to identify a coagglomeration at the optimum TBSR would suggest that a TBSR of 2 – 2.1 shows the best characteristics with a yield of 72.40 % - 77.95 %. However, the Hausner ratio for TBSR of 2.1 is the highest of the sample. Although the flowability is still good, it is lower than the other coagglomerates. Qualitatively analysing the microscope images of the coagglomerates generated shows primary material present in all the samples, seen in Figure 4.13. There is a wide range of agglomerate sizes and irregular non-spherical coagglomerated material present in all the images. For all these reasons it is difficult to suggest which sample is seen as being generated at the $TBSR_{opt}$ and further experiments would be needed for this evaluation to be considered reliable.

A summary of the coagglomerate $TBSR_{opt}$ can be seen in Table 4.4, with values determined for KS6 and KS4 graphite. Further experiments are required for a reliable assessment of the S3 $TBSR_{opt}$.

Table 4.4: Summary of the $TBSR_{opt}$ for the graphite materials analysed

Graphite Material	$TBSR_{opt}$
KS6	3.55
KS4	3.52
S3	(undetermined)

4.3.1.3 Coagglomerate Size Distribution

In the previous section, the $TBSR_{opt}$ was discussed as a single value, however, the optimal TBSR will be within a narrow range of suitable values. Therefore, it can be considered that the coagglomerates generated for KS6 and KS4 graphite had similar $TBSR_{opt}$ ranges of approximately 3.5 – 3.6. Primary particles of KS6 and KS4 graphite have similar shapes but different average size (d_{50}). Therefore, the effect that primary particle size had on the coagglomerates generated was assessed. S3 graphite was not studied in this section due to uncertainty in the $TBSR_{opt}$ value discussed in the previous section.

KS6 coagglomerates formed at the TBSR of 3.52 were sized using an optical microscope and analysed using Fiji (ImageJ). Details of this method are discussed in Section 3.4.1

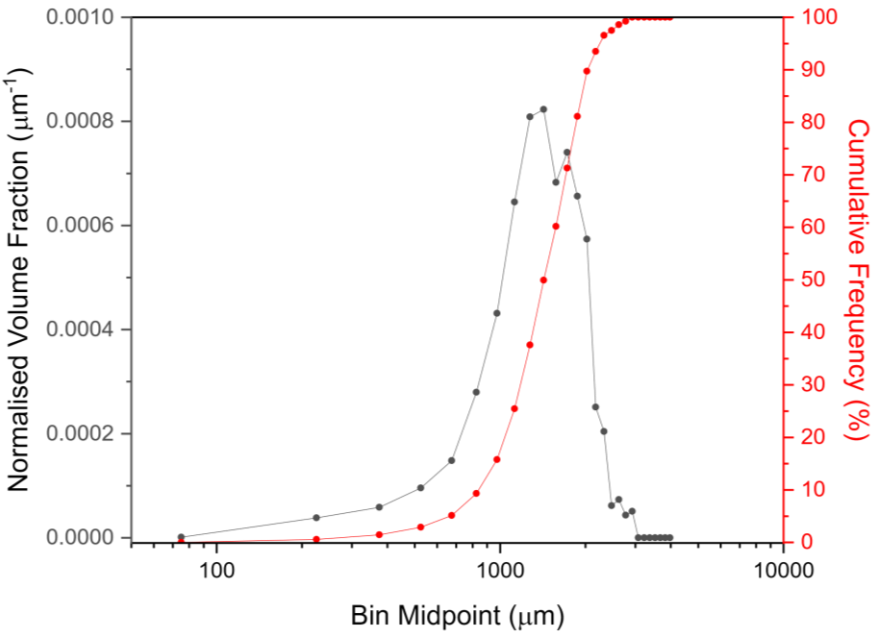

Figure 4.14: Volume based coagglomerate size distribution and cumulative size distribution plotted against midpoint diameters of size bins for KS6 at TBSR = 3.52

The d_{10}, d_{50} and d_{90} were calculated from the cumulative size distribution curve for KS6 and KS4 seen in Figure 4.14 and Figure 4.15, respectively. The values for these can be seen in Table 4.5 along with the calculated span which describes how narrow or wide the coagglomerate size distribution is, and thus a measure of coagglomerate size dispersity.

Table 4.5: Summary of coagglomerate size data and calculated span for KS6 and KS4 coagglomerates generated at TBSR = 3.52

Material	d_{10} (µm)	d_{50} (µm)	d_{90} (µm)	Span
KS6	841	1425	2025	0.831
KS4	825	1659	2625	1.085

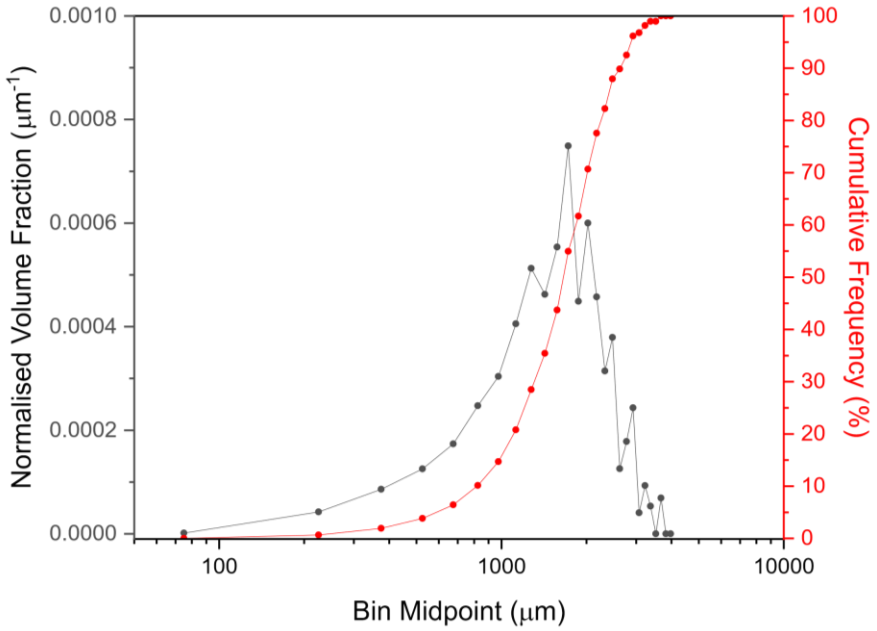

Figure 4.15: Volume based coagglomerate size distribution and continuous size distribution plotted against midpoint diameters of size bins for KS4 at TBSR = 3.52

It can be seen from Figure 4.14 and Figure 4.15 that a relatively narrow size distribution was measured for the KS6 and KS4 coagglomerates with a slight skew such that the distribution around the peak is higher near the smaller coagglomerate sizes rather than the larger ones. This is due to breakages adding to the volume fraction of the smaller sized coagglomerates. Comparing the two size distributions shows that the coagglomerates formed for KS6 and KS4 at TBSR = 3.52 are very similar in size characteristics, with KS6 showing an approximately 16 % smaller d_{50} and 30 % narrower span when compared to KS4. This can be seen more clearly in Figure 4.16. Importantly the coagglomerates formed are on average approximately 1000 µm in diameter, which is too large to be incorporated into an electrode for lithium ion diffusion pathways to be effective [109,110]. This is a big limiting factor for application into electrode manufacturing and further investigation was carried out as part of the next chapter, to understand how coagglomerate average diameter can be reduced to < 100 µm.

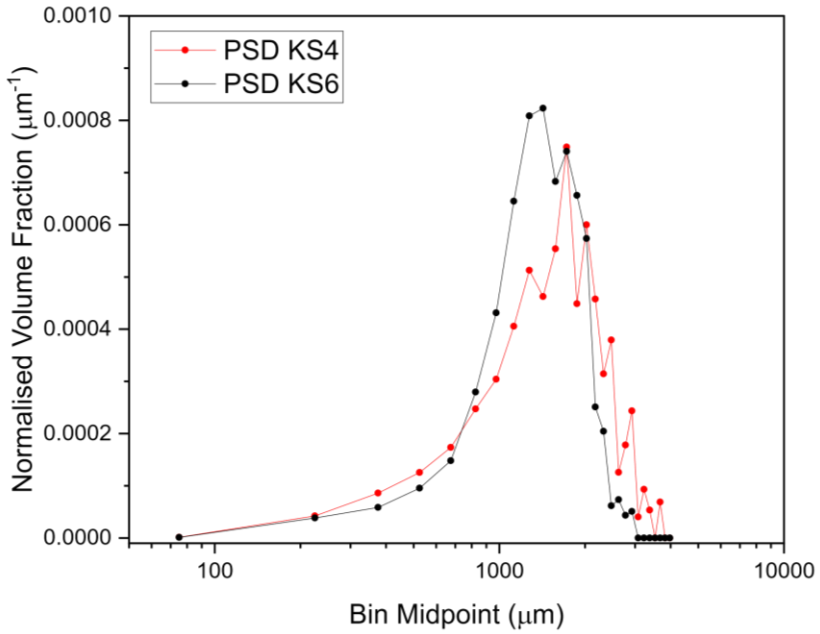

Figure 4.16: Comparison of the volume based coagglomerate size distributions for KS6 and KS4

The mass of agglomerates was measured during the imaging process. Therefore, the porosity was calculated using the mass (m_{agg}) and cumulative volume (V_{agg}) of coagglomerates calculated during the size distribution analysis. Equation 4.5 was used to calculate the porosity, and a summary of these values can be seen in Table 4.6.

$$porosity = \frac{V_{agg} - \left({}^{m_{agg}}/_{\rho_{true}}\right)}{V_{agg}} \tag{4.5}$$

Table 4.6: Summary of porosity data calculated from the cumulative volume and mass of sample found during size distribution analysis

Material	V_{agg} (cm^3)	m_{agg} (g)	ρ_{true} (g/cm^3)	**Porosity**
KS6	1.709	1.247	2.33	**0.687**
KS4	2.593	1.345	2.33	**0.777**

From Table 4.6, the data suggests that KS4 coagglomerates have a higher porosity compared to KS6 coagglomerates, generated at the same TBSR value. This would mean that the packing of primary material into the coagglomerate structure is less dense in the KS4 coagglomerates and there is more voidage between the particles when structured into its coagglomerate matrix. However, the process through which coagglomerate porosimetry was calculated has some unavoidable error.

During imaging coagglomerates not entirely inside the image frame were discounted during the PSD analysis. This was done because the full structure could not be analysed for size properties. This was

not an issue when measuring PSD as a large sample size gave a reliable representation of the coagglomerates produced. However, the total mass of coagglomerates discounted was difficult to quantify and as such will affect the porosity calculation, depending on how many coagglomerates were discounted during the process. The extent of the error is expected to be comparable between KS6 and KS4 coagglomerates but not quantified. Future work could incorporate mercury intrusion porosimetry (MIP) to alleviate this source of error.

Suggesting that there is difference between the two sample porosities cannot be done so confidently due to inherent error. However, if the trend seen holds true some conclusions can be drawn regarding the effect of particle size on coagglomerate properties. When this porosity data is analysed alongside the coagglomerate size distribution it is seen that larger KS6 primary particles are packing better within the coagglomerates. Additionally, the smaller KS4 primary particles are generating larger coagglomerates on average. If the KS4 is not packing as efficiently compared to KS6, then larger spacing between particles will generate a larger average coagglomerate volume. One reason for the higher porosity could be related to the differences in specific surface area of the primary material, where KS4 has the higher specific surface area of 2188 m^2/kg compared to KS6 specific surface area of 1699 m^2/kg. The increased surface area could be reducing the immersion rate of the primary particles within the droplet as they travel to the centre. This would then generate more porous coagglomerate structures. Additionally, Pitt. K, et al. (2018) [12] discussed some analyses on particle size effect, with the conclusion that smaller primary particle sizes require less bridging liquid thus generating larger agglomerates. This compares well to the results seen here and since the same volume of bridging liquid was used to compare KS6 and KS4 coagglomerates, then according to the literature, it would follow that a more porous coagglomerate would form with the smaller KS4 particles.

4.3.2 LFP Coagglomeration

The coagglomeration of LFP particles presented more challenges compared to the graphite materials. Contact angle wettability assessments were carried out for the LFP particles. Although the same water and chloroform system used for graphite coagglomeration showed a preferential difference in the contact angle for LFP, the system showed no signs of coagglomeration using the conventional addition method.

4.3.2.1 LFP Contact Angle & Wettability

The contact angle of LFP with DI water was lower than that compared to graphite, as can be seen in Table 4.7, however it still has a higher contact angle than the chloroform. This is because contact angle is not the only metric to consider for successful coagglomeration as the surface tension also plays a key role. A thermodynamic controlling parameter is introduced as work of particle transfer (ΔW), which defines whether particle transfer upon collision with a bridging liquid droplet will occur, moving from the continuous phase to the bridging liquid. This is discussed and developed in Section 7.2.1 however

the feasibility of a successful coagglomeration process is defined based on the balance of interfacial energies, given by Equation 4.6. For a coagglomeration system to be successful the work of particle transfer should be negative (i.e. $\Delta W < 0$).

$$\Delta W \propto \gamma_{BL,P} - \gamma_{CP,P} \tag{4.6}$$

$$\Delta W \propto [\gamma_{BL} + \gamma_P - W_{BL,P}] - [\gamma_{CP} + \gamma_P - W_{CP,P}] \tag{4.7}$$

$$\Delta W \propto \gamma_{BL} - \gamma_{CP} - W_{BL,P} + W_{CP,P} \tag{4.8}$$

The work exerted on the particle from each side of the interface ($W_{BL,P}$ and $W_{CP,P}$) can be expressed in terms of the contact angle and surface tension of the bridging liquid and continuous phase. This is described by the Young - Dupre equation, given by Equation 4.9, generalised for a liquid – solid interaction. When the Young – Dupre equation [111,112] is substituted into Equation 4.8 the work of particle transfer equation is simplified to give Equation 4.10.

$$W_{Liq,Solid} = \gamma_{Liq} Cos\theta_{Liq,Solid} \tag{4.9}$$

$$\Delta W \propto -\gamma_{BL} Cos\theta_{BL} + \gamma_{CP} Cos\theta_{CP} \tag{4.10}$$

Where:

$\gamma_{BL,P}$	Bridging liquid – particle interfacial energy (mJ/m^2)
$\gamma_{CP,P}$	Continuous phase – particle interfacial energy (mJ/m^2)
γ_{BL}	Bridging liquid surface tension (mJ/m^2)
γ_{CP}	Continuous phase surface tension (mJ/m^2)
θ_{BL}	Bridging liquid contact angle (°)
θ_{CP}	Continuous phase contact angle (°)

Table 4.7: Summary of contact angle and wettability assessment of primary particles with water and chloroform, introducing the work of particle transfer (ΔW) criteria

Material	θ_{CP} (°)	θ_{BL} (°)	ΔW (mJ/m^2)
LFP	60.9	36.8	13.6
KS4	131.6	88.0	-49.3
KS6	116.7	65.2	-44.1
S3	145.5	71.6	-68.6

The surface tension of water (continuous phase) and chloroform (bridging liquid) at 25 °C and 1.01 bar are 72.8 mJ/m^2 and 27.2 mJ/m^2 respectively. Therefore, using Equation 4.10 and contact angle data, the

ΔW for particle transfer was calculated and can be seen in Table 4.7. The graphite systems show a negative ΔW value which is expected since successful coagglomeration is seen for these systems. However, for LFP particles, the ΔW value is positive. This suggests that the process of particle transfer involved for successful coagglomeration will not be feasible with this solvent system.

Surface energy can be described based on the sum of dispersive (γ^d) and polar (γ^p) surface energy components [112]. As can be seen in Table 4.8, graphite is a nonpolar material and the surface energy is comprised almost entirely of dispersive components [113]. Chloroform is also comprised of entirely dispersive surface energy components, which explains why the work of particle transfer is negative for the graphite spherical coagglomeration processes, as similar surface energy profiles lead to stronger interactions. Whereas, LFP has a very strong polar component (177 mJ/m^2) [114] due to phosphate groups in the molecular structure. This means that the interactions from the water are stronger than the chloroform. Therefore, this explains why the work of particle transfer (ΔW) is positive when chloroform is used as a bridging liquid, and hence why spherical coagglomeration through the conventional method was not feasible.

Table 4.8: Breakdown of surface free energy values for materials used in the spherical agglomeration process, based on the dispersive and polar components

Material	γ^d (mJ/m^2)	γ^p (mJ/m^2)	Reference
LFP	41.6	177	[114]
Graphite	50.6	2.8	[113]
Chloroform	27.2	0.0	[115]
Water	27.2	45.6	[116]

As part of a study of LFP coagglomeration, working alongside Dr Kunal Pardikar (University of Sheffield), a novel addition method was developed to enable coagglomeration of solids in systems where the surface energy gradient is not favourable to the bridging liquid. This method is called the modified dispersed phase (MDP) method, discussed in Section 4.2.2.2.

4.3.2.2 TBSR Optimisation

The TBSR is still an important parameter to consider for the coagglomeration of LFP when using the MDP since the particles still need to be immersed within the droplets. The active material is already immersed and thus the carbon black is the main particle involved with particle transfer. However, rearrangement of the active material – carbon black matrix is assumed to occur during the agitation process. Some preliminary experiments carried out by Dr Kunal Pardikar found that a TBSR of 3.16 was approximately the $TBSR_{opt}$ for this system using this new MDP method. The TBSR was varied between 2.09 – 6.47 to investigate the effect on coagglomerates formed, as seen in Figure 4.17. In this

investigation area density was used instead of volume-based particle size distribution, this was a choice made by the primary author of the publication and as such is displayed as presented in the publication [104]. The area density still allows a clear analysis of the bulk properties of the sample when analysing the size distributions.

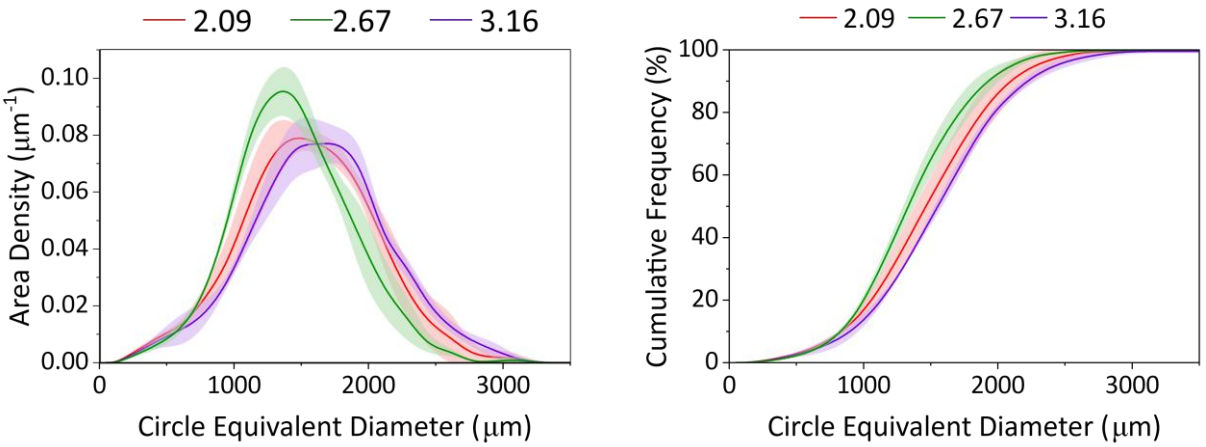

Figure 4.17: Coagglomerate area-based size distribution of LFP - C65 coagglomerates as TBSR is varied (left) and cumulative size distribution (right). Data for TBSR = 6.47 not included due to paste forming. Error bars are a standard deviation based on 3 repeats.

The coagglomerate size distributions show similar results as TBSR is varied. TBSR of 2.09 and 3.16 show very similar size distributions, whereas TBSR of 2.67 shows a slight shift towards lower average size. Therefore, all experiments ran for TBSR 2.09 – 3.16 are within range for successful coagglomeration and hence no observed trend in produced coagglomerate size properties. Due to the volume of MDP bridging liquid being relatively similar there is only small differences between the size distributions. An additional experiment was run with a high TBSR (excess bridging liquid) of 6.47. However, a paste was formed and coagglomerates were not recovered in the product. This sample was therefore discounted during the analysis. The coagglomerates recovered in the other three TBSR experiments showed an average porosity of approximately 64 % when measured. The LFP coagglomerates formed using the MDP method therefore show less porosity and hence higher densification when compared to the porosity of the KS6 and KS4 coagglomerates, as discussed in Section 4.3.1.3. This is to be expected since the 90 % wt/wt of the solids included in the coagglomeration are already immersed within the MDP bridging liquid and therefore undergo densification for a longer amount of time since the particles do not undergo the particle transfer and immersion/diffusion step during nuclei formation.

4.3.2.3 Effect of coagglomeration time

The standard coagglomeration time was run for 10 minutes. To analyse the effect agglomeration time had on coagglomerate structure, experiments were also carried out at 20 and 40 minutes. It was found that there was significant size reduction as time increased, as can be seen in Figure 4.18.

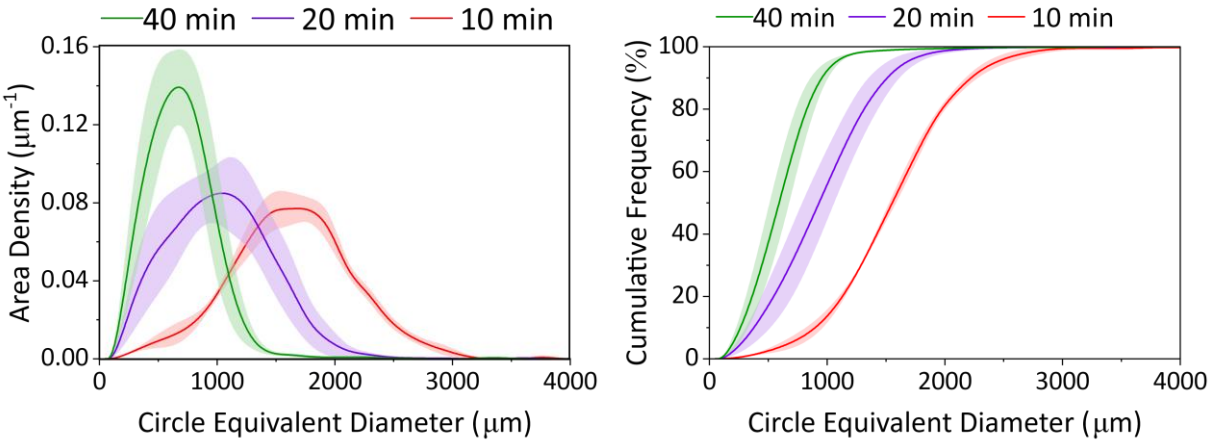

Figure 4.18: Coagglomerate size distribution as a function of coagglomeration time (left) and cumulative size distribution (right). Error bars are a standard deviation based on 3 repeats.

This was expected and could be due to several reasons. Firstly, as time is increased breakage and attrition effects begin to dominate and reduce the agglomerate size followed by densification. This generates a large amount of smaller sized coagglomerates (and some non-spherical artefacts). Secondly, as discussed earlier, DI water has a higher wettability with the LFP, so particles will begin to transfer from the MDP bridging liquid into the bulk continuous phase over time, leading to a size reduction.

4.3.2.4 Effect of solids loading

The effect of solids loading (mass based) was investigated using varying amounts of LFP and C65, whilst maintaining the 90:10 wt/wt ratio of AM:CA. Coagglomerations were carried out at 0.5 %, 1.0 % and 2.0 % wt/wt with respect to the continuous phase DI water. The TBSR was maintained at 3.16 and agglomeration time of 10 minutes. The resulting coagglomerate size distributions can be seen in Figure 4.19.

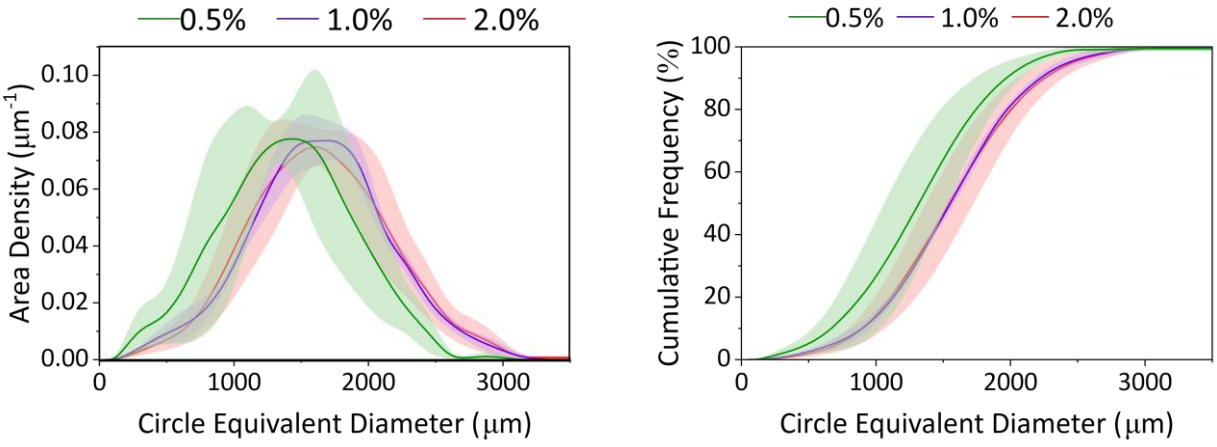

Figure 4.19: Coagglomerate size distribution as a function of solids loading (left) and cumulative size distribution (right). Error bars are a standard deviation based on 3 repeats.

Due to the similarity of the coagglomerate size distributions it is difficult to draw any conclusions regarding the effect of solids loading. It is expected that by increasing the solids loading there would be more collisions which may increase the rate of coagglomerate formation and extent of consolidation/densification. This has been seen in literature, where a higher concentration of particles in the suspension generated larger agglomerates, at a faster rate [16,117]. Further experiments at higher solids loading (>> 2.0 % wt/wt) would be needed to observe the effect of solids loading on coagglomerate properties, and the extent of coagglomeration over time should be investigated to analyse the effect of rate of coagglomerate formation.

4.3.2.5 Effect of impeller speed

To investigate the effect impeller speed had on the coagglomerates formed, four different speeds were used: 700, 1000, 1250 and 1500 RPM. It was found that an impeller speed of 700 RPM was insufficient for suitable dispersion of the particles and the MDP bridging liquid. Due to coagglomerates not being formed, this impeller speed was discounted from the analysis. However, at the other impeller speeds there was high variation in the coagglomerate size distributions as can be seen in Figure 4.20.

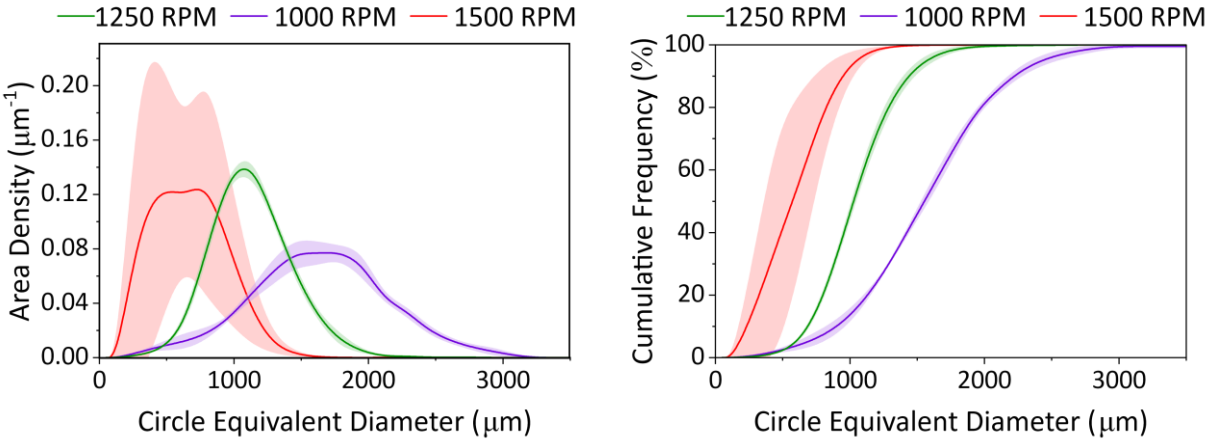

Figure 4.20: Coagglomerate area-based size distribution of LFP-C65 coagglomerates as impeller speed is varied (left) and cumulative size distribution (right). Error bars are a standard deviation based on 3 repeats.

It can be seen that at higher speeds the coagglomerates size decreases, which is expected as more shear is exerted on the system. The reduced size can be attributed to more breakage observed during the experiment with an increase in turbidity. Higher shear will also increase densification of the coagglomerates formed thus reducing the size. Additionally, it was qualititively noted that by increasing the impeller speed the amount of air entrainment increased, which may have had an effect on the rate of chloroform evaporation in the system. This may have contributed to the reduced size of coagglomerates formed by effectively reducing the TBSR. Further experiments would be required to quantitatively confirm this observation and would be considered future work. Additionally, operating in a closed system, with a reflux condenser to capture and recycle the evaporated bridging liquid could

be incorporated into the experimental design. This would prevent any loss of bridging liquid due to evaporation.

4.4 Conclusions

In this chapter, several coagglomeration systems involving both active material and carbon additives has been investigated. This involved identifying suitable systems that generated coagglomerates from a suspension using a mass transfer process based on preferential wettability.

It was found that chloroform acted as a highly effective bridging liquid for coagglomeration of graphite – C65 suspensions using ethyl cellulose as a binding agent. A study of the controlling thermodynamic parameters was included with evidence that contact angle is only one part of a successful coagglomeration system. Surface tension effects should also be considered and combined with contact angle to calculate a ΔW of particle transfer from the continuous phase to the bridging liquid. It was seen that for successful coagglomeration to occur this ΔW value must be negative.

For graphite coagglomeration it was found that there is a minimum impeller speed required for successful coagglomeration of the dense solids and chloroform droplets. The just suspended impeller speed was investigated for the KS6, KS4 and S3 graphite materials used and operating at the higher impeller speed calculated from the just suspended impeller speed generated coagglomerates. It was found that operating below this speed a paste would form due to settling of the bridging liquid and solids when there is limited pumping power from the impeller.

Investigating each graphite material to identify its respective $TBSR_{opt}$ was carried out based on the design characteristics of yield and Hausner ratio. This was found to be useful in defining when this optimum value was found quantitatively, rather than based on qualitative observations based on operator experience. It was found that KS6 and KS4 had similar $TBSR_{opt}$ values around 3.52 – 3.55. The just suspended impeller speed for S3 graphite was higher than the actual operating impeller speed used for these analyses. Therefore, S3 graphite will require further experiments to reliably determine an optimum value when run at the same operating conditions as the KS6 and KS4 graphite.

A good coagglomerating system was developed for the KS6 and KS4 graphite primary material with yields > 90 % and product that falls in the ‘excellent’ flow regime as defined by the Hausner ratio which improves on the primary particle flowability which was found to be ‘passable’ or ‘poor’ as seen in Section 3.2.2.2. Therefore, the coagglomeration has shown to improve the handleability of the electrode material whilst including both the active material and conductive additive in an interlocked matrix, improving the efficiency of downstream processing. This is therefore seen as a successful feasibility study and determined a system for successful coagglomeration of KS6 and KS4 graphite. S3 graphite

also coagglomerated successfully using the same process as KS6 and KS4. However, further optimisation could be carried out to increase the yield from ~ 70 % to > 90 %.

The effect of graphite primary particle size (d_{50}) on coagglomerate properties was investigated. KS6 and KS4 graphite have similar primary particle shape yet different particle sizes, and since they both have similar $TBSR_{opt}$, the effect of particle size on coagglomerate properties was investigated. It was found that the smaller KS4 particles generated slightly larger coagglomerates with higher average porosity (77.7 %) when compared to the porosity of the KS6 coagglomerates (68.7 %). This was due to the packing efficiency of the two materials. The higher specific surface area of the KS4 was discussed as limiting the rate of immersion into the coagglomerates generating more porous, larger coagglomerates.

A novel addition method used to coagglomerate LFP – C65 was introduced based on work carried out in collaboration with Dr Kunal Pardikar. It was found that the solvent system used for graphite did not generate enough of a surface energy gradient to initiate particle transfer of the LFP particles into the chloroform bridging liquid droplets.

The effect of process parameters on the novel MDP method for coagglomeration of LFP – C65 was investigated, analysing the effect on coagglomerate size distributions. Coagglomeration time, solids loading, and impeller speed were investigated with the largest effect being due to coagglomeration time and impeller speed with solids loading showing negligible effect on the coagglomerate size distribution.

Further work will develop the coagglomeration of graphite using the successful system identified as part of this chapter. The following chapter will investigate emulsion generation for reduction of coagglomerate size to length scales (< 100 μm) suitable for electrode manufacturing.

Chapter 5 - Coagglomerate Size Control by Tuning the Bridging Liquid Droplet Size Distribution

5.1 Introduction

The feasibility of the spherical agglomeration process to be implemented into battery electrode manufacturing processes is dependent on not only the chemical properties but also the physical properties. The coagglomerates formed in the experiments described in Chapter 4 showed potential in the process for structuring active materials with inter- and intra- dispersed carbon black suitable for good lithiation and electronic conductivity within the electrode. However, the size of coagglomerates is a key issue and developing a process to generate coagglomerates at length scales suitable for electrodes (<100 μm) is an important consideration which needs to be addressed. The work discussed in this chapter will present approaches taken to reduce the coagglomerate size to <100 μm whilst maintaining the key ratio of 90:10 wt/wt of active material:carbon additive respectively. Within this chapter, both addition method and use of excipients will be discussed, building upon the systems developed in Chapter 4. Where addition method refers primarily to the moment at which bridging liquid is injected to the suspension. The hypothesis is that by injecting the bridging liquid before addition of solids the droplets will form a stable emulsion with smaller droplet size. Which will therefore lead to smaller coagglomerate size.

5.1.1 Objectives

The main research question of this chapter is 'how can the average coagglomerate size be reduced to length scales suitable for battery electrode manufacturing (<100 μm)?' The main objectives are:

- Investigate the influence of bridging liquid addition point on the generation of coagglomerates
- Investigate how the coagglomerate structure changes with reduced coagglomerate size

5.2 Methods

The coagglomeration method was investigated to understand the effect that bridging liquid addition point had on the coagglomerates formed. The materials were based on the study of KS6 graphite coagglomeration carried out in Chapter 4. However, this investigation was carried out before the experiments from Chapter 4 (chronologically) and therefore operates at a lower solid loading of 0.2 wt% with respect to the continuous phase (DI water).

5.2.1 Coagglomerate Generation

The stirred tank setup and materials used were the same as those used in the KS6 coagglomeration study from Chapter 4, Section 4.2.1 . The solids loading was lower, and addition of surfactant was used to enable good dispersion of the solid particles within the continuous phase. Table 5.1 details the run conditions for coagglomeration generation, however the addition method differs.

Table 5.1: Summary of the coagglomeration materials and process parameters used for this study

Material	Desired Amount	Operating Parameter	
KS6 graphite	0.36 g	Impeller speed	900 RPM
C65 carbon black	0.04 g	Impeller geometry	Rushton Turbine
SDS surfactant	0.022 g	Agglomeration time	40 minutes
Water	199.6 g		
Chloroform (BL)	2.89 ml		
TBSR	10		
Ethyl Cellulose	0.022 g		

Use of sodium dodecyl sulphate (SDS) surfactant (Sigma Aldrich) enabled the impeller speed to operate below the N_{JS} as discussed in Section 4.2.2.2, with no deposition of unagglomerated material on the baffles or impeller. SDS has a hydrophilic head and hydrophobic tail suitable for enhancing dispersion of chloroform bridging liquid droplets by reducing the interfacial tension between the two immiscible liquids. Lower interfacial tension of oil-in-water emulsions leads to an increased number of droplets with lower average droplet size with only a low concentration of SDS surfactant required [118]. The coagglomeration time was 40 minutes to ensure good densification of small coagglomerates, as this was found to increase their compressive strength in previous literature [12]. This is important when attempting to generate coagglomerates <100 µm to prevent breakage after they had been generated and dried.

The addition methods used for these experiments had two forms. Firstly, the standard process (called the standard addition method) which is similar to the method described in Section 3.3 Active material and carbon additive were added to DI water continuous phase in an agitated suspension, before injecting the bridging liquid and allowed to coagglomerate, for 40 minutes at 900 RPM. A diagram of this method can be seen in Figure 5.1. Ethyl cellulose polymeric binder was added to the bridging liquid to improve the mechanical strength of the coagglomerates generated and bind material together. SDS surfactant was added to the continuous phase to improve the dispersion of primary particles in suspension.

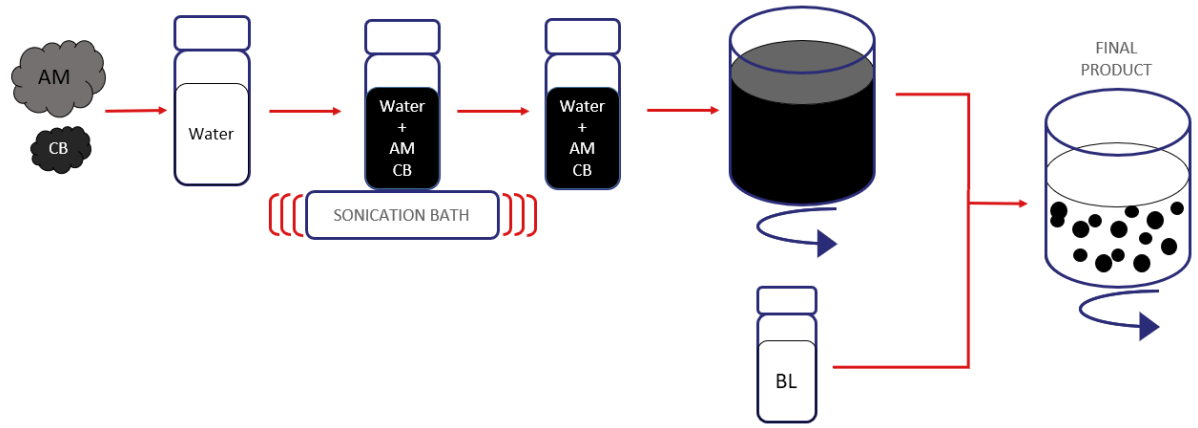

Figure 5.1: Diagram of standard addition mechanism for coagglomeration

The alternative method (called the emulsion addition method) involved generating a basic emulsion. The SDS surfactant was added to the DI water and allowed to dissolve, upon which the chloroform is injected to the solution. This was left for 5 minutes to generate a steady state droplet size distribution in the form of an emulsion with 'cloudy' appearance. Once the droplets had been dispersed, the solids were added which had been sonicated in a vial of 20 ml DI water. The process was then left to agitate at 900 RPM for 40 minutes before the product being filtered through a 32 µm mesh sieve and then dried in a drying cabinet at 50 °C for 24 hours. This method can be seen in Figure 5.2.

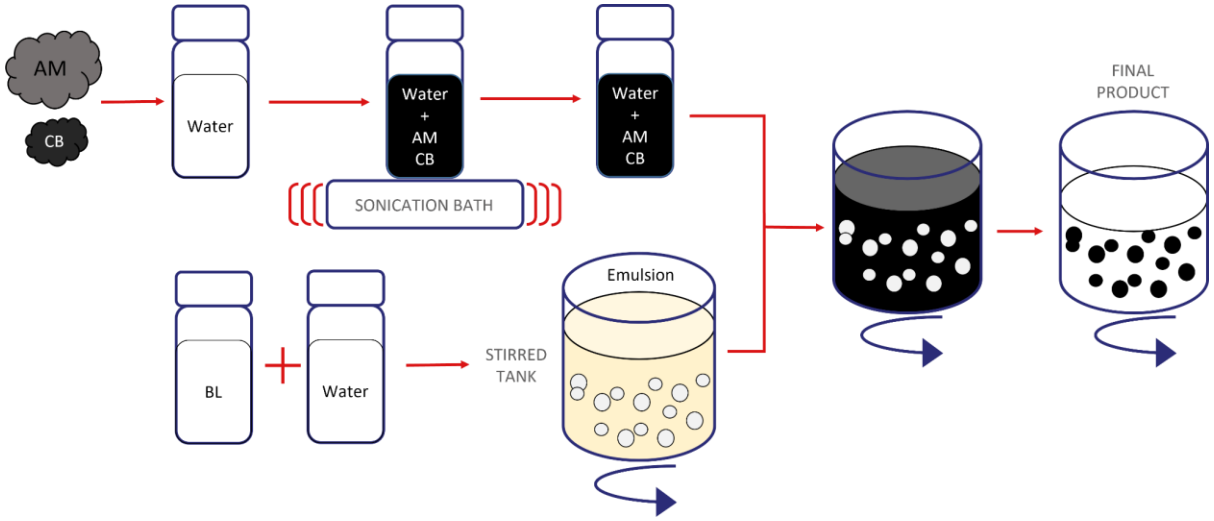

Figure 5.2: Diagram of the emulsion addition method for coagglomeration

Interestingly, the TBSR of 10 is much higher than the $TBSR_{opt}$ discussed in Section 4.3.1 for the same KS6 graphite active material. However, it is expected that due to the rate of collisions being lower due to the decreased solids loading, increasing the bridging liquid volume reduced the time for coagglomeration. If the experiment was left to run longer there is a chance that paste would form as coagglomerate continue densifying. Equally, if the experiment was operated at the $TBSR_{opt}$ of 3.52, due

to the long agglomeration time and open system there is a chance that the chloroform bridging liquid could evaporate. The TBSR would then be too low and coagglomeration would not occur, due to underwetting. Further experiments would be required to quantify the link between collision kinetics and TBSR, but this was not part of this investigation.

5.2.2 Droplet Sizing

A standard stirred tank setup was used to investigate the droplet size distribution, and addition of sodium dodecyl sulfate (SDS) surfactant stabilises the droplets formed in suspension. Chloroform was dyed using Acid Red IV dye (Sigma – Aldrich) and then injected at the correct TBSR into the stirred tank, operating at 900 RPM. A pipette was used to extract a small volume of the droplet suspension at 5, 10, 15 and 20 minutes of agitation. These extracted samples were then injected into a 30 mm petri dish and analysed under the optical microscope. The petri dish was placed in the same position each time and 3 images were taken across the petri dish at three coordinates to reduce bias of image location.

The images were analysed using Fiji (ImageJ) to automate measuring the droplet diameters. Images were first cropped to remove the scale bar, then converted to an RGB stack and then 8-bit greyscale image. The 'Find Edges' tool was used to find the edges of the droplet circles, as seen in Figure 5.3.

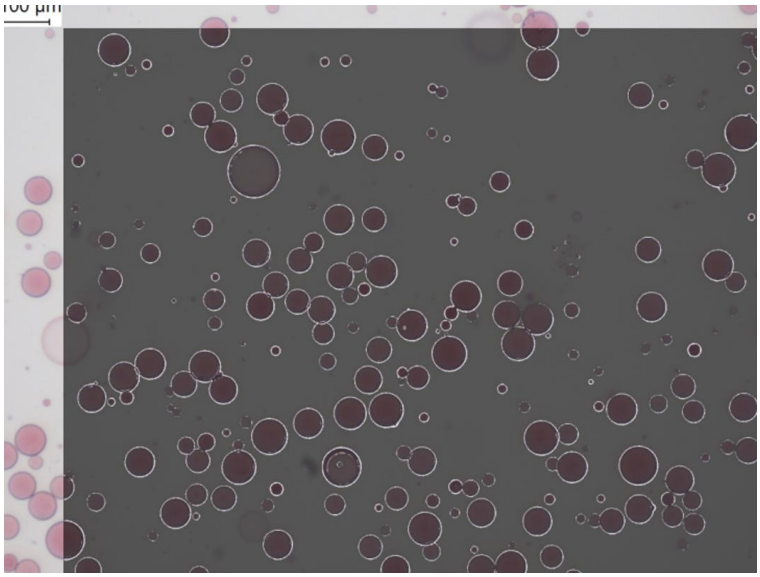

Figure 5.3: Image of droplets captured using the optical microscope and processed in ImageJ (Fiji) to find the edges of the contrasted red droplets

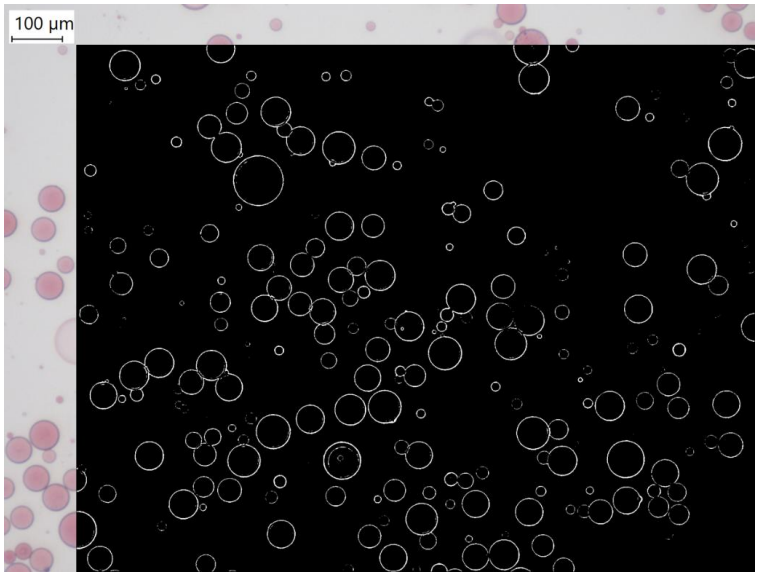

Figure 5.4: Overlay of converted outlined image to a masked image in ImageJ (Fiji)

The outlined image was then converted to a mask which generates a binary image seen in Figure 5.4. The outlined binary image of the droplets was now ready for sizing, which was carried out using the Hough Circle Transform plugin[5] which is trained to identify circular objects, even those that are incomplete. Since the droplets are by nature circular, this was a reliable process for extracting size data over a large sample size. The Hough Circle Transform plugin was run using the easy mode as the circles were easily identifiable. The minimum and maximum search radius was input, where the minimum was based on 10 px diameters as discussed in Section 3.4.1 for ensuring the data was reliable, which at this magnification was equivalent to 7.52 µm. The Hough score threshold is defined as how tolerant the search criteria would be of incomplete circles. Since some of the outlines have gaps or overlapping droplets which appear as incomplete outlines, the Hough score was reduced from 1 to 0.7 to allow for some leniency in the transform. Reduction of the Hough score, lower than 0.7, resulted in poor data and false circles being identified. An example of the successfully produced Hough transform can be seen in Figure 5.5.

[5] "This plugin is a modified version of the Hough circle transform implemented by Hemerson Pistori and Eduardo Rocha Costa. The transform algorithm was based off an original implementation by Mark Schulze. This plugin was developed as part of the University of California, Berkeley Vision Sciences core grant NIH P30EY003176."

Figure 5.5: Image of the droplet sample after the Hough Circle transformation plugin had run with clearly defined circles (droplets) identified

The data is output to a table, in ImageJ (Fiji), and includes droplet diameter values which were converted to a volume-based size distribution using the same method discussed in Section 3.4.1 used for converting number-based size distributions of coagglomerates generated (Equation 3.2). Since the droplet size distribution was measured at different time intervals the effect of time on the droplet size was investigated.

5.2.3 Coagglomerate Characterisation

Imaging of the coagglomerates, to investigate their structure, was carried out using the optical microscopy and SEM methods discussed in Section 3.4 . For the small coagglomerates generated, optical microscopy did not provide sufficient magnification to analyse the products and therefore SEM was employed. Additionally, the methods required for sizing the coagglomerates had to be adapted. Due to the small size of the coagglomerates, the method described in Section 3.4.1 which used the optical microscope to take images and size the coagglomerates in ImageJ (Fiji), was not possible as the resolution was not high enough. Therefore, the Mastersizer 3000 method, discussed for size analysis of the primary material in Section 3.2.1 was used to size the coagglomerates. The sonication setting was set to 0 % and impeller speed set to 2000 RPM, so that coagglomerate breakage was minimised during dispersion in the wet cell. The results were compared to the scales seen in the SEM to assess whether they were reliable. This is because in the wet cell Mastersizer process, agglomeration could occur, and this was the reason it was generally avoided. However, in this case it was found that this process gave a reliable measurement.

5.3 Results

When coagglomerating using the standard addition method the bulk suspension became clear as coagglomerates formed and primary material was consolidated. After 20 minutes though, the suspension began to get more turbid again. This was considered to be due to breakage of the coagglomerates into smaller entities. However, when using the emulsion addition method, the suspension did not clear up and instead remained turbid. This suggested that perhaps either no coagglomeration occurred or the product was small enough to make the suspension appear turbid. Upon filtering the suspension for both addition methods, the products were characterised using imaging and size techniques.

5.3.1 Coagglomerate Structure

The standard addition method generated coagglomerates like those generated in using the experiments described in Chapter 4. Figure 5.6 shows the coagglomerates were large and appear to have a smooth surface, suggesting good densification. This is to be expected with a long coagglomeration time as it allowed further collisions between the impeller, coagglomerates and primary material, leading to further densification of the coagglomerates.

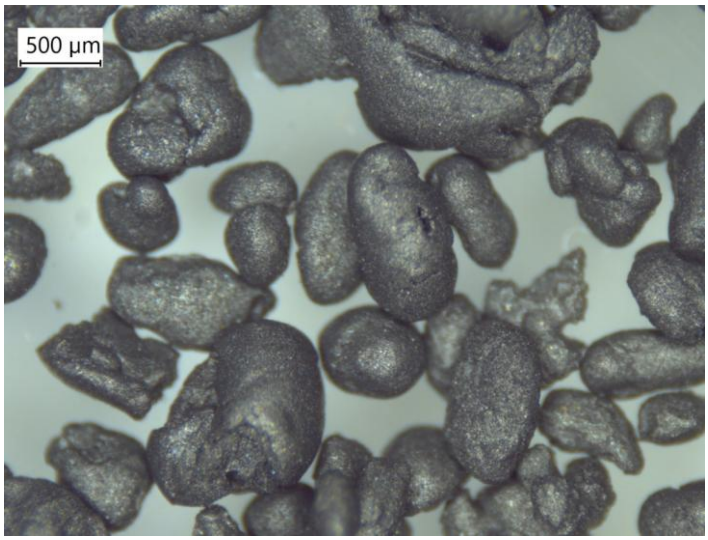

Figure 5.6: Optical microscopy image of KS6-C65 coagglomerates formed using the standard addition method The Coagglomerates formed using the emulsion addition method appeared to show some spherical structure at a much smaller scale than the standard edition method. The optical microscope image seen in Figure 5.7, provides insight however the resolution and magnification limit the analysis.

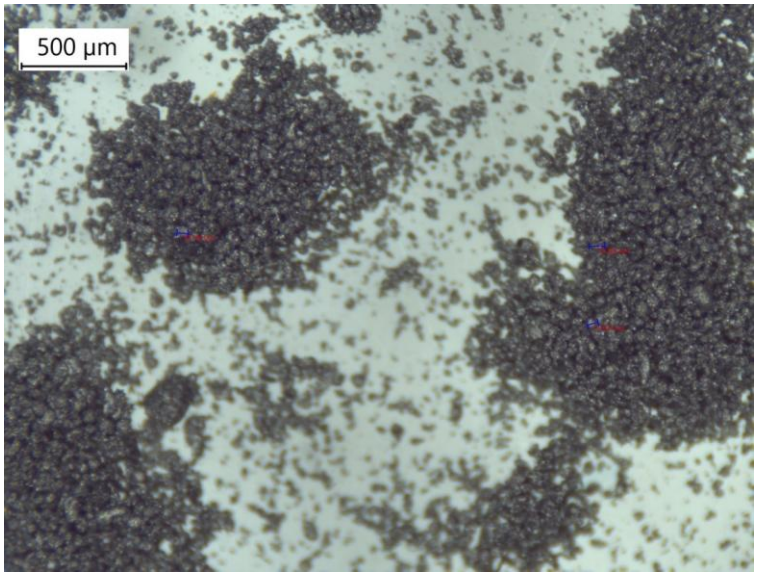

Figure 5.7: Optical microscopy image of KS6-C65 coagglomerates formed using the emulsion addition methodSEM

Figure 5.8 shows the SEM images for coagglomerates generated using the standard addition method. The coagglomerates appear dense but signs of breakage are evident. Additionally, the coagglomerates are irregular in shape, lacking the sphericity expected from a spherical agglomeration process. Since the experiment operated at a higher TBSR of 10, the coagglomerates may be overwetted and more susceptible to deformation during high shear mixing. Coalescence between coagglomerates is also likely to have occurred due to excess bridging liquid on the surface of the coagglomerates.

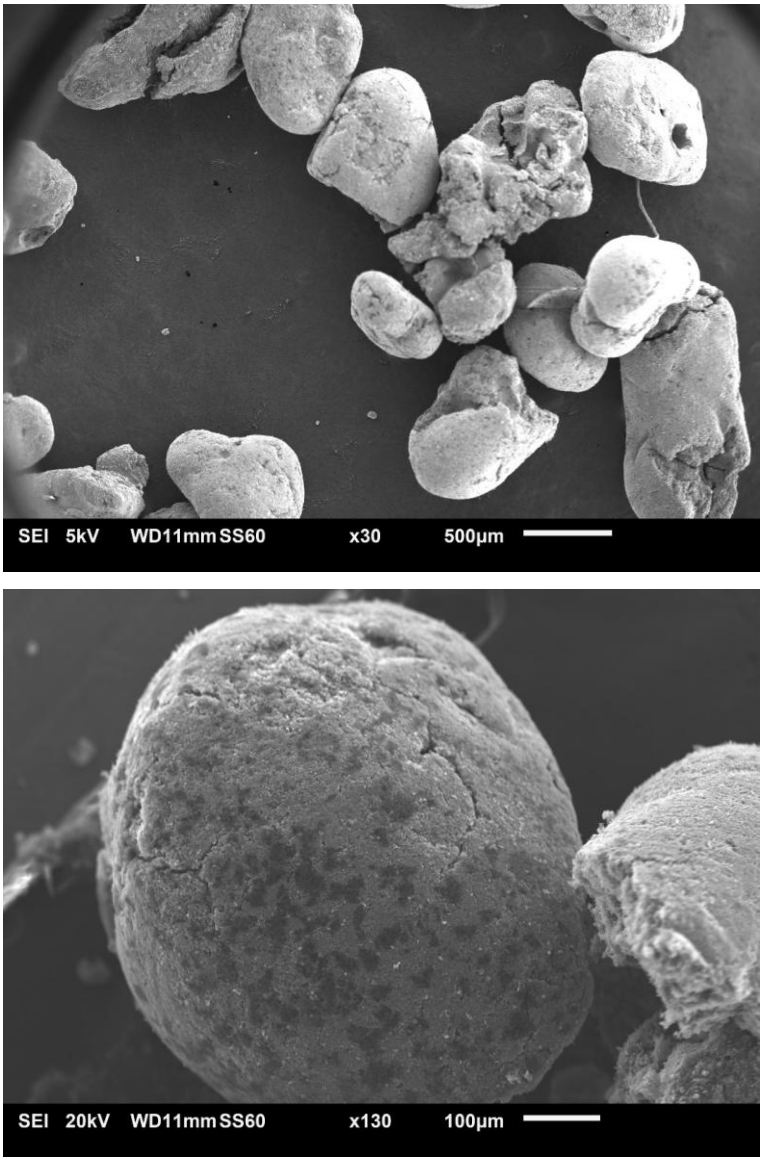

Figure 5.8: SEM images of the coagglomerates formed using the standard addition mechanism

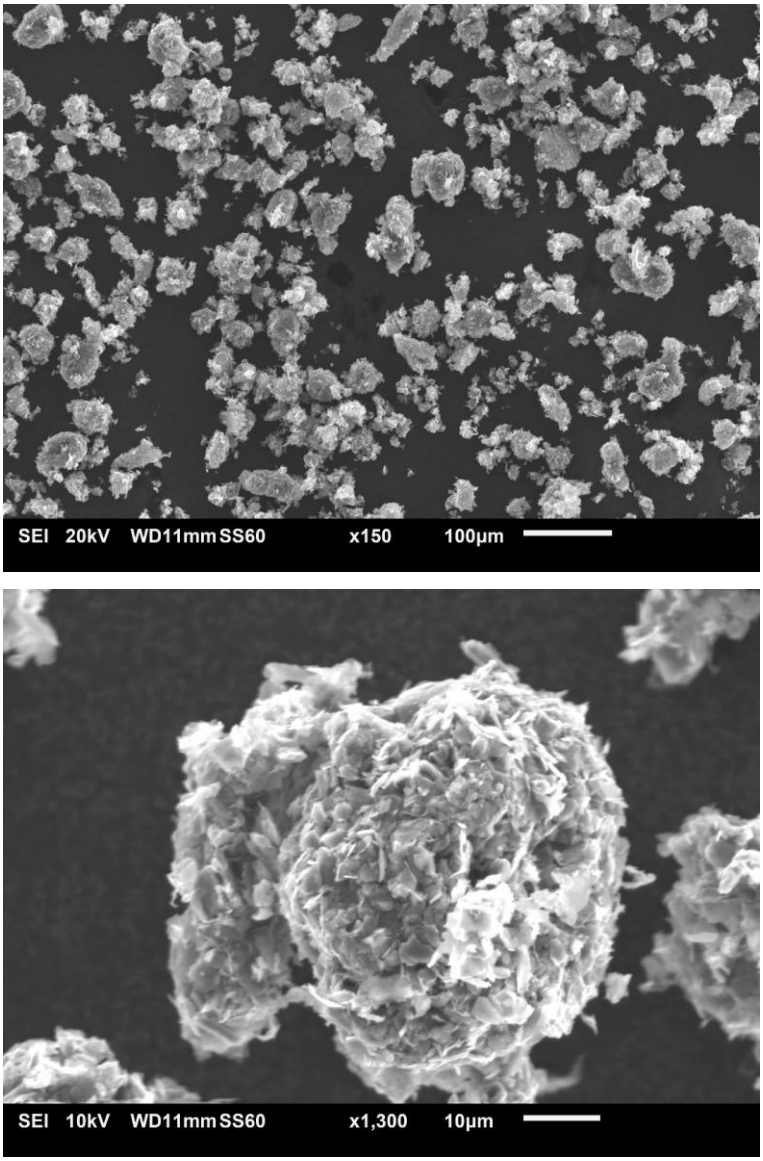

Figure 5.9: SEM images of the coagglomerates formed using the emulsion addition mechanism

Coagglomerates generated using the emulsion addition method, as seen in Figure 5.9, are much smaller than coagglomerates seen in the SEM images from the standard addition method batch. The coagglomerates formed appear more spherical with a rougher surface than the coagglomerates seen in Figure 5.8. Comparison between different size coagglomerates at different magnifications is unreliable though.

In Figure 5.9, the scale bar shows that the coagglomerates formed are <100 µm and further analysis of the size was carried out using the Mastersizer 3000 to analyse the coagglomerate size distribution. The KS6 graphite active material particles can clearly be seen in the emulsion addition mechanism coagglomerates with some evidence of C65 carbon black on the high magnification image.

5.3.2 Droplet Size Distribution

Droplet size distribution was carried out for the formation of emulsions before addition of solids. The droplets were imaged at three locations in a petri dish from a sample extracted from the stirred tank at 5-minute intervals. Examples of the droplets formed can be seen in Figure 5.10:

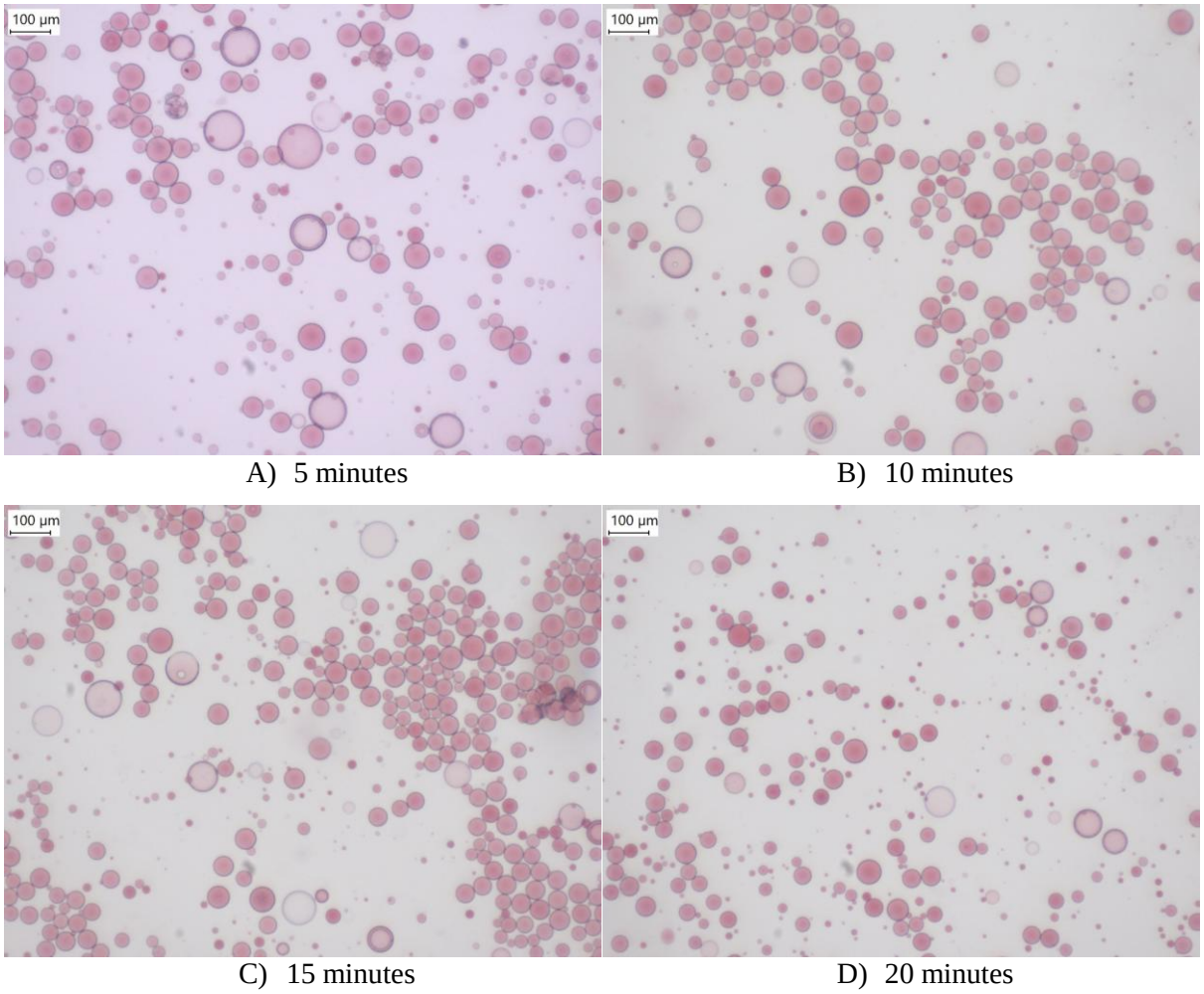

A) 5 minutes B) 10 minutes

C) 15 minutes D) 20 minutes

Figure 5.10: Example image of droplets sampled from the stirred tank during emulsion generation used for calculating a droplet size distribution, at 5-minute time intervals

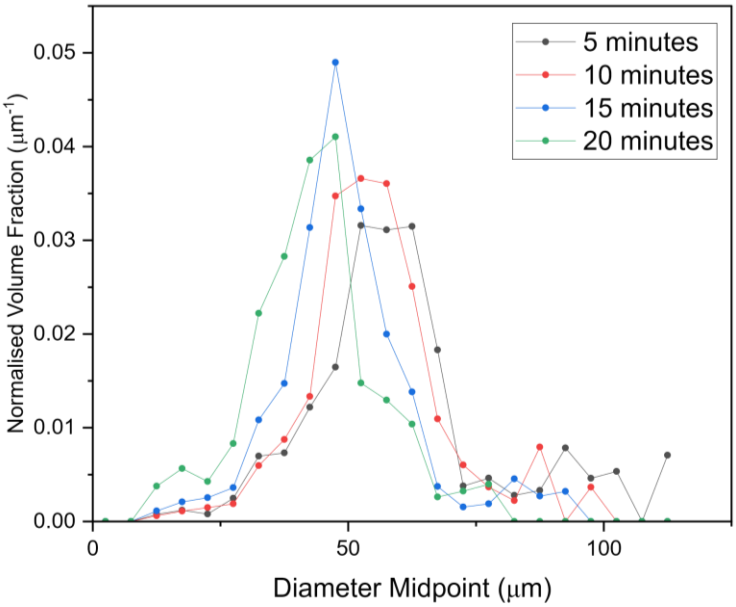

Figure 5.11: Droplet size distribution of chloroform emulsion samples taken at 5-minute intervals

Figure 5.11 shows that during the emulsion addition method droplets are formed at an average of approximately 50 μm diameter. As time increases the droplet size distribution reduces in size. Since particles immerse within the droplets to form nuclei which then grow through layering and coalescence, the agglomerate size will be correlated to the droplet size. Where smaller droplets will form smaller coagglomerates, if operating at the optimum TBSR.

Droplet size was not measured during the standard addition method as the dark suspension prevented the ability to draw samples and measure using microscopy. However, droplet formation can be described by the dimensionless Weber number, which is a balance of inertial forces and surface tension, given by Equation 5.1 for a stirred tank [119].

$$\mathrm{We} = \frac{Inertial\ Forces}{Surface\ Tension} = \frac{\rho N^2 D^3}{\sigma} \tag{5.1}$$

Where:

- ρ Density of the dispersed phase fluid (kg/m^3)
- N Rotational speed of the impeller (RPM)
- D Diameter of the impeller (m)
- σ Surface tension of the droplet (N/m)

In a stirred tank the inertial forces are a function of the shear applied to the system that leads to droplet deformation and the surface tension is related to the solvent properties in the multiphase system. There

is a critical Weber number above which the deformation forces dominate and breakage occurs generating smaller droplets ($We \gg We_{Crit}$) [119].

For the standard addition method droplet breakage is occurring at the same time as particle transfer during the agglomeration process. The particle transfer process is quick and therefore the bridging liquid solvent properties change. As primary particles are incorporated into the bridging liquid the density and viscosity change leading to higher shear forces required to deform the droplets. Therefore, the critical Weber number required for droplet breakage is higher and thus it can be assumed that the droplet size distribution is higher in the standard addition method compared to the emulsion addition method.

Application of computation fluid dynamics (CFD) would be beneficial for understanding the droplet formation mechanisms particularly when solids are added to the suspension at the same time as the bridging liquid. This should be considered for future work.

5.3.3 Coagglomerates Size Distribution

A volume-based size distribution was calculated for the two samples generated using different addition mechanisms.

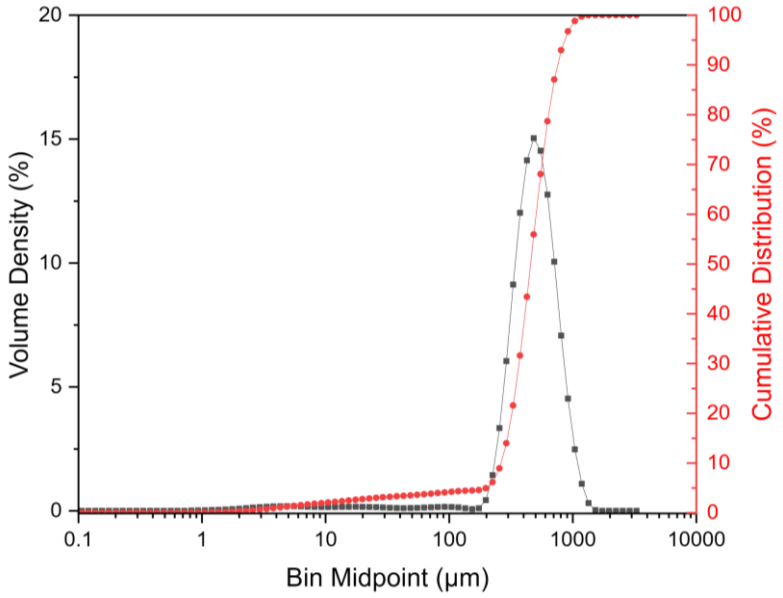

Figure 5.12: Volume based size distribution for coagglomerates generated using the standard addition mechanism based on an average of 10 repeat measurements

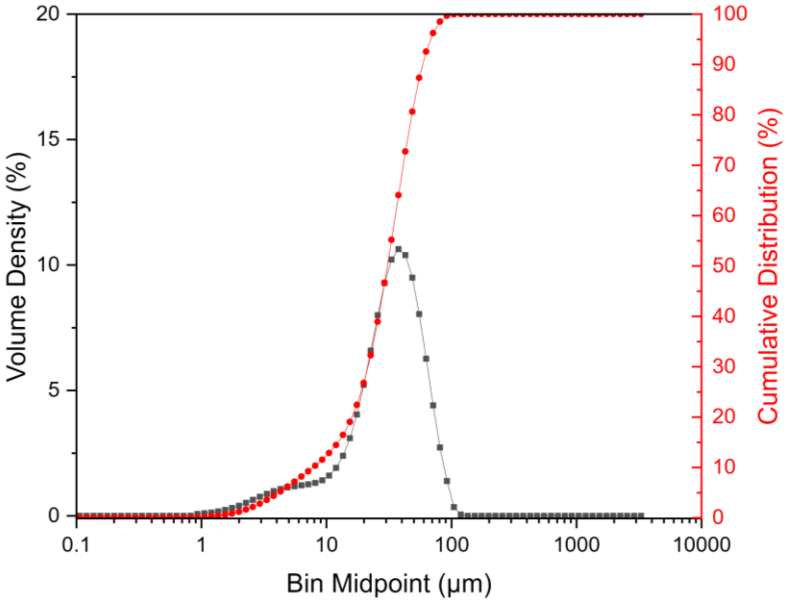

Figure 5.13: Volume based size distribution for coagglomerates generated using the emulsion addition method based on an average of 10 repeat measurements

For the standard addition method, there doesn't appear to be much breakage (Figure 5.12 a). However, for the emulsion addition method (Figure 5.12 b) the secondary slight peak between 1 – 10 µm, could be due to remaining primary material that was not coagglomerated or breakage that occurs during the Mastersizer 3000 processing. The emulsion addition mechanisms size distribution clearly shows a reduced average coagglomerate size with a d_{50} of 32.7 µm. This is ten-fold less than the standard addition mechanism which had a d_{50} of 486 µm. Table 5.2 summarises the size characteristics of the distributions for both mechanisms. Interestingly, the emulsion addition method coagglomerate size distribution shows a d_{90} of 62.6 µm suggesting that the majority of coagglomerates formed were <100 µm, which makes them suitable length scales for electrode manufacturing.

Table 5.2: Size characteristic data extracted from the particle size distributions seen in Figure 5.12 and Figure 5.13

Addition Method	d_{10} (µm)	d_{50} (µm)	d_{90} (µm)	$d_{4,3}$ (µm)
Standard Method	281	486	803	510
Emulsion Method	8.33	32.7	62.6	34.8

Since chloroform has a much higher affinity to the KS6 – C65 solids than DI water, and the stirred tank operates in a turbulent regime suggesting high collision rate, then the rate of particle transfer of the solids from the continuous phase to the dispersed phase is expected to be high. During the standard addition method, a stream of chloroform is injected to the solid suspension which is then subject to shear and mass transfer at the same time. It is therefore assumed that the droplet breakage is limited by

the immersion of solids into the bridging liquid suspension due to an increase in the critical Weber number. The value of the critical Weber number is dynamic as the concentration of particles immersed within the bridging liquid increases with time. Whereas, in the emulsion addition method the chloroform has time to form droplets in the continuous phase stabilised by the SDS surfactant. Then, when the primary particles immerse within the droplets, they are limited by the size of the droplets which are already at a stable size distribution. Some coalescence and growth will occur, however, starting nuclei formed from a smaller droplet size ensures the maximum coagglomerates size is also limited during the growth and consolidation stage.

5.4 Conclusions

This investigation displays the benefit of surfactant addition and generating emulsions to template coagglomerate size before addition of solids. It has been shown that by allowing the chloroform droplet size distribution to equilibrate before addition of the solids, the coagglomerates formed are smaller in average diameter than the standard addition method. SEM imaging and coagglomerate size distribution showed that the coagglomerate generated through the emulsion addition method have a d_{50} of 32.7 µm. When the bridging liquid is added after the particles are suspended the droplet breakage and reduction in size is limited by the increase in viscosity due to solids immersion. The coagglomerate size was found to be much larger using the standard addition method, with a d_{50} of 486 µm. This suggests that droplet generation and stabilisation is a useful route for pre-processing of the bridging liquid, as a method of size control. Droplet size control ensures that the nucleation and therefore final coagglomerates size is limited by the size of the initial droplets. Electrodes are generally manufactured at approximately 100 µm and therefore controlling the coagglomerate size is important for the implementation into dry manufacturing processes. This has been shown to be possible and that the size of the coagglomerate is strongly linked to the size of the initial droplet and nuclei formed.

Future work could incorporate the use of an emulsion generation process to create smaller more uniform droplet distributions, which can then be used to generate drop controlled coagglomerates. Additionally, scaling this study to systems which operate at higher solids loading would be beneficial to ensure the results are comparable and important for high manufacturing throughput.

Chapter 6 - Study of Hollow Agglomerate Formation Through Mechanistic Understanding during Spherical Agglomeration of Battery Materials

6.1 Introduction

In this study, the spherical agglomeration technique is manipulated to produce hollow coagglomerated particulate structures for application in battery electrode manufacture. In particular, the rate limiting particle immersion mechanism is exploited, which allows for the tailoring of particle structure. The coagglomerates show advantageous properties for dry electrode manufacturing, through compression of an interlocked matrix of active material and carbon additive. Hollow structures have been seen in previous electrochemical literature to provide beneficial properties to electrode performance [120,121]. Whilst the agglomerate structures formed in previous chapters are highly porous, a hollow structure would provide additional surface area for greater ionic conductivity. Additionally, the stressful volume change caused by lithium intercalation and deintercalation can be reduced due to the excess volume available for particle expansion. This would in turn reduce the effect of microcracking and hence increase the lifespan of the electrode/battery. However, this could also be considered a drawback as this would reduce the volumetric energy density of the battery due to the large voids.

This investigation builds upon the coagglomeration of S3 graphite as an active material (alongside C65 carbon black) to look at the effect that bridging liquid viscosity has on the coagglomerate structure. A mechanistic modelling paper by Arjmandi-Tash et al. (2019) [76] explored the rate limiting mechanisms involved in the production of agglomerates. The modelling work is very beneficial for understanding the rate kinetics involved in the spherical agglomeration process, however it has its limitations. The paper only focusses on the nucleation kinetics which occur before the growth and breakage phase, as discussed in the literature review. The mathematical model suggested that during this nucleation stage there are two rate limiting mechanisms: the collision model, and the immersion model.

The collision model assumes that if particles reach the surface of the droplet, they immediately immerse to the centre such that the droplet surface is open for more collisions to occur. Through this assumption, the rate is limited therefore by the propensity for particles and droplets to interact.

The immersion rate limiting mechanism assumes that collisions are constant, and that the droplet surface is always coated with a layer of particles from collisions. This model suggests that the spherical agglomerates are therefore only limited by the rate of immersion from the droplet surface to the centre. Figure 6.1 shows how particles interact with a droplet interface during the immersion limited mechanism, with solids at the surface of the droplet immersing towards the centre. Equation 6.1

describes the immersion mechanism limited rate equation proposed by Arjmandi-Tash et al. (2019) [76].

$$Q_{imm} = \frac{\Psi D_p \gamma Cos\theta}{30\mu_d} \frac{1}{H_2(t) - H_1(t)} \frac{\phi_{cp}^2}{(1 - \phi_{cp})} \tag{6.1}$$

Where:

Ψ	Sphericity factor of the particle
D_p	Sauter mean particle diameter (m)
γ	Interfacial tension (mJ/m^2)
θ	Contact angle
μ_d	Bridging liquid viscosity (Pa.s)
$H_2(t) - H_1(t)$	Wall thickness (for time = t) (m)
ϕ_{cp}	Critical packing liquid volume fraction

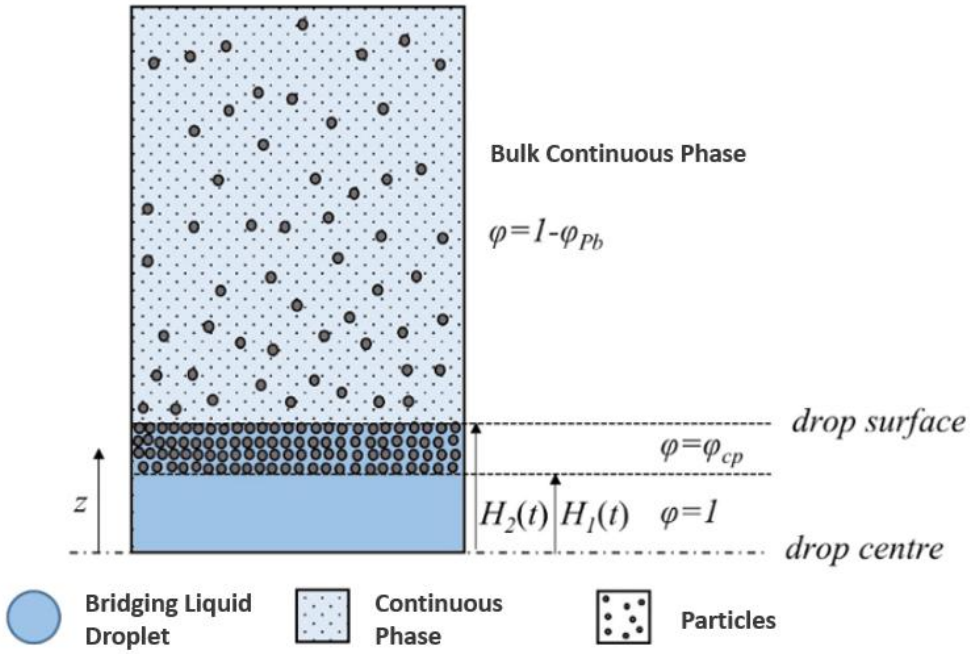

Figure 6.1: Schematic adapted from Arjmandi-Tash. O, et al. (2019) outlining the immersion limited mechanism, with the following caption: "$H_2(t)$ corresponds to the radius of the nucleus; $H_1(t)$ is the radius of the core; φ is the liquid volume fraction; φ_{cp} is the critical-packing liquid volume fraction; φ_{pb} is the particles' volume fraction in the bulk mother solution"

Both the collision limited, and immersion limited rate models will affect the agglomeration procedure in some way. However, due to the turbulent nature of stirred tank flow, it is assumed that the collisions are sufficient to ensure that the coagglomeration rate limiting mechanisms are primarily due to

immersion of the particles within the droplets. In these two mechanisms, bridging liquid droplet viscosity only appears in the immersion-based model. This suggests that through increasing the viscosity of the droplets, the rate of immersion of particles from the droplet surface to the centre can be reduced without influencing the rate of collisions.

6.1.1 Objectives

The main aim for this chapter is to manipulate the rate limiting mechanisms and investigate whether increasing the viscosity of the bridging liquid will reduce the extent of immersion over a specific time and control the agglomerate microstructure. The main objectives of this investigation are:

- Compare how the size of droplets formed in a stirred tank is affected by increasing bridging liquid viscosity
- Investigate how bridging liquid viscosity effects the work of particle transfer (ΔW) through surface energy characterisation of the bridging liquid
- Measure the effect bridging liquid viscosity on coagglomerate size distribution and morphology

6.2 Methods

6.2.1 Coagglomerate Generation

Coagglomerate generation was carried out using the standard method for S3 graphite – C65 carbon black with water as the continuous phase and chloroform as the bridging liquid. Table 6.1 details all the parameters used in this chapter as standard. For investigating the effect of viscous bridging liquid, the amount of ethyl cellulose polymeric binder was varied, referred to by its respective mass fraction in the chloroform. Additionally, surfactant was used to aid in the dispersion of the solids and chloroform droplets within the stirred tank. It was found that addition of a small amount sodium dodecyl sulphate (equivalent to 0.05 CMC [122]) enabled reliable coagglomerate generation without any fouling or deposition on the stirred tank walls or baffles.

Table 6.1: Summary of material and operating parameters for viscous bridging liquid coagglomeration generation

Material	**Desired Amount**	**Operating Parameter**	
S3 graphite	1.8 g	Impeller speed	900 RPM
C65 carbon black	0.2 g	Impeller geometry	Rushton Turbine
SDS surfactant	0.022 g	Agglomeration time	10 minutes
Water	198 g		
TBSR	2		
Ethyl Cellulose	**0.5 wt% - 10 wt%**		

The coagglomeration method was similar to that described in Section 3.3 with the additional step of adding SDS to the agitating continuous phase. In Chapter 4 it was seen that higher impeller speeds were required to prevent a paste forming during the coagglomeration process. However, by adding surfactant the impeller speed was able to be reduced to 900 RPM. This was because the surfactant helped aid in the dispersion of the primary particles and bridging liquid droplets. By dispersing the droplets better and reducing the attractive forces between them, the chance of forming a paste were reduced. This also prevented the particles from depositing on the beaker walls, baffles or impeller. This was allowed to equilibrate for 5 minutes before adding the solids and then the viscous bridging liquid. After the 10-minute coagglomeration time had passed, the stirred tank was turned off and the suspension filtered first through a 32 µm sieve mesh and the pass-through product was filtered in a Buchner filter to capture unagglomerated primary particles. The coagglomerates on the sieve were then left to dry in a drying cabinet set to 50 °C for 24 hours, as standard for the previous coagglomeration experiments.

6.2.2 Viscous Solvent Characterisation

As the viscosity of the solvent was increased, the characteristics it exhibited were measured to identify any differences that may affect coagglomerate formation. This was particularly important for the droplet size distribution in a stirred tank and the wettability characteristics of the solvents with increasing ethyl cellulose concentration.

6.2.2.1 Bridging Liquid Rheometry

The viscosity of the modified bridging liquids was an important parameter to quantify. This was important to assess how viscosity changed as a function of ethyl cellulose concentration. Additionally, how shear rate affected the behaviour of the viscous solvents was assessed, particularly to see if the viscous solutions exhibited any non-newtonian behaviour. The method was based on a similar method described in a paper by Reynolds et al. (2022) [123]. A Netzsch Kinexus Pro rheometer was used with a 40 mm cone and plate geometry, with a 1° cone angle. The sample stage was covered to minimise evaporation of the chloroform during analysis. A small volume approximately 3 ml was injected onto the surface of the bottom plate, then the top plate was lowered. The volume in the gap was adjusted, either by scraping some of the sample away or adding more, based on filling the gap volume such that the sample wasn't exceeding the cone and plate diameter as can be seen in Figure 6.2 [124]. For the diagram shown below, β is the cone angle, R is the plate radius and ω is the rotational speed proportional to the shear rate.

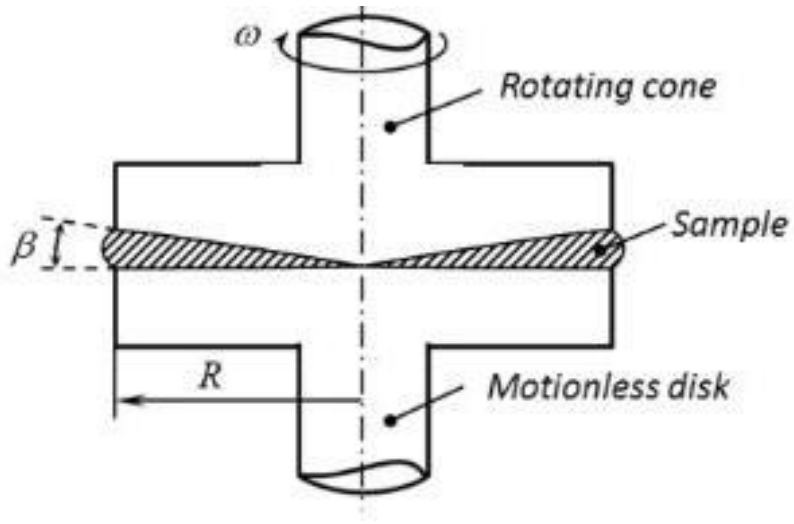

Figure 6.2: Diagram of typical cone and plate rheometer geometry [124]

The software linked to the rheometer was setup so that a 'recipe' was loaded which dictated the rheometer run conditions. Samples were tested across the shear rate range of 0.01 – 10,000 s^{-1} where a shear viscosity value was recorded when an equilibrium was reached, defined as maintaining a value within 1 % error for 10 seconds [123]. Chloroform with increasing ethyl cellulose concentration solutions were analysed at 0.5, 2, 4, 6, 8 and 10 wt%, due to time constraints 1 wt% ethyl cellulose concentration was not analysed.

6.2.2.2 Droplet Size Distribution

The same method as described in Section 5.2.2 was used for analysis of the droplet size distribution, however different viscosity bridging liquids were assessed for the effect on droplet size distribution. Viscous bridging liquid was injected into the continuous phase at a TBSR of 2, as per the standard coagglomerate process. Samples were taken at 5-, 10-, 15- and 20-minute intervals from the stirred tank using a pipette and placed in a petri dish and imaged using an optical microscope. The droplet size analysis was carried out for bridging liquids containing 0.5, 1, 2, 4, 6, 8 and 10 wt% of ethyl cellulose polymeric binder, with respect to the mass of chloroform (bridging liquid). The Hough circle transform plugin was used to measure the size of droplets using ImageJ (Fiji) and then converted from a number-based distribution to a volume-based distribution using Equation 3.2.

6.2.2.3 Contact Angle & Wettability

Using the method discussed in Section 4.2.1.1 to assess solvent wettability characteristics, the various viscous bridging liquids contact angles were measured. The contact angle was measured using the contact angle plugin through ImageJ (Fiji) to fit the curves using an ellipse. This was to account for gravitational effects on large droplets which deformed the droplet profile, as discussed in Section 4.2.1.1.

The surface tension of the droplets was also carried out using the pendant drop method. Whilst other methods are available such as Du Noüy ring method and Wilhelmy plate method, the pendant drop method is reliable and versatile. Additionally, the pendant drop method allows a smaller amount of solvent to be used, which is particularly important when working with chloroform. It is important to note that measuring the surface tension of volatile solvents using the pendant drop method must be done so quickly whilst maintain accuracy and good safety practices. This is due to the high evaporation rate of the droplet. However, this was not seen to be an issue during the measurements presented in this chapter. Surface tension measurements were important as addition of the polymeric binder into the bridging liquid may have altered the value. Using the same contact angle goniometer setup, as discussed for contact angle measurements, droplets of each viscous bridging liquid were analysed using the pendant drop method. The needle was positioned in the camera field of view, so that, as the bridging liquid was dispensed the droplet profile was able to be captured. Figure 6.3 shows an example of the droplet formed at the tip of the needle/capillary before detachment occurred.

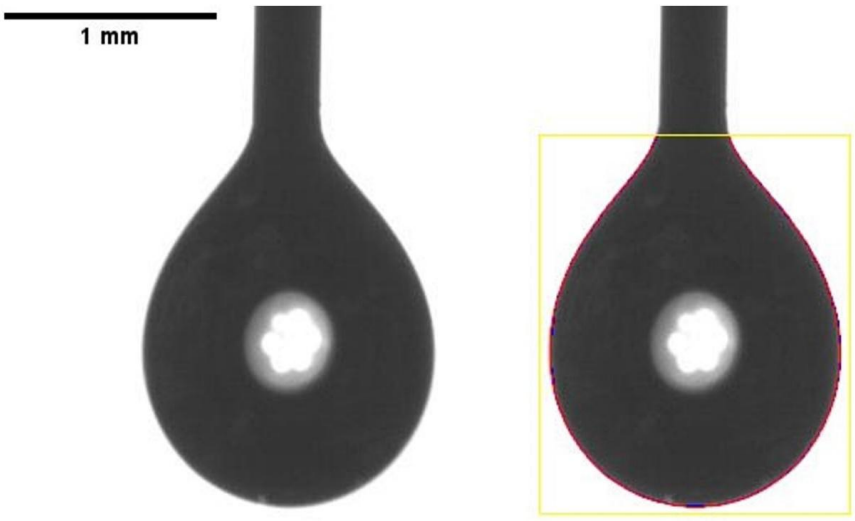

Figure 6.3: Droplet of chloroform solution with 1.0 wt% ethyl cellulose forming a pendant drop during surface tension analysis (left) and fitted curve using the Pendant drop plugin [125] which used density contrast times gravitational acceleration, Δρg, to fit the droplet curve (right)

The red curve, seen in Figure 6.3, was fit using a Pendant Drop plugin [125] in ImageJ (Fiji) based on fitting to the profile of the droplet. The method involved selection of the droplet profile (seen by the yellow box in Figure 6.3), then running the plugin. A dialog box opened where fitting parameters were selected. The density contrast between the droplet and surrounding air, multiplied by gravitational acceleration, Δρg, was input as a known constant against which the other fitting parameters were varied to find the curve of the droplet. Once the curve had been fit, the resulting surface tension was calculated based on Equation 6.2:

$$\gamma = \Delta\rho g l_c^2 \tag{6.2}$$

Where:

γ Surface Tension (mN/m)

$\Delta\rho$ Density Contrast (g/mm^3)

g Gravitational Acceleration (mm/s^2)

l_c Capillary Length (mm)

The process was repeated three times across a range of bridging liquid viscosities, based on increasing ethyl cellulose concentration between 0.5 wt% - 10 wt% with respect to the chloroform. To validate the reliability of the data, the Worthington Number (Wo) was calculated based on the surface tension, which was proposed in literature to define the accuracy of a surface tension measurement based on the ratio of the free pendant volume to the maximum pendant volume, V_d/V_{max} [126]. The Wo number, given by Equation 6.3, can be seen below:

$$\mathrm{Wo} = \frac{\Delta\rho g V_d}{\pi\gamma D_n} \tag{6.3}$$

Where:

γ Surface Tension (mN/m)

$\Delta\rho$ Density Contrast (g/mm^3)

g Gravitational Acceleration (mm/s^2)

V_d Droplet Volume (mm^3)

D_n Needle Diameter (mm)

Where the Wo ~ 1, the surface tension measurement through pendant drop analysis was found to be accurate, and where Wo $\ll$ 1, the surface tension measurement was inaccurate [126]. A video was taken at 60 frames per second, so that the surface tension measurement could be assessed over time, and Wo number used to indicate accuracy of the measurement which is dependent on the droplet profile. This allowed the most accurate measurement of surface tension to be taken based on Wo number.

These measurements for surface tension were then used to analyse the ΔW values, initially proposed in Section 4.3.2.1. Since the measurement of interfacial energy difference was a function of both contact angle and surface tension, the relevant data was captured so that the effect of bridging liquid viscosity was investigated.

6.2.3 Coagglomerate Characterisation

Coagglomerates generated were characterised based on size, porosity and tapped density. Additionally, to evaluate the internal structure of the coagglomerates for any hollow properties, X-Ray Computed Tomography (XRCT) scans were carried out by Dr Martin Corfield at the Sheffield Tomography Centre.

6.2.3.1 Optical & SEM Imaging

Coagglomerates generated were imaged using optical microscopy discussed in Section 3.4.1 for size analysis the light source was placed underneath the microscope slide. Whereas, for viewing the coagglomerate structure between experiments, a top-down lighting setup was used. Where hollow internal structures were observed, a needle was used to roughly cross section the coagglomerate to view the internal structure.

Analysis of the coagglomerates required a higher magnification than the optical microscope could resolve. Therefore, the SEM was used to analyse the coagglomerate structures in more detail. This allowed the surface structure to be assessed and observe the internal structure of the hollow shells. Stainless steel stubs were prepared with carbon tape to which coagglomerates were sprinkled over. The stub was tapped to remove any loose coagglomerates. This method prevented the deformation of the sensitive structures. When analysis of the internal structure was required, some of the coagglomerates were broken apart before attaching to the carbon tape. Due to the material being conductive, no sputter coating was required. Four sample stubs, prepared with coagglomerates, were placed in a holder. Images were taken at 55x and 230x magnification to observe both the surface and macro structure.

6.2.3.2 X-Ray Computed Tomography (XRCT)

Coagglomerate internal structure was important to analyse and observe, however without breaking the structure this was impossible through optical and SEM imaging. Therefore, XRCT was carried out using the Zeiss Xradia 620 Versa which has a minimum spatial resolution of 500 nm making it suitable for these measurements. The process involved using a manufactured sample holder made from PEEK polymer to hold the coagglomerates in place (manufactured in-house, University of Sheffield). PEEK polymer was used due to its low X-ray attenuation and thus low effect on the projections of coagglomerates, an AutoCAD Inventor 3D model of the part can be seen in Figure 6.4, where dimensions are given in millimetres (mm).

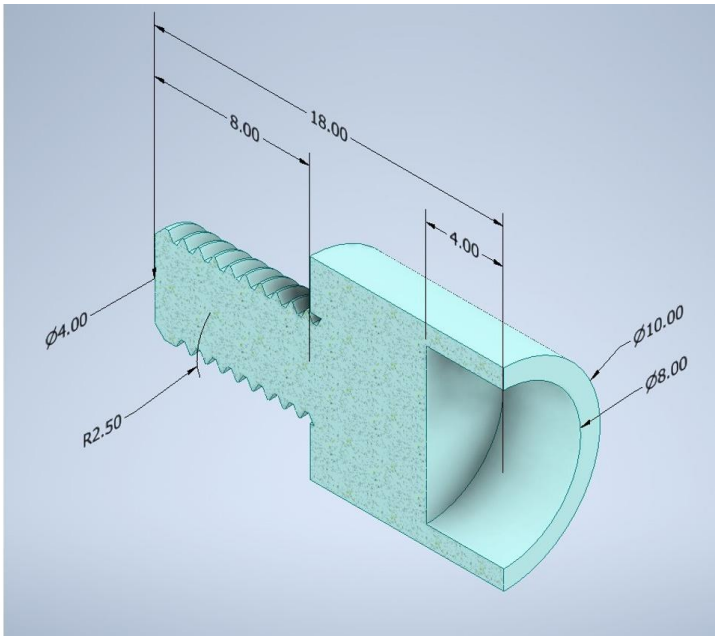

Figure 6.4: AutoCAD Inventor 3D model of XRCT sample holder manufactured out of PEEK polymer with all dimensions given in millimetres (mm)

Samples of coagglomerates from the 6 wt% and 10 wt% ethyl cellulose based coagglomerates were loaded into the sample holder, which was attached to an aluminium rod using the screw thread to position the sample in line with the beam for analysis. The measurement was run at 8 mm field of view which was chosen to maximise the number of coagglomerates included in the scan, whilst using a 4 μm resolution. Since the d_{50} of the S3 graphite primary particles used for the coagglomerates was 16.3 μm, the individual particles were not able to be resolved reliably. However, the coagglomerate properties were more important for this analysis – particularly wall thickness, envelope volume and void volume within the hollow coagglomerate. Figure 6.5 shows a reconstruction of the 3D scan with axes shown for reference and can clearly be seen that the volume was occupied by a reliable number of particles for analysis.

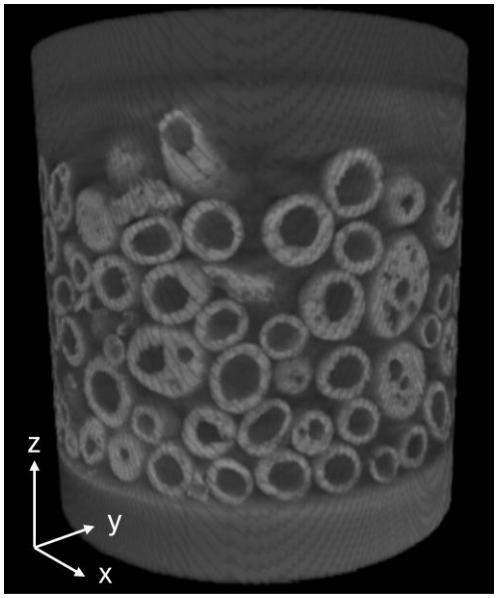

Figure 6.5: 3D reconstruction of the coagglomerates scanned for analysis using x-ray computer tomography, with axes shown

The projections from the XRCT scans were then processed in collaboration with the Nextrode Group at the University College London[6] to quantify average size properties of the coagglomerates. The scans were output as 2048 slices through the z-axis where each slice had a thickness equivalent to 3.92 μm. An example of this can be seen in Figure 6.6, where the lighter pixels were representative of the coagglomerates.

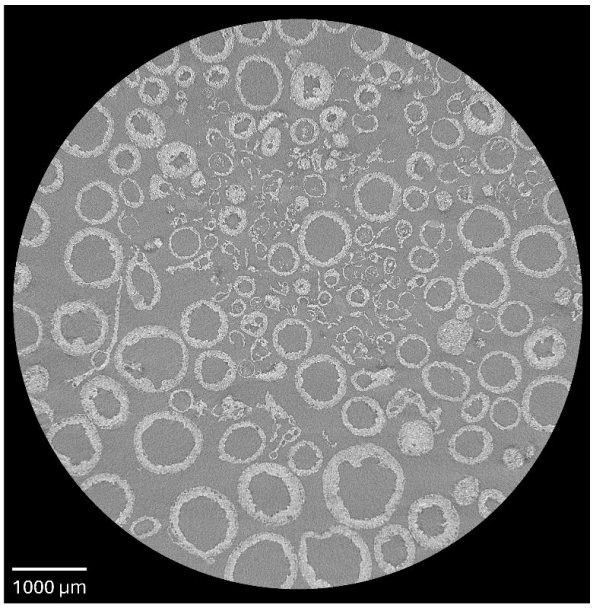

Figure 6.6: Example of a slice from the z-axis output from the XRCT scan for the 10 wt% ethyl cellulose coagglomerates

[6] XRCT post processing carried out by Will Dawson (Nextrode Group, University College London)

These were processed using imaging software called ilastik [127] which leveraged machine learning models to aid in segmentation of pixels. The software was used to differentiate the pixels that represent coagglomerates and those that are background signal. The software was trained over 6 slices per axis to allow for three-dimensional training. Which output a binary segmented image of the slices. An example of this process can be seen in Figure 6.7, where the original image (left) has been trained using a brush process (middle) and the output image with classified voxels based on the training algorithm (right).

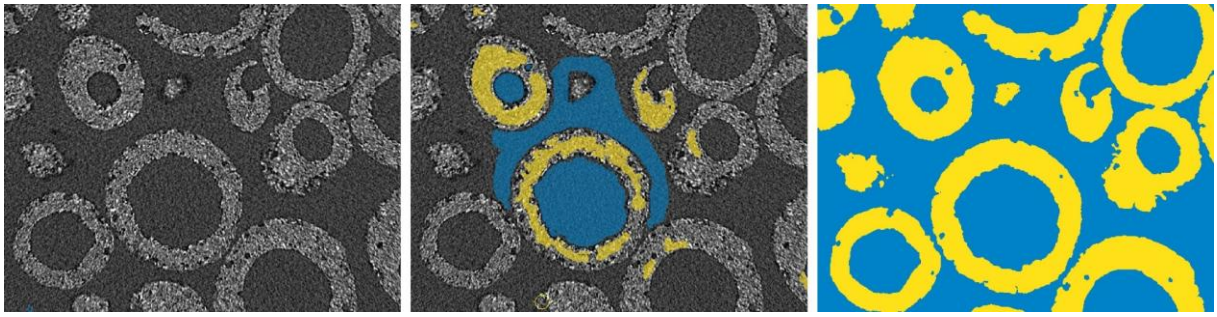

Figure 6.7: Original section of a XRCT z-slice (left), training method using brush to provide example data for segmentation (middle) and the output binary image with voxel classification completed (right)

Once the data had been classified based on which voxels were coagglomerate materials, the background was subtracted from the images such that the reconstruction was only occupied by coagglomerate data. Amiro – Aviso software was used to reconstruct the scan and isolate coagglomerates through 3D cropping, metrics for analysis coagglomerate size properties were quantified, with a focus on wall thickness, void volume and envelope volume.

6.3 Results and Discussion

6.3.1 Bridging Liquid Rheometry

Figure 6.8 shows the shear viscosity (Pa.s) of the viscous bridging liquids across a range of shear rates (s^{-1}) measured using a rheometer. The shear viscosity of the viscous bridging liquids can be seen as reaching an equilibrium for the 2 – 6 wt% ethyl cellulose solutions. The 0.5 wt% solution however does not show a clear trend of any sort with a decreasing shear viscosity as shear rate is increased up to a point. Then the shear viscosity increases again after approximately 100 s^{-1}. One reason for this could be due to chloroform evaporation during the rheometry process leading to a higher concentration chloroform in solution as time passed. The shear viscosity of the highest 10 wt% solution appears to decrease as shear rate is increased suggesting some non-Newtonian behaviour, particularly shear thinning as can be seen in Figure 6.8.

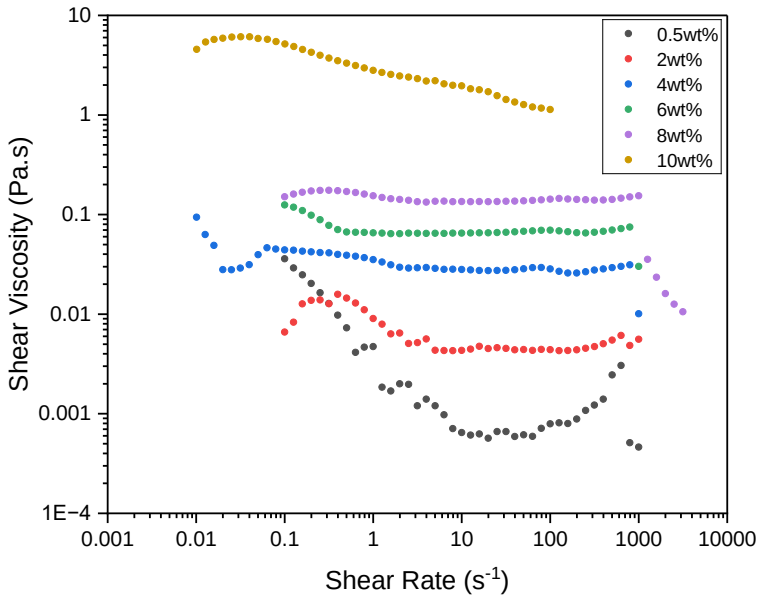

Figure 6.8: Shear viscosity (Pa.s) as a function of shear rate (s^{-1}) for chloroform solutions with increasing concentration of ethyl cellulose (wt/wt), shear viscosity is increasing as the polymer concentration increases in solution

The shear thinning behaviour seen at 10 wt% versus the lower concentration solutions is due to increased polymer entanglement which is overcome at the higher shear rates applied by the rheometer over time. As the shear increases, and the polymer entanglement decreases, then the measured shear viscosity will also decrease. If the shear rate was increased further, a steady state shear viscosity would eventually be achieved. However, this was not tested in this assessment. It would be beneficial in future work to measure the viscosity of the solutions at a constant shear rate to assess the steady state characteristics of the samples. However, due to time constraints working with Birmingham University equipment this was not possible. Importantly, comparing the shear viscosity of the different concentrations at a shear rate of 100 s^{-1}, increasing the concentration of ethyl cellulose in chloroform increased the shear viscosity, as shown in Figure 6.10.

The shear rates seen in the stirred tank were calculated based on empirical formulas and trends discussed in literature. Using Equation 6.4 and Figure 6.9 the power number (N_P) was estimated based on the stirred tank Reynolds number (N_{Re}) for a Rushton turbine using the geometry equivalent to curve 3 [128]. Then Equation 6.6 [129] was used to calculate the shear rate (γ) in the stirred tank based on the estimated power (P), from Equation 6.5.

$$N_{Re} = \frac{\rho N D^2}{\mu} \tag{6.4}$$

$$N_P = \frac{P}{\rho N^3 D^5} \tag{6.5}$$

$$\gamma = \sqrt{\frac{P}{\mu V}} \tag{6.6}$$

Where:

- ρ Density of the bulk fluid (kg/m^3)
- N Impeller speed (s^{-1})
- D Internal vessel diameter (m)
- μ Dynamic viscosity of the bulk fluid (kg/m.s)
- P Power exerted on the bulk fluid (kg.m^2/s^3)
- V Volume of the fluid in the vessel (m^3)
- γ Shear rate applied to the fluid (s^{-1})

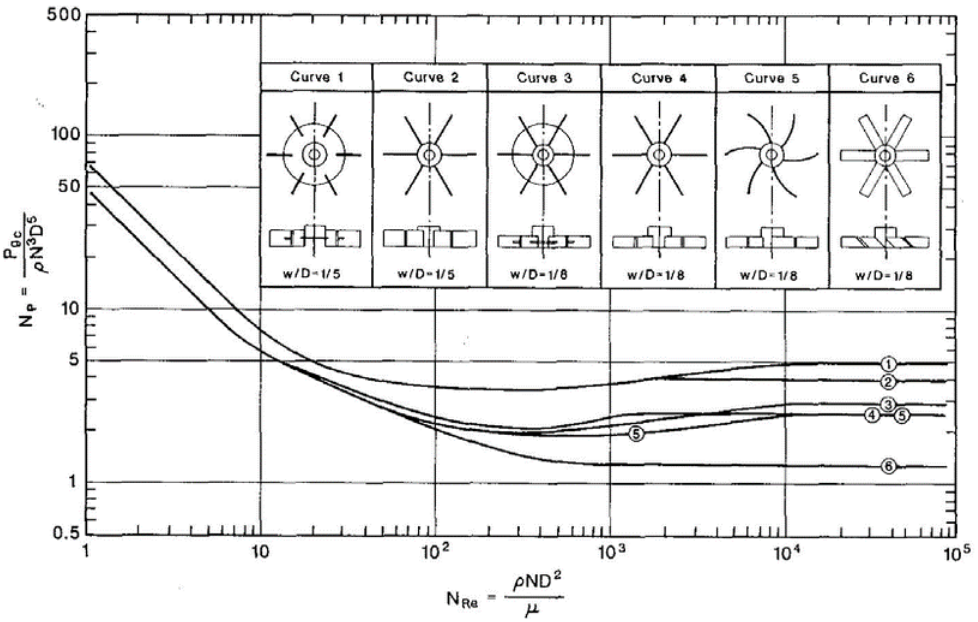

Figure 6.9: Relationship of Reynolds number vs power number for the shown Rushton Turbine geometries for Newtonian fluids [128]

This correlation estimates that, for a Reynolds number of 13500, the power number was approximately 3. Rearranging Equation 6.5 to find the power exerted on the fluid in the stirred tank, an approximation of the shear rate applied during spherical agglomeration was calculated using Equation 6.6 [129]. It was found that the stirred tank operates with a shear rate of approximately 1100 s^{-1}, which is beyond what was measured accurately during the rheometry experiments. Therefore, the viscosity of the viscous bridging liquids in the stirred tank cannot be directly determined. However, the trends are shown for increasing ethyl cellulose concentration in Figure 6.10 and how the high viscosity bridging liquids show shear thinning behaviour compared to the lower viscosity bridging liquids in Figure 6.8. Additionally,

it can be seen in Figure 6.10 that three distinct regimes may have been observed, indicated by the difference in gradient. These plots require further validation with extra experimental work done to reliably confirm. However, the plot appears to show that as polymer concentration is increased the solution moves from a dilute regime through a semi-dilute regime, and then on to the start of a concentrated regime. Initially the polymer is dilute and interacts primarily with the solvent, however as the concentration increases the regime moves into the semi-dilute regime where polymer-polymer interactions become significant. As polymer concentration increases further, the polymer-polymer interactions dominate, and the shear viscosity increases rapidly as entanglement between polymer chains increases [130].

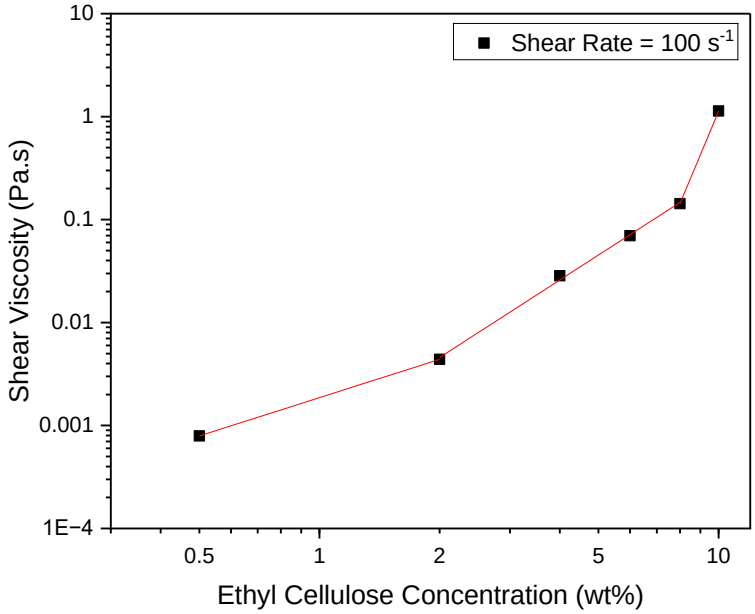

Figure 6.10: Trend of shear viscosity (Pa.s) vs ethyl cellulose concentration in chloroform (wt/wt) with accompanying lines indicating three different regimes of polymer entanglement as the concentration increases

Additionally, by fitting the power law model (shown in Equation 6.7) to the plotted data of shear stress (Pa) versus shear rate (s^{-1}) the Newtonian or non-Newtonian behaviour of the solutions can be captured. For the experimental rheology data captured the power law model has been fit to approximate the power law coefficients, as can be seen in Figure 6.11 and Table 6.2.

$$\tau = K\gamma^{n} \tag{6.7}$$

Where:

τ Shear stress (Pa)

K Power law constant to be fitted

γ Shear rate (s^{-1})

n Power law constant

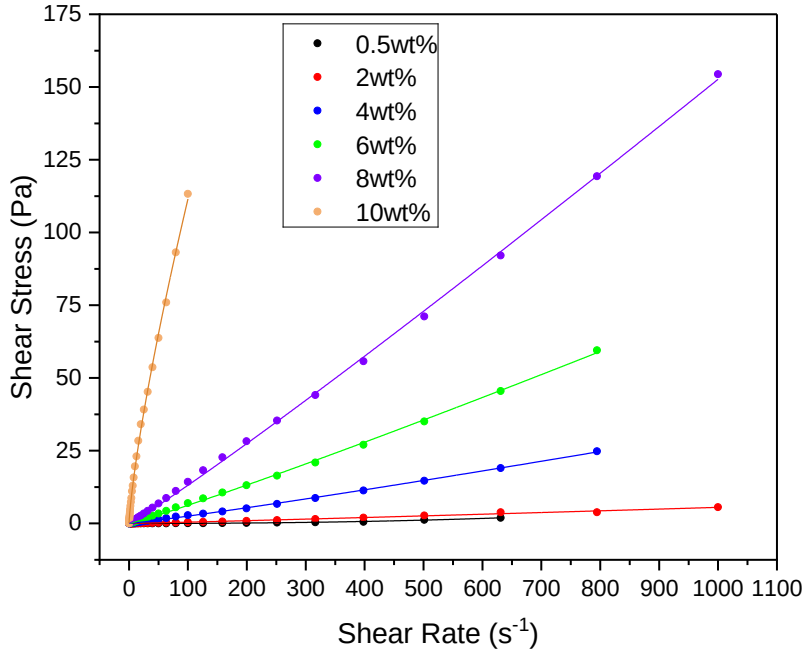

Figure 6.11: Shear stress versus shear rate plotted from the rheological experimental data. Power law curves have been fit to the data to identify rheological behaviour as ethyl cellulose concentration increases

Table 6.2: Power law coefficients from the fitted experimental data and the accuracy of the line of fit, which indicates the apparent rheological behaviour based on the n - coefficient

Ethyl Cellulose Concentration (wt%)	K	n	Adj. R-square	Apparent Rheological Behaviour
0.5	9.8E-7	2.25	0.992	Shear thickening
2.0	0.003	1.09	0.991	Newtonian
4.0	0.016	1.10	0.999	Newtonian
6.0	0.043	1.08	0.999	Newtonian
8.0	0.097	1.06	1.000	Newtonian
10.0	3.153	0.774	0.999	Shear thinning

Where $n > 1$ the fluid is shear thickening and the shear stress increases with shear rate exponentially, just as can be seen with 0.5 wt% ethyl cellulose concentration. This is assumed to be due to the small concentration of polymer forming clusters as the shear rate increases, but remaining relatively dispersed when shear rate is low, thus leading to shear thickening although the viscosity remains low compared to the other solutions. As the polymer concentration is increased the polymer-polymer interactions increase and the intrinsic entanglement before applying shear is higher. At the highest polymer concentration of 10 wt% ethyl cellulose, this then leads to shear thinning behaviour where $0 < n < 1$ for the fitted power law model. The regions in between as polymer concentration increases show the

transition from shear thickening to shear thinning behaviour, although the relative viscosity clearly increases.

6.3.2 Contact Angle & Wettability

The assessment of contact angle based on the viscous bridging liquids was carried out and showed some deviation from the pure chloroform solvent wettability assessment, with respect to the S3 graphite active material. As bridging liquid viscosity increased so did the initial contact angle. Compared to the pure chloroform contact angle tests carried out for previous chapters, which showed rapid immersion of the solvent into the powder bed capillaries, as the viscosity increased, it was observed that the droplet immersion and spreading reduced. Figure 6.12 represents three repeats taken across different points on the particle bed surface, with standard deviation. The standard deviation for the lower viscosity samples is large and thus it is hard to draw reliable conclusions between 0 – 1 wt% solutions. Ultimately, it was found that, increasing the ethyl cellulose concentration increases the initial contact angle of the solution on S3 graphite.

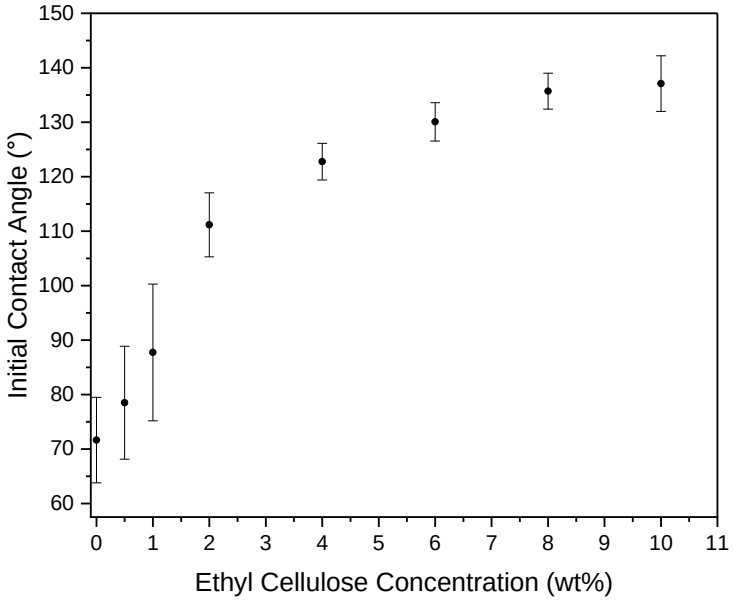

Figure 6.12: Effect of increased ethyl cellulose concentration in chloroform solution on the initial contact angle for an S3 graphite powder surface

The proposed thermodynamic value of ΔW presented in Chapter 4 for analysing the feasibility for a coagglomeration system to be successful is important to analyse as the bridging liquid has increased in viscosity. For this analysis, the surface tension of viscous bridging liquids was also required.

For surface tension analysis using ImageJ (Fiji) the density contrast multiplied by gravitational acceleration ($\Delta\rho g$) was calculated for each viscosity of bridging liquid, which can be seen in Table 6.3. Three free hanging droplets were assessed for surface tension using the pendent drop plugin [125] and accuracy of the results was checked using the Wo number. For each frame taken during the pendant drop process, the droplet with the Wo number closest to 1 was used as the optimal droplet shape from

which the surface tension was calculated. The values for surface tension and respective Wo number can be seen in Table 6.3, alongside the density contrast values.

Table 6.3: Surface tension measurements taken using Pendent drop plugin on ImageJ (Fiji) software and the respective Worthington Number used to assess accuracy of the surface tension measurement, mean value and standard deviation given based on three repeats

EC Conc. (wt/wt%)	$\Delta\rho g$ (g/mm^{2}s^2)	Surface Tension (mN/m)	Worthing Number
0.5	13.20	24.56 ± 0.14	0.835
1.0	13.02	22.96 ± 0.02	0.850
2.0	12.91	23.41 ± 0.19	0.833
4.0	13.04	25.93 ± 0.68	0.984
6.0	12.74	25.34 ± 0.39	0.996
8.0	12.64	25.93 ± 1.88	0.992
10.0	12.54	27.11 ± 0.15	0.980

Table 6.4 shows the average contact angle and surface tension measurements as bridging liquid viscosity increased. The continuous phase (DI water) has an average contact angle and surface tension of 145.5° and 72.8 mN/m, respectively. Equation 4.10, from Chapter 4, was then used to calculate the work of particle transfer (ΔW), also given in Table 6.4. The ΔW values increase as ethyl cellulose concentration increases in the chloroform. However, the value of work remains negative suggesting that the coagglomeration will be successful, and transfer of particles from the bulk continuous phase to the bridging liquid will be feasible with this solvent setup.

Table 6.4: Contact angle and surface tension data for increasing viscosity of bridging liquid and the effect on thermodynamic work of particle transfer from the continuous phase (water), standard deviation error based on three repeats

EC Conc. (wt/wt%)	Contact Angle (°)	Surface Tension (mN/m)	ΔW (mJ/m^2)
0.5	78.5 ± 10.4	24.56 ± 0.14	-65.1
1.0	87.7 ± 12.6	22.96 ± 0.02	-60.9
2.0	111.2 ± 5.9	23.41 ± 0.19	-51.5
4.0	122.8 ± 3.4	25.93 ± 0.68	-46.0
6.0	130.1 ± 3.5	25.34 ± 0.39	-43.7
8.0	135.7 ± 3.3	25.93 ± 1.88	-41.4
10.0	137.1 ± 5.1	27.11 ± 0.15	-40.1

6.3.3 Droplet Sizing

Since it was seen during the rheology experiments that the effect of shear on the viscous bridging liquids was different based on the viscosity/ethyl cellulose concentration, the droplet size distribution was investigated for the various solutions. Initially the effect of time on the droplet diameter distribution

was investigated using the 0.5 wt% chloroform solutions, as seen in Chapter 5. It was found that as the suspension of droplets were agitated for 20 minutes, with samples taken at 5-minute intervals, the droplet size distribution decreases slightly.

The variation is minimal but suggests that the droplets are relatively stable across the time which coagglomeration experiments are run for, and the droplet distribution reaches steady state quickly. Some reduction could be due to loss of chloroform due to the open system and thus air entrainment in the suspension.

Further analysis of the droplet size distribution looked at the effect of viscosity of the chloroform bridging liquid solutions. In this case, samples were taken for the different viscosities at time, t = 10 minutes to investigate the effect of viscosity, and example images at each viscosity can be seen in Figure 6.13.

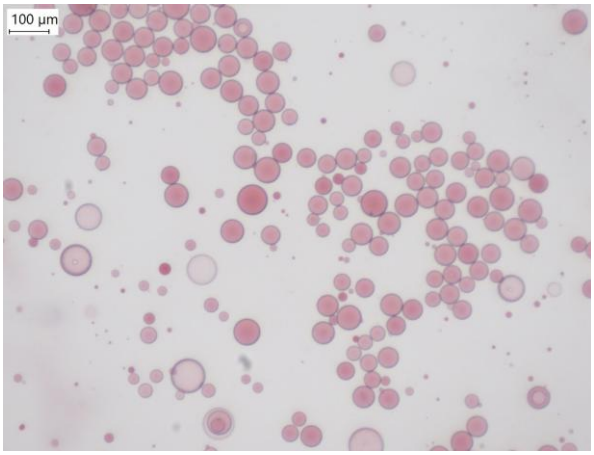

A) 0.5 wt% ethyl cellulose in chloroform

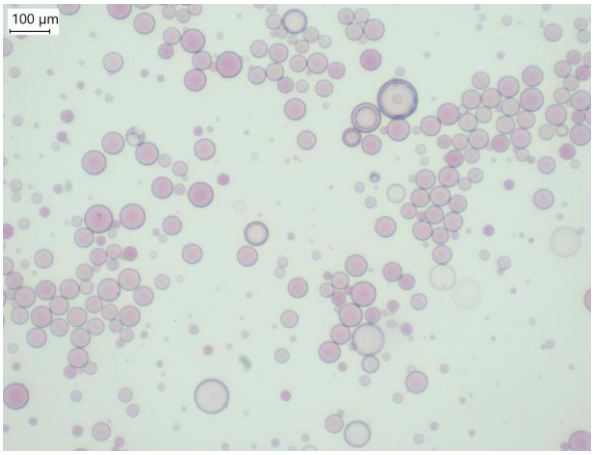

B) 1.0 wt% ethyl cellulose in chloroform

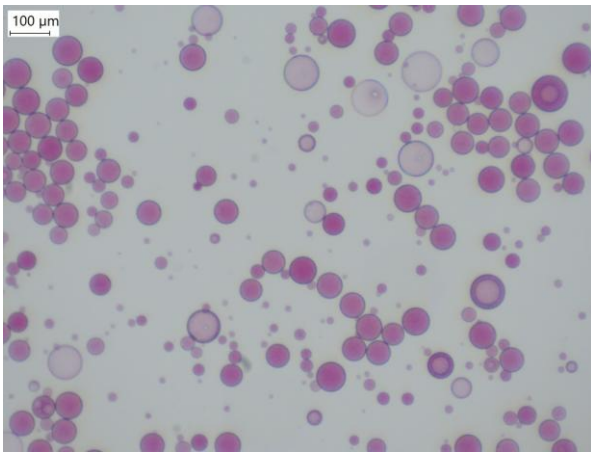

C) 2.0 wt% ethyl cellulose in chloroform

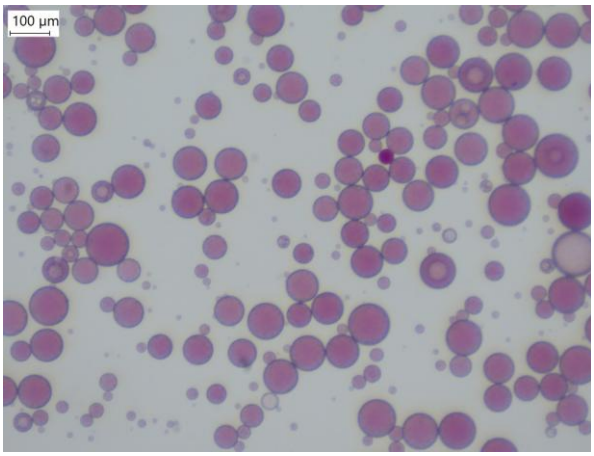

D) 4.0 wt% ethyl cellulose in chloroform

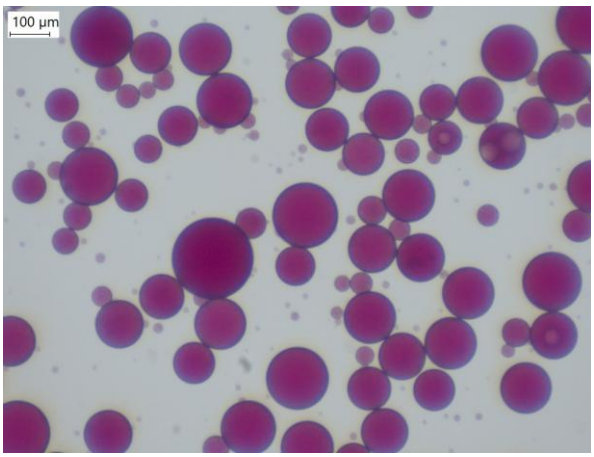

E) 6.0 wt% ethyl cellulose in chloroform

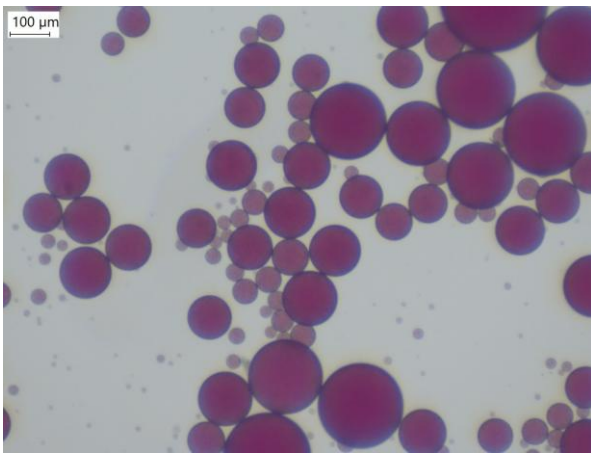

F) 8.0 wt% ethyl cellulose in chloroform

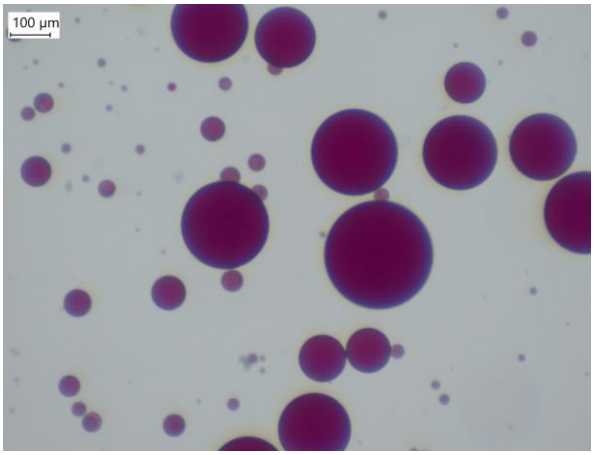

G) 10.0 wt% ethyl cellulose in chloroform

Figure 6.13: Example of droplet images taken at 72x magnification and time t=10 mins during agitation in a stirred tank as chloroform ethyl cellulose concentration increases

It can be seen in Figure 6.14 (A – G) that as the viscosity is increased (higher ethyl cellulose concentration) the droplet size distribution exhibits a larger average droplet size. The droplet size distribution shows relatively monodisperse peaks for the low viscosity suspensions (Figure 6.14 A – D), however, as viscosity increases (Figure 6.14 E – G) the distribution becomes more polydisperse. This follows that shown in literature, which also states droplet size distribution span increases as viscosity is increased [131]. This can be seen in Figure 6.14 (E – G) where the droplet size distribution spans a wider range, suggesting the distribution has not reached a drop-size equilibrium at 10 minutes. This was due to more dramatic dynamic effects of viscous droplets during the 'necking' process, in which a droplet will break into two or more daughter droplets. The elastic properties of higher viscosity droplets allow this process to take longer and/or require more energy to reach this critical splitting point. The volume moment mean diameter ($d_{4,3}$) was calculated, as seen in Table 6.5, from the droplet diameters measured during the droplet size distribution. Primary particles immerse into the droplet to form nuclei and eventually grow, through layering and coalescence, to form dense coagglomerates. Therefore, the $d_{4,3}$ value was measured and used in Section 7.3 for comparing to the coagglomerate size distribution and provide insight to the magnitude of growth that occurs, from droplet to agglomerate.

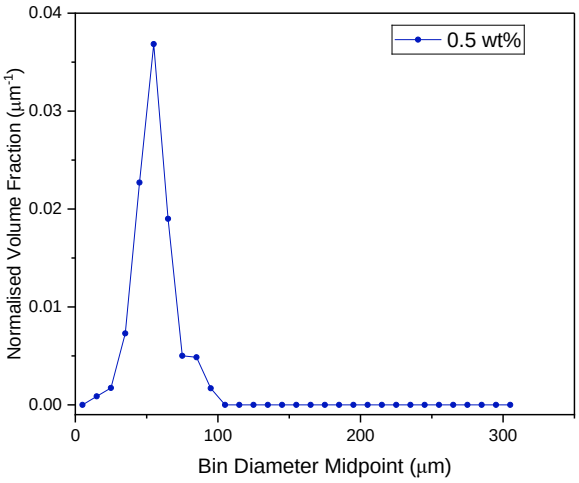

A) 0.5 wt% ethyl cellulose in chloroform

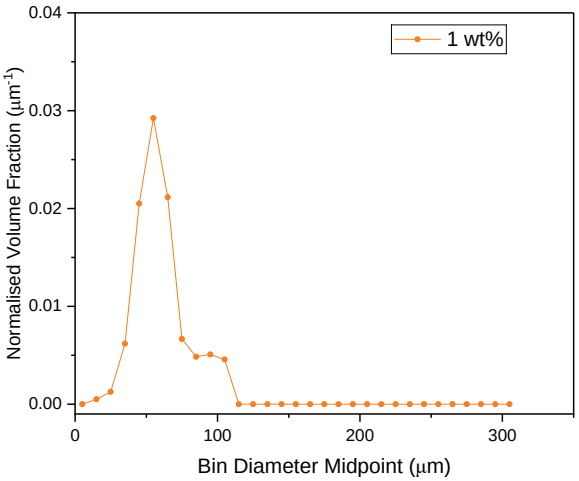

B) 1.0 wt% ethyl cellulose in chloroform

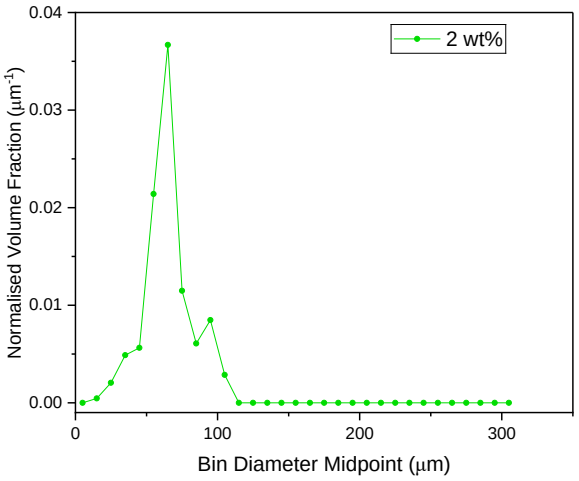

C) 2.0 wt% ethyl cellulose in chloroform

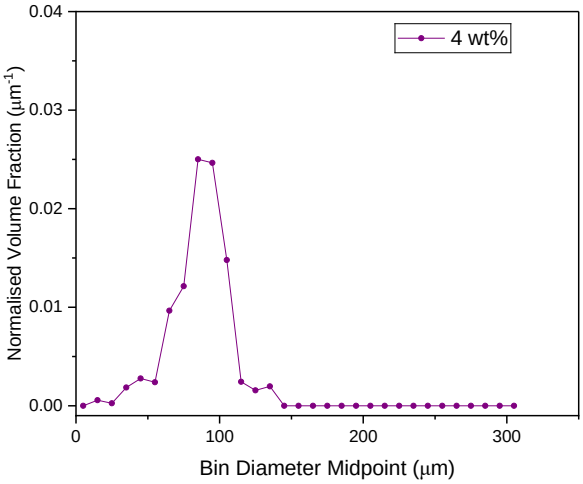

D) 4.0 wt% ethyl cellulose in chloroform

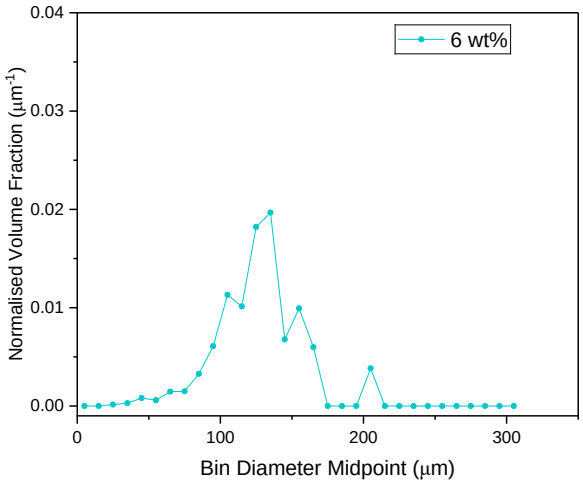

E) 6.0 wt% ethyl cellulose in chloroform

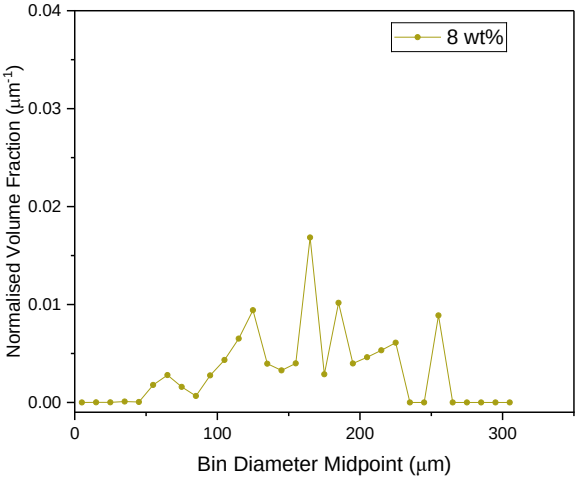

F) 8.0 wt% ethyl cellulose in chloroform

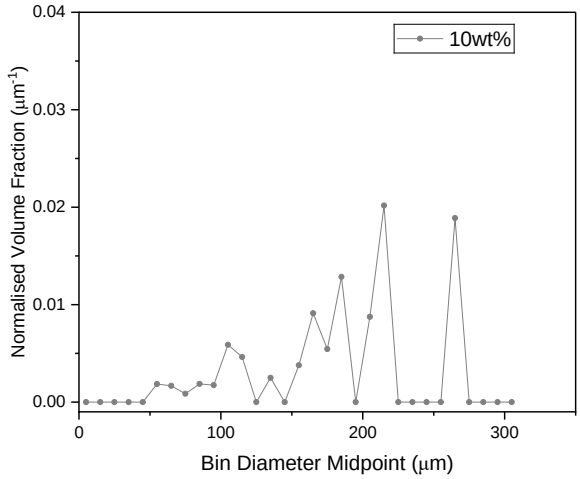

G) 10.0 wt% ethyl cellulose in chloroform

Figure 6.14: Volume based droplet size distribution of the chloroform solution droplets with increasing ethyl cellulose concentration taken at t = 10 minutes

Table 6.5: Measured $d_{4,3}$ values for the droplet size distributions at different viscosity bridging liquid droplets in suspension, for samples measured after 10 minutes in a stirred vessel

Ethyl Cellulose Concentration (wt/wt%)	$d_{4,3}$ (μm) (t = 10 minutes)
0.5	55.39
1.0	59.62
2.0	65.40
4.0	86.22
6.0	127.05
8.0	163.85
10.0	186.81

6.3.4 Coagglomerate Generation

Coagglomerates were generated and imaged using optical microscopy and SEM to investigate the effect of bridging liquid viscosity. The coagglomerates were all carried out using the same run conditions and at a TBSR of 2.

Coagglomerates were generated in triplicate for each bridging liquid viscosity denoted by its respective ethyl cellulose concentration for ease of labelling. At lower viscosities (Figure 6.15 A – B) smooth well defined coagglomerates are formed. However, as the viscosity increases there appears to be more coalescence occurring seen by the larger coagglomerates which look like several spheres compressed together, particularly in Figure 6.15 D. This is due to the increased concentration of ethyl cellulose at the surface leading to adhesion between coagglomerates and further densification under agitation of

these compounded structures. As the viscosity of bridging liquid increases further, some pores are observed in the structures. Although difficult to distinguish against the grey material, this effect can be seen in Figure 6.15 E where there are black dots on the surface of the coagglomerates which are not seen in the lower viscosity coagglomerates. This is due to trapped droplets of chloroform escaping during the drying process by evaporating through the solid layer formed during densification of the coagglomerates. This process leaves a vapour escape hole from which the chloroform evaporated. This suggests that the dried structure therefore has some existence of pores inside the structure. For the 6 wt% coagglomerates generated, a clearer image of the evaporation holes can be seen in Figure 6.16.

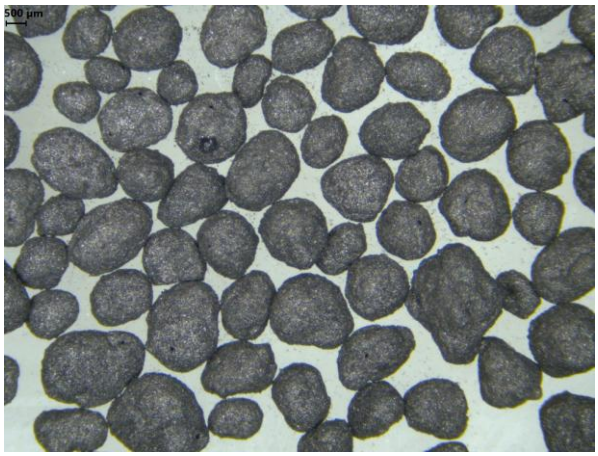

A) Ethyl Cellulose Conc. = 0.5 wt%

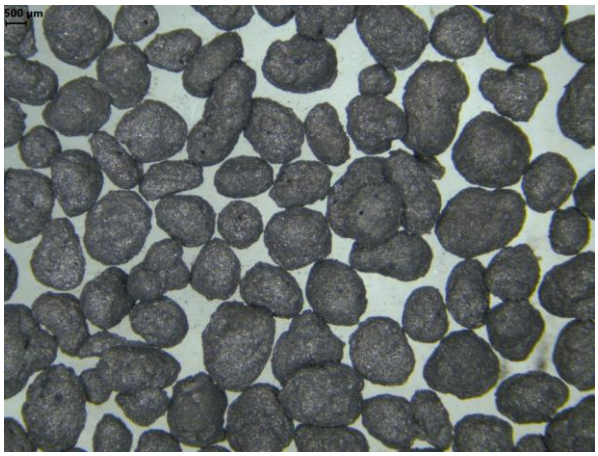

B) Ethyl Cellulose Conc. = 1.0 wt%

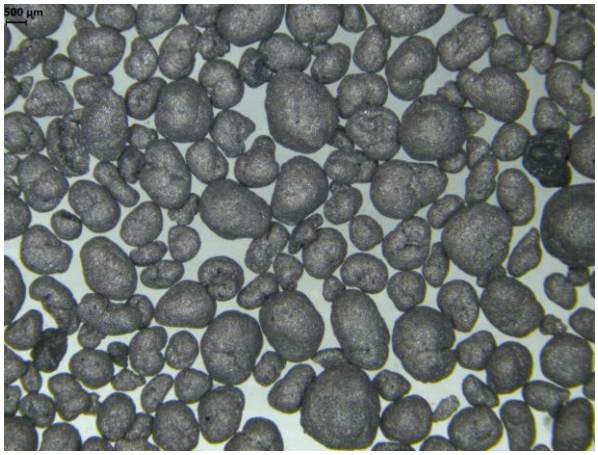

C) Ethyl Cellulose Conc. = 2.0 wt%

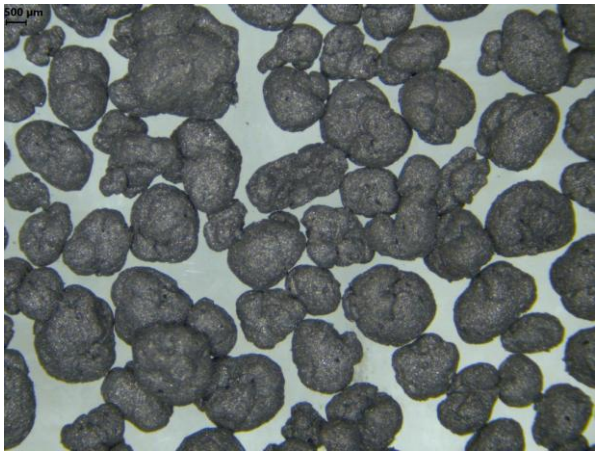

D) Ethyl Cellulose Conc. = 4.0 wt%

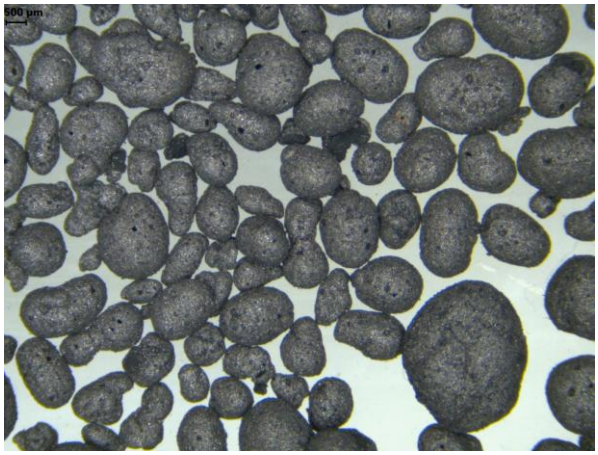

E) Ethyl Cellulose Conc. = 6.0 wt%

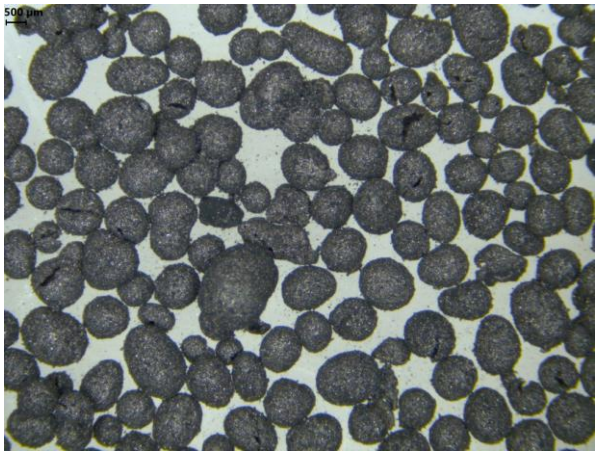

F) Ethyl Cellulose Conc. = 8.0 wt%

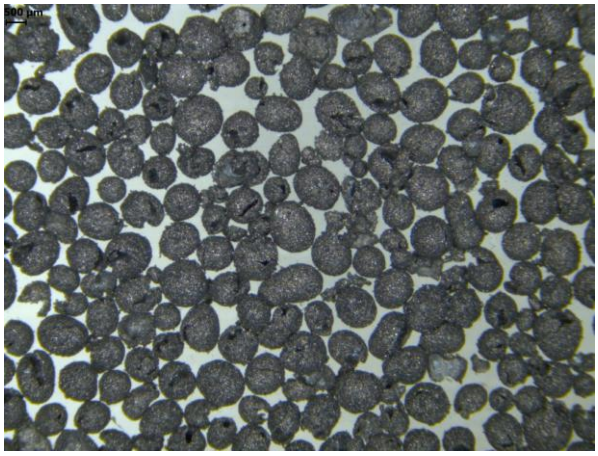

G) Ethyl Cellulose Conc. = 10.0 wt%

Figure 6.15: Optical microscope images of coagglomerate generated at increasing ethyl cellulose concentration in chloroform bridging liquids (A – G)

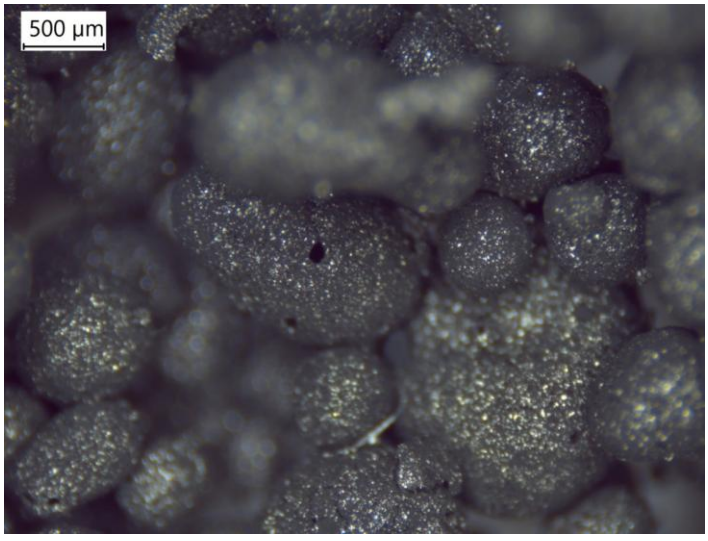

Figure 6.16: Higher magnification image of 6 wt% ethyl cellulose concentration bridging liquid coagglomerate, with evidence of internal pore structure due to observed chloroform evaporation escape hole

Due to this a cross section was crudely created to observe the internal structure of the coagglomerate under optical microscope, seen in Figure 6.17, which shows a hollow structure and clear shell wall generated at this viscosity of bridging liquid. Increasing the bridging liquid viscosity further to 8 – 10 wt% ethyl cellulose concentration, it can be seen in Figure 6.15 F – G there appears to be more primary material on the coagglomerate surfaces, appearing ‘fluffy’ in texture compared to the lower viscosity coagglomerates. The reason is due to the hollow structures generated which can be seen in the cross section, Figure 6.18.

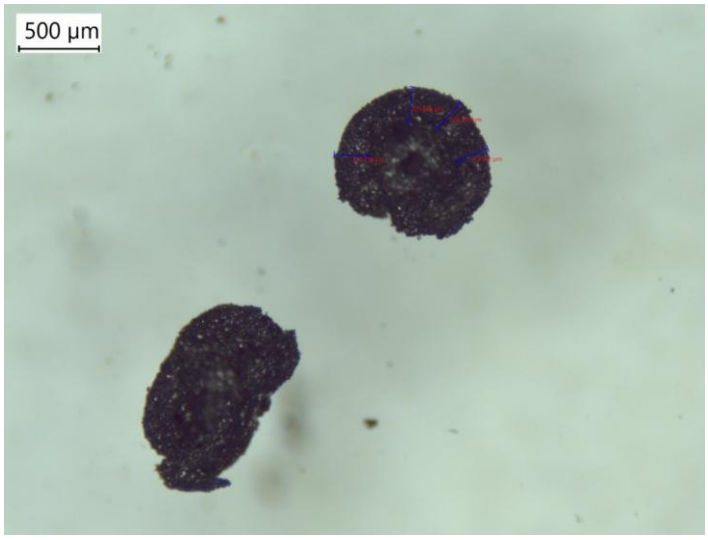

Figure 6.17: Cross section of a 6 wt% ethyl cellulose concentration coagglomerate

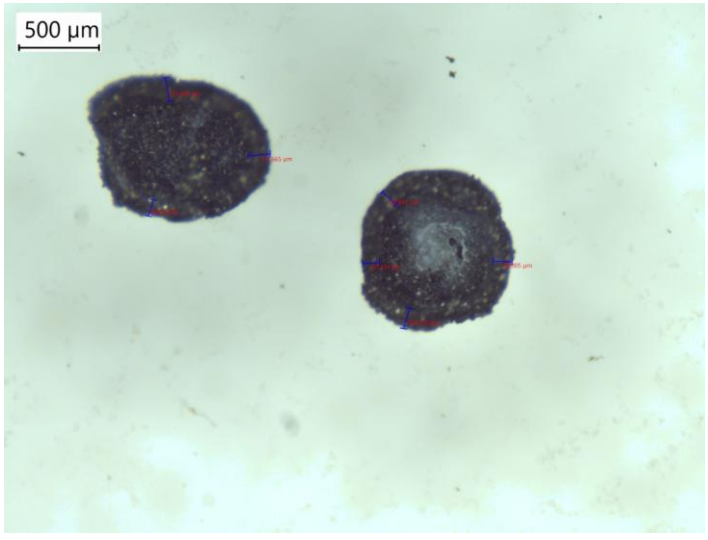

Figure 6.18: Cross section of a 10 wt% ethyl cellulose concentration coagglomerate

The immersion rate of the primary particles into the viscous droplet is limited and therefore the effective working volume of coagglomeration is lower due to the volume of chloroform in the hollow void not interacting with the primary particles. Therefore, if the working volume of chloroform is lower, then

the working TBSR is lower. It was seen in Section 4.3.1 that when TBSR<$TBSR_{opt}$ there is a higher amount of primary material unagglomerated and in the final product. Therefore, as viscosity is increased the effective TBSR must be increased to account for the unused fraction inside the shell wall. Additionally, in Figure 6.15 F – G the same chloroform evaporation escape holes can be seen, however, with the thinner shell wall fracturing during this process.

The extent of analysis using optical microscopy is limited to a qualitative one and further investigation was carried out using SEM. The SEM was used to investigate the hollow structure in more detail and observe the surface properties.

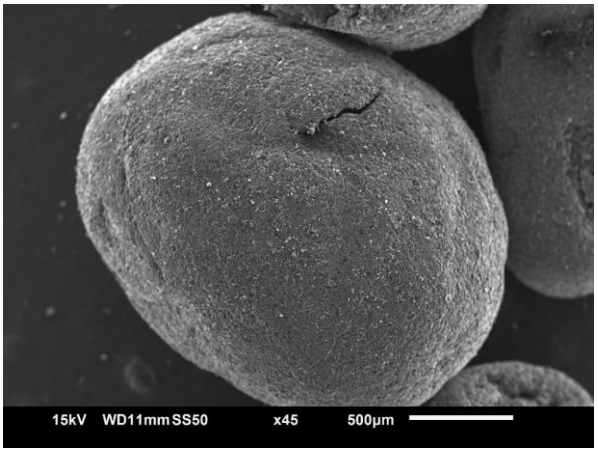

A) Ethyl Cellulose Conc. = 0.5 wt%

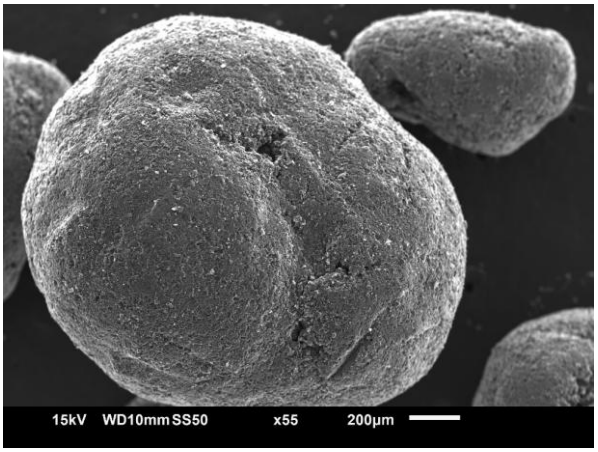

B) Ethyl Cellulose Conc. = 1.0 wt%

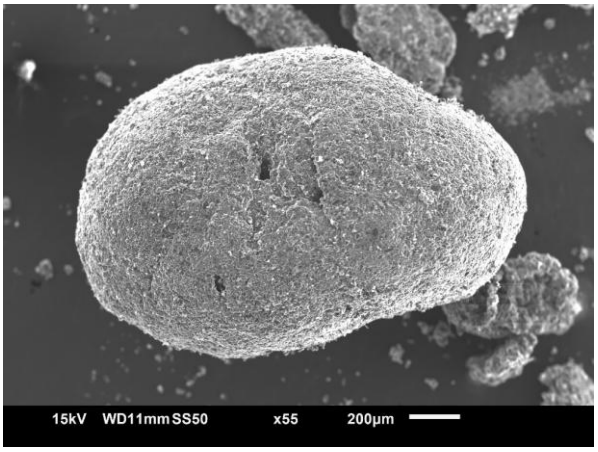

C) Ethyl Cellulose Conc. = 2.0 wt%

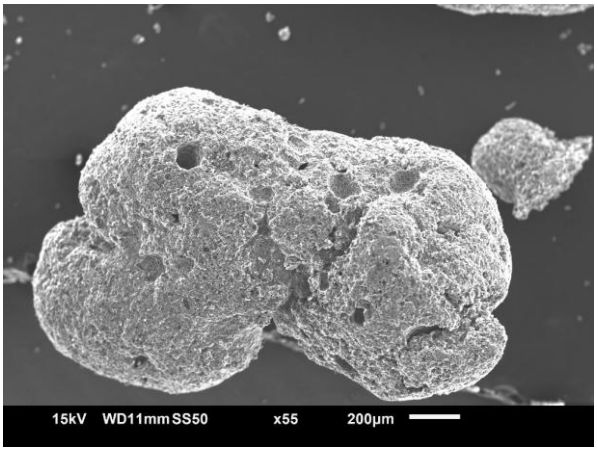

D) Ethyl Cellulose Conc. = 4.0 wt%

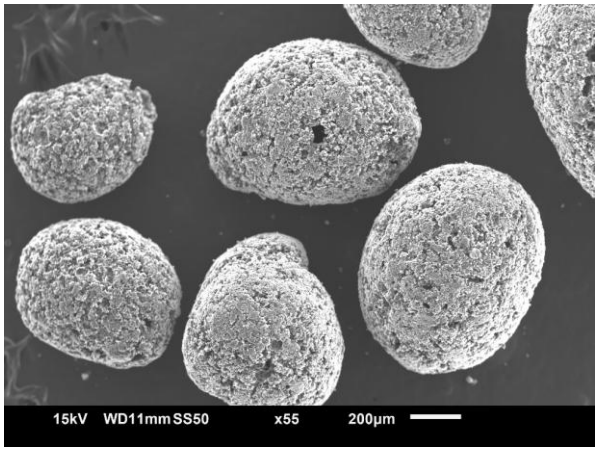

E) Ethyl Cellulose Conc. = 6.0 wt%

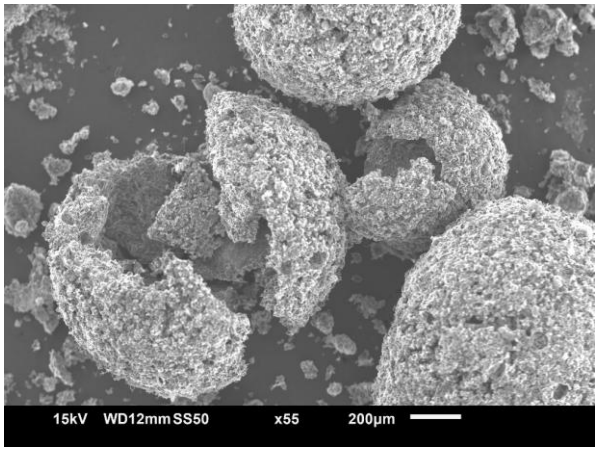

F) Ethyl Cellulose Conc. = 8.0 wt%

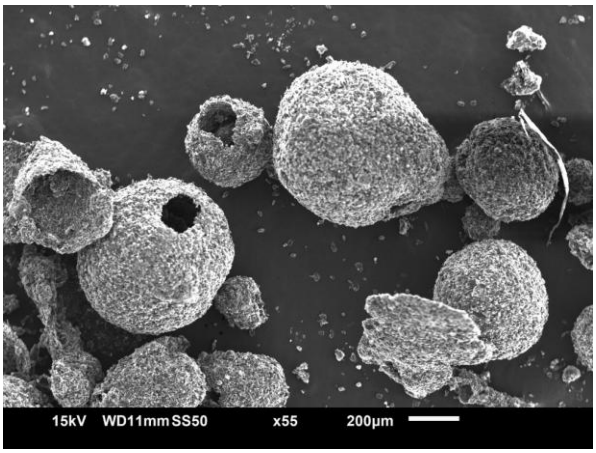

G) Ethyl Cellulose Conc. = 10.0 wt%

Figure 6.19: SEM images of coagglomerate generated at increasing ethyl cellulose concentration in chloroform bridging liquids (A – G)

The collection of SEM images seen in Figure 6.19 were all taken at the same magnification (except for image A). It can clearly be seen that there is a size reduction as the bridging liquid viscosity increases. The droplet size distribution discussed in Section 6.3.3 showed that the bridging liquid droplets average size increased as viscosity increased. One reason for the coagglomerate size not also increasing with viscosity, could be due to the immersion of the particle within the droplet.

For the low viscosity bridging liquids, the mechanism of coagglomeration occurs as expected based on literature where the primary particles immerse into the droplet and the excess bridging liquid is 'squeezed' to the surface of the coagglomerates where further primary particles adhere, and growth occurs. Additionally, where the surface of the coagglomerate has bridging liquid present coalescence can occur and a larger coagglomerate is formed.

For higher viscosity bridging liquids, since the rate of immersion is so slow, there is essentially an excess of primary particles and the working bridging liquid volume is lower, as discussed previously. Therefore, there is no excess bridging liquid and growth through layering and coalescence are both limited.

The coagglomerates seen in Figure 6.19 D at an ethyl cellulose concentration of 4 wt% appear porous in structure which suggests that the immersion was limited, but not to an extent of generating stable hollow structures. However, it could be that some small volume hollow voids are present but with coalescence still able to occur leading to porous structures, rather than well-defined hollow spheres.

Observation of the 6 wt% and 10 wt% coagglomerates, seen in Figure 6.20 and Figure 6.21, shows that the structures are primarily formed from the S3 graphite active material, with the C65 carbon black also deposited on the surface. It is assumed that the C65 is dispersed throughout the coagglomerate internal structure too, but this cannot be resolved easily using SEM. Although the hollow structure is more evident using the SEM imaging, analysis of the wall thickness and void volume is not able to be captured.

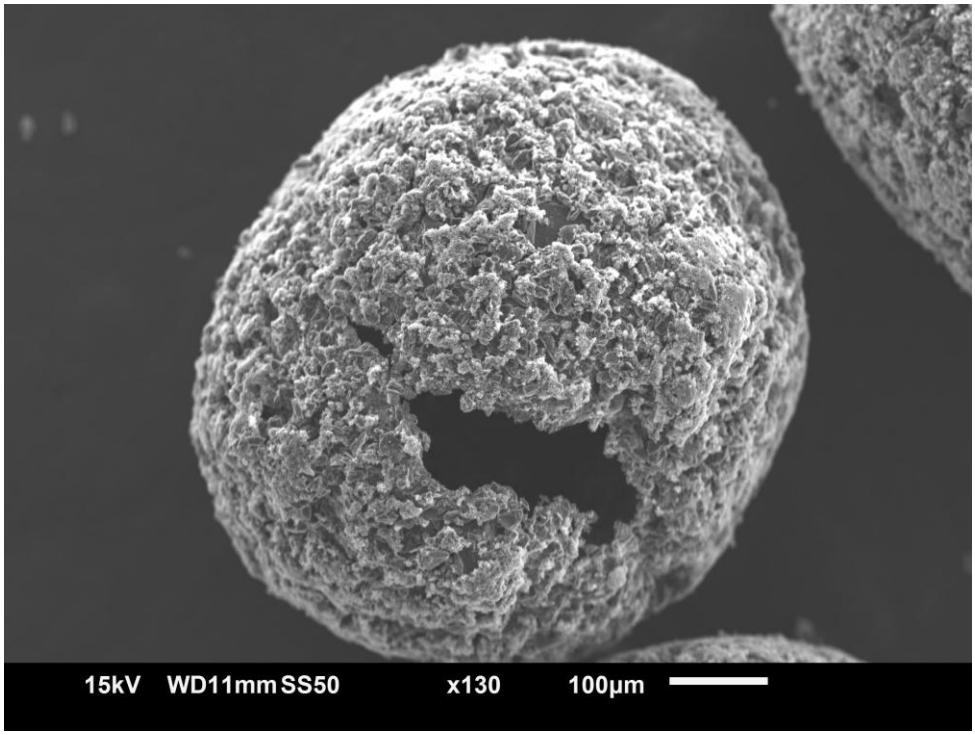

Figure 6.20: SEM image of 6 wt% ethyl cellulose concentration coagglomerate

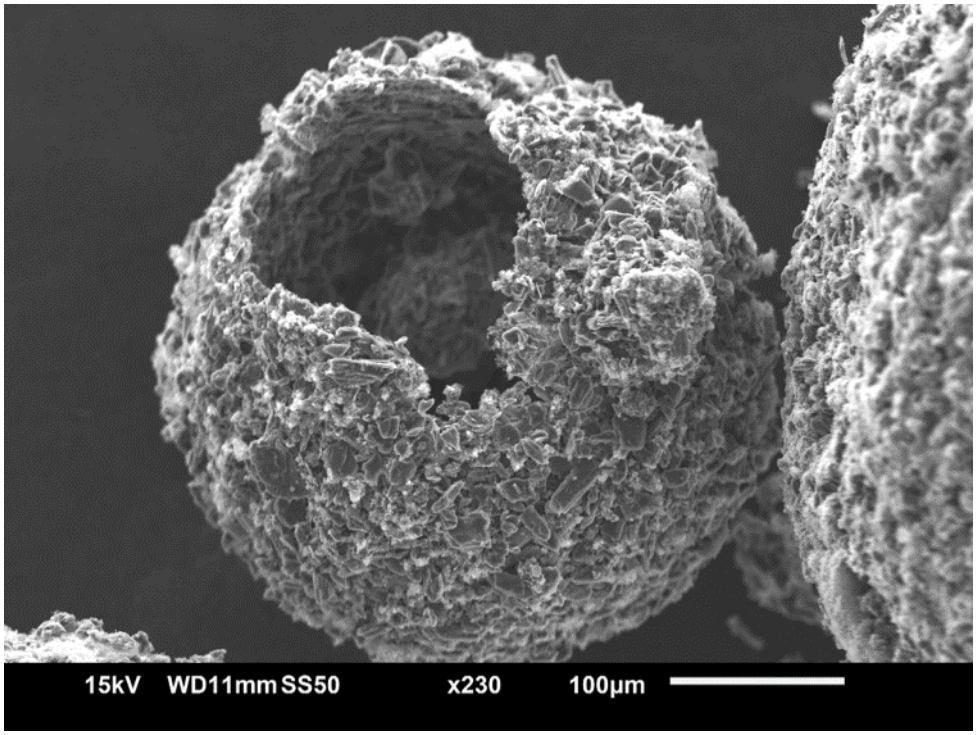

Figure 6.21: SEM image of 10 wt% ethyl cellulose concentration coagglomerate

The surface of the coagglomerates seen in Figure 6.20 and Figure 6.21 appear rough compared to the lower viscosity generated coagglomerates, which relates back to the discussion earlier about an excess of primary particles due to low TBSR being deposited on the surface.

6.3.5 Coagglomerate Size Distribution

The batches of coagglomerates formed were sized, including the repeat experiments, to understand further about the size distribution of the product formed at different bridging liquid viscosity. The three repeats were analysed together in a total volume based coagglomerate size distribution for each ethyl cellulose concentration, these PSD's can be seen in Figure 6.22 (A - H).

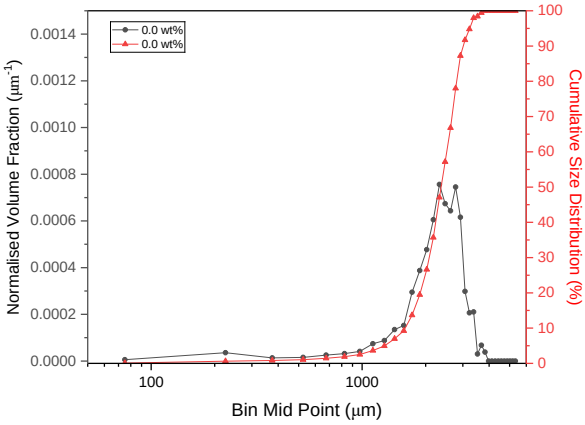

A) Ethyl Cellulose Conc. = 0.0 wt%

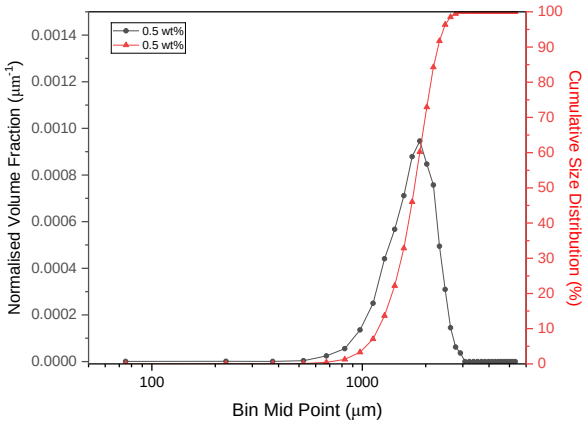

B) Ethyl Cellulose Conc. = 0.5 wt%

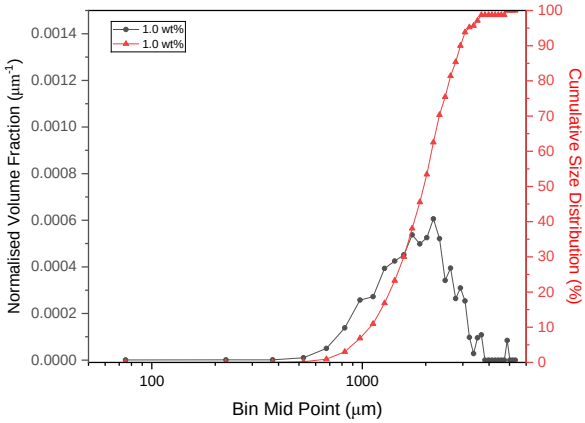

C) Ethyl Cellulose Conc. = 1.0 wt%

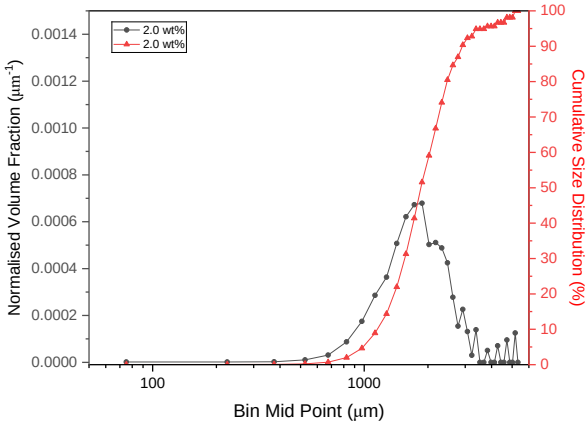

D) Ethyl Cellulose Conc. = 2.0 wt%

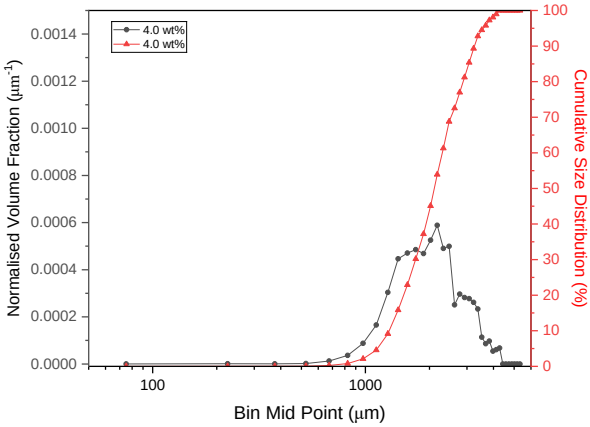

E) Ethyl Cellulose Conc. = 4.0 wt%

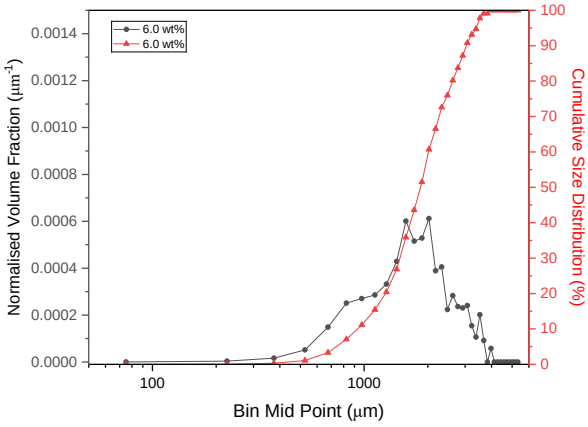

F) Ethyl Cellulose Conc. = 6.0 wt%

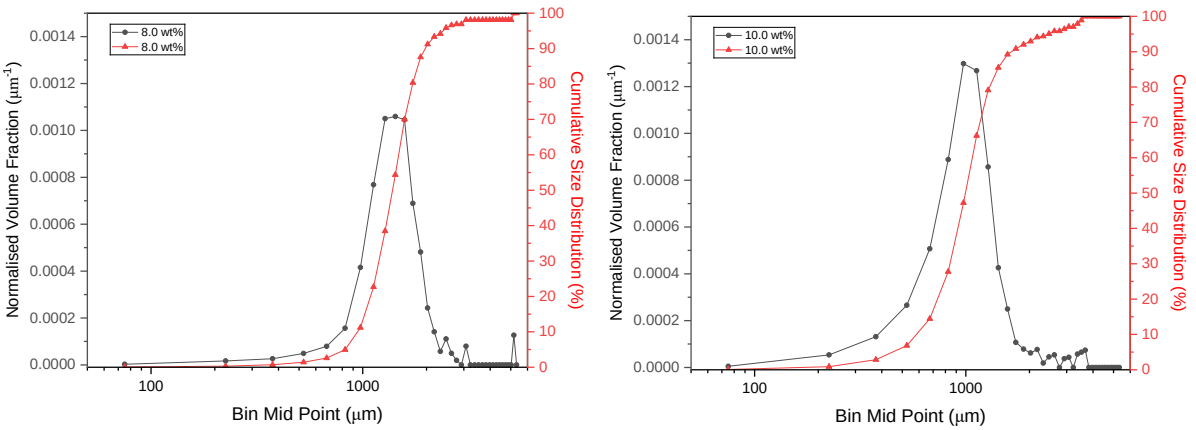

G) Ethyl Cellulose Conc. = 8.0 wt%

H) Ethyl Cellulose Conc. = 10.0 wt%

Figure 6.22: Coagglomerate size distribution as viscosity of bridging liquid is increased

At the lowest viscosity at 0 wt% ethyl cellulose concentration, the volume moment mean ($d_{4,3}$) can be seen to be high compared to the other coagglomerates, given in Table 6.6. As the ethyl cellulose concentration is increased to 0.5 wt% the $d_{4,3}$ decreases. This may be due to the slight emulsifier properties that ethyl cellulose possesses and thus reducing the effects of coalescence in the system.

Table 6.6: Summary of size distribution data for the coagglomerates formed for increasing bridging liquid viscosity

Ethyl Cellulose Conc. (%)	d_{10} (µm)	d_{50} (µm)	d_{90} (µm)	$d_{4,3}$ (µm)
0.0	1600	2368	3017	2340
0.5	1192	1767	2291	1828
1.0	1090	1960	2925	2074
2.0	1155	1852	2909	2081
4.0	1294	2108	3255	2465
6.0	933	1846	3041	1992
8.0	946	1384	1974	1554
10.0	587	997	1646	1566

As ethyl cellulose concentration increases further to 4 wt% the $d_{4,3}$ increases again, which could be due to the adhesive effects of ethyl cellulose making the bridging liquid 'sticky' leading to more coalescence. This was discussed earlier and can be seen in Figure 6.15 D. However, as the viscosity increased further and immersion rate is limited, the $d_{4,3}$ decreases again. This is due to the factors discussed earlier relating to a low working volume of bridging liquid creating an effectively low TBSR and therefore excess of primary particles. This excess of primary particles prevents the effect of coalescence and thus the larger coagglomerate sizes make up less of the volume fraction.

6.3.6 X-Ray Computer Tomography

Scan data was reconstructed and processed with the collaboration of Will Dawson (Nextrode Group, University College London). Images were provided as 2048 z-stack slices, as seen in Figure 6.23, these slices are 1 voxel thick and therefore 3.92 µm. After running the pixel classification process using ilastik on the 2D z-stack slices, the ROI data that was output was able to be used for reconstruction based on what was identified as solid or background signal. An example of the three-dimensional structure can be seen in Figure 6.24, shown for the 6 wt% coagglomerates generated. This represents well how the coagglomerates have been segmented from the background signal.

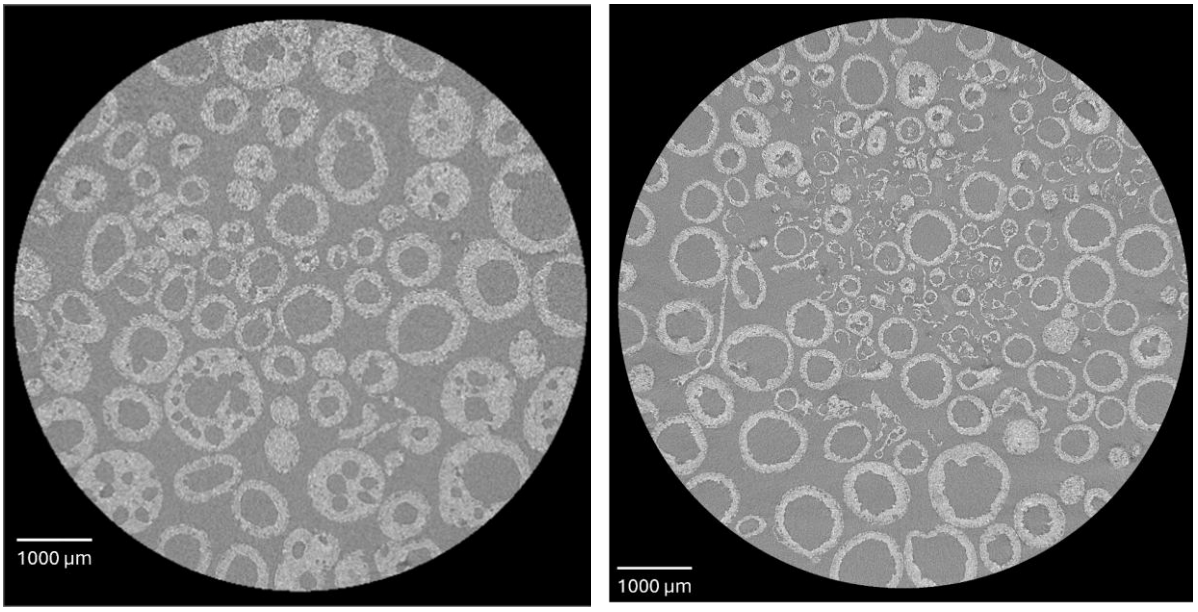

A) 6 wt% Ethyl Cellulose in Chloroform B) 10 wt% Ethyl Cellulose in Chloroform

Figure 6.23: Single z-stack slice from an XRCT scanned bed of 6 wt% and 10 wt% ethyl cellulose coagglomerates

Figure 6.24: Reconstructed 3D render of the XRCT data, where machine learning software (iLastik) was used to identify the regions of solid or air after training of a bed of coagglomerates (Will Dawson, UCL)

XRCT was primarily used to measure the shell wall thickness and void volume of the hollow coagglomerates. This metric was used to confirm how viscosity reduced the immersion rate. The mean wall thickness was measured across five points on each axis XYZ of five separate coagglomerates cropped out from the bulk. Some measurements had to be discarded if there was a hole in the wall of the coagglomerate as the process run through the Amira - Aviso software could not complete. As can be seen in Figure 6.23, there is a large variation in wall thickness across both coagglomerate samples. Additionally, in some of the coagglomerates, the wall of particles contains smaller voids which increases the values of error.

A general trend is observed, that suggests that the mean wall thickness is higher for the lower viscosity bridging liquid at 6 wt% when compared to the 10 wt% coagglomerates. This can be seen in Figure 6.25, however, the large standard deviation observed is a function of both the method and the irregular structure of the coagglomerates.

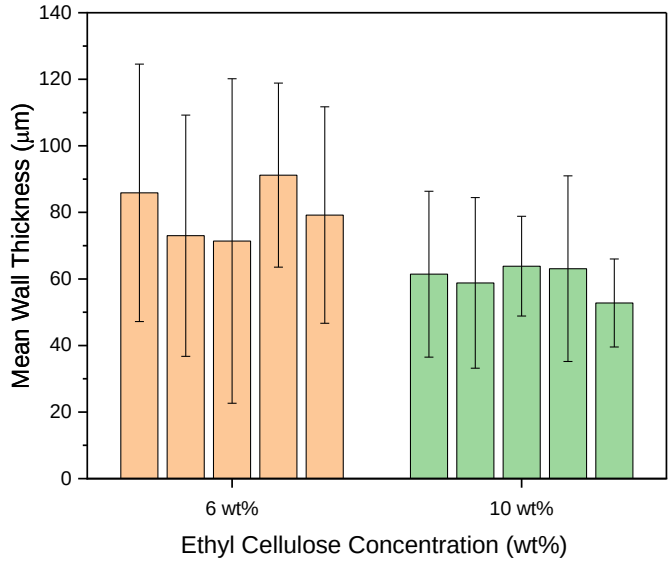

Figure 6.25: Distribution of mean wall thickness directly measured for 5 coagglomerates at different ethyl cellulose concentrations using Amira - Aviso post processing software analysis for a cropped coagglomerate with standard deviation based on 5 measurements

This suggests that increasing the bridging liquid viscosity decreases the rate of immersion into the droplet during the coagglomeration process and through observations of the XRCT image data hollow agglomerate structures are created using high viscosity bridging liquids.

A more reliable method for comparing mean wall thickness is based on the volume of the coagglomerate structures. The method involves comparing the envelope volume with the void volume to quantify proportionally how much of the total volume is void. The volume is an easier measurement to gather from the post processing as it relies only on the accuracy of segmentation and voxel classification of the coagglomerates. Since a voxel has known volume, the void volume and envelope volume can be found which enables a comparison based on the ratio of the two values. The relationship is such that, if the wall thickness is decreasing the ratio of void volume to envelope volume will tend to 1. Therefore, when comparing two different hollow coagglomerate batches, generated at different viscosity bridging liquids, the steeper the slope of best fit line the thinner the wall thickness. Hence, in this case, it can be seen in Figure 6.26 that the higher viscosity 10 wt% coagglomerates have a higher proportion of void volume for a given envelope volume than the 6 wt% coagglomerates. The Pearson's R values suggest that the lines of best fit provide a reliable metric to compare the effect of immersion rate using XRCT post processing data.

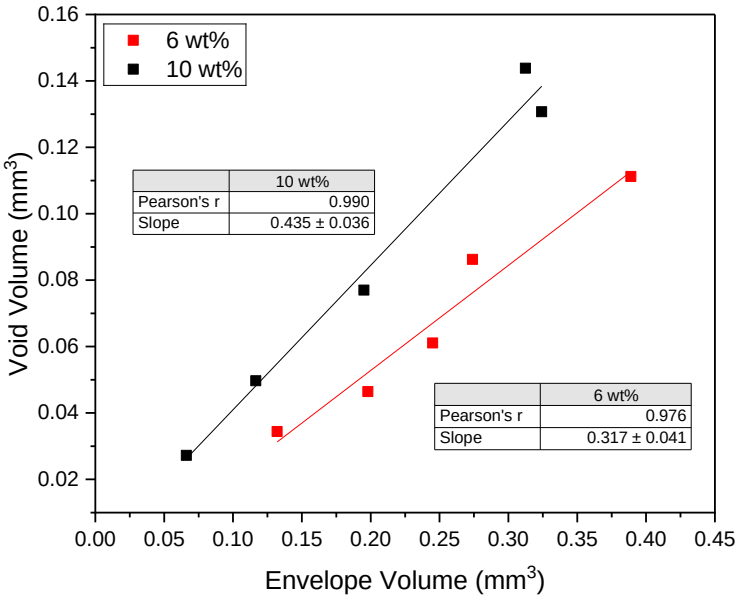

Figure 6.26: Relationship between envelope volume and void volume calculated for five coagglomerates generated using two viscosity bridging liquids

Additionally, since the volumes can be calculated from the voxel classification an average wall thickness can be estimated based on the equivalent volume sphere for those specified volumes. If perfect sphericity is assumed, then the volume of a sphere equation can be rearranged such that the envelope radius and void radius can be estimated using Equation 6.8. These two values can therefore be used to calculate the average wall thickness using Equation 6.9.

$$r = \sqrt[3]{\frac{3V}{4\pi}} \tag{6.8}$$

$$\tau = r_e - r_v \tag{6.9}$$

Where:

r Radius of a sphere (mm)

V Volume of a sphere (mm^3)

τ Hollow sphere wall thickness (mm)

r_e Radius of envelope volume (mm)

r_v Radius of void volume (s^{-1})

Through these calculations it is found that the 6 wt% hollow coagglomerates have an average wall thickness of 136.01 ± 15.36 µm. In comparison, the 10 wt% hollow coagglomerates have an average wall thickness of 88.47 ± 18.74 µm. The average and standard deviation is based on the five coagglomerates measured during the XRCT post processing. This agrees with the previous analysis that

increasing the viscosity of the bridging liquid decreases the wall thickness of the hollow coagglomerates formed.

6.4 Conclusions

Hollow coagglomerates have successfully been generated through viscous bridging liquids, containing an interlocked matrix of active material and conductive additive. Hollow structures inherently show improved compressive capabilities and thus hollow coagglomerates of electrode material present an exciting feedstock for electrode manufacturing, and potential benefits to dry manufacturing.

Increasing the viscosity of the chloroform bridging liquid appeared to show different solvent properties critical to the coagglomeration process, particularly with respect to contact angle, work of particle transfer (ΔW) and droplet size distribution. It was found that at higher viscosity the droplet size distribution was shifted towards larger sizes. Additionally, the droplets formed did not significantly change in size over the time of 20 minutes suggesting a stable drop size distribution within 5 minutes.

The contact angle measurements increased as bridging liquid viscosity increased and therefore increased the work of particle transfer (ΔW) exhibited by the viscous chloroform on the S3 graphite particles. However, for all bridging liquid viscosities analysed the ΔW remained negative suggesting successful coagglomerate generation. This was confirmed experimentally as coagglomerates were generated at each bridging liquid viscosity tested.

Increasing the viscosity of the bridging liquid showed hollow structures being formed above 6 wt% ethyl cellulose concentrations. This however came with an increase in primary particles in the product, considered to be due to the lack of working volume of bridging liquid. Since the immersion rate is lower in the viscous chloroform coagglomeration experiments, the chloroform core is unused and thus the system is essentially operating at a reduced TBSR. Future work would benefit from calculating a new term, which accounts for the unused fraction of bridging liquid in hollow coagglomeration generation, with the aim of adding calculated excess to enable higher yield of coagglomerates. This should be done by increasing the bridging liquid amount to account for the unused fraction of chloroform in the core of the hollow agglomerate and measure the extent of agglomeration or yield, to assess how the hollow volume effects the TBSR.

Interestingly, it was found that the coagglomerate size at the higher viscosity began to reduce in average size, even though the droplet size distribution study suggested that droplets formed at higher viscosity bridging liquids were larger than those at lower viscosity. This relates again to the reduced working volume of bridging liquid, meaning that there is less available at the surface during coagglomeration preventing coalescence.

XRCT was used to analyse the internal structure of the coagglomerates that displayed hollow structures. It was found as expected that increasing the viscosity the wall thickness reduced, and comparing the envelope volume versus the void volume provided a useful metric for analysing effect of viscosity on the immersion. A higher gradient on the best fit line, seen in Figure 6.26, suggests a greater reduction to the rate of immersion.

Therefore, it was found that generation of coagglomerates with hollow structures can be achieved through use of viscous bridging liquids and increasing the viscosity leads to a greater void volume within the coagglomerate. Excitingly, if the 10 wt% hollow coagglomerates are processed through compression onto electrode current collectors, the electrode thickness would be approximately equivalent to double the hollow coagglomerate wall thickness, for a monolayer of coagglomerates. This is within the range of a thick electrode (<200 μm) which are currently being researched due to the increased capacity and energy density that they offer.

Chapter 7 - Regime Map Development Discussion and Formation of Dimensionless Parameters from Experimental Observations

7.1 Introduction

Dimensionless analysis of common engineering processes enables comparisons to be made between systems with varying components. It also aids in the process of scale-up from lab scale to industrial manufacturing as the governing mechanisms are maintained at scale. A regime map for the spherical agglomeration of battery material can provide a predictive framework for tailoring structures to the required need. This reduces the dependence on a trial-and-error approach which at an industrial scale could cause large expense if the conditions are found to produce an undesirable product. By using dimensionless numbers to express the regime map, operating parameters can be chosen across different scales of production whilst targeting specific coagglomerate attributes required. This is particularly important for electrode design as the structure of the coagglomerates can provide a range of advantages, for example, sphericity, uniformity and porosity can improve the energy density, ionic conductivity and even downstream processes such as electrode film formation. The key takeaway is the cost reduction due to faster processing at higher yields with less off-spec product.

For the spherical coagglomeration systems discussed in the previous chapters, analysis of the energy balance was carried out to build upon the mechanistic understanding, particularly for the novel structures generated as part of the wider research discussed in this thesis. This chapter will propose some dimensionless numbers to describe the energy balance, and when data is plotted against these numbers, regions will be identified to propose a regime map. From the previous chapters it was found spherical agglomeration relies heavily on the wettability characteristics of the solid – solvent system. However, simply using contact angle as a quantification for successful coagglomeration is basic and does not accurately describe some systems. Other factors affect the extent of coagglomeration and the characteristics of the coagglomerate products. As a starting point, an energy balance is carried out on the particle transferring from the continuous phase to the bridging liquid droplet, based on the energetic mechanisms that play a role. Investigating the variables involved in the balance of forces, can allow dimensionless numbers to be proposed with an accompanying regime map.

7.1.1 Objectives

The main aim of this chapter is to identify dimensionless numbers that can help define a regime map in aid of describing the mechanisms seen during the experimental analysis of spherical coagglomeration. The objectives are as follows:

- Perform an energy balance on the process of particle engulfing between the continuous phase and bridging liquid at the interface between the two solvents
- Propose dimensionless numbers that describe the energy balance and coagglomeration
- Propose a regime map with regions that describe products seen as part of experimental investigations in previous chapters

7.2 Energy Balance for Particle Transfer

An energy balance was carried out for the process of a solid particle (graphite, carbon black) successfully immersing into a bridging liquid droplet (chloroform) from the continuous phase (DI water). A diagram of the mechanism can be seen in Figure 7.1, showing the balance of energetic mechanisms that effect the particle transfer.

As the particle transfers from the continuous DI water phase to the bridging liquid chloroform droplet during agitation in the stirred tank, the energy balance can be seen to be a balance of interfacial energy, kinetic energy and the opposing viscous dissipation energy change.

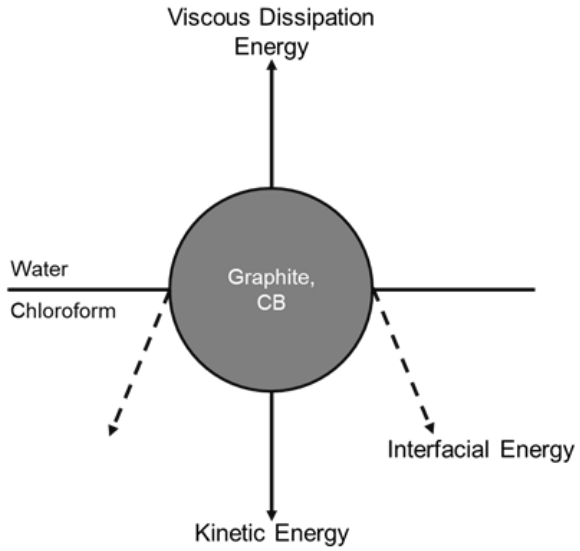

Figure 7.1: Energy balance around a particle transferring from the continuous phase to the bridging liquid droplet at the interface

7.2.1 Interfacial Energy

As discussed in Section 4.3.2.1, the work of particle transfer (ΔW) was proposed as a term to define whether a system is thermodynamically favourable for spontaneous transfer of a particle to be engulfed into one fluid to another when $\Delta W < 0$. Figure 7.2 shows this process for an 2D slice of the chloroform droplet – DI water interface. Equation 7.1 – 7.3, describe the mathematical theory used to calculate the ΔW which is based on the interfacial energies between each fluid and the solid of interest.

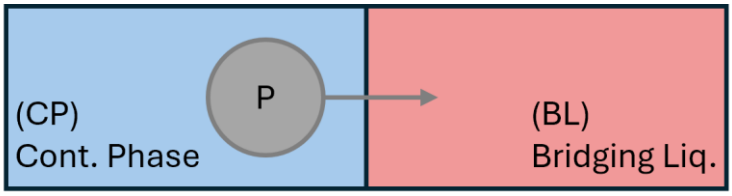

Figure 7.2: Diagram of particle (P) being engulfed through an immiscible interface of a continuous phase (CP) and a dispersed phase bridging liquid droplet (BL)

As discussed in Section 4.3.2.1, the work of particle transfer from the continuous phase (CP) to the bridging liquid droplet (BL), seen in Figure 7.2, is defined as the change in energy per unit area of the particles surface, or the balance of interfacial energies:

$$\Delta W \propto \gamma_{BL,P} - \gamma_{CP,P} \tag{7.1}$$

$$\Delta W \propto \gamma_{BL} - \gamma_{CP} - W_{BL,P} + W_{CP,P} \tag{7.2}$$

Which simplifies to be a function of contact angle and surface tension difference between the two fluids by substituting in the Young-Dupre equation to give:

$$\Delta W \propto -\gamma_{BL}\mathrm{Cos}\theta_{BL} + \gamma_{CP}\mathrm{Cos}\theta_{CP} \tag{7.3}$$

Where:

$\gamma_{BL,P}$ Bridging liquid – particle interfacial energy (mJ/m^2)

$\gamma_{CP,P}$ Continuous phase – particle interfacial energy (mJ/m^2)

γ_{BL} Bridging liquid surface tension (mJ/m^2)

γ_{CP} Continuous phase surface tension (mJ/m^2)

θ_{BL} Bridging liquid contact angle (°)

θ_{CP} Continuous phase contact angle (°)

For the experiments seen in Section 6.3.2 regarding coagglomeration with viscous bridging liquids, the ΔW was tabulated by calculating contact angle and surface tension of the viscous bridging liquids with respect to the S3 graphite used. A summary of this can be seen in Table 7.1:

Table 7.1: Summary of ΔW values based on the difference in interfacial energies of different viscosity chloroform solutions and DI water (EC = ethyl cellulose)

Solvent	γCosθ	ΔW (mJ/m^2)
Water	-59.996	N/A
0.0 wt% EC in Chloroform	8.551	-68.6
0.5 wt% EC in Chloroform	5.076	-65.1
1.0 wt% EC in Chloroform	0.908	-60.9
2.0 wt% EC in Chloroform	-8.454	-51.5
4.0 wt% EC in Chloroform	-14.036	-46.0
6.0 wt% EC in Chloroform	-16.308	-43.7
8.0 wt% EC in Chloroform	-18.559	-41.4
10.0 wt% EC in Chloroform	-19.859	-40.1

Increasing the chloroform viscosity through increasing ethyl cellulose concentration results in a decrease of the ΔW. However, it remains negative suggesting that chloroform remains energetically favourable for particle transfer of S3 graphite from the DI water continuous phase to the chloroform droplets. The magnitude of this energy gradient is reducing, which may play a role in the effects seen in reducing the immersion when generating hollow coagglomerates. Additionally, as the viscosity increased and the ΔW decreased, the opposing viscous dissipation will have increased.

7.2.2 Viscous Dissipation

The viscous dissipation, defined as the opposing energy in Figure 7.1, is a result of the friction and volume change that occurs during the particle transfer. The resistance to the immersion of a solid into the bridging liquid droplet leads to movement between the fluid layers and thus friction, so particle energy is transferred to heat and dissipated [132,133]. Increasing viscosity leads to greater friction within the fluid and therefore greater dissipation of energy. The mathematical models used to describe this phenomenon are complex and vary depending on the system geometry. Use of computational fluid dynamics (CFD) would normally be used to assess the motion of fluids and resistances that occur in a turbulent flow regime. The mapping of velocity gradients across turbulent flow is difficult due to the presence of turbulent eddies and highly localised differences in velocity. This is beyond the scope of this thesis. However, what can be assessed is that viscous dissipation is a function of viscosity and strain rate, for which strain rate is also a function of these complex changes in velocity across the turbulent flow.

7.2.3 Kinetic Energy

Particles are under constant agitation and shear due to the power imparted by the Rushton turbine during mixing. This means the particles have kinetic energy that will enhance the movement of particles from the continuous phase to the bridging liquid droplets upon collisions. The probability of collisions increases with kinetic energy whilst also increasing the probability that a collision will successfully lead to immersion of the particle into the droplet as per the energy balance. Kinetic energy in a turbulent flow regime is also complex to model due to the presence of eddies within the fluid. The Turbulent Kinetic Energy (TKE) equation [134] is an example of a mathematical model used to describe the fluctuating system and CFD again would be required to analyse how this affects the process of spherical coagglomeration, due to the variation in velocity vectors across 3-dimensions. Ultimately, what is important to be drawn from this is that (turbulent) kinetic energy is a function of velocity.

7.3 Dimensionless Numbers

Dimensionless numbers help to simplify mechanisms, whilst enabling comparison between different systems. In this case, the aim is to develop dimensionless numbers that describe the process of successful coagglomeration based on the movement of particles from the continuous phase to the bridging liquid droplets. Working from the theory discussed in the previous section, the three main components involved in the energy balance, interfacial energy, kinetic energy and viscous dissipation, can be described as functions:

$$Interfacial\ energy\ =\ f(\gamma_i, \theta_{i,j}) \tag{7.4}$$

$$Viscous\ dissipation\ =\ f(\mu, v) \tag{7.5}$$

$$Kinetic\ energy\ =\ f(v) \tag{7.6}$$

Therefore, defining a dimensionless number capturing these effects is important to describing the mechanisms. One such number that already exists is the Capillary Number which defines the ratio between viscous forces and interfacial tension forces. It is given by equation 7.7:

$$\mathrm{Ca} = \frac{\mu v}{\sigma} \tag{7.7}$$

Where:

- μ Droplet viscosity ($kg.m^{-1}.s^{-1}$)
- v Droplet velocity ($m.s^{-1}$)
- σ Surface tension ($kg.s^{-2}$)

The components in this dimensionless number relating the ratio of viscous forces and interfacial tension whilst containing a velocity term somewhat describe the components seen to be key for the spherical agglomeration particle transfer energy balance. Hence, an adapted version of this equation was proposed, Ca*:

$$\mathrm{Ca}^{*} = \frac{\mu_d v_d}{-\Delta W} \tag{7.8}$$

Where:

μ_d Droplet viscosity ($kg.m^{-1}.s^{-1}$)

v_d Droplet velocity ($m.s^{-1}$)

ΔW Work of particle transfer ($mJ.m^{-2}$)

The modified capillary number Ca* describes the ratio of viscous forces to interfacial tension forces, which were seen in the energy balance as energetically opposing. A high capillary number would suggest that viscous forces dominate, as can be seen in Chapter 6 when increasing the viscosity led to a reduced immersion rate and viscous dissipation was dominant. Velocity in this equation is a simplified version and is assumed to be based on the maximum energy applied by the impeller which is a function of the impeller speed:

$$v_d = \frac{RPM}{60} \pi D_{imp} \tag{7.9}$$

Where:

RPM Impeller rotation per minute (min^{-1})

D_{imp} Impeller diameter (m)

This is a simplification of the velocity profile within the stirred tank. However, for the scope of this thesis it enables a comparison of the modified capillary number for coagglomerates generated. The interfacial tension balance in this case is described based on the ΔW which is more relevant to the system being described for spherical agglomeration. Where Ca* < 0, this can only be due to the ΔW > 0 which, as discussed earlier, suggests the particles will not move from the continuous phase to the bridging liquid droplets. The modified capillary number has been calculated based on this theory for coagglomerates generated at their optimum TBSR and plotted against another dimensionless number, called growth number:

$$Growth\ Number = \frac{d_{agg_{4,3}}}{d_{drop_{4,3}}} \tag{7.10}$$

Where:

$d_{agg_{4,3}}$ Volume moment mean diameter of the agglomerate (m)

$d_{drop_{4,3}}$ Volume moment mean diameter of the droplet (m)

This growth number is proposed to assess the growth of coagglomerates based on the droplet size that was initially measured. This was considered relevant as a reduced capillary number is predicted to reduce the rate of growth. Since the mechanisms for the growth stage rely on the movement of bridging liquid 'squeezed' from the centre as particles immerse in the droplets, it is assumed that the capillary number describes the ability for fluid displacement in the droplet. As viscous forces dominate, the displacement of particle and fluid is resisted and the bridging liquid cannot be 'squeezed' to the surface as easily to allow for further growth due to layering or coalescence.

7.4 Regime Mapping

The coagglomerates generated and discussed throughout this thesis at their respective optimum TBSR were investigated to calculate the modified capillary number (Ca*) and growth number. These values can be seen in Table 7.2 and Table 7.3, and were plotted in Figure 7.3. Due to time constraints during the rheology experiments, the viscosity for 0 and 1 wt% was not measured directly and instead values were taken from supplier data for 0 wt% and extrapolated from the measured data for 1 wt%. Additionally, the $d_{4,3}$ droplet diameter was not measured for 0 wt% and therefore assumed to be approximately similar to that of the 0.5 wt% droplet size distribution.

Table 7.2: Summary of the modified capillary number calculated for experiments carried out as part of this Thesis

Identifier	μ_d (kg.m^{-1}.s^{-1})	RPM (min^{-1})	v_d (m.s^{-1})	ΔW (mJ.m^{-2})	**Ca***
0.0wt% EC	0.000536	900	1.414	-68.6	**7.04**
0.5 wt% EC	0.000793	900	1.414	-65.1	**10.97**
1.0 wt% EC	0.001	900	1.414	-60.9	**14.8**
2.0 wt% EC	0.00439	900	1.414	-51.5	**76.65**
4.0 wt% EC	0.02845	900	1.414	-46.0	**557.12**
6.0 wt% EC	0.06974	900	1.414	-43.7	**1436.67**
8.0 wt% EC	0.1429	900	1.414	-41.4	**3103.71**
10.0 wt% EC	1.133	900	1.414	-40.1	**25405.06**
$KS6_{opt}$	0.000793	1250	1.963	-44.1	**22.47**
$KS4_{opt}$	0.000793	1250	1.963	-49.3	**20.12**

Table 7.3: Summary of the Growth Number calculated for experiments carried out as part of this Thesis

Identifier	$d_{agg\ 4,3}$ (m)	$d_{drop\ 4,3}$ (m)	**Growth Number**
0.0wt% EC	2339.57	55.39	**43.32**
0.5 wt% EC	1827.65	55.39	**33.00**
1.0 wt% EC	2074.21	59.62	**34.79**
2.0 wt% EC	2081.11	65.40	**31.82**
4.0 wt% EC	2465.08	86.22	**28.59**
6.0 wt% EC	1992.63	127.05	**15.68**
8.0 wt% EC	1554.07	163.85	**9.48**
10.0 wt% EC	1566.35	186.81	**8.38**
$KS6_{opt}$	1518.59	55.39	**27.42**
$KS4_{opt}$	1902.15	55.39	**34.34**

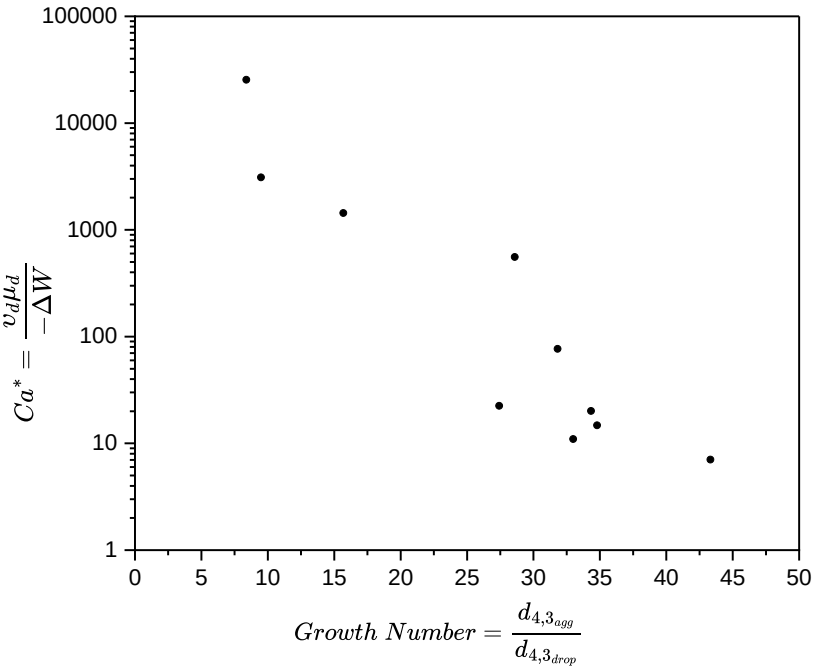

Figure 7.3: Plot of modified capillary number and growth number for data calculated in this thesis

Figure 7.3 shows a negative correlation with a smaller capillary number tending to larger growth numbers as bridging liquid can access the surface of the agglomerate and exhibit growth through layering or coalescence. As the data tends towards higher capillary numbers due to high viscosity coagglomeration experiments, the growth number tends to decrease which is expected as the displacement of particle and fluid is inhibited by the viscous forces which are dominant. Some boundaries are qualitatively proposed to relate to specific structures seen during the coagglomeration process based around these dimensionless numbers and can be seen in Figure 7.4, since these are not

exact boundaries, dotted lines are used. These boundaries need validating in future work and can be evaluated through an extensive design of experiments (DOE) covering areas across the regime map. By carrying out experiments across the range of the map the borders for different regions of agglomerate structures will be more clearly defined and will likely not be discrete. The transition between agglomerate structures is predicted to be a gradual change and this will be captured through an extensive DOE.

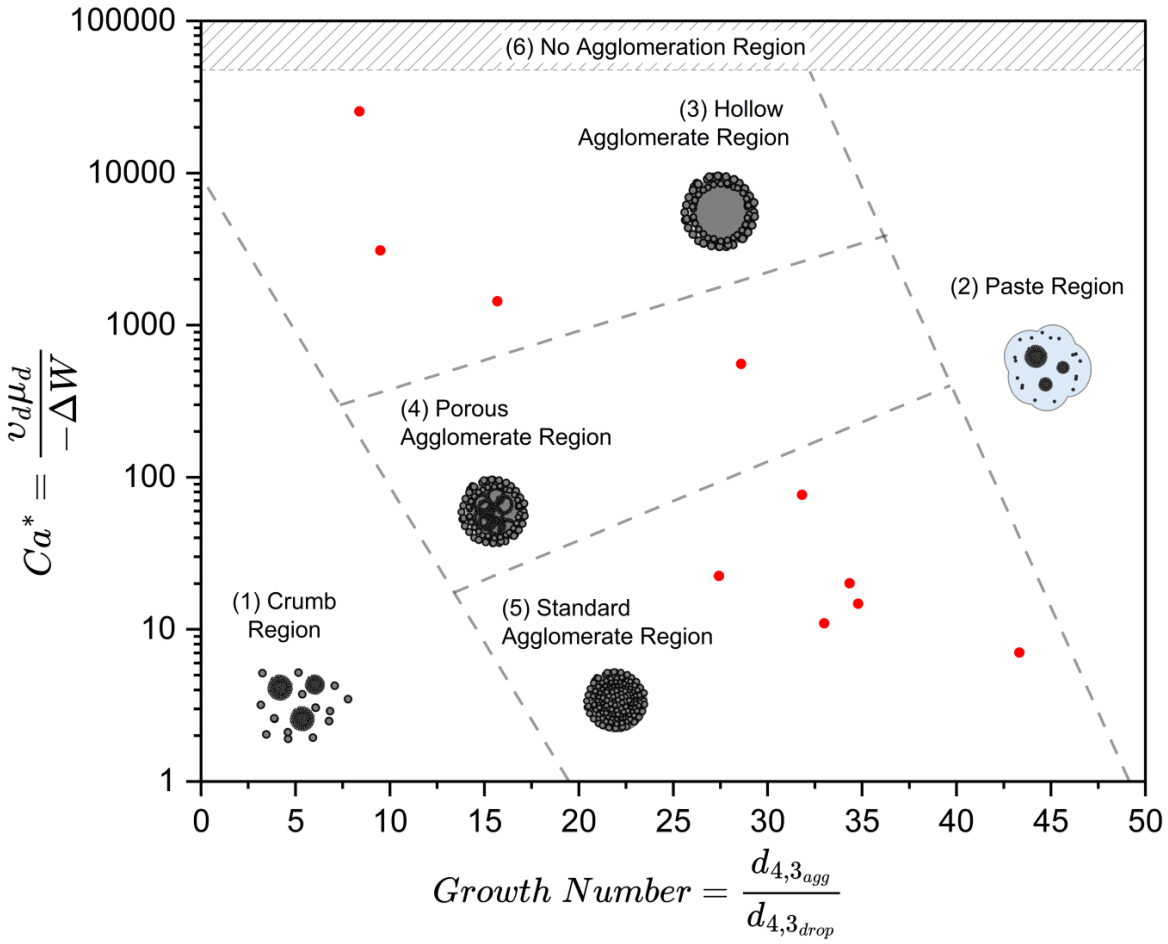

Figure 7.4: Regime map based on the modified capillary number and growth number with regions identified based on observations from experiments

The regime map areas (1 – 6) are proposed based on coagglomerates generated as part of this work and observations about their structure:

Region 1 – Crumb: Coagglomerates show a lack of growth with a high volume of primary material remaining. This occurs where Ca* is not high suggesting a low dominance of viscous resistance, which is assumed to be due to low TBSR. It should be noted that formation of a crumb did not occur frequently as experiments were based on using an optimum TBSR.

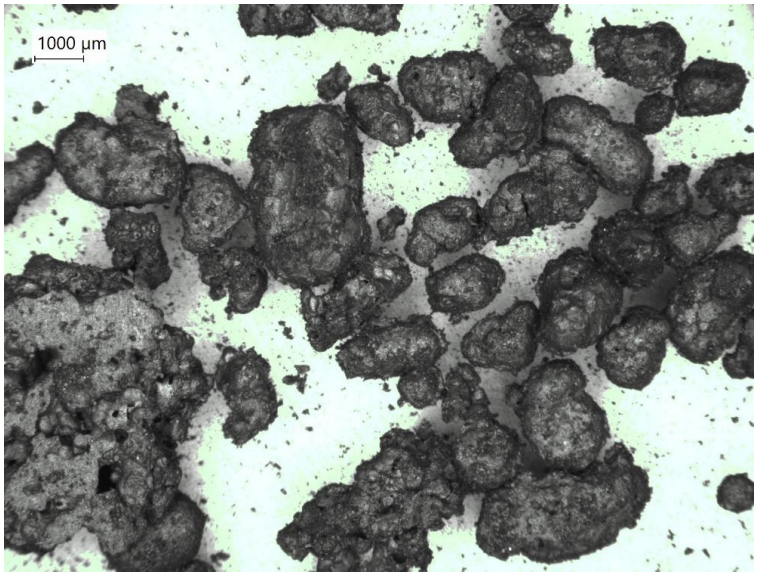

Figure 7.5: Example of coagglomerates formed in the crumb region (low TBSR)

Region 2 – Paste: Agglomerate growth is high due to an excess of bridging liquid available. Even at high Ca* values this effect is assumed to be observed and therefore it is proposed that this region is due to high TBSR. It should be noted that formation of a paste also did not occur frequently as experiments were based on using an optimum TBSR.

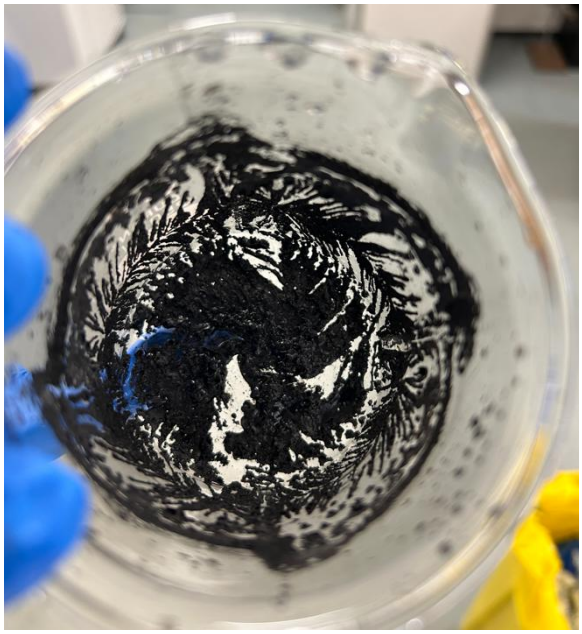

Figure 7.6: Example of paste region product where solid material is over wetted and deposited at the base of the beaker (high TBSR)

Region 3 – Hollow Agglomerates: These structures occur when viscous resistances dominate at high Ca* and 'squeezing' of the bridging liquid to the surface during immersion is slower. This resistance to solid and fluid displacement captured by the high Ca* means that growth through layering and/or coalescence is not expected and as such a lower growth number is observed for these conditions. Wall thickness of the hollow structure decreases as Ca* increases. This was observed for the 6 – 10 wt% ethyl cellulose concentration viscous coagglomerate experiments.

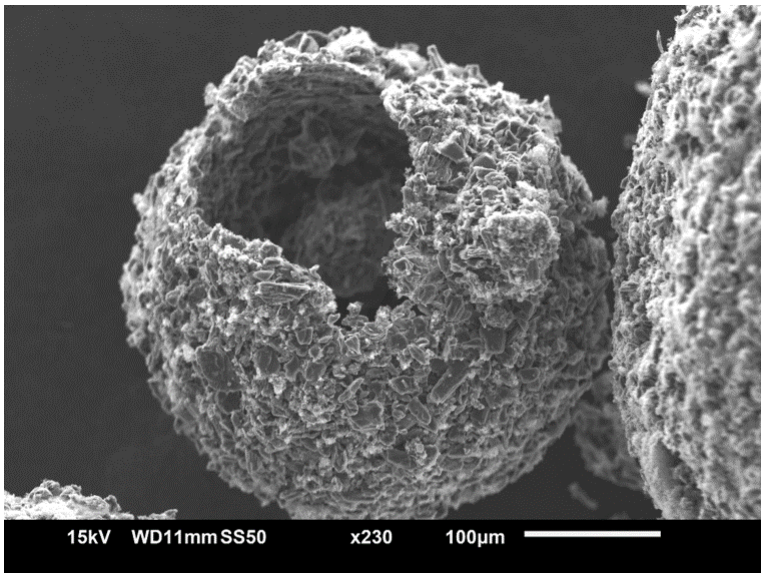

Figure 7.7: Example of hollow coagglomerate formed with high viscosity bridging liquid

Region 4 – Porous Agglomerates: These structures occur when there is a balance of viscous and interfacial energies leading to slower movement of solid within the droplet, but still faster immersion than the hollow agglomerate regime. Therefore, some hollow nuclei are initially seen but bridging liquid being 'squeezed' to the surface enables growth through coalescence with other nuclei and larger coagglomerates structures are generated with regions of porosity. This was seen in the 4 wt% ethyl cellulose concentration viscous coagglomeration experiments.

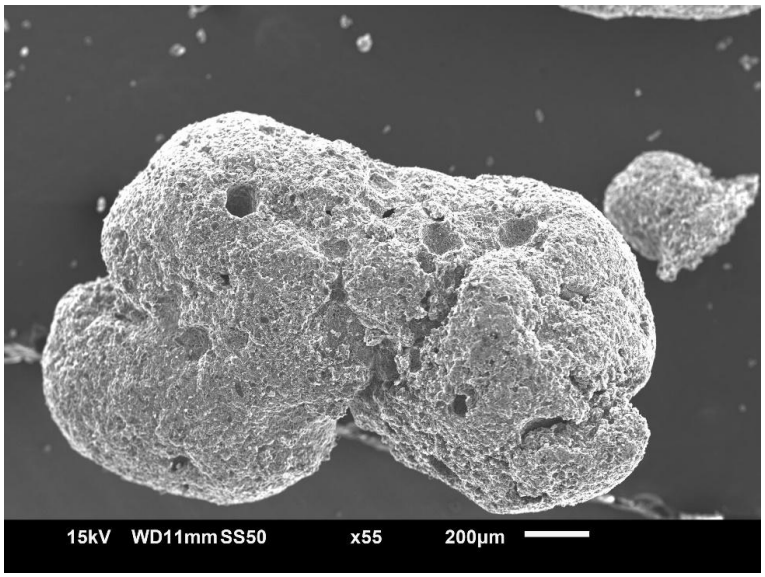

Figure 7.8: Example of porous coagglomerate formed with viscous bridging liquid

Region 5 – Dense Agglomerates: The work of particle transfer dominates as viscous effect is minimised, leading to unhindered thermodynamically favourable particle transfer from the continuous phase to the bridging liquid droplets. In this case bridging liquid can be 'squeezed' to the surface and growth occurs, hence the high growth numbers exhibited, and denser coagglomerates formed.

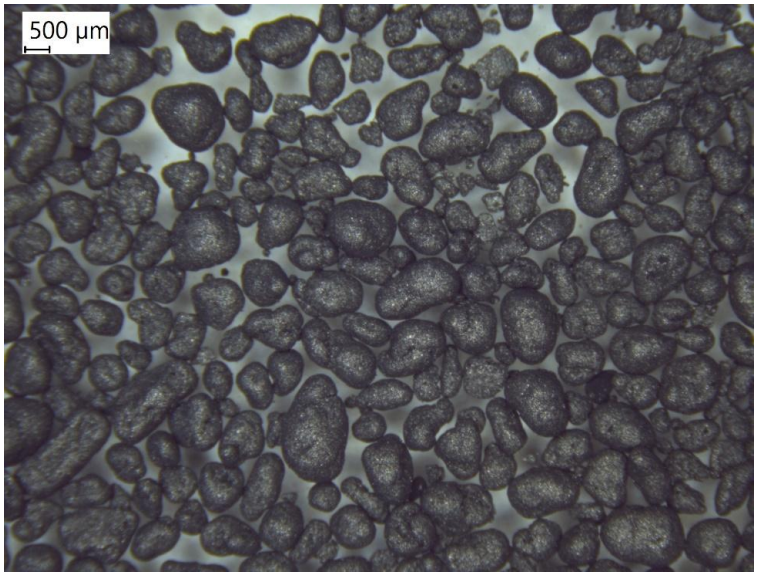

Figure 7.9: Example of standard coagglomerates formed with high growth number and low capillary number

Region 6 – No Agglomeration: For high modified capillary numbers the viscous effects massively dominate over the interfacial energy. This means that viscous dissipation is out competing the transfer of particles from one phase to the other, and coagglomerates cannot be formed. This is an assumed region which has not been experimentally validated and will be important for future work.

The boundaries proposed for the regime map are only estimates based on observations of the structures seen during analysis of the data from experiments throughout this thesis. Further work is required to validate these boundaries with experiments at different capillary numbers. It is also important to note that the process is dynamic and a function of time, therefore this is a snapshot of the system where the coagglomeration was run for 10 minutes. Also, for volatile, solvents like chloroform, the experiments were not run ad infinitum as a closed system was not used, and the eventual loss of chloroform to atmosphere would occur.

7.5 Conclusions

The regime map proposed has potential in describing the mechanisms involved based on the energy balance for mass transfer of a particle from a continuous phase to a bridging liquid droplet. Discussion of energy balance found that the feasibility of mass transfer is a function of velocity, viscosity and ΔW based on interfacial tension and contact angle. The capillary number was identified as a good descriptor of this energy balance incorporating the viscous resistances and balance of interfacial energies. Therefore, a modified capillary number was proposed based on adapted terms from the energy balance.

A growth number was also proposed to quantify the extent of growth from initial droplets to coagglomerate products. This term was seen to be correlated to the capillary number with a negative trend. This was determined to be due to the ability for bridging liquid to be displaced to the surface of the nuclei, which is inhibited when viscous resistances dominate at higher modified capillary number.

A regime map was proposed based on the plotted data for modified capillary and growth number. These boundaries are initial ideas of where structures are seen, and further experimental work is required at boundary conditions to validate the proposed regime map boundaries. However, this current regime map provides an insight to the structures seen throughout this thesis and the governing mechanisms developed into dimensionless numbers. These dimensionless numbers can be used to develop coagglomeration systems outside of the materials used in this investigation.

Chapter 8 - Outlook for Industrial Scale Application of Spherical Agglomeration for Battery Materials

8.1 Introduction

The study of spherical agglomeration presented in this thesis has demonstrated the feasibility of battery materials to be agglomerated in suspension and the ability to generate tuneable agglomerate structures by controlling certain process conditions. However, this has only been investigated at a lab scale. Whilst this provides key insights to developing this technology one must look at the applicability of this technology at an industrial scale to understand the functionality. This chapter will discuss key motivation and limitations to adopting this technology and provide insight to future work which could alleviate some of the concerns associated with these limitations.

Engineering technologies must look to maintain and improve upon the environmental sustainability of previous processes. However, commercial application will also be focused heavily on the cost attributes of new technologies. The work discussed in this chapter will investigate both the sustainability and cost effects of implementing spherical agglomeration into an industrial processing line in place of the wet slurry cast process that is used in most battery manufacturing plants around the world. Whilst the application of spherical agglomerates into an electrode manufacturing process has never been done before, assumptions are made regarding how the unit operations may be ordered.

8.1.1 Objectives

The main aim of this chapter is to assess the feasibility for spherical agglomeration to be adopted into commercial manufacturing of battery electrodes. The main objectives are as follows:

- Discuss the difference in unit operations between a potential spherical agglomeration-based process line and that which uses traditional slurry cast processing
- Compare the solvents required for the two processes and calculate the energy required for the downstream drying stage
- Discuss the future outlook of spherical agglomeration for industrial manufacturing of battery electrodes

8.2 Electrode Manufacturing Process Line

Typical electrode manufacturing uses a wet slurry cast approach where the unit operations begin with the electrode formulation being mixed under high shear with a solvent to generate a slurry. This is then cast on to a current collector at a desired thickness, where it will proceed to undergo drying. After this

drying step the electrode is calendered to a desired porosity by reducing the thickness. In comparison, the application of spherical agglomeration in electrode manufacturing has not been proved or implemented, however it could operate as follows. The primary particles are agglomerated in a stirred tank with a continuous phase and a dispersed phase, preferably in a continuous system. The agglomerated structures are then transferred to a washing and drying stage to remove any residual solvents, after which they would proceed to the hot roller presses which are similar to the calendering stage described in the wet slurry cast process. The two manufacturing approaches do not differ downstream of these unit operations and the electrode films proceed to the cell making section of the manufacturing line. As such the two different lines of unit operations can be seen in Figure 8.1 and Figure 8.2. The two process lines show similarity; however, the main area of difference is the film formation and drying process. This is because the slurry cast process produces a wet film before drying, whereas the proposed spherical agglomeration process dries the agglomerates before direct film formation.

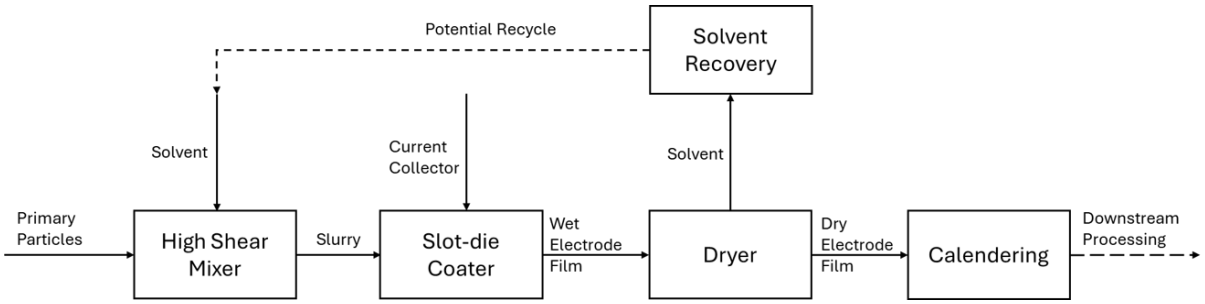

Figure 8.1: Typical unit operations for generating electrode films using the slurry cast method, before downstream processing of the dry electrode films

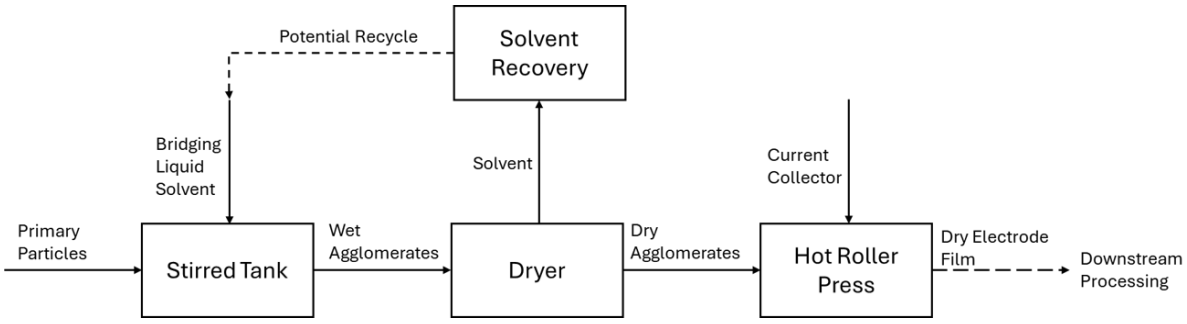

Figure 8.2: Proposed unit operations for generation of dry electrode films from spherical agglomerates generated at the beginning of the process

8.2.1 Drying Energy Requirements

Both process flow diagrams show the need for solvents to form the respective precursor to electrode films, in either a wet slurry or wet agglomerates. An analysis has been carried out to assess the estimated quantity of solvents required for each process based on the experimental work carried out in earlier chapters of this thesis and a typical laboratory scale slurry cast method. Although this is at a smaller

scale, it will provide insight to the comparison between the two methods. Table 8.1 shows data for the approximate mass of solids and the solvents required for a slurry cast process and some of the spherical agglomeration (SA) data, which was then used to calculate the weight percentage of solvent required.

Table 8.1: Calculated solvent weight percentage for the slurry cast and spherical agglomeration process

Method	Solid	Solvent	Mass Solid (g)	Mass Solvent (g)	wt/wt% solvent
Slurry Cast	NMC	NMP	5	3.0	37.50
SA	Graphite	Chloroform	2	2.7	57.51
SA	LFP	Chloroform	2	4.5	69.09

Although this was not assessed at an industrial scale if the processes were to be scaled up it is assumed that they would follow the same trend. It can be seen from Table 8.1 that, on a laboratory scale, the slurry cast process uses less solvent compared to a typical spherical agglomeration process. However, the energy requirements for drying must also be considered. This requires a calculation of the energy change based on sensible heat for a solvent to reach its boiling point, plus the latent heat of vaporisation. To calculate this, the following assumptions have been made:

- No heat loss to the surroundings – direct transfer of heat between dryer and sample
- Closed system – no gain or loss of mass during drying
- Ideal gas behaviour during vaporisation
- Operating at ambient pressure with no deviation
- Solvents are initially at ambient temperature (25 °C)
- Uniform temperature distribution during sensible heating
- Specific heat capacity is constant based on the value at ambient temperature (25 °C)

Equation 8.1 shows the specific sensible heat change of a solvent based on the temperature change and specific heat capacity of the solvent.

$$q = C_p \Delta \mathrm{T} \quad (\mathrm{kJ/kg}) \tag{8.1}$$

Where:

q Specific sensible heat (kJ/kg)

C_p Specific heat capacity (kJ/kg.K)

ΔT Temperature change (K)

Table 8.2: Sensible heat required to raise solvents to their boiling point and the heat of vaporisation required for evaporisation of solvents during the drying unit operation

Solvent	C_p (kJ/kg.K)	Boiling point (°C)	q (kJ/kg)	Δh_{vap} (kJ/kg)	ref
NMP	1.75	202	309.8	448.4	[135–137]
Chloroform	0.55	62	20.3	261.7	[138,139]

As can be seen in Table 8.2, a basic estimate of the energy required to evaporate/dry the product for each method has been compared based on the solvent used. This is the sum of the sensible heat and the heat of vaporisation, which for NMP is almost 2.7x the energy requirement when compared to chloroform, and therefore vast operational cost savings. This assessment was carried out for ideal conditions, however in a real drying process the increased surface area of the spherical agglomerates would also enable faster drying times. Additionally, compared to the slurry cast films there would be no migration of conductive additive and binder during the evaporation process, which was discussed as an issue in Section 2.1.6 . The continuous phase solvent that is used as a bulk fluid for spherical agglomeration to take place in does not need to be considered if the process is operating at optimum conditions. If the process is operating in ideal conditions, all the primary particles should be captured by the dispersed phase droplets and ultimately removed during filtration. This allows the continuous phase solvent to be reused for future spherical agglomeration processes, and potentially in the future designed to operate continuously.

8.3 UN Sustainability Goals

The United Nations (UN) presents a list of 17 sustainable development goals (SDG) the world needs to adhere to for a sustainable future. SDG 7 relates to ‘affordable and clean energy’ which will rely heavily on reliable energy storage. Due to the often unreliability of clean energy sources, a good energy storage infrastructure will play a key role in the future. Therefore, it is important to identify where advancements can be made in the manufacturing of electrodes. It has been seen that the requirements for drying are significantly reduced using the proposed spherical agglomeration process and as such the cost and energy savings will be reduced. However, other factors play a key role in the assessment of sustainability.

NMP is well known to be highly toxic with a particular impact on fertility [140,141]. Therefore, SDG 3 and 8, regarding good health and decent work respectively, are significantly impacted. The UN aims to significantly reduce the amount of harm done by hazardous chemicals, and whilst NMP is used in large quantities for electrode manufacturing, careful control and safe working conditions must be ensured to minimise risk of occupational exposure. Alternative solvents or no solvent manufacturing must be investigated to ensure this goal is achieved. The responsible consumption and production SDG

12, highlights the need for proper management of chemicals throughout their life cycle and this plays into the effect on water systems and biodiversity which are discussed in SDG 6 and 15 (‘clean water and sanitation’ and ‘life on land’). NMP release into the environment can have serious impact on the pollution of clean water and ecosystems.

Dry electrode manufacturing can help drive movement towards some of the SDG’s, particularly SDG 8 and 12 by generating a safer work environment free of toxic solvents and reducing energy consumption as there is no intensive drying stage. Whilst dry electrode manufacturing reduces energy consumption and therefore greenhouse gas (GHG) emissions, the progression of battery technology towards higher energy density and longer battery life times will enable a more sustainable energy infrastructure [142].

Finally, the adoption of spherical agglomeration technology in battery manufacturing may hold the key for a more circular battery life cycle. The fundamental mechanisms for spherical agglomeration rely on the preferential wetting of particles with a bridging liquid solvent. This allows preferential separation of materials by tuning the solvent choice [17,18,93]. The current process of battery recycling utilises shredding and magnetic properties to separate out the current collector foils from the bulk electrode. However, what remains is the ‘black mass’ which incorporates cathodic and anodic active materials and conductive additive [143]. Optimisation of the spherical agglomeration process could enable the direct separation of these two materials with different surface energy properties by choosing a suitable bridging liquid which has preferential wettability to one of the solids of interest. This has yet to be proven but presents an interesting avenue of research to enhance the circular life cycle of battery manufacturing and meet the targets described in SDG 12 (responsible consumption and production) by retaining or recovering valuable materials reducing the need for virgin mining of raw materials.

8.4 Scale-up and Commercial Considerations for Spherical Agglomeration

Looking at the key concerns for applying spherical agglomeration processes to industrial scales allows these limitations to be addressed and optimise the process further. Whilst spherical agglomeration of battery materials has not been implemented on industrial scales, some work with pharmaceutical ingredients for scale up has been carried out [144]. The authors showed successful spherical agglomeration in a 300 L stirred tank which is a significantly larger volume than most systems, equivalent to a pilot plant scale. They discussed how the power per mass was a key parameter for identifying suitable mixing speeds to achieve comparable agglomerate structures seen at smaller scales. However, studies are limited in the application of large-scale continuous processing. Further work will be required to design a suitable continuous processing method that has suitable control over the final

agglomerate structures. This is key to enabling efficient and cost-effective manufacturing particularly for electrode manufacturing which currently operates continuously.

Should a stirred tank system be used, then optimal conditions will need to be investigated such that there are no ‘deadzones’ or local fluctuations in turbulence. Homogeneous distribution of the primary particles and bridging liquid droplets is important for efficient agglomeration. Without this, regions with high concentration of bridging liquid can occur and this increases the effective TBSR in local areas whilst leaving other areas depleted of bridging liquid. A well distributed system will enable efficient processing and more reliable product generation. Stirred tank design is well documented but spherical agglomeration in a stirred tank has not been carried out at that scale particularly for battery materials where some materials sink (graphite, LFP) and some tend to float (carbon black), so further investigation into this will be required for commercial adoption.

8.5 Conclusions

The consensus in battery manufacturing is that dry processes need to be investigated and implemented in future manufacturing lines. This is due to the reduced cost and inherent safety improvements. This also aligns well with the SDG’s outlined by the UN, reducing the impact on humans and the environment. Spherical agglomeration for the materials discussed in this thesis show a greater solvent requirement per kg of solid than a wet slurry process. However, other battery materials to be agglomerated may show a lower solvent requirement per kg of solid, and it is assumed that this comes down to the packing density of the particles in the spherical agglomerate structures. Lower porosity agglomerates will require lower bridging liquid volumes. Although the solvent requirements were higher for the spherical agglomeration experiments carried out in this thesis compared to wet slurry casting, the cost and energy requirement to evaporate the solvent used would be 2.7x lower than for NMP, which is typically used in slurry cast processes. The specific energy for sensible heat change and enthalpy of vaporisation were calculated and summed to give a total energy requirement of 282 kJ/kg for chloroform and 758 kJ/kg for NMP. In addition to this, the toxicity of NMP is also a major concern and by removing this from the manufacturing process there is less risk to occupational exposure. In conclusion, the pseudo-dry processing of spherical agglomerates directly into electrode films has many benefits when compared to the traditional slurry cast process. These benefits align well with the sustainable development goals of the United Nations.

Chapter 9 - Conclusions and Future Work

9.1 Conclusions

The main aim of this research was to develop a coagglomeration system for battery active material and conductive additives. This was successfully completed based on fundamental wettability criteria. This was built upon by proposing a thermodynamic quantification for predicting feasible coagglomeration. Additionally, hollow and porous coagglomerate structures were developed by manipulating the rate mechanisms involved in the immersion of particles into bridging liquid droplets. To help predict the structures generated, dimensionless numbers have been proposed and plotted to develop a regime map for coagglomerate production.

Successful coagglomeration was found to be dependent on both wettability and a suitable impeller speed to suspend the particles, due to the high density of battery active materials. Chloroform was found to be a suitable bridging liquid for graphite coagglomeration but not for lithium iron phosphate (LFP) when dispersed in a DI water continuous phase. Optimum TBSR for various graphite coagglomerate systems was found by quantifying product based on their flowability and yield. A novel method for spherical coagglomeration of LFP was developed for solvent systems with non-preferential wettability, called the modified dispersed phase (MDP) method. The process parameters of a batch coagglomeration process was investigated which found that agglomeration time and impeller speed densified the coagglomerates and reduced the average size distributions.

Coagglomerates were generated at length scales <100 μm through an alternative addition method where an emulsion is first generated using surfactant to stabilise the bridging liquid droplets, before solids were added. This enabled coagglomerates to be templated and limited by droplet size distribution. It was found that injecting the bridging liquid after particles were dispersed, inhibited the drop breakup and thus nuclei formed were larger, leading to larger coagglomerates. Therefore, the addition method plays a significant role in the size of coagglomerates generated.

Reducing the rate of immersion through increasing bridging liquid viscosity was found to generate hollow agglomerates at higher viscosities. This is an important result particularly for dry electrode production where hollow particles, which are defined as soft, press more efficiently, as is seen in pharmaceutical industry for tablet pressing. Thermodynamic analysis of viscous bridging liquids found that increasing the viscosity increased the contact angle between the bridging liquid and solid. This reduced the interfacial energy difference between continuous and bridging liquid phases. However, the work of particle transfer was still negative and thus transfer is spontaneous at the interface. The viscous dissipation forces dominate reducing the rate of immersion, therefore generating hollow

coagglomerates. XRCT was used to analyse the internal structure of the coagglomerates generated, and wall thickness and void volume were used to characterise the difference. It was found that increasing the viscosity of the bridging liquid reduced the wall thickness of the coagglomerates generated as predicted based on the rate mechanisms that were proposed.

The thermodynamic analysis of the particle transfer was investigated further using an energy balance to identify the balance of energies involved in the mechanism. This was then developed to propose a modified capillary number and growth number. These dimensionless numbers were plotted to form a regime map to aid in predicting coagglomerate structures. This is important for developing coagglomeration systems for different active materials and conductive additives.

Finally, a brief study on the outlook of spherical agglomeration for application at an industrial scale was carried out and found that the proposed process had many benefits to cost, energy and safety, whilst aiding in the transition to a more sustainable future outlined by the UN sustainable development goals.

9.2 Future Work

The research discussed in this thesis is highly novel and opens many avenues for spherical agglomeration in battery manufacturing research. However, the proposed future work recommendations that would be most valuable to this work are as follows:

- Development of the interfacial energy gradient that dictates feasibility of the particle transfer from continuous phase to bridging liquid droplet, to incorporate dispersive and polar surface energies that some battery materials exhibit. This will enable faster identification of suitable solvent systems for successful spherical coagglomeration.
- Carry out electrochemical analysis of electrodes formed using coagglomerates, with a particular focus on the benefits of producing dry electrodes with the generated coagglomerates. Additionally, how hollow coagglomerate structures may benefit the dry electrode production process should be investigated.
- Investigate the feasibility of using the spherical coagglomeration process to recycle electrodes by preferentially wetting dispersed material in a stirred vessel. This can operate selectively if solvents are chosen based on the affinity to specific materials and offers a potential route to recycling electrode materials.
- Further validation of the boundaries conditions to validate the regime map is vital for developing a system to predict coagglomerate properties. Using alternative active materials would also benefit the development of this regime map.

As stated earlier, there are various avenues that this research has introduced as potential areas of interest. However, for improvement of battery manufacturing processes with a focus on saving time and cost, it

is important to further develop the research surrounding coagglomerates for dry electrode manufacturing. This will prevent the use of harmful solvents and save money in the drying process. The research presented here shows the feasibility of spherical coagglomeration of battery materials and discusses some novel structures generated. The benefit of future work comes in implementation of these products into the electrode structure, where the interlocked coagglomerate matrix of inter- and intra-distributed conductive additive may aid in the manufacture of homogeneous electrodes with improved ionic and electronic conductivity.

Chapter 10 - Bibliography

[1] N. Rietmann, B. Hügler, T. Lieven, Forecasting the trajectory of electric vehicle sales and the consequences for worldwide CO2 emissions, Journal of Cleaner Production 261 (2020) 121038. https://doi.org/10.1016/j.jclepro.2020.121038.

[2] J. Deng, C. Bae, A. Denlinger, T. Miller, Electric Vehicles Batteries: Requirements and Challenges, Joule 4 (2020) 511–515. https://doi.org/10.1016/j.joule.2020.01.013.

[3] T. Lombardo, A.C. Ngandjong, A. Belhcen, A.A. Franco, Carbon-Binder Migration: A Three-Dimensional Drying Model for Lithium-ion Battery Electrodes, Energy Storage Materials 43 (2021) 337–347. https://doi.org/10.1016/j.ensm.2021.09.015.

[4] S. Jaiser, M. Müller, M. Baunach, W. Bauer, P. Scharfer, W. Schabel, Investigation of film solidification and binder migration during drying of Li-Ion battery anodes, Journal of Power Sources 318 (2016) 210–219. https://doi.org/10.1016/j.jpowsour.2016.04.018.

[5] B. Kovačič, F. Vrečer, O. Planinšek, Spherical crystallization of drugs., Acta Pharmaceutica (Zagreb, Croatia) 62 (2012) 1–14. https://doi.org/10.2478/v10007-012-0010-5.

[6] P. Kurumkar, S. Dewani, I.B. Pathan, H. Sonaye, Preparation of spherical crystal agglomerates via crystallo-co-agglomeration technique, Digest Journal of Nanomaterials and Biostructures 7 (2012) 1223–1236.

[7] F. Degen, O. Krätzig, Future in Battery Production: An Extensive Benchmarking of Novel Production Technologies as Guidance for Decision Making in Engineering, IEEE Trans. Eng. Manage. 71 (2024) 1038–1056. https://doi.org/10.1109/TEM.2022.3144882.

[8] N. Nitta, F. Wu, J.T. Lee, G. Yushin, Li-ion battery materials: present and future, Materials Today 18 (2015) 252–264. https://doi.org/10.1016/j.mattod.2014.10.040.

[9] Y. Lu, Y. Zhang, Q. Zhang, F. Cheng, J. Chen, Recent advances in Ni-rich layered oxide particle materials for lithium-ion batteries, Particuology 53 (2020) 1–11. https://doi.org/10.1016/j.partic.2020.09.004.

[10] K.J. Park, H.G. Jung, L.Y. Kuo, P. Kaghazchi, C.S. Yoon, Y.K. Sun, Improved Cycling Stability of Li[Ni0.90Co0.05Mn0.05]O2 Through Microstructure Modification by Boron Doping for Li-Ion Batteries, Advanced Energy Materials 8 (2018) 1–9. https://doi.org/10.1002/aenm.201801202.

[11] S.H. Jung, U.H. Kim, J.H. Kim, S. Jun, C.S. Yoon, Y.S. Jung, Y.K. Sun, Ni-Rich Layered Cathode Materials with Electrochemo-Mechanically Compliant Microstructures for All-Solid-State Li Batteries, Advanced Energy Materials 10 (2020). https://doi.org/10.1002/aenm.201903360.

[12] K. Pitt, R. Peña, J.D. Tew, K. Pal, R. Smith, Z.K. Nagy, J.D. Litster, Particle design via spherical agglomeration: A critical review of controlling parameters, rate processes and modelling, Powder Technology 326 (2018) 327–343. https://doi.org/10.1016/j.powtec.2017.11.052.

[13] Y. Javadzadeh, Z. Vazifehasl, S.M. Dizaj, M. Mokhtarpour, Spherical Crystallization of Drugs, in: Advanced Topics in Crystallization, InTech, 2015: pp. 137–144. https://doi.org/10.5772/59627.

[14] C. Subero-Couroyer, D. Mangin, A. Rivoire, A.F. Blandin, J.P. Klein, Agglomeration in suspension of salicylic acid fine particles: Analysis of the wetting period and effect of the binder injection mode on the final agglomerate size, Powder Technology 161 (2006) 98–109. https://doi.org/10.1016/j.powtec.2005.08.014.

[15] K. Pitt, J.D. Tew, B. Ahmed, C. Brown, I. Houson, A.L. Robertson, K.P. Girard, J.L. Quon, J.D. Litster, R.M. Smith, Spherical agglomeration kinetics: A mechanistic approach, Powder Technology (2024) 120082. https://doi.org/10.1016/j.powtec.2024.120082.

[16] A.F. Blandin, D. Mangin, A. Rivoire, J.P. Klein, J.M. Bossoutrot, Agglomeration in suspension of salicylic acid fine particles: Influence of some process parameters on kinetics and agglomerate final size, Powder Technology 130 (2003) 316–323. https://doi.org/10.1016/S0032-5910(02)00210-3.

[17] J.R. Farnand, H.M. Smith, I.E. Puddington, Spherical agglomeration of solids in liquid suspension, Can J Chem Eng 39 (1961) 94–97. https://doi.org/10.1002/cjce.5450390209.

[18] J.P. Sutherland, The agglomeration of aqueous suspensions of graphite, The Canadian Journal of Chemical Engineering 40 (1962) 268–272. https://doi.org/10.1002/cjce.5450400609.
[19] A. Accardo, G. Dotelli, M.L. Musa, E. Spessa, Life cycle assessment of an NMC battery for application to electric light-duty commercial vehicles and comparison with a sodium-nickel-chloride battery, Applied Sciences (Switzerland) 11 (2021) 1–32. https://doi.org/10.3390/app11031160.
[20] C. Zhang, W. Jiang, W. He, W. Wei, Heteroepitaxial interface of layered cathode materials for lithium ion batteries, Energy Storage Materials 37 (2021) 161–189. https://doi.org/10.1016/j.ensm.2021.02.009.
[21] Z. Ogumi, Interfacial Reactions of Lithium-ion Batteries, Electrochemistry 78 (2010) 319–324. https://doi.org/10.5796/electrochemistry.78.319.
[22] N. Ogihara, Y. Itou, Impedance Analysis Using Symmetric Cells for Understanding Electrochemical Behaviour of Porous Electrodes for Lithium-ion Batteries, R&D Review of Toyota CRDL 48 (2017) 17–24.
[23] C. Usubelli, M.M. Besli, S. Kuppan, N. Jiang, M. Metzger, A. Dinia, J. Christensen, Y. Gorlin, Understanding the Overlithiation Properties of LiNi 0.6 Mn 0.2 Co 0.2 O 2 Using Electrochemistry and Depth-Resolved X-ray Absorption Spectroscopy, Journal of The Electrochemical Society 167 (2020) 080514. https://doi.org/10.1149/1945-7111/ab8a9d.
[24] F.H. Gandoman, Y. Firouz, M.S. Hosen, T. Kalogiannis, J. Jaguemont, M. Berecibar, J. Van Mierlo, Reliability assessment of NMC li-ion battery for electric vehicles application, 2019 IEEE Vehicle Power and Propulsion Conference, VPPC 2019 - Proceedings (2019) 1–6. https://doi.org/10.1109/VPPC46532.2019.8952180.
[25] Z. Chen, W. Zhang, Z. Yang, A review on cathode materials for advanced lithium ion batteries: Microstructure designs and performance regulations, Nanotechnology 31 (2020). https://doi.org/10.1088/1361-6528/ab4447.
[26] Y. Li, Y. Lu, P. Adelhelm, M.M. Titirici, Y.S. Hu, Intercalation chemistry of graphite: Alkali metal ions and beyond, Chemical Society Reviews 48 (2019) 4655–4687. https://doi.org/10.1039/c9cs00162j.
[27] Y. Guo, Y. Wei, H. Li, T. Zhai, Layer Structured Materials for Advanced Energy Storage and Conversion, Small 13 (2017) 1–22. https://doi.org/10.1002/smll.201701649.
[28] C.W. Chang-Jian, B.C. Ho, C.K. Chung, J.A. Chou, C.L. Chung, J.H. Huang, J.H. Huang, Y.S. Hsiao, Doping and surface modification enhance the applicability of Li4Ti5O12 microspheres as high-rate anode materials for lithium ion batteries, Ceramics International 44 (2018) 23063–23072. https://doi.org/10.1016/j.ceramint.2018.09.110.
[29] Q. Wang, B. Liu, Y. Shen, J. Wu, Z. Zhao, C. Zhong, W. Hu, Confronting the Challenges in Lithium Anodes for Lithium Metal Batteries, Advanced Science 2101111 (2021) 1–25. https://doi.org/10.1002/advs.202101111.
[30] K. Feng, M. Li, W. Liu, A.G. Kashkooli, X. Xiao, M. Cai, Z. Chen, Silicon-Based Anodes for Lithium-Ion Batteries: From Fundamentals to Practical Applications, Small 14 (2018). https://doi.org/10.1002/smll.201702737.
[31] J. Entwistle, R. Ge, K. Pardikar, R. Smith, D. Cumming, Carbon binder domain networks and electrical conductivity in lithium-ion battery electrodes: A critical review, Renewable and Sustainable Energy Reviews 166 (2022) 112624. https://doi.org/10.1016/j.rser.2022.112624.
[32] H. Bockholt, M. Indrikova, A. Netz, F. Golks, A. Kwade, The interaction of consecutive process steps in the manufacturing of lithium-ion battery electrodes with regard to structural and electrochemical properties, Journal of Power Sources 325 (2016) 140–151. https://doi.org/10.1016/j.jpowsour.2016.05.127.
[33] W.B. Hawley, J. Li, Electrode manufacturing for lithium-ion batteries—Analysis of current and next generation processing, Journal of Energy Storage 25 (2019) 100862. https://doi.org/10.1016/j.est.2019.100862.
[34] G. Bridgewater, M.J. Capener, J. Brandon, M.J. Lain, M. Copley, E. Kendrick, A comparison of lithium-ion cell performance across three different cell formats, Batteries 7 (2021). https://doi.org/10.3390/batteries7020038.

[35] R. Dugas, J.D. Forero-Saboya, A. Ponrouch, Methods and Protocols for Reliable Electrochemical Testing in Post-Li Batteries (Na, K, Mg, and Ca), Chemistry of Materials (2019). https://doi.org/10.1021/acs.chemmater.9b02776.
[36] W. Kao-ian, R. Pornprasertsuk, P. Thamyongkit, T. Maiyalagan, S. Kheawhom, Rechargeable Zinc-Ion Battery Based on Choline Chloride-Urea Deep Eutectic Solvent, Journal of The Electrochemical Society 166 (2019) A1063–A1069. https://doi.org/10.1149/2.0641906jes.
[37] M.S.K. Mutyala, J. Zhao, J. Li, H. Pan, C. Yuan, X. Li, In-situ temperature measurement in lithium ion battery by transferable flexible thin film thermocouples, Journal of Power Sources 260 (2014) 43–49. https://doi.org/10.1016/j.jpowsour.2014.03.004.
[38] D. Schreiner, T. Zünd, F.J. Günter, L. Kraft, B. Stumper, F. Linsenmann, M. Schüßler, R. Wilhelm, A. Jossen, G. Reinhart, H.A. Gasteiger, Comparative Evaluation of LMR-NCM and NCA Cathode Active Materials in Multilayer Lithium-Ion Pouch Cells: Part I. Production, Electrode Characterization, and Formation, Journal of The Electrochemical Society 168 (2021) 030507. https://doi.org/10.1149/1945-7111/abe50c.
[39] A. Soto, A. Berrueta, P. Sanchis, A. Ursua, Analysis of the main battery characterization techniques and experimental comparison of commercial 18650 Li-ion cells, Proceedings - 2019 IEEE International Conference on Environment and Electrical Engineering and 2019 IEEE Industrial and Commercial Power Systems Europe, EEEIC/I and CPS Europe 2019 (2019) 1–6. https://doi.org/10.1109/EEEIC.2019.8783862.
[40] H. Lei, Y.Y. Han, The measurement and analysis for Open Circuit Voltage of Lithium-ion Battery, Journal of Physics: Conference Series 1325 (2019). https://doi.org/10.1088/1742-6596/1325/1/012173.
[41] S. Yin, W. Deng, J. Chen, X. Gao, G. Zou, H. Hou, X. Ji, Fundamental and solutions of microcrack in Ni-rich layered oxide cathode materials of lithium-ion batteries, Nano Energy 83 (2021). https://doi.org/10.1016/j.nanoen.2021.105854.
[42] C. Liao, F. Li, J. Liu, Challenges and Modification Strategies of Ni-Rich Cathode Materials Operating at High-Voltage, Nanomaterials 12 (2022) 1888. https://doi.org/10.3390/nano12111888.
[43] S. Kalluri, M. Yoon, M. Jo, H.K. Liu, S.X. Dou, J. Cho, Z. Guo, Feasibility of Cathode Surface Coating Technology for High-Energy Lithium-ion and Beyond-Lithium-ion Batteries, Advanced Materials 29 (2017). https://doi.org/10.1002/adma.201605807.
[44] J. Niu, M. Wang, T. Cao, X. Cheng, R. Wu, H. Liu, Y. Zhang, X. Liu, Li metal coated with Li3PO4 film via atomic layer deposition as battery anode, Ionics 27 (2021) 2445–2454. https://doi.org/10.1007/s11581-021-04030-z.
[45] R.J. Martín-Palma, A. Lakhtakia, Vapor-Deposition Techniques, in: Engineered Biomimicry, Elsevier, 2013: pp. 383–398. https://doi.org/10.1016/B978-0-12-415995-2.00015-5.
[46] Y. Cao, T.D. Hatchard, R.A. Dunlap, M.N. Obrovac, Mechanofusion-derived Si-alloy/graphite composite electrode materials for Li-ion batteries, Journal of Materials Chemistry A 7 (2019) 8335–8343. https://doi.org/10.1039/c9ta00132h.
[47] M. Chen, E. Zhao, D. Chen, M. Wu, S. Han, Q. Huang, L. Yang, X. Xiao, Z. Hu, Decreasing Li/Ni Disorder and Improving the Electrochemical Performances of Ni-Rich $LiNi_{0.8}Co_{0.1}Mn_{0.1}O_2$ by Ca Doping, Inorg. Chem. 56 (2017) 8355–8362. https://doi.org/10.1021/acs.inorgchem.7b01035.
[48] S. He, A. Wei, W. Li, X. Bai, L. Zhang, X. Li, R. He, L. Yang, Z. Liu, An in-depth analysis detailing the structural and electrochemical properties within Br− modified LiNi0.815Co0.15A0.035O2 (NCA) cathode material, Electrochimica Acta 318 (2019) 362–373. https://doi.org/10.1016/j.electacta.2019.06.061.
[49] H. Li, P. Zhou, F. Liu, H. Li, F. Cheng, J. Chen, Stabilizing nickel-rich layered oxide cathodes by magnesium doping for rechargeable lithium-ion batteries, Chem. Sci. 10 (2019) 1374–1379. https://doi.org/10.1039/C8SC03385D.
[50] L. Wu, X. Tang, X. Chen, Z. Rong, W. Dang, Y. Wang, X. Li, L. Huang, Y. Zhang, Improvement of electrochemical reversibility of the Ni-Rich cathode material by gallium doping, Journal of Power Sources 445 (2020) 227337. https://doi.org/10.1016/j.jpowsour.2019.227337.

[51] P. Hou, H. Zhang, Z. Zi, L. Zhang, X. Xu, Core-shell and concentration-gradient cathodes prepared via co-precipitation reaction for advanced lithium-ion batteries, Journal of Materials Chemistry A 5 (2017) 4254–4279. https://doi.org/10.1039/c6ta10297b.
[52] N. Takami, Y. Harada, T. Iwasaki, K. Hoshina, Y. Yoshida, Micro-size spherical TiO2(B) secondary particles as anode materials for high-power and long-life lithium-ion batteries, Journal of Power Sources 273 (2015) 923–930. https://doi.org/10.1016/j.jpowsour.2014.09.170.
[53] V.G. Pol, E. Lee, D. Zhou, F. Dogan, J.M. Calderon-Moreno, C.S. Johnson, Spherical Carbon as a New High-Rate Anode for Sodium-ion Batteries, Electrochimica Acta 127 (2014) 61–67. https://doi.org/10.1016/j.electacta.2014.01.132.
[54] M. Weber, J.K. Mayer, A. Kwade, The Carbon Black Dispersion Index DI_CB : A Novel Approach Describing the Dispersion Progress of Carbon Black Containing Battery Slurries, Energy Tech 11 (2023) 2201299. https://doi.org/10.1002/ente.202201299.
[55] L. Pfaffmann, S. Jaiser, M. Müller, P. Scharfer, W. Schabel, W. Bauer, F. Scheiba, H. Ehrenberg, New method for binder and carbon black detection at nanometer scale in carbon electrodes for lithium ion batteries, Journal of Power Sources 363 (2017) 460–469. https://doi.org/10.1016/j.jpowsour.2017.07.102.
[56] R. Dominko, M. Gaberšček, J. Drofenik, M. Bele, J. Jamnik, Influence of carbon black distribution on performance of oxide cathodes for Li ion batteries, Electrochimica Acta 48 (2003) 3709–3716. https://doi.org/10.1016/S0013-4686(03)00522-X.
[57] R. Dominko, M. Gaberscek, J. Drofenik, M. Bele, S. Pejovnik, J. Jamnik, The role of carbon black distribution in cathodes for Li ion batteries, Journal of Power Sources 119–121 (2003) 770–773. https://doi.org/10.1016/S0378-7753(03)00250-7.
[58] N. Susarla, S. Ahmed, D.W. Dees, Modeling and analysis of solvent removal during Li-ion battery electrode drying, Journal of Power Sources 378 (2018) 660–670. https://doi.org/10.1016/j.jpowsour.2018.01.007.
[59] M. Stein, A. Mistry, P.P. Mukherjee, Mechanistic Understanding of the Role of Evaporation in Electrode Processing, J. Electrochem. Soc. 164 (2017) A1616–A1627. https://doi.org/10.1149/2.1271707jes.
[60] J. Klemens, A. Wurba, D. Burger, M. Müller, W. Bauer, S. Büchele, O. Leonet, J.A. Blázquez, I. Boyano, E. Ayerbe, H. Ehrenberg, J. Fleischer, A. Smith, P. Scharfer, W. Schabel, Challenges and Opportunities for Large-Scale Electrode Processing for Sodium-Ion and Lithium-Ion Battery, Batteries & Supercaps 6 (2023) e202300291. https://doi.org/10.1002/batt.202300291.
[61] R. Tao, B. Steinhoff, C.H. Sawicki, J. Sharma, K. Sardo, A. Bishtawi, T. Gibbs, J. Li, Unraveling the impact of the degree of dry mixing on dry-processed lithium-ion battery electrodes, Journal of Power Sources 580 (2023) 233379. https://doi.org/10.1016/j.jpowsour.2023.233379.
[62] W. Bauer, D. Nötzel, V. Wenzel, H. Nirschl, Influence of dry mixing and distribution of conductive additives in cathodes for lithium ion batteries, Journal of Power Sources 288 (2015) 359–367. https://doi.org/10.1016/j.jpowsour.2015.04.081.
[63] M.D. Bouguern, A.K. Madikere Raghunatha Reddy, X. Li, S. Deng, H. Laryea, K. Zaghib, Engineering Dry Electrode Manufacturing for Sustainable Lithium-Ion Batteries, Batteries 10 (2024) 39. https://doi.org/10.3390/batteries10010039.
[64] Y. Liu, R. Zhang, J. Wang, Y. Wang, Current and future lithium-ion battery manufacturing, iScience 24 (2021) 102332. https://doi.org/10.1016/j.isci.2021.102332.
[65] B. Ludwig, J. Liu, I.M. Chen, Y. Liu, W. Shou, Y. Wang, H. Pan, Understanding Interfacial-Energy-Driven Dry Powder Mixing for Solvent-Free Additive Manufacturing of Li-Ion Battery Electrodes, Advanced Materials Interfaces 4 (2017) 1–8. https://doi.org/10.1002/admi.201700570.
[66] D.J. Kirsch, S.D. Lacey, Y. Kuang, G. Pastel, H. Xie, J.W. Connell, Y. Lin, L. Hu, Scalable Dry Processing of Binder-Free Lithium-Ion Battery Electrodes Enabled by Holey Graphene, ACS Appl. Energy Mater. 2 (2019) 2990–2997. https://doi.org/10.1021/acsaem.9b00066.
[67] H. Chen, C. Wang, H. Kang, B. Zhi, C.L. Haynes, A. Aburub, C.C. Sun, Microstructures and pharmaceutical properties of ferulic acid agglomerates prepared by different spherical crystallization methods, International Journal of Pharmaceutics 574 (2020) 118914. https://doi.org/10.1016/j.ijpharm.2019.118914.

[68] M. Ueda, Y. Nakamura, H. Makita, Y. Imasato, Y. Kawashima, Particle design of enoxacin by spherical crystallization technique. I. Principle of ammonia diffusion system (ADS)., Chemical and Pharmaceutical Bulletin 38 (1990) 2537–2541. https://doi.org/10.1248/cpb.38.2537.
[69] D. Amaro-González, B. Biscans, Spherical agglomeration during crystallization of an active pharmaceutical ingredient, Powder Technology 128 (2002) 188–194. https://doi.org/10.1016/S0032-5910(02)00196-1.
[70] J. Thati, Å.C. Rasmuson, Particle engineering of benzoic acid by spherical agglomeration, European Journal of Pharmaceutical Sciences 45 (2012) 657–667. https://doi.org/10.1016/j.ejps.2012.01.006.
[71] A.H.L. Chow, M.W.M. Leung, A study of the Mechanisms of Wet Spherical Agglomeration of Pharmaceutical Powders, Drug Development and Industrial Pharmacy 22 (1996) 357–371. https://doi.org/10.3109/03639049609042001.
[72] Y. Kawashima, F. Cui, H. Takeuchi, T. Niwa, T. Hino, K. Kiuchi, Parameters determining the agglomeration behaviour and the micromeritic properties of spherically agglomerated crystals prepared by the spherical crystallization technique with miscible solvent systems, International Journal of Pharmaceutics 119 (1995) 139–147. https://doi.org/10.1016/0378-5173(94)00380-N.
[73] H. Zhang, Y. Chen, J. Wang, J. Gong, Investigation on the spherical crystallization process of cefotaxime sodium, Industrial and Engineering Chemistry Research 49 (2010) 1402–1411. https://doi.org/10.1021/ie901001c.
[74] J. Thati, Å.C. Rasmuson, On the mechanisms of formation of spherical agglomerates, European Journal of Pharmaceutical Sciences 42 (2011) 365–379. https://doi.org/10.1016/j.ejps.2011.01.001.
[75] J.D. Tew, K. Pitt, R. Smith, J.D. Litster, True bridging liquid-solid ratio (TBSR): Redefining a critical process parameter in spherical agglomeration, Powder Technology 430 (2023) 119010. https://doi.org/10.1016/j.powtec.2023.119010.
[76] O. Arjmandi-Tash, J.D. Tew, K. Pitt, R. Smith, J.D. Litster, A new mathematical model for nucleation of spherical agglomerates by the immersion mechanism, Chemical Engineering Science: X 4 (2019) 100048. https://doi.org/10.1016/j.cesx.2019.100048.
[77] X. Cheng, F. Li, L. Luo, Z. Ding, L. Zeng, Y. Mao, X. Huang, H. Hao, On the selection of wetting liquid for spherical agglomeration of cefotaxime sodium, Powder Technology 363 (2020) 593–601. https://doi.org/10.1016/j.powtec.2019.12.002.
[78] L. Madec, H. Muhr, E. Plasari, Development of new methods to accelerate and improve the agglomeration of submicron particles by binding liquids, Powder Technology 128 (2002) 236–241. https://doi.org/10.1016/S0032-5910(02)00187-0.
[79] D. Posadas-Navarro, C. Palacios, A. Blancas-Cabrera, M.A. Trujillo-Roldán, M. Salinas-Vázquez, G. Ascanio, Flow Patterns of Multiple Axial-Radial Impellers for Potential Use in Aerated Stirred Tanks, Chem Eng & Technol 45 (2022) 860–867. https://doi.org/10.1002/ceat.202100521.
[80] M. Jaszczur, A. Młynarczykowska, A General Review of the Current Development of Mechanically Agitated Vessels, Processes 8 (2020) 982. https://doi.org/10.3390/pr8080982.
[81] Q. Zhu, H. Xiao, R. Zhang, S. Geng, Q. Huang, Effect of impeller type on preparing spherical and dense Ni1−−Co Mn (OH)2 precursor via continuous co-precipitation in pilot scale: A case of Ni0·6Co0·2Mn0·2(OH)2, Electrochimica Acta 318 (2019) 1–13. https://doi.org/10.1016/j.electacta.2019.06.008.
[82] K. Morishima, Y. Kawashima, Y. Kawashima, H. Takeuchi, T. Niwa, T. Hino, Micromeritic characteristics and agglomeration mechanisms in the spherical crystallization of bucillamine by the spherical agglomeration and the emulsion solvent diffusion methods, Powder Technology 76 (1993) 57–64. https://doi.org/10.1016/0032-5910(93)80041-8.
[83] A.P. Pawar, A.R. Paradkar, S.S. Kadam, K.R. Mahadik, Crystallo-co-agglomeration: A novel technique to obtain ibuprofen paracetamol agglomerates, AAPS PharmSciTech 5 (2004). https://doi.org/10.1208/pt050344.
[84] N.M. Mahajan, A.D. Malghade, N.G. Dumore, R.R. Thenge, Design and Development of Crystallo-co-agglomerates of Ritonavir for the Improvement of Physicochemical Properties, Turk J Pharm Sci 15 (2018) 248–255. https://doi.org/10.4274/tjps.44227.

[85] A. Pawar, A. Paradkar, S. Kadam, K. Mahadik, Agglomeration of ibuprofen with talc by novel crystallo-co-agglomeration technique, AAPS PharmSciTech 5 (2004) 30–35. https://doi.org/10.1208/pt050455.
[86] N. Jadhav, A. Pawar, A. Paradkar, Design and evaluation of deformable talc agglomerates prepared by crystallo-Co-agglomeration technique for generating heterogenous matrix, AAPS PharmSciTech 8 (2007) E61–E67. https://doi.org/10.1208/pt0803059.
[87] M.M. Gupta, A. Chatterjee, T. Kumawat, Troubleshooting the Poor Flow Problem of Valsartan Drug Powder Using the Crystallo-Co-Agglomeration Technique, Cureus (2023). https://doi.org/10.7759/cureus.38590.
[88] K. Garala, J. Patel, A. Patel, M. Raval, A. Dharamsi, Influence of excipients and processing conditions on the development of agglomerates of racecadotril by crystallo-co-agglomeration, Int J Pharma Investig 2 (2012) 189. https://doi.org/10.4103/2230-973X.106996.
[89] S.S. Deshkar, G.R. Borde, R.N. Kale, B.A. Waghmare, A.B. Thomas, Formulation of cilostazol spherical agglomerates by crystallo-co-agglomeration technique and optimization using design of experimentation, Int J Pharm Investig 7 (2017) 164–173. https://doi.org/10.4103/jphi.JPHI_39_17.
[90] D. Shah, K. Sorathia, Design and evaluation of sustained release spherical agglomerates of Fluvastatin sodium by crystallo-co-agglomeration, J App Pharm Sci 7 (2017) 99–108. https://doi.org/10.7324/JAPS.2017.70914.
[91] M. Maghsoodi, O. Taghizadeh, G. Martin, A. Nokhodchi, Particle design of naproxen-disintegrant agglomerates for direct compression by a crystallo-co-agglomeration technique, International Journal of Pharmaceutics 351 (2008) 45–54. https://doi.org/10.1016/j.ijpharm.2007.09.033.
[92] J. Drzymala, R. Markuszewski, T.D. Wheelock, Agglomeration with heptane of coal and other materials in aqueous suspensions, Minerals Engineering 1 (1988) 351–358. https://doi.org/10.1016/0892-6875(88)90025-8.
[93] J. Schreier, U. Bröckel, Mehrdimensionale selektive Umbenetzungsagglomeration – Bestimmung der Reinheit von Graphitagglomeraten, Chemie Ingenieur Technik 95 (2023) 1623–1628. https://doi.org/10.1002/cite.202200140.
[94] Mastersizer 3000 User Manual, (2013).
[95] Y.A. Akimov, Mie scattering theory: A review of physical features and limitations, (2024). http://arxiv.org/abs/2401.04146 (accessed June 13, 2024).
[96] F. Ma, Y. Fu, V. Battaglia, R. Prasher, Microrheological modeling of lithium ion battery anode slurry, Journal of Power Sources 438 (2019) 226994. https://doi.org/10.1016/j.jpowsour.2019.226994.
[97] Imerys C-Nergy Super C65 Datasheet, (2021). https://www.imerys.com/product-ranges/c-nergy.
[98] H.H. Hausner, Friction conditions in a mass of metal powder., Polytechnic Inst. of Brooklyn. Univ. of California, Los Angeles, 1967.
[99] G.W. Lee, J.H. Ryu, W. Han, K.H. Ahn, S.M. Oh, Effect of slurry preparation process on electrochemical performances of LiCoO2 composite electrode, Journal of Power Sources 195 (2010) 6049–6054. https://doi.org/10.1016/j.jpowsour.2009.12.101.
[100] A. Yonaga, S. Kawauchi, Y. Mori, L. Xuanchen, S. Ishikawa, K. Nunoshita, G. Inoue, T. Matsunaga, Effects of dry powder mixing on electrochemical performance of lithium-ion battery electrode using solvent-free dry forming process, Journal of Power Sources 581 (2023) 233466. https://doi.org/10.1016/j.jpowsour.2023.233466.
[101] K.L. Sorenson, Comparative Studies on Oxygen Mass Transfer for the Design and Development of a Single-Use Fermentor, 2010. https://digitalcommons.usu.edu/etd/738/.
[102] O.A. Adeleke, Premium ethylcellulose polymer based architectures at work in drug delivery, International Journal of Pharmaceutics: X 1 (2019) 100023. https://doi.org/10.1016/j.ijpx.2019.100023.
[103] T. Wagner, Particlesizer Plugin, ImageJ (Fiji), (2017). https://zenodo.org/badge/latestdoi/18649/thorstenwagner/ij-particlesizer.
[104] K. Pardikar, J. Capindale, K. Pitt, I. Abdi-Rahman, D. Cumming, R. Smith, Spherical agglomeration for local control of electrode microstructure: Generation of structured

agglomerates, Powder Technology 454 (2025) 120688. https://doi.org/10.1016/j.powtec.2025.120688.
[105] Y. Wei, C.Q. Jia, Intrinsic wettability of graphitic carbon, Carbon 87 (2015) 10–17. https://doi.org/10.1016/j.carbon.2015.02.019.
[106] T. Huhtamäki, X. Tian, J.T. Korhonen, R.H.A. Ras, Surface-wetting characterization using contact-angle measurements, Nat Protoc 13 (2018) 1521–1538. https://doi.org/10.1038/s41596-018-0003-z.
[107] C. Devarajulu, VITU, L. Muruganandam, Chemical Engineering Department, SCALE, VIT University, Vellore, TN 632014, India, Effect of Impeller Clearance and Liquid Level on Critical Impeller Speed in an Agitated Vessel using Different Axial and Radial Impellers, JAFM 9 (2016) 2753–2761. https://doi.org/10.29252/jafm.09.06.24824.
[108] B. Ahmed, O. Arjmandi-Tash, J.D. Litster, R.M. Smith, Mechanistic modelling of spherical agglomeration processes, Powder Technology 417 (2023) 118254. https://doi.org/10.1016/j.powtec.2023.118254.
[109] M. Müller, L. Pfaffmann, S. Jaiser, M. Baunach, V. Trouillet, F. Scheiba, P. Scharfer, W. Schabel, W. Bauer, Investigation of binder distribution in graphite anodes for lithium-ion batteries, Journal of Power Sources 340 (2017) 1–5. https://doi.org/10.1016/j.jpowsour.2016.11.051.
[110] H. Gao, Q. Wu, Y. Hu, J.P. Zheng, K. Amine, Z. Chen, Revealing the Rate-Limiting Li-Ion Diffusion Pathway in Ultrathick Electrodes for Li-Ion Batteries, The Journal of Physical Chemistry Letters 9 (2018) 5100–5104. https://doi.org/10.1021/acs.jpclett.8b02229.
[111] M.E. Schrader, Young-Dupre Revisited, Langmuir 11 (1995) 3585–3589. https://doi.org/10.1021/la00009a049.
[112] J.N. Israelachvili, Intermolecular and surface forces, 3rd ed, Academic Press, Burlington, MA, 2011.
[113] N. Rohman, T. Mohiuddin, M.S. Al-Ruqeishi, Surface free energy of graphene-based coatings and its component elements, Inorganic Chemistry Communications 153 (2023) 110855. https://doi.org/10.1016/j.inoche.2023.110855.
[114] J. Li, C. Rulison, J. Kiggans, C. Daniel, D.L. Wood, Superior Performance of $LiFePO_4$ Aqueous Dispersions via Corona Treatment and Surface Energy Optimization, J. Electrochem. Soc. 159 (2012) A1152–A1157. https://doi.org/10.1149/2.018208jes.
[115] V. León, A. Tusa, Y.C. Araujo, Determination of the solid surface tensions, Colloids and Surfaces A: Physicochemical and Engineering Aspects 155 (1999) 131–136. https://doi.org/10.1016/S0927-7757(99)00020-5.
[116] A. Zdziennicka, J. Krawczyk, K. Szymczyk, B. Jańczuk, Components and parameters of liquids and some polymers surface tension at different temperature, Colloids and Surfaces A: Physicochemical and Engineering Aspects 529 (2017) 864–875. https://doi.org/10.1016/j.colsurfa.2017.07.002.
[117] J. Katta, A. Rasmuson, Spherical crystallization of benzoic acid, International Journal of Pharmaceutics 348 (2008) 61–69. https://doi.org/10.1016/j.ijpharm.2007.07.006.
[118] N.E. Shlegel, P.P. Tkachenko, P.A. Strizhak, Influence of viscosity, surface and interfacial tensions on the liquid droplet collisions, Chemical Engineering Science 220 (2020) 115639. https://doi.org/10.1016/j.ces.2020.115639.
[119] C.P. Booth, J.W. Leggoe, Z.M. Aman, The use of computational fluid dynamics to predict the turbulent dissipation rate and droplet size in a stirred autoclave, Chemical Engineering Science 196 (2019) 433–443. https://doi.org/10.1016/j.ces.2018.11.017.
[120] Y. Liu, X. Li, F. Zhang, L. Zhang, T. Zhang, C. Li, Z. Jin, Y. Wu, Z. Du, H. Jiao, Y. Jiang, Y. Yan, Q. Li, W. Kong, Hollow CoS/C Structures for High-Performance Li, Na, K Ion Batteries, Front. Chem. 10 (2022) 845742. https://doi.org/10.3389/fchem.2022.845742.
[121] X. Zhu, J. Tang, H. Huang, T. Lin, B. Luo, L. Wang, Hollow structured cathode materials for rechargeable batteries, Science Bulletin 65 (2020) 496–512. https://doi.org/10.1016/j.scib.2019.12.008.
[122] A. Dominguez, A. Fernandez, N. Gonzalez, E. Iglesias, L. Montenegro, Determination of Critical Micelle Concentration of Some Surfactants by Three Techniques, J. Chem. Educ. 74 (1997) 1227. https://doi.org/10.1021/ed074p1227.

[123] C.D. Reynolds, S.D. Hare, P.R. Slater, M.J.H. Simmons, E. Kendrick, Rheology and Structure of Lithium-Ion Battery Electrode Slurries, Energy Tech 10 (2022) 2200545. https://doi.org/10.1002/ente.202200545.
[124] L. Lang, S. Alexandrov, E. Lyamina, V.M. Dinh, The Behavior of Melts with Vanishing Viscosity in the Cone-and-Plate Rheometer, Applied Sciences 10 (2019) 172. https://doi.org/10.3390/app10010172.
[125] A. Daerr, A. Mogne, Pendent_Drop: An ImageJ Plugin to Measure the Surface Tension from an Image of a Pendent Drop, JORS 4 (2016) 3. https://doi.org/10.5334/jors.97.
[126] J.D. Berry, M.J. Neeson, R.R. Dagastine, D.Y.C. Chan, R.F. Tabor, Measurement of surface and interfacial tension using pendant drop tensiometry, Journal of Colloid and Interface Science 454 (2015) 226–237. https://doi.org/10.1016/j.jcis.2015.05.012.
[127] S. Berg, D. Kutra, T. Kroeger, C.N. Straehle, B.X. Kausler, C. Haubold, M. Schiegg, J. Ales, T. Beier, M. Rudy, K. Eren, J.I. Cervantes, B. Xu, F. Beuttenmueller, A. Wolny, C. Zhang, U. Koethe, F.A. Hamprecht, A. Kreshuk, ilastik: interactive machine learning for (bio)image analysis, Nat Methods 16 (2019) 1226–1232. https://doi.org/10.1038/s41592-019-0582-9.
[128] R.L. Bates, P.L. Fondy, R.R. Corpstein, Examination of Some Geometric Parameters of Impeller Power, Ind. Eng. Chem. Proc. Des. Dev. 2 (1963) 310–314. https://doi.org/10.1021/i260008a011.
[129] Tulus, Mardiningsih, Sawaluddin, O.S. Sitompul, A.K.A.M. Ihsan, Shear rate analysis of water dynamic in the continuous stirred tank, IOP Conf. Ser.: Mater. Sci. Eng. 308 (2018) 012048. https://doi.org/10.1088/1757-899X/308/1/012048.
[130] R. Kol, P. Nachtergaele, T. De Somer, D.R. D'hooge, D.S. Achilias, S. De Meester, Toward More Universal Prediction of Polymer Solution Viscosity for Solvent-Based Recycling, Ind. Eng. Chem. Res. 61 (2022) 10999–11011. https://doi.org/10.1021/acs.iecr.2c01487.
[131] H. Zhou, J. Yang, S. Jing, W. Lan, Q. Zheng, S. Li, Influence of Dispersed-Phase Viscosity on Droplet Breakup in a Continuous Pump-Mixer, Ind. Eng. Chem. Res. 58 (2019) 23458–23467. https://doi.org/10.1021/acs.iecr.9b05239.
[132] I. Waini, U. Khan, A. Zaib, A. Ishak, I. Pop, Thermophoresis particle deposition of $CoFe_2O_4$ - TiO_2 hybrid nanoparticles on micropolar flow through a moving flat plate with viscous dissipation effects, HFF 32 (2022) 3259–3282. https://doi.org/10.1108/HFF-12-2021-0767.
[133] R.J. Gordon, ed., Calculation and measurement techniques for momentum, energy and mass transfer, American Inst. of Chemical Engineers, New York, NY, 1987.
[134] A.G. De Mitri, R. De L. Amaral, H.L. De Moura, J.S. Ayala, J.R. Nunhez, G.J. De Castilho, Tilted PIV: A novel approach for estimating the turbulent kinetic energy in stirred tanks, Measurement 217 (2023) 113112. https://doi.org/10.1016/j.measurement.2023.113112.
[135] A.N. Novikov, Heat capacity and density of methylpyrrolidone solutions of sodium and potassium perchlorates at different concentrations and 298.15 K, Russ. J. Phys. Chem. 84 (2010) 1337–1339. https://doi.org/10.1134/S003602441008011X.
[136] L.W. McKeen, Solvent Systems, in: Fluorinated Coatings and Finishes Handbook, Elsevier, 2016: pp. 107–118. https://doi.org/10.1016/B978-0-323-37126-1.00006-0.
[137] P. Kneisl, J.W. Zondlo, Vapor pressure, liquid density, and the latent heat of vaporization as functions of temperature for four dipolar aprotic solvents, J. Chem. Eng. Data 32 (1987) 11–13. https://doi.org/10.1021/je00047a003.
[138] A.S. Rodgers, J. Chao, R.C. Wilhoit, B.J. Zwolinski, Ideal Gas Thermodynamic Properties of Eight Chloro- and Fluoromethanes, Journal of Physical and Chemical Reference Data 3 (1974) 117–140. https://doi.org/10.1063/1.3253135.
[139] V. Majer, L. Šváb, V. Svoboda, Enthalpies of vaporization and cohesive energies for a group of chlorinated hydrocarbons, The Journal of Chemical Thermodynamics 12 (1980) 843–847. https://doi.org/10.1016/0021-9614(80)90028-2.
[140] K. Sitarek, J. Stetkiewicz, Assessment of Reproductive Toxicity and Gonadotoxic Potential of N-Methyl-2-Pyrrolidone in Male Rats, International Journal of Occupational Medicine and Environmental Health 21 (2008). https://doi.org/10.2478/v10001-008-0006-z.
[141] K. Sitarek, J. Stetkiewicz, W. Wąsowicz, Evaluation of Reproductive Disorders in Female Rats Exposed to *N* -Methyl-2-Pyrrolidone, Birth Defects Research Pt B 95 (2012) 195–201. https://doi.org/10.1002/bdrb.21001.

[142] R. Tao, B. Steinhoff, X.-G. Sun, K. Sardo, B. Skelly, H.M. Meyer, C. Sawicki, G. Polizos, X. Lyu, Z. Du, J. Yang, K. Hong, J. Li, High-throughput and high-performance lithium-ion batteries via dry processing, Chemical Engineering Journal 471 (2023) 144300. https://doi.org/10.1016/j.cej.2023.144300.
[143] C. Lei, K.S. Ryder, A.P. Abbott, J.M. Yang, Using ultrasonic oil–water nano-emulsions to purify lithium-ion battery black mass, RSC Sustainability 3 (2025) 1516–1523. https://doi.org/10.1039/D4SU00771A.
[144] S.C. Kosnik, Z. Leuter, K. Schwickert, Achieving New Scales: The First Successful Pilot Plant Spherical Crystallization, Org. Process Res. Dev. 29 (2025) 311–321. https://doi.org/10.1021/acs.oprd.4c00350.